DISSERTATION

Two-Color Synergistic Photochemistry for Network Formation and Lithography

Jan Patrick Hobich

2025

DISSERTATION

zur

Erlangung der Doktorwürde (Dr. rer. nat.)

der

Gesamtfakultät für Mathematik, Ingenieur- und Naturwissenschaften

der

Ruprecht-Karls-Universität Heidelberg

vorgelegt von

Jan Patrick Hobich

aus Bad Homburg

Tag der mündlichen Prüfung

05. Dezember 2025

Two-Color Synergistic Photochemistry for Network Formation and Lithography

Gutachter

Prof. Dr. Eva Blasco

Prof. Dr. Christopher Barner-Kowollik

Für meinen kleinen Bruder Morten.

Ich liebe dich.

„Wie definierst du dein Glück? Zwei Schritte vorwärts und niemals einen zurück!"

MORE10, Sommertage (2021)

Eidesstattliche Versicherung

gemäß § 8 der Promotionsordnung für die Naturwissenschaftlich-Mathematische Gesamtfakultät der Universität Heidelberg.

1. Bei der eingereichten Dissertation zu dem Thema „*Two-Color Synergistic Photochemistry for Network Formation and Lithography*“ handelt es sich um meine eigenständig erbrachte Leistung.
2. Ich habe nur die angegebenen Quellen und Hilfsmittel benutzt und mich keiner unzulässigen Hilfe Dritter bedient. KI-basierte Tools (DeepL und OpenAI GPT-5) wurden zur Unterstützung genutzt, jedoch ausschließlich zur sprachlichen Überarbeitung und Fehlerkorrektur, nicht jedoch zur eigenständigen Erstellung von Inhalten oder Argumentationsstrukturen. Insbesondere habe ich wörtlich oder sinngemäß aus anderen Werken übernommene Inhalte als solche kenntlich gemacht.
3. Die Arbeit oder Teile davon habe ich bislang nicht an einer Hochschule des In- oder Auslands als Bestandteil einer Prüfungs- oder Qualifikationsleistung vorgelegt.
4. Die Richtigkeit der vorstehenden Erklärungen bestätige ich.
5. Die Bedeutung der eidesstattlichen Versicherung und die strafrechtlichen Folgen einer unrichtigen oder unvollständigen eidesstattlichen Versicherung sind mir bekannt.

Ich versichere an Eides statt, dass ich nach bestem Wissen die reine Wahrheit erklärt und nichts verschwiegen habe.

Heidelberg, den 22.10.2025

Jan Patrick Hobich

Acknowledgements

First, I would like to express my heartfelt gratitude to my supervisory team – **Christopher**, **Eva**, and **Hatice** – who have each played a substantial role in my development throughout my PhD. Having three supervisors might sound stressful and complicated, but that was never the case for me. I am deeply thankful for the continuous support and constructive feedback I received, especially during the early stages when nothing seemed to work. Your patience and encouragement kept me motivated through those challenging times. I truly appreciate how promptly you respond to my emails (almost at lightspeed) and I am fully aware that this is a great privilege. Throughout my PhD, I always felt respected, trusted, and supported. It was clear to me that you did not only care about the results I produced, but also about me as a person and when I went through personal difficulties, I did not hesitate to share them with you, knowing that I would be met with empathy and understanding.

Christopher, there were many moments when I felt disappointed with my results and uncertain about upcoming meetings, but your consistently encouraging and positive attitude always lifted me up and I left every meeting with a good feeling. You motivated me, made me feel appreciated, and gradually helped me build more confidence. I was especially happy when we finally met in person after 1.5 years, and I truly enjoyed our open, fruitful scientific discussions in such a positive atmosphere. I am very grateful that I was able to conduct my PhD in your group, even though I was a photochemistry novice, and for how much I have learned from you, including your genuine passion for photochemistry.

Eva, even though my PhD situation was somewhat complex, with supervisors in different countries and me being based at KIT, I always felt welcome in Heidelberg and as part of the group. I am very thankful that you made it possible for me to pursue my PhD under the joint supervision of you, Christopher, and Hatice. Although I spent the least amount of time with you in Heidelberg, I truly value your calm and reliable manner, and I always felt that I could fully trust you.

Hatice, I have known you the longest. While I was working on my PhD, you managed to advance to a full professorship in Kaiserslautern. From my Vertiefer and Master studies, through my time as a Hiwi, up to my PhD, you have been my mentor. You have continuously believed in me and pushed me to grow, even though we tend to operate on different timescales and I sometimes needed a bit of time to adapt. I have always felt your trust in my abilities, even at times when I doubted myself. Beyond the scientific work, I have always felt that you see and appreciate me as a person. I particularly enjoyed activities like the KIT run or get-togethers with the Softies. Your cheerful attitude and curiosity for chemistry were a great source of motivation when I first met you, I am so glad to be one of your first PhD students and I am sure there will be many more to come. I will always appreciate your trust and

support over all these years, which you kept up, even when you were facing challenging times. Thank you so much!

I would also like to thank all the other **Softies** of the SML – first and foremost Birgit and Meryem – who showed me how valuable a pleasant and fun working atmosphere can be. I truly enjoyed my time and learned a lot at the SML.

My thanks also go to the **Blasco group**, who always welcomed me with open arms whenever I visited Heidelberg for events such as the Christmas parties and group trips. Special thanks to Joël, Clara, Philipp, Christoph, Marcus and Niklas, but honestly, the whole group was always eager to chat and made me feel integrated and treated as part of the team. Therefore, I always have warm feelings when visiting Heidelberg.

Since part of my PhD was carried out in Brisbane, I would also like to thank the **Macroarc group at QUT**. I had a wonderful time in Australia and learned a lot about myself during my stay. I really enjoyed being surrounded by so many peers, which created a lively and social atmosphere and made it easy to feel welcome and meet new people. My time in Australia often felt like a holiday, even when I was working on campus, and I am very thankful for that experience.

Now I would like to thank the Microarc node at INT, where I spent most of my working time during the PhD. I am very glad that I could work with such excellent scientists and wonderful people at INT. Special thanks go to **Matthias**, my former office buddy and Australia companion. I always enjoy spending time with you and I am genuinely happy that I somehow convinced you not to try your luck with a PhD in another group. Especially during our time in Australia, I was incredibly grateful to have a real friend by my side. I enjoyed all our small trips, culinary adventures, and simply having someone to rely on, far from home. Now that we practically live next door to each other, I am sure we will stay in touch. Thank you, Matthias!

On my journey from a photochemistry beginner throughout my entire PhD, **Florian** played a major role, especially when discussing new ideas, results, or any kind of problem. I have great respect for you, particularly for your passion for science and the pursuit of truth. Even though your opinions may sometimes seem blunt (and may hurt a bit), I've come to understand that this stems from your honesty and directness which are qualities I have come to deeply appreciate and that have undoubtedly enhanced the quality of my work. I also want to thank you for always having your door open and taking the time to discuss things with me, despite your busy schedule.

Xingyu, I am really happy that we met in Brisbane, and it's great that you also joined our KIT node in Germany. I truly enjoyed our scientific collaboration, and it's always fun talking and joking with you. I really appreciate that cheerful atmosphere. **Aidan**, you have become a good friend along the way. I

always enjoy having a drink with you or just talking random nonsense. Hopefully, I will get to visit you in Würzburg one day! **Steven**, you are definitely the funniest physicist I know, and I really enjoyed sharing an office with you. I also appreciate the table tennis matches against **Josephine**, as well as our random chats or drinks after work. I'm genuinely happy that we somehow became an unofficial group together with the Wegener INT physicists. I also want to thank **Linh** for all the jokes and fun moments, even though we pretty much only met each other in the lab. **Natalia**, I am very happy you joined our group last year. I really enjoy our chats and admire your diligence and commitment to learning and producing high-quality work. **Julian**, although we didn't work closely together, your motivation and drive truly inspired me at a time when I was feeling discouraged, helping me keep my head up and carry on.

Phillip, you were the first student I supervised, and I learned a lot from the experience. I am really glad you decided to stay for your master's thesis after your Hiwi work, and I wish you all the best for your own PhD! **Willie**, as the second student I supervised, I truly admire how quickly you adapted, jumping from your first semester straight into OCF-level synthesis. You were an enormous help during the final stages of my PhD, saving me a lot of time and tedious synthesis work. You are diligent, motivated, and eager to learn and I hope you'll stay with the group a while longer.

I would also like to thank my longest-standing chemistry mates, the "Pelikane" – **Daniel**, **Marten**, **Nico**, **Pirmin**, and **Timo**. We went through thick and thin together, and you made it possible for me to truly enjoy my studies with plenty of fun and without ever losing motivation. Even though we only meet from time to time now, you all hold a very special place in my life.

Beyond work, I've had tremendous support and great times throughout my studies and PhD, and I would like to give special thanks to my invaluable friends from school, whom I deeply value – **Stefan**, **Florian**, **Emi**, **Lars**, **Nico**, and **Nicolai**. I also want to thank my newer friends from the "**Sockenfreuende**" who became part of my life during my studies. I am especially thankful to **Sofie**, for always being by my side, for your unwavering support throughout this journey and for making my life so much brighter.

Last but not least, I want to thank my family. **Oma Käthe**, thank you for always being there for me and for the occasional financial support, which definitely made my life easier. **Lars**, my dear middle brother, even though we don't see each other regularly, I know I can always rely on you and that you'll support me without hesitation whenever I need help. **Morten**, my dear little brother, I miss you a lot and want to thank you sincerely for teaching me so much about myself and about life. I always enjoyed our fun times and joking around, and you can be sure that I love you! And finally, **Sabine** and **Thomas**, my one and only parents, I am infinitely grateful for your love and support throughout my whole life. You made it easy for me to find my path because you always trusted me to make my own (and hopefully right) decisions. Thank you for always believing in me and supporting me in every possible way.

Abstract

The advent of precision photochemistry is a logical consequence from advances in light-generation technologies that enable access to almost any desired wavelength, coupled with wavelength-resolved reactivity insights into complex photochemical processes. Beyond optimizing individual photoreactions, the integration of multiple wavelengths into a single system unlocks entirely new reaction modes. The synergistic two-color reaction represents a particularly powerful mode, in which an irreversible transformation (i.e., bond formation) is enabled – or significantly enhanced – only when two distinct wavelengths of light coincide in the same volume element. Herein, a synergistic two-color reaction system is introduced, based on the interplay of two photoswitches activated at different wavelengths. A diaryl indenone epoxide (DIO) undergoes ring expansion under ultraviolet light (365 nm), whereas a bridged ring-strained azobenzene (SA) performs *cis*-to-*trans* isomerization under visible light (430 nm) irradiation. When triggered simultaneously, the photoactivated species readily undergo cycloaddition to form the DIOSA cycloadduct, which was structurally elucidated by single-crystal X-ray diffraction (SXRD). The photochemical synergistic ratio ϕ_{syn} is introduced as a function of product yield to quantitatively assess the effectiveness of dual-color irradiation under defined reaction conditions such as photon flux and starting material ratio. A reduced form, ϕ_{syn}^{0} – extrapolated to infinitesimal small conversion – serves as a conversion-independent metric for comparing the efficiency of synergistic photochemistries under varied reaction conditions and across different systems.

Building on the above model study, the reaction was next transferred from the small-molecule to the macromolecular scale to enable synergistic two-color polymer network formation and lithography as a wavelength-gated strategy with enhanced spatiotemporal control over crosslinking. For photoresist preparation, DIO and SA moieties were incorporated into different multifunctional macromolecular scaffolds and dissolved in acetophenone. The successful translation of the synergistic model reaction into crosslinking for network formation was first confirmed via size-exclusion chromatography (SEC) kinetics under one- and two-color light-emitting diode (LED) exposure. Finally, the reaction was implemented in a dual-laser lithography setup, enabling the synergistic fabrication of intricate geometries such as ring segments and butterfly architectures under specifically optimized printing conditions.

Kurzfassung

Präzisionsphotochemie ist eine logische Folge technologischer Fortschritte in der Lichterzeugung, die den Zugang zu nahezu jeder gewünschten Wellenlänge eröffnen, kombiniert mit wellenlängenaufgelösten Erkenntnissen zur Reaktivität komplexer photochemischer Prozesse. Über die Optimierung einzelner Photoreaktionen hinaus eröffnet die Integration mehrerer Wellenlängen in einem System völlig neue Reaktionsmodi. Ein besonders leistungsstarker Ansatz ist die synergistische Zwei-Farben-Reaktion, bei der ein irreversibler Prozess (z. B. Bindungsbildung) nur dann ermöglicht oder erheblich beschleunigt wird, wenn zwei unterschiedliche Wellenlängen des Lichts im gleichen Volumenelement überlappen. In dieser Arbeit wird ein synergistisches Zwei-Farben-Reaktionssystem vorgestellt, das auf der Kombination von zwei bei unterschiedlichen Wellenlängen aktivierten Fotoschaltern basiert. Ein Diarylindenon-Epoxid (DIO) durchläuft unter Bestrahlung mit ultraviolettem Licht (365 nm) eine Ringerweiterung, während ein verbrücktes, ringgespanntes Azobenzol (SA) unter Bestrahlung mit sichtbarem Licht (430 nm) eine *cis*-zu-*trans*-Isomerisierung erfährt. Bei gleichzeitiger Aktivierung reagieren die photoaktivierten Spezies über eine Cycloaddition zu dem Cycloaddukt DIOSA, dessen Struktur durch Einkristalldiffraktometrie (SXRD) aufgeklärt wurde. Zur quantitativen Bestimmung der synergistischen Effizienz einer Zwei-Farben-Bestrahlung unter definierten Reaktionsbedingungen wie Photonenfluss und Eduktverhältnis wird der photochemische Synergiefaktor ϕ_{syn} als Funktion der Produktausbeute eingeführt. Eine reduzierte Form, ϕ_{syn}^{0} – extrapoliert auf infinitesimal kleine Umsätze – dient als umsatzunabhängige Metrik zum Vergleich der synergistischen Effizienz unter unterschiedlichen Reaktionsbedingungen und über verschiedene Systeme hinweg.

Aufbauend auf dieser Modellstudie wurde die Reaktion auf die makromolekulare Ebene übertragen, mit dem Ziel, synergistische Zwei-Farben-Polymernetzwerkbildung und Lithografie als wellenlängengesteuerte Strategie für eine verbesserte räumliche und zeitliche Kontrolle der Vernetzung zu realisieren. Zur Herstellung des Fotolacks wurden DIO- und SA-Einheiten in multifunktionale makromolekulare Gerüste eingebaut und in Acetophenon gelöst. Die erfolgreiche Übertragung der Modellreaktion auf die Polymernetzwerkbildung wurde zunächst durch Gel-Permeations-Chromatographie (GPC)-Kinetiken unter Ein- und Zwei-Farben-Belichtung mit Leuchtdioden (LEDs) bestätigt. Schließlich wurde die Reaktion in einem laserbasierten Lithografieaufbau implementiert, was die synergistische Herstellung komplexer Geometrien wie Ringsegmente und einer Schmetterlingsstruktur unter speziell optimierten Druckbedingungen ermöglichte.

Abbreviations

2D	two-dimensional
3D	three-dimensional
4D	four-dimensional
A	Absorbance
A_1	parameter for exponential fit for one-color kinetics
A_2	parameter for exponential fit for two-color kinetics
AIBN	azobisisobutyronitrile
APAT	*N*,*N*-(dimethyl)aminopyrene aryl tetrazole
ATR-IR	attenuated total reflectance infrared spectroscopy
c	Concentration
CAD	computer-aided design
COSY	^{1}H-^{1}H Correlation Spectroscopy
$Đ$	dispersity
DBU	1,8-diazabicyclo[5.4.0]undec-7-ene
DCM	Dichloromethane
DIO	diaryl indenone epoxide
DIO'	metastable DIO isomer after photoactivation
DIOnor	cycloadduct of the reaction between photoactivated DIO and norbornene
DIO-OH	DIO derivative with a hydrohexyl functionality
DIOSA	cycloadduct of the reaction between photoactivated DIO and SA
DLP	digital light processing
DMAP	4-dimethylaminopyridine
DMF	dimethylformamide
DMSO	dimethyl sulfoxide
DRI	refractive index detector
DSC	differential scanning calorimetry
e.g.	exempli gratia / for example
EA	ethyl acetate
EHA	2-ethylhexyl acrylate
E_{pulse}	laser pulse energy above the aluminum block
eq.	Equivalents
et al.	et alii (and others)
f_{rep}	laser repetition rate
HMBC	^{1}H-^{13}C Heteronuclear Multiple Bond Correlation
HRMS	high resolution mass spectrometry
HSQC	^{1}H-^{13}C Heteronuclear Single Quantum Correlation
I	intensity of attenuated light
i.e.	id est / that is to say
I_0	intensity of incident light
I_{DIOnor}	LC integral of the DIOnor at the beginning of the reaction
$I_{DIOnor,max}$	LC integral of the DIOnor at the end of the reaction

I_{DIOSA}	normalized LC integral of the DIOSA compound at the end of the reaction
$I_{DIOSA,max}$	normalized LC integral of the DIOSA compound at the beginning of the reaction
^{i}PrOH	isopropanol
IR	Infrared
IR	internal conversion
I_{SA}	normalized LC integral of the SA compound at the end of the reaction
$I_{SA,0}$	normalized LC integral of the SA compound at the beginning of the reaction
ISC	Intersystem crossing
I_{TMB}	LC integral of TMB at the beginning of the reaction
$I_{TMB,max}$	LC integral of TMB at the end of the reaction
ITX	isopropyl thioxanthone
k_1	parameter for exponential fit for one-color kinetics
k_2	parameter for exponential fit for two-color kinetics
l	path length
LC-MS	liquid Chromatography-mass spectrometry
LED	light-emitting diode
MC	merocyanine
M_n	number average molar mass
Mono LISA	monochromatic tunable laser with a custom-designed 3D printing platform
N_A	Avogadro's number
NIR	near-infrared
NITEC	nitrile-imine mediated tetrazole-ene cycloaddition
NMR	nuclear magnetic resonance
NOESY	nuclear Overhauser effect spectroscopy
N_p	number of photons
o-MBA	*ortho*-methyl benzaldehyde
OPO	optical parametric oscillators
PEG	polyethylene glycol
PEGDA	polyethylene glycol diacrylate
PMMA	poly(methyl methacrylate)
polyDIO	polymer bearing multiple DIO moieties
PSS	photostationary state
PTFE	poly (tetrafluoroethylene)
Py-Chal	pyrene chalcone
SA	ring-strained azobenzene
SA'	metastable SA isomer after photoactivation
SA-3arm	photoresist compound with three SA moieties
SA-OH	SA derivative with a hydrohexyl functionality
SEC	size-exclusion chromatography
SLA	Stereolithography
S_n	excited singlet state n
STED	stimulated emission depletion
STP	Spirothiopyran
SXRD	single-crystal X-ray diffraction

$t_{1/2}$	half-life
TEGMA	triethylene glycol methyl ether methacrylate
T_g	glass transition temperature
TGA	thermogravimetric analysis
THF	Tetrahydrofuran
TLP	two-photon lithography
TMB	1,3,5-trimethoxybenzene
T_n	excited triplet state n
T_λ	wavelength-dependent glass transmission
UV-Vis	ultraviolet-visible
V	Volume
VR	vibrational relaxation
Y_1	yield under one-color irradiation
Y_2	yield under two-color irradiation
Y_{lower}	lower 95% confidence band for the yield
Y_{upper}	lower 95% confidence band for the yield
ε	extinction coefficient
ρ	product yield for quantum yield calculations
Φ_λ	photon flux at wavelength λ
ϕ_{syn}	synergistic ratio
ϕ_{syn}^0	conversion-independent synergistic ratio

Contents

List of Publications and Conference contributions:

The results described in this thesis and part of the theoretical background were published and additionally presented at conferences. The published work of the author as first coauthor (and shared first coauthor, marked here with a "‡") includes:

Peer-reviewed articles:

- **J. Hobich**, E. Blasco, M. Wegener, H. Mutlu, C. Barner-Kowollik, *Macromol. Chem. Phys.* **2023**, *224*, 2200318.
  (Thesis section: 2.4)
- **J. Hobich**, F. Feist, P. Werner, J. A. Carroll, O. Fuhr, E. Blasco, H. Mutlu, C. Barner-Kowollik, *Angew. Chem. Int. Ed.* **2025**, *64*, e202413530.
  (Thesis sections: 1, 4.1 – 4.3)
- **J. Hobich‡**, X. Wu‡, F. Feist, W. Scheibel, N. Herdt, P. Somers, E. Blasco, H. Mutlu, C. Barner-Kowollik, *Angew. Chem. Int. Ed.* **2025**, e202518815.
  (Thesis sections: 4.4 – 4.6)

Conferences:

- **J. Hobich**, F. Feist, P. Werner, J. A. Carroll, O. Fuhr, E. Blasco, H. Mutlu, C. Barner-Kowollik, "Quantification of Synergistic Two-Colour Covalent Bond Formation", 29th IUPAC Symposium on Photochemistry, July 2024.
- **J. Hobich‡**, X. Wu‡, F. Feist, W. Scheibel, N. Herdt, P. Somers, E. Blasco, H. Mutlu, C. Barner-Kowollik, "Synergistic Two-Color Photochemical Network Formation and Lithography", Bayreuth Polymer Symposium 2025, September 2025.

1. Introduction

Three-dimensional (3D) printing has emerged as a versatile platform for fabrication of complex architectures with high precision, especially via light-based techniques such as stereolithography (SLA), digital light processing (DLP), and two-photon lithography (TPL).[1-6] Recent advances in the field of 3D printing build on the incorporation of multiple wavelengths of light, which extends the design space of additive manufacturing far beyond the limitations of single-color systems.[7-9] Distinct wavelengths can be harnessed to finetune spatial and temporal control for greater accuracy, while at the same time enabling fundamentally new reaction modes based on synergistic, antagonistic, orthogonal, and cooperative mechanisms.[8-10] These modes open avenues toward photochemically addressable materials with enhanced function and structural complexity. Within this framework, synergistic photochemistry is especially powerful, as it combines the rapid formation of polymer networks with high precision over the crosslinking.[11] In a synergistic two-color system, a targeted process such as covalent bond formation occurs exclusively at the intersection of two specific wavelengths of light. The dual-gated mechanism enables spatially localized and temporally controlled photochemical activation, thereby suppressing undesired side reactions and enhancing pattern resolution. Indeed, synergistic approaches have already shown considerable promise in projection-based lithography and 3D microfabrication.[11-15]

The class of molecular photoswitches represents highly attractive candidates for the development of such systems, as they reversibly alter their structure upon light irradiation.[16-20] By tuning their chemical structures, photochemical properties such as absorbance profiles and wavelength-dependent reactivities can be precisely adjusted, enabling the rational design of λ-orthogonal reactivity windows.[21-26] Recent advances in engineering photoswitches with red-shifted absorbance spectra and enhanced quantum yields have markedly broadened their applicability, allowing efficient isomerization under mild conditions across the visible and even into the near-infrared region. These advancements make photoswitches particularly well-suited as key components in synergistic photochemistries, where selective activation with multiple distinct wavelengths is essential.[17, 27-29]

One of the earliest demonstrations of a synergistic system was reported by our group in 2022, employing two distinct photoswitches that can be independently activated at different wavelengths to induce covalent crosslinking of a polymer network under two-color irradiation.[30] In that system, however, once converted to their reactive isomers, the photoswitches did not rapidly revert to their unreactive forms at ambient conditions. This limitation restricts the applicability of the approach for

processes such as light-sheet printing, where all reactivity must cease immediately upon deactivation of at least one light source.[8]

Herein, a dual-photoswitch system was developed that enables synergistic two-color covalent bond formation.[31] The synergy relies on two complementary components: a diarylindenone epoxide (DIO) and a ring-strained azobenzene derivative (SA) from the diazocine family.[32] Upon UV (ultraviolet) irradiation (365 nm), DIO undergoes ring expansion to form a reactive isomer, DIO',[33] while visible light (430 nm) induces *cis*-to-*trans* isomerization of SA to SA'.[34-36] Notably, both parent compounds remain inert in the absence of light, yet their photogenerated isomers possess complementary reactivities: DIO' selectively reacts with ring-strained double bonds, whereas *trans*-configured SA' bears a highly strained azo bond that undergoes cycloaddition, driven by strain-release.[33, 35] When activated simultaneously, the two photoswitches undergo selective covalent bond formation to yield the cycloadduct DIOSA (**Figure 1**).

Mechanistic studies at the small-molecule scale combined structural and kinetic analyses via photochemical action plots,[37] single-crystal X-ray diffraction (SXRD), liquid chromatography-mass spectrometry (LC-MS), and nuclear magnetic resonance (NMR) spectroscopy. To quantify synergistic efficiency, the synergistic ratio ϕ_{syn} was introduced as a benchmark metric for multi-color photochemical systems, enabling assessment of spatial selectivity and light-gated reactivity. A conversion-independent variant, ϕ_{syn}^{0}, was further established to allow comparability across diverse reaction conditions and even different systems. Beyond the fundamental photochemical insights, the results provide a foundation for tailoring advanced photoresists suitable for synergistic two-color lithography and 3D printing.[31]

Building on these findings, the dual-switch concept was translated from the small-molecule to the macromolecular level, yielding a photoresist system composed of DIO and SA units tailored for synergistic two-color crosslinking.[38] Embedding the photoswitches within polymer architectures enabled dual-wavelength control over network formation that was suitable for lithographic fabrication, a transition that marks a critical step from fundamental photochemistry toward application-oriented materials science. The capabilities of the system were demonstrated through lithographic patterning experiments under one- and two-color irradiation, highlighting the benefits of synergistic activation. More broadly, the potential of wavelength-encoded photochemistry is emphasized, with a focus on next-generation 3D printing techniques. Triggering specific responses by orthogonal light inputs not only improves control over the formation of polymer networks but also paves the way for rapid fabrication of intricate architectures with high resolution by exploiting two-color photochemical synergy. Accordingly, this advance establishes a framework for precision

photochemistry and highlights how the rational designed of molecular photoswitches can be harnessed for next-generation additive manufacturing applications.[39]

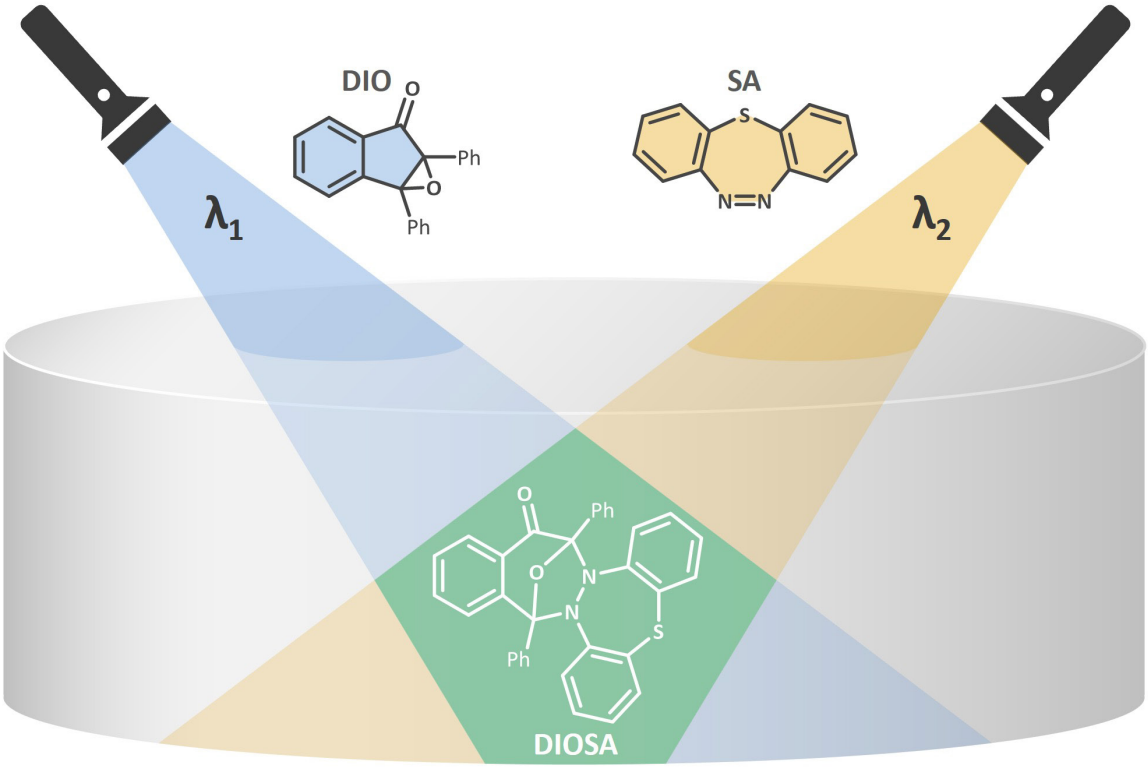

Figure 1. Schematic illustration of synergistic two-color photochemistry for the reaction between a diaryl indenone epoxide (DIO) and a ring-strained azobenzene (SA) to DIOSA. Adapted from Hobich *et al*.[31]

2. Theoretical Background

2.1 Photochemistry Fundamentals

Light has always played a key role in the development and preservation of life on earth as we know it today.[40] In particular, photosynthesis produces oxygen and simultaneously binds carbon dioxide into organic substances that serve as basis of the food chain.[41] Inspired by its enormous significance in nature, the chemistry of light has also received a substantial attention, as it offers unprecedented potential and possibilities, particularly for the design and manipulation of polymer materials.[42-44] A fundamental asset of photochemistry is the simplicity and precise control over where and when light is applied as a stimulus, which is referred to as spatiotemporal control.[45-47] Moreover, visible light in particular is harmless to living organisms, which gives it great potential for use in biological and medical applications.[45, 48]

One of the very first and important understandings of photochemistry, independently reported by Grotthuss (1818)[49] and Draper (1841)[50] states that light needs to be absorbed first in order for a photochemical reaction to occur. More specifically, the process of absorption describes how a photon provides the energy for an electronic transition to an excited state, which is the first step for all subsequent photophysical and photochemical processes. When a beam of light is passed through a sample, the Beer-Lambert-law describes the relationship between the absorbance A of a molecule in solution to the intensity of the incident and attenuated light, I_o and I, respectively. Additionally, the absorbance is proportional to the extinction coefficient ε, a wavelength-dependent intrinsic value of the molecule, concentration c and the path length l in solution.[51, 52]

$$log_{10}\left(\frac{I_o}{I}\right) = A = \varepsilon cl$$

Absorption of a photon leads to an electronic transition from the singlet ground state S_0 of a molecule to an exited singlet state S_x which depends on the energy of the photon and occurs on a timescale of 10^{-15} s.[53] Relaxation of the electron back to S_0 can occur via various pathways that are visualized in a Jablonski diagram (**Figure 2**).[54] Usually absorption leads to a higher vibrational state of S_1 or S_2, followed by relaxation to the lowest vibrational level within 10^{-12} s via vibrational relaxation (VR).[53] For simplification, the following relaxation pathways assume absorption with a transition of $S_0 \rightarrow S_1$ as shown in **Figure 2**. Non-radiative decay can now occur via internal conversion (IC) between two spin states of the same multiplicity ($S_1 \rightarrow S_0$) on a timescale of 10^{-12} s[53] and subsequent VR to the lowest vibrational state of S_0. Intersystem crossing (ISC) is the spin-forbidden analogue to IC with a transition between different multiplicities ($S_1 \rightarrow T_1$) and occurs on the timescale of 10^{-10} s.[55] Transitions,

facilitated by emission of a photon are termed radiative decay and typically proceed from the lowest vibrational state of S_1 after VR to an elevated vibrational state of S_0, followed by VR. Since part of the energy dissipated via VR, the emitted photon is of lower energy, i.e. longer wavelength, compared to the incident light and independent of its wavelength which is also known as "Kasha's rule". Therefore, the emission maximum is red-shifted to longer wavelengths relative to the absorbance maximum (Stokes-shift). Fluorescence is the spin-allowed transition ($S_1 \rightarrow S_0$) for radiative decay while phosphorescence is a spin-forbidden transition ($T_1 \rightarrow S_0$) that occur on timescales of nanoseconds and of microseconds up to seconds, respectively.[53, 56]

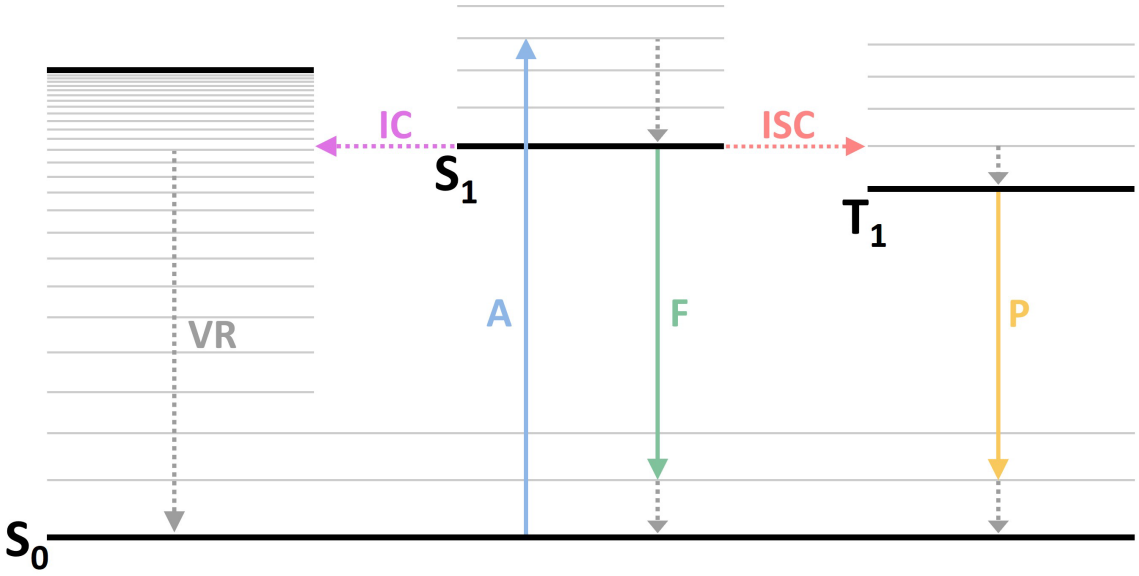

Figure 2. Jablonski Diagram, summarizing the different relaxation pathways after electronic transition $S_0 \rightarrow S_1$ via photon absorption (A, blue). Vibrational relaxation (VR, grey), radiative transitions: fluorescence (F, green) and phosphorescence (P, yellow), non-radiative transitions: internal conversion (IC, pink) and intersystem crossing (ISC, red). Adapted from Ref.[57]

Nevertheless, a photoexcitation does not necessarily have to end with a decay over radiative and non-radiative pathways to the ground state. Instead, the energy provided by the absorbed photon can also generate species that are prone to undergo chemical reactions in their excited states, e.g. bond cleavage, bond formation or isomerization.[58] While these processes can originate from both singlet and triplet states, triplet states in particular play an important role in photochemistry, as many photochemical reactions have been shown to occur from there. Some examples are the homolytic bond-cleavage of photoinitiators,[59, 60] photoinduced cycloadditions[61, 62] and photoenolization.[63, 64]

2.2 Photoswitches

Photoswitches are molecules that reversibly isomerize between at least two different molecular structures upon irradiation with light, resulting in changes of the geometry and π-conjugation. Consequently, the physical and chemical properties of the isomers differ as well, resulting in alterations of polarity and absorbance spectrum and therefore the color, a behavior known as photochromism. Other properties of interest are their rate of reversibility, fatigue resistance and the operational wavelength range for the activation of a switching process.[46, 65]

Generally, a distinction is made between T- and P-type photoswitches that focuses on the type of pathways for the reversion after activation with light. On the one hand, T-type photoswitches undergo thermal reversion from the metastable to the thermally stable isomer, which does not mean that reversion always proceeds rapidly as lifetimes can range from nanoseconds[66] to millennia.[67] The majority of photoswitches reverse thermally, for example azobenzenes, spiropyrans and indigo dyes. On the other hand, P-type photoswitches isomerize purely via photochemical activation in both directions, e.g. diarylethenes and fulgides. Nevertheless, most T-type photoswitches can undergo photochemical reversion as well and are not limited to thermal means, with dihydroazulenes[68] being an exception. The two main modes of photoswitching reactions are *cis*/*trans* (*Z*/*E*) isomerization (e.g. azobenzenes and indigo dyes) and electrocyclization/ring-opening via bond formation or cleavage (e.g. spiropyrans and diarylethenes). Some of the most important photoswitches and their reversible reactions are depicted in **Figure 3**.[46, 69, 70]

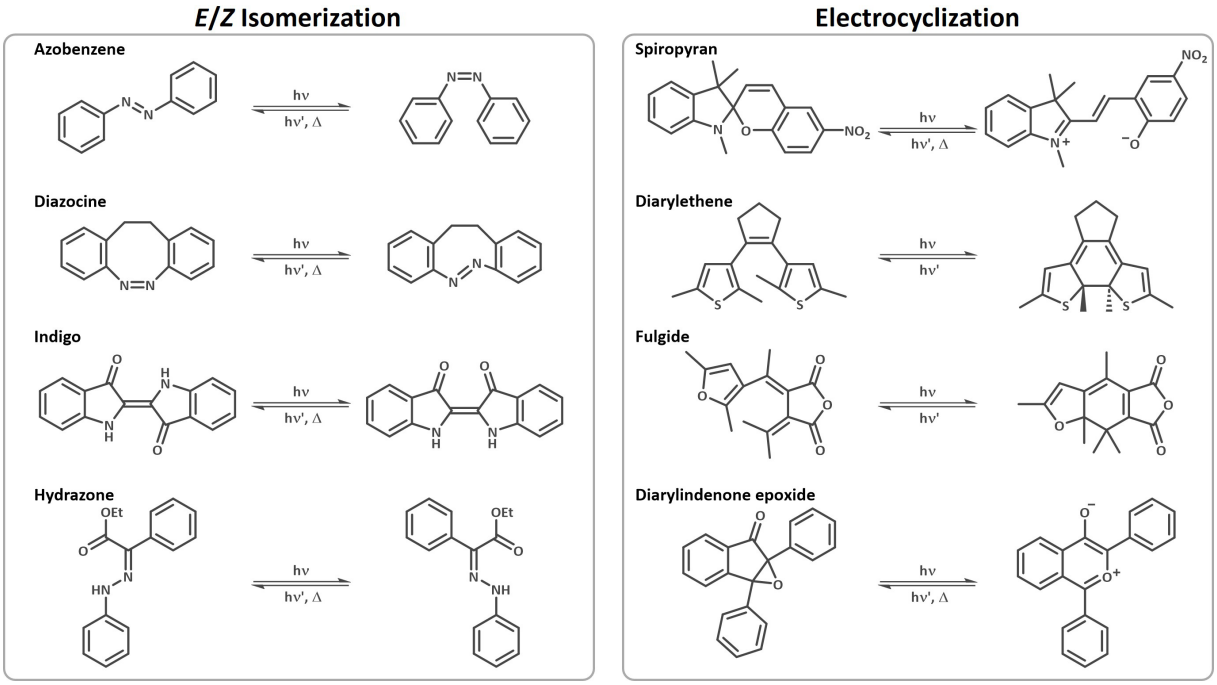

Figure 3. Overview of different photoswitches and their reversible isomerization reactions, separated into *E*/*Z* isomerization (left) and electrocyclization (right). Adapted from Boelke *et al*.[69]

Since photochemical isomerization is usually reversible and absorbance spectra as well as the reactivity windows of the different isomers usually overlap, irradiation at a specific wavelength will trigger the reaction in both directions to a certain degree. A wavelength-dependent equilibrium – where forward and reverse reaction rates are identical – will be reached at some point, when increasing the intensity of light will only contribute to a faster cycling of the photoswitches without further altering the ratio of the different isomers. The point of equilibrium is called the photostationary state (PSS) and is defined as

$$PSS = \frac{n_B}{n_A} = \frac{\Phi_{A\rightarrow B} * \varepsilon_A}{\Phi_{B\rightarrow A} * \varepsilon_B}$$

for the photoisomerization between A and B (A ⇋ B) at a specific wavelength with *n* the amount of matter and ε the extinction coefficient at a specific wavelength for A and B, respectively. Φ represents the quantum yields at the specific wavelength for the forward (A → B) and the reverse reaction (B → A), respectively, and gives the number of times a photoswitching process occurs in relation to the number of photons absorbed.[71] It should be noted that the above definition does not consider thermal reversion processes and only focuses on the photochemical switching. Understanding of the PSS plays an important role for any application, specifically because choosing a different wavelength can drastically alter the equilibrium of the switching reaction. Ideally, high PSS with conversions above 90% are targeted to fully harness the property changes induced upon irradiation.[71]

The most common commercial application for photoswitches (i.e. spiropyrans, spirooxazines and naphthopyrans) are photochromic glasses with a reversible darkening effect that occurs under exposure to bright sunlight and reverts in the dark.[72] Moreover, the potential of precise spatiotemporal control over the reversible isomerization makes photoswitches a fascinating class of molecules for research in the fields of materials properties, biology, medicine and additive manufacturing.[8, 12, 16, 73] In the following, azobenzene and spiropyran will be discussed in more detail, as they are the most common photoswitches undergoing *cis*-*trans* isomerization and electrocyclization, respectively.

Since the first report on the photochromism of azobenzene in 1937 by Hartley,[74] it has evolved into one of the most extensively studied classes of photoswitches due to its facile synthesis and versatility. By now several new important classes of photoswitches have been established that are derived from the azobenzene core structure, such as diazocines[75] or azoheteroarenes.[76] In the dark, azobenzene is present in the thermodynamically stable *trans* configuration, minimizing steric hindrance between the aryl groups, attached to the nitrogen atoms of the N=N azo bond. Upon irradiation with UV (ultraviolet) light (≈340 nm), a *trans* to *cis* isomerization occurs around the azo double bond (**Figure 3**), bringing the aryl groups closer together and introducing a dipole moment.[46] As a T-type photoswitch,

reversion of the metastable *cis*- to the *trans*-azobenzene occurs thermally but can also be triggered photochemically with blue light (≈450 nm).[46] To date, a very large library of azobenzene compounds has emerged by varying the aryl groups attached to the azo bonds, with a variety of thermal half-lives and addressable wavelengths.[73, 77] The versatility with regard to functionalization and the ensuing diversity of properties established azobenzenes for applications in different fields ranging from drug delivery[78] over vision restoration[79] to solar thermal fuels.[46, 77, 80]

Photoswitching of spiropyrans was first described by Fischer and Hirshberg in 1952[81]. Since then, spiropyrans have been widely studied and incorporated into a variety of dynamic materials with their most prominent application being photochromic lenses.[69, 82] Spiropyran is the name given to the colorless, thermodynamically stable isomer that undergoes ring opening at the spiro moiety under UV light irradiation (≈365 nm), thereby forming the strongly colored merocyanine.[46] The color change is due to an auxochromic effect from the connection of both aryl groups via a delocalized π-system and the zwitterionic state, which red-shift the absorbance strongly into the visible range. Reversion is now possible either thermally or upon irradiation with visible light (≈550-600 nm).[46] The spiropyran/merocyanine photoswitch is particularly interesting because the two isomers differ drastically in color, polarity, volume, pK_a and redox properties, which has enabled applications in the fields of data storage,[82] drug delivery,[83] chemical sensors[84] and two-color 3D printing.[12, 46, 85, 86]

Typically, photoswitches are engineered for stability to enable a high number of switching cycles and to minimize side reactions and photobleaching. However, for some photoswitches only one of the isomers is capable of undergoing selective reactions, allowing its reactivity to be controlled by light. Two such compounds play a particularly important role in this work, namely a diarylindenone epoxide and a diazocine, which will therefore be discussed in detail in Sections **2.2.1** and **2.2.2**, respectively.

2.2.1 Diarylindenone epoxides

Photoswitching behavior of diarylindenone epoxide (DIO) was first reported by Ullmann in 1964[87] who further studied the isomerization mechanism between the different configurations, shown in **Figure 4**.[88] Despite its discovery several decades ago, DIO has remained of minor importance relative to established photoswitches such as azobenzenes and spiropyrans. Upon UV light irradiation (≈365 nm), the colorless, thermodynamically stable isomer DIO undergoes ring-opening at the C-C epoxy bond, resulting in the deep purple oxidopyrylium compound DIO'. Reason for the strong redshift of the absorbance from UV to the visible light is due to the formation of a delocalized π-system that stretches over the whole molecule and the zwitterionic structure which is similarly observed for the spiropyran-merocyanine switching.[89] The activation of DIO occurs from an n-π* transition and results in

conversion of up to 11% at the PSS when irradiating at 365 nm. The metastable DIO' has a half-life of approximately 50 minutes (at 25°C). Photochemical reversion occurs from an n-π* transition as well, leading to complete deactivation when irradiated with green light at 520 nm. A drawback of DIO' is its oxygen sensitivity, which leads to the formation of several side products, when photoswitching is performed at ambient conditions.[31, 33]

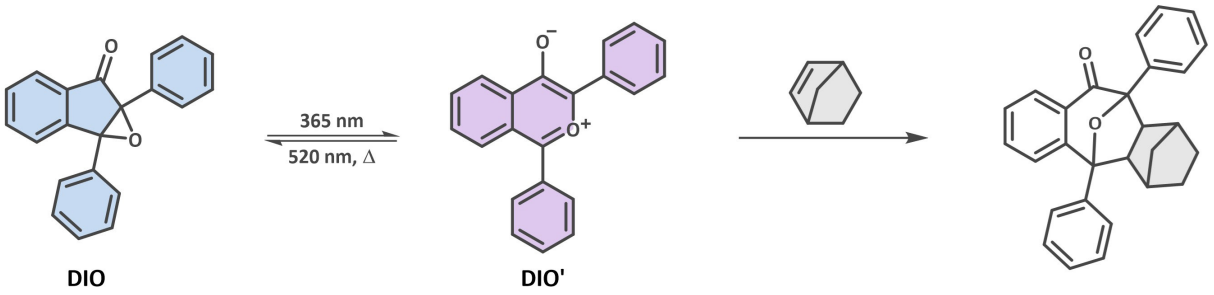

Figure 4. Reversible photoisomerization via epoxide-opening/closing between DIO and DIO' under UV (365 nm) and visible light (520 nm), or thermally, followed by a subsequent cycloaddition of DIO' with a ring-strained double bond (e.g. norbornene).[31]

Synthesis of DIO is straightforward via a two-step reaction, first the palladium-catalyzed Larock indenone synthesis,[90] followed by oxidation with hydrogen peroxide and sodium hydroxide to introduce the photoswitchable epoxide moiety.[33] The group of Yu employed this approach to synthesize and characterize the photoswitching behavior of a library of 24 DIO compounds.[33] These derivatives featured different substitution patterns of electron donating and withdrawing groups attached to the aryl rings with half-lives ranging from hundreds to ten thousands of seconds.

Shortly after the discovery of the photoswitching of DIO, Ullman reported the photoactivated cycloaddition of DIO to the C=C double bond of norbornadiene.[91] While the thermally stable DIO isomer is inert in the dark, photoisomerization yields DIO', which readily undergoes cycloadditions to a variety of alkenes and alkynes, especially if they are under ring-strain.[33] Similar reactivity is also observed for oxidopyrylium compounds which are often employed for natural product synthesis.[92-94] A key advantage of DIO is its reactivity that can be readily toggled "on" and "off" by either UV or visible light irradiation, respectively, providing spatiotemporal control over the reaction process. This asset was previously harnessed for high-resolution lithographic surface decoration and bioorthogonal labeling on living cells.[33]

Recently, Yu and Su[95] reported a modified version of DIO based on a 1,4-naphtoquinone instead of the indenone core with extremely short half-lives in the microsecond range at 20 °C. The isomerization proceeds over a singlet diradical intermediate that is insensitive to triplet oxygen and was employed for bioorthogonal photoclick labelling on living cells.

2.2.2 Diazocines

Diazocines are a subclass of azobenzene photoswitches that were first reported by Herges in 2009.[32] Similar to azobenzene, the photoswitching involves *cis*/*trans* isomerization of an azo bond. However, in the case of diazocines the two aryl groups connected to the azo bond are additionally covalently linked at the *ortho*-position relative to the nitrogen atoms of the azo unit. While the parent compound is connected by an ethylene bridge,[32] also diazocines with ether,[96] thioether[97] and amine groups[98] were reported. The bridged connectivity introduces a ring-strain into the photoswitch, resulting in reverse stability compared to regular azobenzenes, with a thermally stable *cis*-isomer.[70] The *trans*-isomer is accessible by irradiation with blue light (≈400 nm) and reverts back thermally or photochemically by irradiation with green light (≈500 nm).[99] Compared to azobenzene, the ring-strained diazocine geometry results in a redshift of the activation wavelengths and an increased n-π* band separation that facilitates the separate addressing of either isomerization.[70] Furthermore, the molecular isomerization dynamics are accelerated and increase the photoswitching efficiency due to steric constraints.[100] In general, both the *cis*- and *trans*-isomers of the diazocine family are highly stable when exposed to oxygen and can undergo numerous switching cycles without noticeable photobleaching.[99]

Diazocines are usually prepared by first introducing the covalent bridge between two nitroaryl groups, followed by reduction of the nitro functionalities, in the presence of zinc and barium hydroxide, to an azo bond under ring-closure.[101] As the intramolecular ring-closing step introduces significant ring strain, the reaction proceeds inefficiently, and several alternative synthetic strategies have therefore been developed with improved yields.[34, 102]

The main focus for research into diazocines is in the field of photopharmacology for precision medicine.[103] Interestingly, the *cis*-isomers is usually pharmacologically inactive while photoinduced isomerization allows for the pharmacological activation of the corresponding diazocine. Harnessing the photochemical reversion at longer wavelengths allows for the straightforward spatiotemporal control over the biological activity. For example, Cabré *et al.* reported a photoswitchable neurotransmitter derived from a *cis*-diazocine, which is inactive in the *cis* form but becomes active in the *trans*-configuration.[104] Further applications of diazocines are researched in the fields of stimuli-responsive self-assembly[105] and enabling *de novo* protein synthesis.[106]

Diazocines are generally regarded as reliable and inert photoswitches, capable of undergoing numerous switching cycles without significant side reactions.[99] In 2020, however, the groups of Deng and Yu[35] introduced modified diazocine derivatives in which the bridge consisted of a single atom (C, O, N, or S), yielding seven-membered rings with higher ring strain compared to the canonical eight-membered structure. Remarkably, only the sulfur-bridged derivative (SA) met the requirements of a

reversible photoswitch. The increased ring strain drastically shortens the thermal lifetime of the metastable isomer at 25 °C to the microsecond range, in contrast to the hour-scale lifetimes observed for ethylene-bridged diazocines.[32] Despite maintaining a high resistance to photobleaching, the strain-loaded *trans*-isomer readily acts as a dipolarophile in photo-click reactions with nitril imines as shown in **Figure 5**. As a result, the reaction can be triggered under blue-light irradiation (≈430 nm), with the photoswitch immediately reverting thermally in the dark – an approach successfully applied for protein modification in live cells.[35]

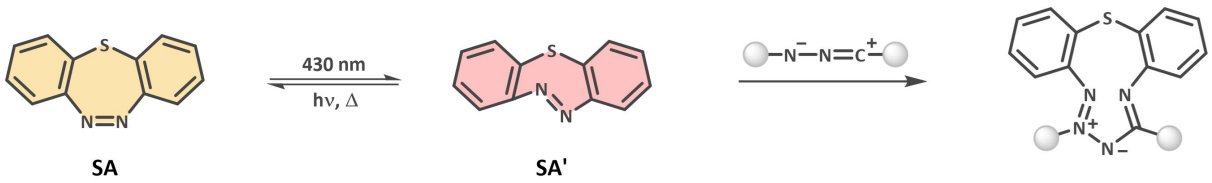

Figure 5. *Cis-trans* photoisomerization of the thioether bridged diazocine between *cis* (SA) and *trans* (SA') leading to ring-strain loading and subsequent cycloaddition to a nitril imine.[35]

2.3 Action Plots

Photochemists aim to identify the most suitable wavelength for driving a reaction with maximum efficiency. At first glance, inspecting the Ultraviolet-visible (UV-Vis) absorbance spectrum may appear to provide a straightforward answer by simply choosing an absorbance maximum. However, the situation is more complex: while the absorbance spectrum reveals the wavelengths at which photon absorption and the associated electronic transitions are most probable, it does not guarantee that the desired photoreaction will follow.[37] As illustrated by the numerous possible relaxation pathways in Jablonski diagram **Figure 2**, absorbed energy can dissipate in many ways other than the targeted reaction.[54] Therefore, not only the extinction, obtained via UV-Vis spectroscopy but also the quantum yield (number of reactions per photon) has to be considered.[39] This effect is probably most notable in anti-Kasha molecules with a chemically inactive first electronic transition.[107] Nevertheless, the assumption of a direct correlation is still prevalent and often the absorbance maximum is chosen as the wavelength for irradiation of a chromophore without further studying the wavelength-dependent reactivity and thus potentially employing suboptimal irradiation conditions.[37]

Gescheidt and Barner-Kowollik were the first to encounter and intricately study the appearance of a mismatch between absorbance and reactivity maximum that was red-shifted to longer wavelengths.[108] Specifically, activation of oxime ester photoinitiators proceeded nearly four times faster under irradiation at 405 nm, approximately 80 nm red-shifted relative to its absorbance maximum at 327 nm. Since then, the apparent mismatch has repeatedly been observed in many other systems (e.g. photocycloaddition,[109, 110] photocleavage,[111, 112] photoswitching,[31, 113] photopolymerization[114] and photochemical ring contraction[115]), demonstrating that it is not a coincidence but rather a general phenomenon that had been severely underestimated.[37, 116, 117]

Consequently, our group focused on further investigating the reactivity mismatch and developed the so-called action plot as an analogue to the absorbance spectrum, which provides the wavelength-dependent reactivity of a photoactive compound, including the wavelength dependent quantum yields for a specific reaction trajectory.[37] Usually, action plot (or the resulting wavelength dependent quantum yields) and absorbance spectrum are depicted in an overlay to visualize their deviations as shown in **Figure 6A** for the photoactivated [2+2] cycloaddition of *trans*-PyChal (**Figure 6B**) with an approximately 50 nm red-shifted reactivity maximum.[118] In most cases, the action plot presents a bathochromic shift, allowing for more efficient reactions at longer wavelengths. Only in some cases does the wavelength-dependent reactivity coincide[31] with the absorbance spectrum or undergo a hypsochromic shift.[112]

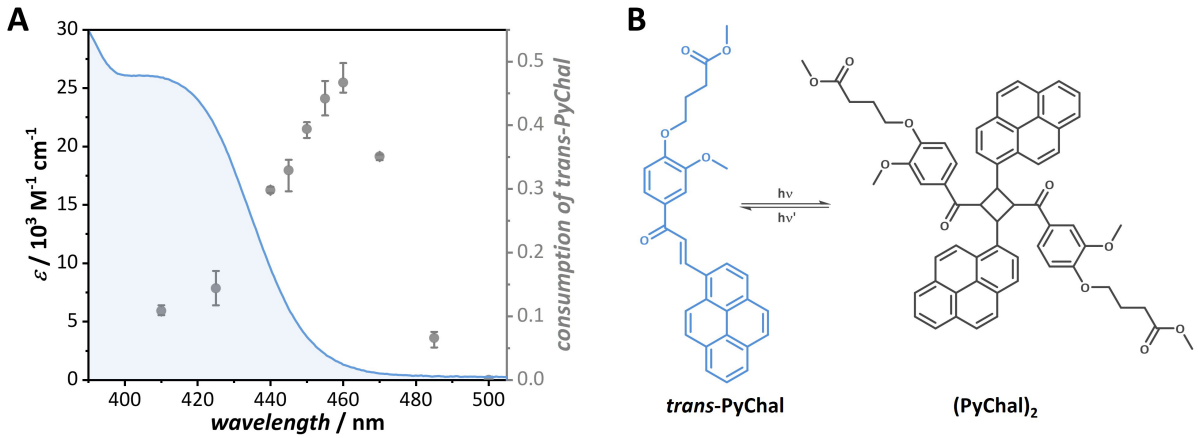

Figure 6. (**A**) Absorbance spectrum and action plot of the photoactivated [2+2] cycloaddition of *trans*-PyChal to $(PyChal)_2$, showing a mismatch between absorbance and redshifted reactivity maxima. (**B**) Schematic depiction of the [2+2] cycloaddition of *trans*-PyChal to $(PyChal)_2$. Adapted from Carroll *et al.*[118]

Currently, several explanations for the mismatch between absorbance spectra and action plots are under consideration, and it is discussed if an interplay of these factors accounts for the observed mismatch between reactivity and absorptivity. Proposed factors range from concentration effects, multiple chromophores, and photostationary states to multiphoton processes.[118] More recently, however, a new theory was put forward by our group,[118] inspired by the red-edge effect known from fluorescence spectroscopy, which is now considered a prime candidate for explaining the appearance of red-shifted reactivities compared to the absorbance spectra. The red-edge effect describes the excitation-wavelength-dependent photoluminescence that undergoes a significant bathochromic shift when exciting at the "red-edge" of the absorbance spectrum.[119, 120] The effect can be explained by the distribution of different microenvironments for a chromophore in solution, which though dynamically changing can be viewed as static for the duration of photon absorption and will rearrange shortly after.

Most chromophores are surrounded by solvent molecules in configurations that minimize the ground-state energy, as illustrated for microenvironment A in **Figure 7**. However, due to environmental fluctuations, a fraction of chromophores will be solvated under less favorable conditions (microenvironment B), resulting in a higher ground-state energy. Importantly, reduced stabilization of the ground state does not necessarily extend to the excited state, since changes in the magnitude and/or direction of the dipole moment will alter solvation effects. Thus, a microenvironment that is energetically unfavorable for the ground state may in fact stabilize the excited state, lowering its energy. Although only a small fraction of chromophores absorb at the red edge with a reduced energy gap between ground and excited states, the effective population of an excited state depends not only on the number of electronic transitions (measured in an absorbance spectrum), but also on the excited-state lifetime. In microenvironment B, the lower-energy excited state may exhibit significantly longer lifetimes. Consequently, even a minor fraction of chromophores can contribute

disproportionately to fluorescence and reactivity behavior, thereby giving rise to the significant red-shifts in fluorescence emission spectra and photochemical action plots, respectively. This effect is expected to be particularly pronounced in bimolecular processes, where excited-state lifetime is a key factor.[118]

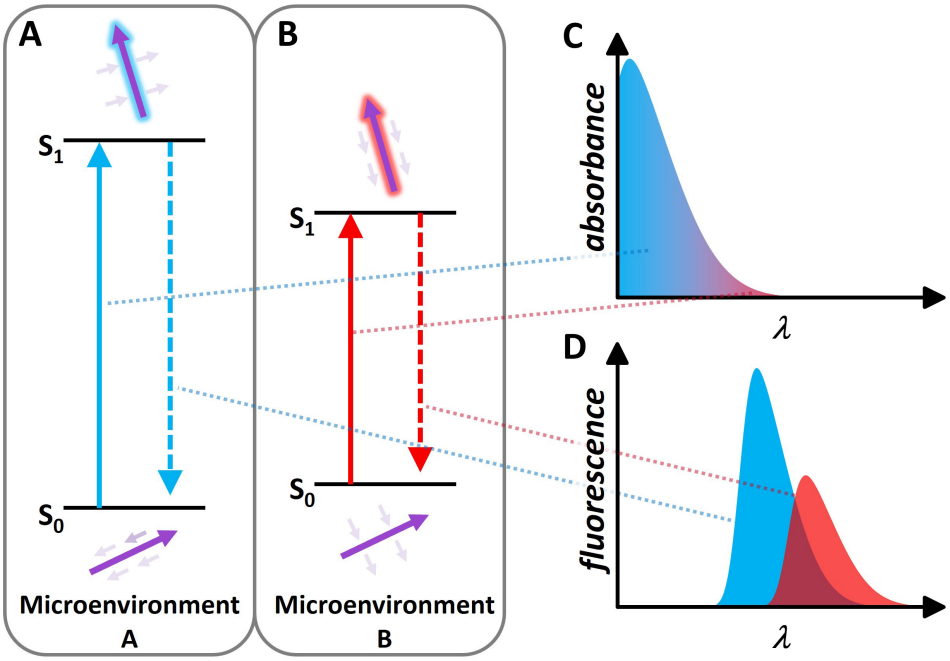

Figure 7. Illustration of the absorption and fluorescence transitions of the same chromophore in different microenvironments. (**A**) Microenvironment A represents the prevalent microenvironment with a minimized ground state energy for S_0. (**B**) Microenvironment B is thermodynamically less favorable in the ground state S_0 but stabilizes the excited state S_1. (**C**) Illustration of an absorbance spectrum with the corresponding ranges for absorption in the prevalent microenvironment A (blue) and on the red edge for microenvironment B (red). (**D**) Illustration of wavelength-dependent fluorescence spectra after absorption in microenvironment A (blue) and B (red). Adapted from Carroll *et al.*[118]

Wavelength-resolved mapping of chromophore reactivity (i.e. wavelength dependent quantum yields) has become feasible through the development of affordable optical parametric oscillators (OPOs), i.e. tunable nanosecond pulsed lasers that can emit monochromatic light across a broad spectral range from the deep UV to the near-infrared.[37] For the action plot measurement, a stock solution of a chromophore is prepared, filled into a crimp vial and positioned in a sample holder. Sample irradiation is then achieved by reflecting the monochromatic laser light upwards through the bottom of the vial and the solution in order to irradiate the whole sample evenly as shown in **Figure 8**. This process is then repeated for a set of different wavelengths of choice.[37]

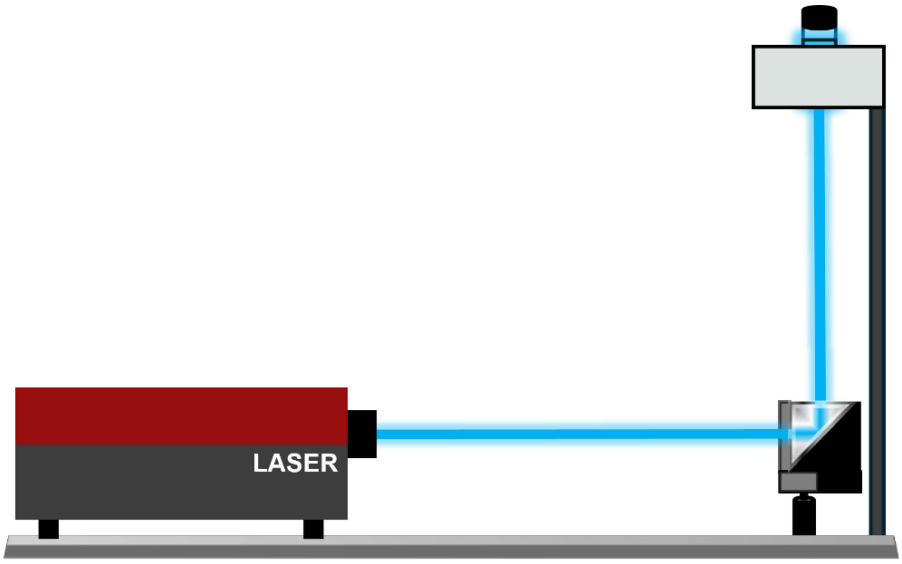

Figure 8. Schematic representation of the setup used to conduct the photochemical action plots measurements.

While the general setup of an action plot experiment is straightforward, the specific sample conditions must be tailored to each chromophore with respect to concentration, solvent, volume, potential reaction partner, wavelength range, number of photons, photon flux, and characterization method. Therefore, when planning an experiment with a specific chromophore, first a kinetic measurement is performed employing irradiation, usually at the absorbance maximum, with the same sample preparation as for the subsequent action plot. The kinetic measurement allows an estimation of the number of photons required to achieve measurable conversion in the action plot while remaining within the linear kinetic regime, which is typically up to approximately 30% conversion. Working below that threshold is essential in order to gain quantitative insights into the wavelength-dependent reactivities.[37] Next, identical samples are irradiated at different wavelengths but always with the same number of photons. After irradiation the samples are typically characterized quantitatively via nuclear magnetic resonance (NMR) spectroscopy or liquid chromatography-mass spectrometry (LC-MS). Recently, action plot characterizations have also been performed with online UV-Vis monitoring, offering the advantage of direct feedback. This approach is especially interesting when investigating the reversible isomerization of photoswitches.[31, 113] In principle real time monitoring could also be extended to other techniques, such as infrared (IR) and NMR spectroscopy.

2.4 Two-Color Photochemistry

In addition of space and time, the possibility of working with distinct wavelengths adds a third dimension of control to the application of light as a stimulus and enables a plethora of new and exciting opportunities.[46] These opportunities arise from the spectral nature of light and the possibility of employing different wavelengths to selectively activate or deactivate a chromophore, thus triggering disparate responses in a system.[46] To fully harness the advantages of light as a spectrum, it is essential that these responses can be addressed separately of each other – a concept termed λ-orthogonality – that has been investigated and reviewed extensively in recent years.[10, 37, 46, 121, 122] In particular, the development of novel printing techniques and the design of advanced photoresists for light-induced three-dimensional (3D) printing are based on the use of two discrete wavelengths.[8, 11, 12, 30, 123, 124]

In the following sections, the focus will be on contemporary approaches for two-color 3D printing based on four different reaction modes shown in **Figure 9**, i.e. synergistic, cooperative, orthogonal and antagonistic interactions between light and photoresist – a taxonomy introduced by our group.[9] In synergistic systems, covalent bond formation serving as a crosslinking event of a photoresist only occurs where both colors of light intersect in time and space and enables the realization of extremely fast and precise printing techniques.[11, 12] Cooperative systems are similar to synergistic ones, with the difference that two-color irraditation must not occur simultaneously, but can also be sequential to induce a printing process with potential for the fabrication of structures with varying material properties from a single photoresist.[9, 125] Orthogonal systems allow two separate reactions to be triggered by different colors of light in an independent manner, thereby enabling the introduction of diverse materials properties by employing a single photoresist.[126] Lastly, the antagonistic reaction mode is based on one wavelength that triggers a printing process and another wavelength that suppresses it. The antagonistic behavior can be harnessed by drawing inspiration from stimulated emission depletion (STED) microscopy to enable printing on the micro- and nanoscale, well below the diffraction limit.[85, 124, 127]

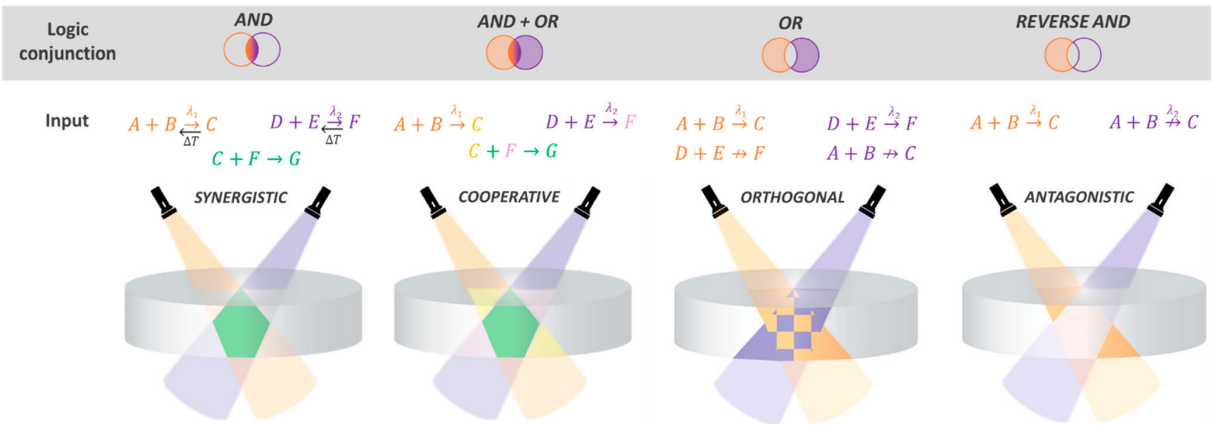

Figure 9. Reaction mode taxonomy for two-color photochemistry, i.e. synergistic, cooperative, orthogonal and antagonistic, introduced by our group. Adapted with permission.[9] Copyright 2023, American Chemical Society.

2.4.1 Printing with Two Colors of Light

Additive manufacturing has emerged as a highly versatile tool for the custom fabrication of three dimensional structures with major applications in the automotive,[128] healthcare[129] and electronics industries.[130] Especially, 3D printing approaches based on light have become increasingly popular and diverse techniques were developed, such as stereolithography, digital light processing and direct laser writing, allowing fabrication from the macro- to the nanoscale.[131] These methods rely on the photochemically induced crosslinking and hardening of a liquid photoresist upon irradiation with a light source with a narrow wavelength distribution, such as a laser or LED.[132] The concept of two-color 3D printing, achieved by introducing a second source of light at a different wavelength, has attracted significant attention in recent years.[12, 85, 123, 126] In the following sections, the different two-color modes shown in **Figure 9**, i.e. synergistic, cooperative, orthogonal and antagonistic, will be examined in detail, guided by current advances in the field. Beyond the general realization and implementation of new printing approaches, comparisons to the benchmark two-photon absorption method for 3D nanoprinting will be provided to emphasize the unique advantages of two-color strategies.[8]

2.4.1.1 Synergistic

Synergy describes the principle that the combination of two or more factors yields an outcome greater than the sum of their individual contributions.[133] Teamwork serves as an illustrative example where the strengths and ideas of multiple individuals merge to foster innovation and enhance efficiency.[133] Likewise, the use of two distinct colors of light in additive manufacturing gives rise to synergistic interactions that pave the way for novel and superior printing methodologies.[12, 123]

Light-sheet printing, introduced by Wegener and coworkers in 2019,[123] is currently one of the most promising concepts based on synergistic photochemistry, offering the potential for rapid and precise fabrication down to the microscale. Inspired by light-sheet optical microscopy, the method harnesses synergistic interactions between the photoresist and two distinct wavelengths of light, with printing occurring only at the intersection of both beams. This is achieved by focusing light of one wavelength into a thin sheet that passes through the photoresist, onto which an image of a second wavelength is projected (**Figure 10**). By moving the sheet across the resist while simultaneously adapting the projected image, complex 3D structures can be fabricated within short timeframes. In contrast to the state-of-the art two-photon printing, which occurs in a minuscule volume element in the focal point of the laser (termed as voxel), sheetwise printing offers the potential to be incomparably faster while still retaining microscale precision. In addition, rather than relying on costly and space-demanding

femtosecond lasers, the method can be implemented with far more economical and compact continuous-wave (CW) lasers or even light-emitting diodes (LEDs).[123]

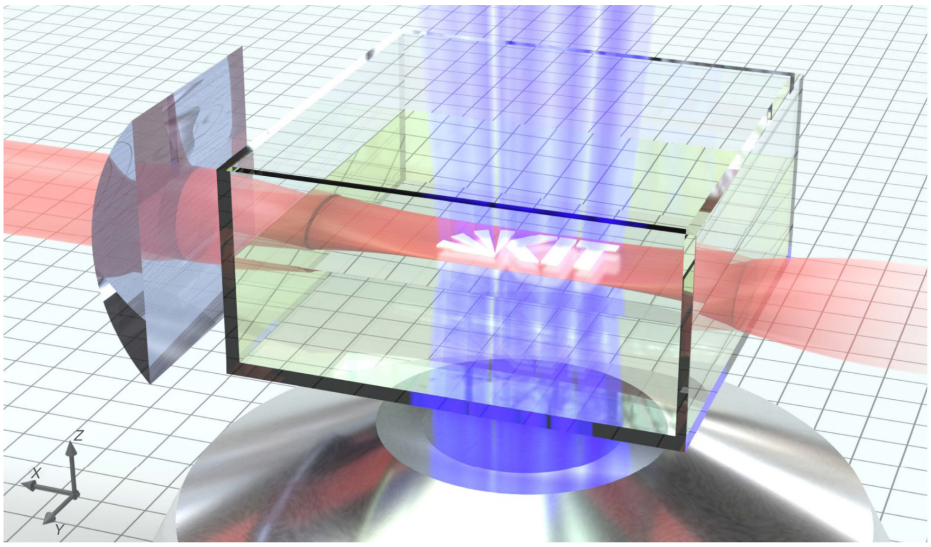

Figure 10. Model illustration of light-sheet printing, where an image of one wavelength (violet-blue) is projected into a sheet of light of another wavelength (orange). Only at the intersections of both wavelengths a printing process is initiated. Reproduced with permission.[11] Copyright 2023, Springer Nature.

After outlining the theoretical advantages and practical opportunities of light-sheet printing, it is essential to highlight the second key component alongside the optical setup, the "AND-photoresist".[123] Designing such a resist is extremely challenging, as it must fulfill several strict criteria at the molecular level to ensure printing occurs exclusively under simultaneous two-color irradiation. A crosslinking event, i.e. a photochemically induced covalent-bond formation, can only take place when both wavelengths of light intersect within a defined volume element of the resist. To achieve precise control, any photochemical response triggered by one wavelength must proceed in complete λ-orthogonality to the other. Furthermore, once irradiation ceases any wavelength-dependent changes in the resist must instantly revert, thereby preventing sequential printing and enabling true spatiotemporal control. The system must therefore be fully reversible in the dark, with the sole exception being the crosslinking reaction, which must remain permanent and irreversible.[8]

The first significant breakthrough in the field of two-color 3D printing via synergistic photochemistry was achieved by Hecht and coworkers in 2020,[12] who introduced a linear volumetric printing technique known as *xolography*. The setup is based on the concept of light-sheet printing, employing a sheet of UV light (375 nm) onto which an image of visible light (550 nm assumed center wavelength) is projected (**Figure 11B**). Crosslinking of the acrylate-based photoresist proceeds through two-step activation of a dual-color photoinitiator, comprising a spiropyran photoswitch linked to a benzophenone photoinitiator. UV irradiation drives the isomerization of spiropyran to merocyanine, which then absorbs visible light and activates the benzophenone moiety, initiating radical generation

and thus the printing process (**Figure 11A**). The dual-wavelength concept enabled the fabrication of structurally complex objects with both high resolution and printing speed. However, the response is not fully λ-orthogonal, as merocyanine absorbs in the UV region as well, leading to uncontrolled competing initiation.[8, 12, 30] Since the initial report in 2020,[12] *xolography* printers have undergone substantial advancements in regard to printing speed, feature sizes, and the versatility of employed light-sheet wavelengths (375, 385, and 405 nm). Moreover, the technique has gained broad acceptance within the scientific community and has been applied across diverse research areas, spanning from multimaterial printing[15] and the fabrication of optical elements[134] to material research and manufacturing in space.[135]

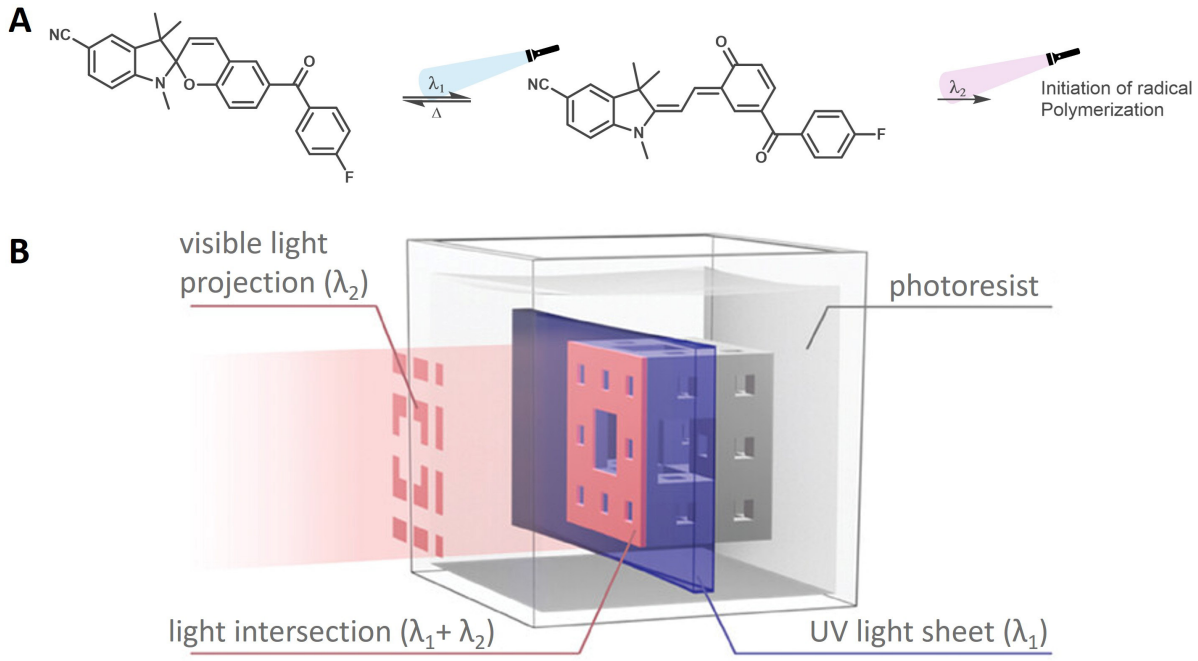

Figure 11. (**A**) Chemical structures and mechanism for the two-color activation of a spiropyran photoswitch with an integrated benzophenone photoinitiator in *xolography*.[12] Adapted from Ref.[8] (**B**) Illustration of the working principle of *xolography*.[135] B was adapted with permission.[135] Copyright 2024, Wiley-VCH GmbH.

In 2022, Hahn *et al.* published a research paper[11] on the previously conceptualized light-sheet (micro)printing.[123] The photoresist consisted of dipentaerythritol hexaacrylate as the crosslinkable monomer, diacetyl as the photoinitiator, and (2,2,6,6-tetramethylpiperidin-1-yl)oxyl as both triplet quencher and radical scavenger. The setup employed two CW lasers, one at 440 nm for projection and another at 660 nm for the light-sheet. Unlike *xolography*,[12] where photochemical synergy arises from photoswitching followed by radical initiation, here the process relied on sequential excitation of an electron, first from the ground state at 440 nm, then re-excitation from T_1 to higher triplet states T_n at 660 nm, ultimately leading to radical initiation (**Figure 12A**). Microstructure fabrication (**Figure 12B**)

was demonstrated by printing onto a slanted borosilicate glass rod (1 mm diameter) immersed in the photoresist, achieving peak printing rates of 7 × 10^6 voxels s^{-1} at a voxel volume of 0.55 µm^3.[11]

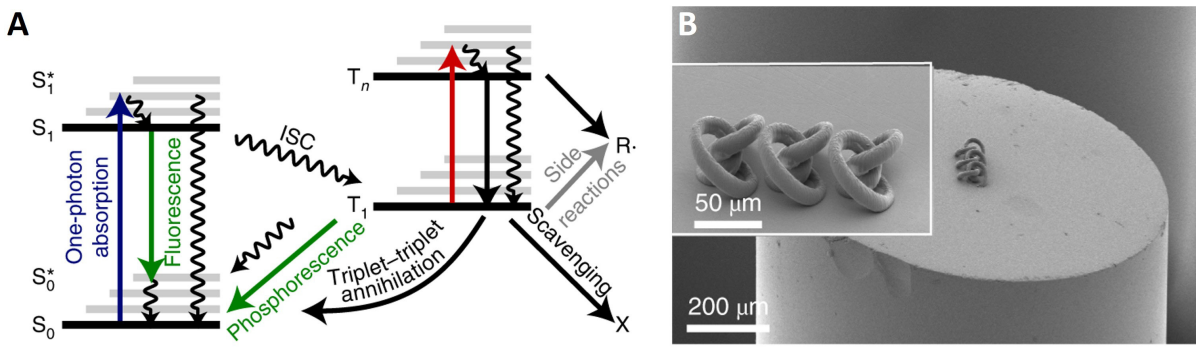

Figure 12. (**A**) Jablonski diagram of the photoinitiator diacetyl illustrating the two-step absorption, first of 440 nm (blue arrow), then 660 nm (red arrow), followed by radical initiation. (**B**) Knot-like microstructures, printed in parallel vial light-sheet microprinting. A and B reproduced with permission.[11] Copyright 2023, Springer Nature.

Another promising strategy toward a synergistic system, relying on the fully λ-orthogonal activation of two distinct photoswitches, was introduced by our group in 2022.[30] Only after activating both photoswitches by irradiation with two distinct colors do they undergo an efficient covalent bond-forming reaction, enabling irreversible crosslinking of a polymer network. The concept combines the *trans*-to-*cis* isomerization of an azobenzene at 385 nm with the reversible generation of a diketene at 600 nm, followed by a [4+2] cycloaddition between *cis*-azobenzene and the diketene (**Figure 13**). Notably, both photoactivation processes are fully reversible, a key prerequisite for achieving precise control and suppressing unwanted side reactions during printing. Yet, the photoactivated diketene does not revert rapidly under ambient conditions but requires elevated temperatures of approximately 70 °C. As a result, the reversible character of the system cannot be harnessed during printing under standard conditions, which significantly narrows its practical applicability, for instance for light-sheet printing.[30]

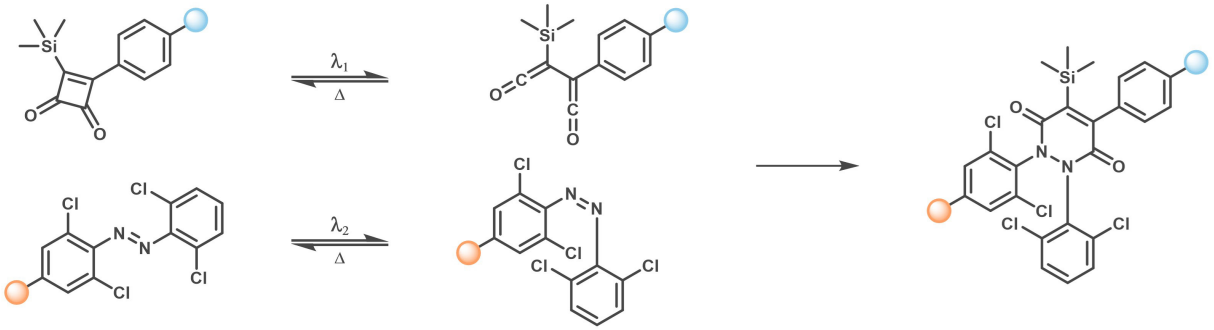

Figure 13. Synergistic two-color light activated formation of covalent bonds between a diketene (top) and a *cis*-azobenzene (bottom) upon exposure to light of 385 and 625 nm, respectively.[30] Adapted from Ref.[8]

Although the field of two-color printing has emerged only recently and is still in its infancy, several promising approaches based on synergistic photochemistry have already been developed[12, 30, 123] and are likely to inspire further investigations in the field.[8]

2.4.1.2 Cooperative

The cooperative reaction mode resembles the synergistic one considering that two distinct wavelengths are required for network formation. The key difference lies in the activation principle: synergistic photochemistry demands simultaneous irradiation with both colors of light ('AND'), as bond formation only occurs when the two photoactivation steps coincide. In contrast, the cooperative case is sequence-independent ('AND' + 'OR'), since each wavelength independently triggers a separate covalent bond-forming event, yet crosslinking and network formation still require dual-color activation, achievable through suitable monomer design.[9, 125]

Recently, our group reported the first cooperative network formation relying on fully sequence-independent λ-orthogonal photochemistry.[125] Building on our earlier work with small-molecule reactions,[136] we designed a photoresist composed of poly(methyl methacrylate) (PMMA) chains bearing maleimide moieties, and a poly (ethylene glycol) (PEG)-based heterotelechelic linker featuring an *ortho*-methyl benzaldehyde (*o*-MBA) unit on one end and an *N*,*N*-(dimethyl)aminopyrene aryl tetrazole (APAT) unit on the other. Both chromophores react with maleimide via photoinduced cycloadditions: at 325 nm *o*-MBA reacts as a photocaged diene in a Diels-Alder reaction, while APAT undergoes a nitrile-imine mediated tetrazole-ene cycloaddition (NITEC) at 450 nm. The heterotelechelic molecule serves as a two-step crosslinker, since one-color irradiation leading to the reaction of only a single chromophore merely serves to decorate the maleimide-containing polymer with side chains. However, activation of the second chromophore interconnects different polymer chains and thereby induces network formation. By harnessing the λ-orthogonal reactivities of two distinct chromophores toward the same reaction partner, cooperative network formation was thus established, requiring two-color activation that may occur either simultaneously or sequentially in a fully sequence-independent manner. This strategy opens new opportunities for the design of advanced photoresists for multimaterial printing and provides valuable insight into the similar yet distinct synergistic mode.[9, 125]

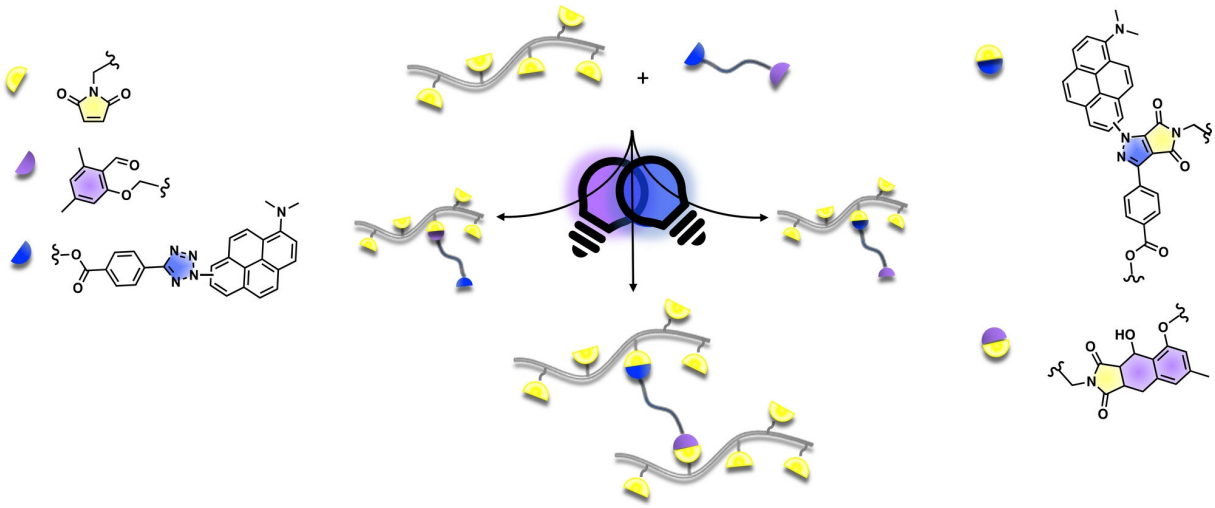

Figure 14. Illustration of the photochemical polymer postmodifications under one-color and the cooperative network formation under two-color irradiation of a photoresist consisting of a maleimide-containing polymer (yellow) and a heterotelechelic dilinker featuring two fully sequence-independent λ-orthogonal chromophores *o*-MBA (violet, 325 nm) and APAT (blue, 450 nm). Reproduced from Eren *et al.*, licensed under CC BY-NC 4.0.[125]

2.4.1.3 Orthogonal

In 1977, Merrifield and Barany[137] introduced the concept of chemical orthogonality in their report of a novel protecting group for peptide synthesis. At that time, the term referred to different protecting groups that could be selectively removed one after another by applying distinct reaction conditions (e.g. pH, redox, light).[138] Today, orthogonality more broadly describes the ability to induce multiple specific responses in a chemical system independently of one another by adjusting the process parameters. In this context, photochemistry holds immense potential, as the full spectrum of light gives rise to an almost limitless number of possible wavelengths to trigger different events.[46]

λ-Orthogonality describes the ability to selectively activate different chromophores by applying distinct colors of light. The two different modes of λ-orthogonal behavior need to be established first, i.e. sequence-selective and sequence-independent. In sequence-selective systems, orthogonality is only achieved when irradiation is applied in the right order, typically proceeding from longer to shorter wavelengths, since most chromophores show overlapping absorbances and reactivity profiles in the UV region and can therefore not be addressed independently in this range.[139-141] As orthogonality here is only ensured under specific conditions, the restricted λ-orthogonality will be termed λ-selectivity in the following. In contrast, sequence-independent λ-orthogonality refers to the ideal case, where distinct activation of each chromophore is entirely unrelated to the irradiation sequence and will simply be referred to as λ-orthogonality, herein.[10, 37, 46, 136, 142]

The key advantage of λ-orthogonality lies in the ability to selectively activate different chromophores by choice of the applied wavelength, thereby enabling multimaterial 3D printing from a single photoresist. While alternative strategies for multimaterial printing exist, such as vat exchange,[143, 144] in which the printing platform switches between photoresists with an intermediate cleaning step, or grayscale printing,[145] a λ-orthogonal dual-color photoresist offers a more straightforward route and allows for greater material diversity.[146] Moreover, a single photoresist cartridge would be sufficient for the fabrication of complex structures that integrate, for example, soft and rigid domains or conductive and insulating elements.[37] Developing such multicomponent photoresists would substantially broaden the scope of 3D printing in an efficient and accessible manner, representing a crucial step toward its practical feasibility and eventual integration into our daily lives.[8]

Several multimaterial photoresists have been developed, but most rely on λ-selective printing of different materials in a defined sequence. For instance, Boydston[147] and Hawker[148] employed radical and/or cationic photopolymerizations of disparate monomers to generate “stiff” and “flexible” domains, whereas Schlögl and co-workers[149] combined coumarin [2+2] cycloaddition with thiol-ene click chemistry to achieve similar material properties.

In 2023, Boydston and co-workers reported a novel approach to introducing different material properties by employing two colors of light within a single vat.[150] Unlike conventional strategies based on crosslinking different networks at separate wavelengths, one wavelength was dedicated to printing, while the other was used to adjust the color of the object. Fabrication was carried out using a poly (ethylene glycol) diacrylate (PEGDA)-based photoresist, crosslinked via type II radical initiation of camphorquinone and a tertiary amine co-initiator under visible (white) light in a DLP setup. Color control over the printed structure was achieved by photolysis of triarylsulfonium hexafluorophosphate salts at 365 nm, generating Brønsted acids that triggered a color change in the photoresponsive dye bromocresol green. By tuning the UV exposure dose, colors ranging from blue over green to yellow were realized. To mitigate outgrowth caused by UV irradiation and improve feature definition, hydroquinone was added as a radical inhibitor. **Figure 15** illustrates several computer-aided design (CAD) models alongside the resulting printed structures, demonstrating successful fabrication of well-defined multicolored 3D objects.[150]

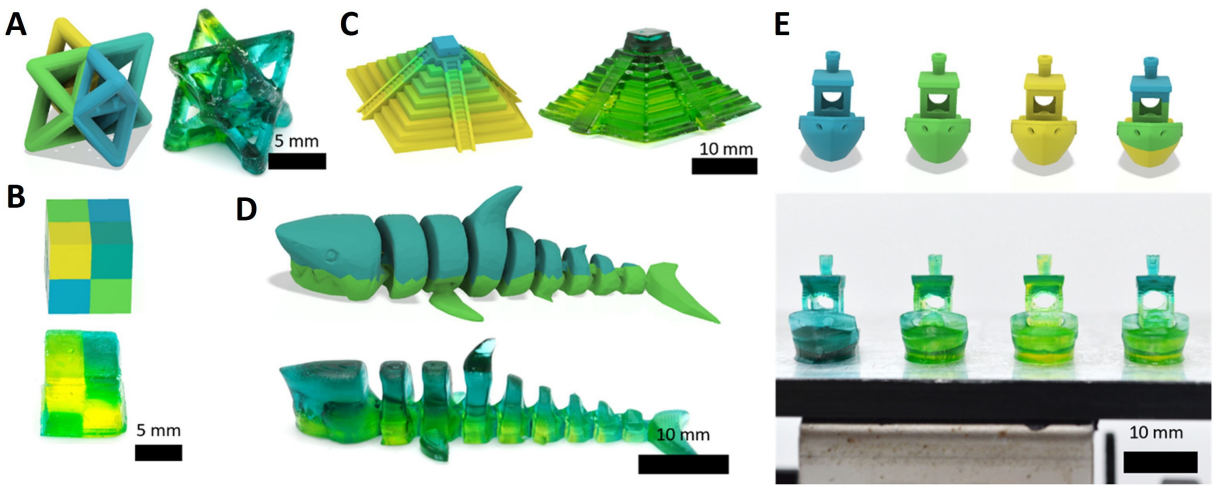

Figure 15. Dual-wavelength 3D printed objects with multiple colors and the corresponding CAD models. (**A**) Multi-color octet truss. (**B**) Multi-color cube. (**C**) Gradient multi-color pyramid. (**D**) Two-toned shark. (**E**) Multi-colored benchy fleet. Adapted from Chin *et al.*, licensed under CC BY 4.0.[150]

In 2019, we reported the development and fabrication of the first photoresist based on sequence-independent λ-orthogonal photochemistry.[126] The system relies on two separate dimerization reactions of, first a photocaged diene that is generated by irradiation of an *o*-MBA with UV light (330 nm), and second a styrylpyrene, activated by visible light (435 nm). Simply by varying the applied wavelength, two distinct materials were printed from a single photoresist, establishing the first platform technique for λ-orthogonal photoresists.[8, 126]

Building on this work we developed a novel λ-orthogonal photoresists in combination with a suitable printing setup for straightforward multimaterial fabrication by combining a monochromatic tunable laser with a custom-designed 3D printing platform (Mono LISA).[151] The beam path for the Mono LISA setup is shown in depicted in **Figure 16**.

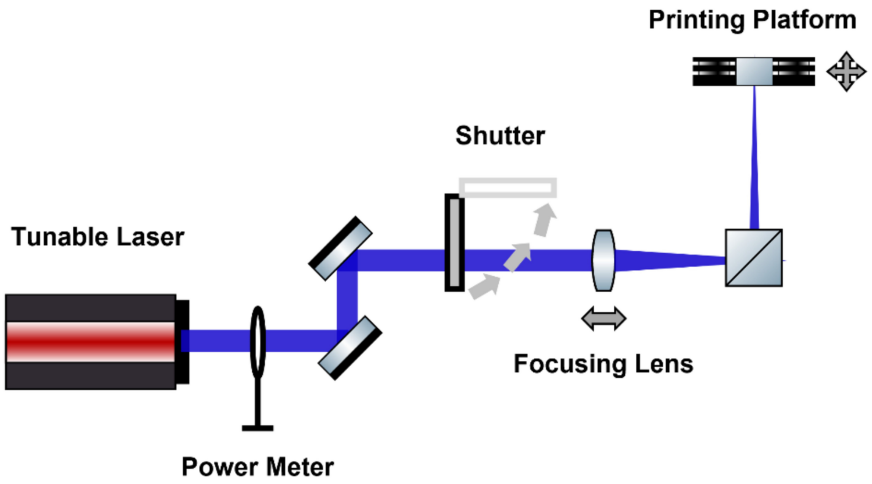

Figure 16. Schematic of Mono LISA printing setup, showing the beam path and various components. Adapted from Wu *et al.*, licensed under CC BY 4.0.[151]

The first crosslinking reaction of the photoresist is also based on the dimerization of *o*-MBA, whereas styrylpyrene was exchanged with a pyrene chalcone (Py-Chal) (**Figure 17**). Accordingly, the new λ-orthogonal activation windows were determined via action plot measurements to be 350 nm for *o*-MBA and 440 nm for Py-Chal. In order to generate disparate materials depending on the wavelengths employed, *o*-MBA and Py-Chal were attached to a PMMA and a triethylene glycol methyl ether methacrylate (TEGMA) backbone, respectively, thus either introducing hard or soft materials properties. Furthermore, the Mono LISA setup is not limited to one specific λ-orthogonal system, but serves a general multimaterial printing platform for diverse λ-orthogonal photoresists due to the wavelength-versatility of the tunable laser.[151]

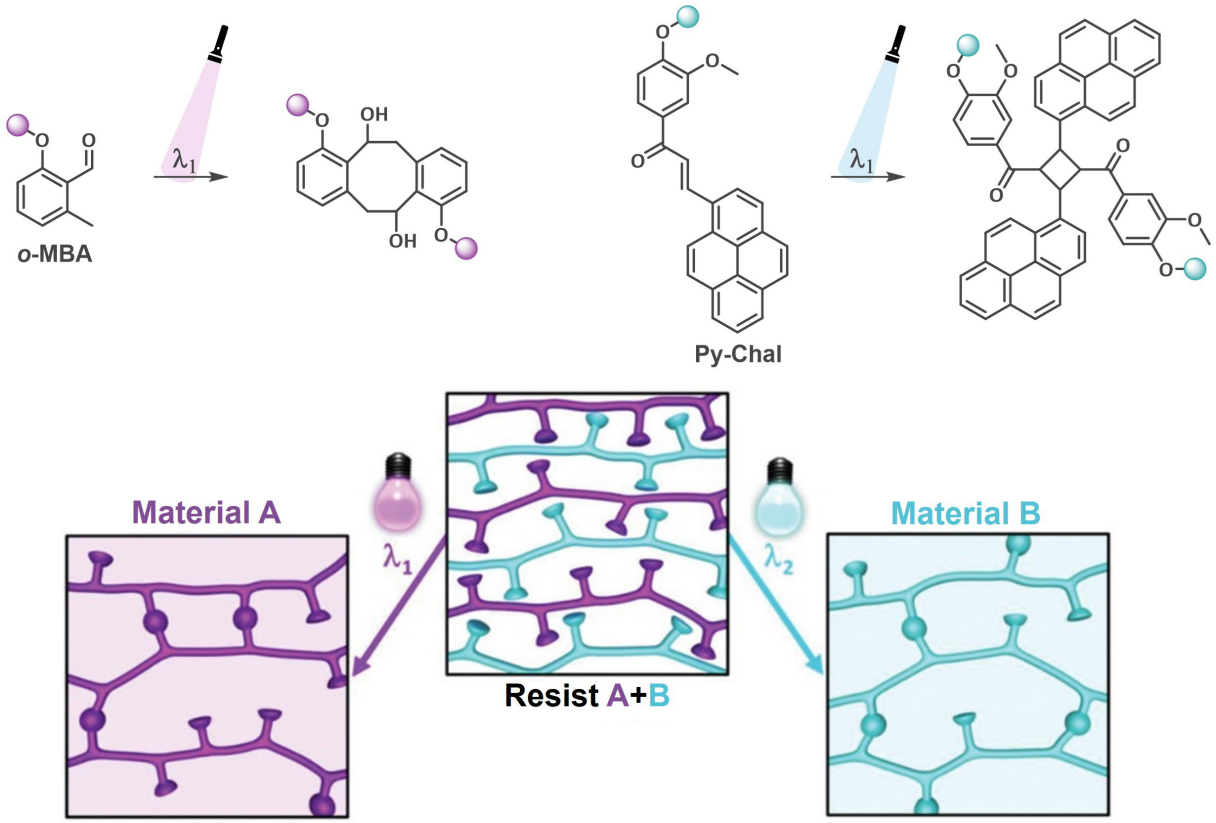

Figure 17. General concept of λ-orthogonal 3D printing with a single multimaterial photoresist. Material A is crosslinked upon exposure to wavelength λ_1 (350 nm, *o*-MBA-dimerization) and material B with wavelength λ_2 (440 nm, Py-Chal-dimerization).[151] Adapted with permission.[126] Copyright 2019, Wiley-VCH GmbH.

Conclusively, designing photoresists for λ-orthogonal 3D printing of intricate multimaterial structures undoubtedly poses a great challenge. Nevertheless, the ability to generate a wide variety of complex materials from a single formulation holds immense potential to greatly broaden the application range of 3D printing.[8, 9, 146]

2.4.1.4 Antagonistic

Probably the most fundamental movements of the human arm are governed by the antagonistic interplay of biceps and triceps. These muscles perform contrary actions of stretching and flexing and only their coordinated activity enables precise and controlled motion.[152] The concept of achieving balance by applying opposing forces can also be translated to photochemistry, where distinct wavelengths of light selectively induce either activation or deactivation of a chromophore. In 3D printing, the antagonistic principle has been harnessed to manufacture objects with exceptionally high resolution.[85, 153-155]

The possibility of printing 3D structures at the micro- and nanoscale unlocks a wide range of potential applications in fields such as photonics, biophysics, and optofluidics.[156] Currently, nanometer-scale precision can be achieved through electron-beam lithography, yet this method is confined to planar structures (2D and 2.5D) and requires expensive equipment.[157-159] In contrast, multiphoton absorption polymerization lithography has emerged as a powerful tool for fabricating 3D structures with transverse feature sizes below 100 nm.[156] This approach employs a focused, femtosecond near-infrared laser to trigger crosslinking reactions exclusively within the laser focal volume, as the required simultaneous absorption of two photons is otherwise highly improbable. Consequently, solidification occurs only within the focus with maximum photon density, ensuring minimal voxel sizes and enabling nanoscale precision.[127]

However, the attainable resolution cannot be indefinitely improved by downsizing the laser focus, as the laws of diffraction define a fundamental limit. Since the diffraction limit is proportional to the laser wavelength, one option is to employ shorter wavelengths to enhance resolution.[160] Unfortunately, by increasing the photon energy the process would shift to single-photon absorption, thereby losing the advantageous multiphoton mechanism and sharply reducing, rather than improving, the resolution.[127, 160]

In 2014, Stefan Hell received the Nobel Prize in Chemistry for his work on the development of STED microscopy, which achieves sub-diffraction imaging through the antagonistic interactions of two distinct wavelengths of light.[161, 162] The concept of STED microscopy served as inspiration for a novel two-color approach aiming to realize high-resolution 3D printing by employing a tailored photoresist and laser setup. In such systems, one wavelength excites a chromophore to trigger crosslinking, while a second wavelength depletes the excited state via stimulated emission, thereby suppressing polymerization.[163] The approach is generally based on a two-photon lithography setup for the printing and the deactivating laser beam of another wavelength is shaped around the excitation focus, e.g. in a doughnut shape. As a result, the effective voxel size can be progressively reduced by increasing the intensity of the depletion beam, effectively bypassing the diffraction limit.[5, 8, 85, 124, 154, 156, 158, 160]

One of the first laser-photoresist systems based on STED-inspired two-color printing was reported by Wegener and colleagues in 2010.[124] The photoresist consisted of pentaerythritol triacrylate as crosslinkable monomer combined with isopropyl thioxanthone (ITX) as the photoinitiator (**Figure 18A**). Radical crosslinking was initiated through two-photon absorption of ITX at 810 nm. Upon additional irradiation with green laser light (532 nm), however, stimulated emission of the excited ITX species was favored over radical generation. To minimize voxel size, the depletion beam was shaped in a doughnut profile around the excitation focus, as shown in **Figure 18B**. Using this setup, the linewidth was reduced from 155 nm to 65 nm, effectively halving the resolution relative to diffraction-limited conditions (**Figure 18C**).[8, 124]

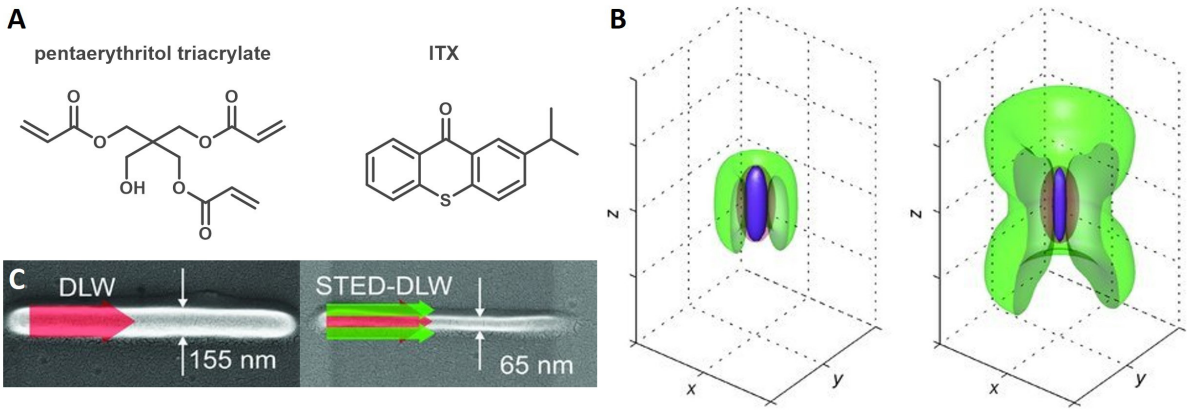

Figure 18. (**A**) Components of the photoresist for STED-inspired 3D printing, i.e., monomer pentaerythritol triacrylate and photoinitiator isopropyl thioxanthone (ITX). (**B**) Calculated iso-intensity surfaces of the foci of the depletion laser (532 nm, green) and the excitation laser (810 nm, red). The blue surfaces illustrate regions in space that are sufficiently excited but not sufficiently depleted, corresponding to the effectively exposed regions. With increasing STED-power (compare left and right), the effectively exposed region shrinks. (**C**) Polymer line width by two-photon printing of the same photoresist without (top, red arrow) and with addition of a depletion laser (bottom, green arrow). B and C reproduced with permission.[124] Copyright 2010, Wiley-VCH. Adapted from Ref.[8]

In 2019, our group introduced a photoresist based on a copolymer of methyl methacrylate (MMA) and spirothiopyran (STP)-functionalized methacrylate, representing a single-component system that does not require a photoinitiator.[85] STP belongs to the family of spiropyran photoswitches and undergoes a ring-opening isomerization to its merocyanine (MC) form via 820 nm two-photon absorption (**Figure 19**). Within the photoresist, the generated MC species engage in supramolecular interactions that act as physical crosslinks, thereby enabling the fabrication of free-standing 3D structures. In contrast, irradiation at 640 nm induces the photoreversion of MC back to STP through a single-photon process. Harnessing the reversible isomerization, the lower wavelength served as an additional parameter to enhance resolution, reducing the achievable linewidth from 55 nm to 31 nm.[85]

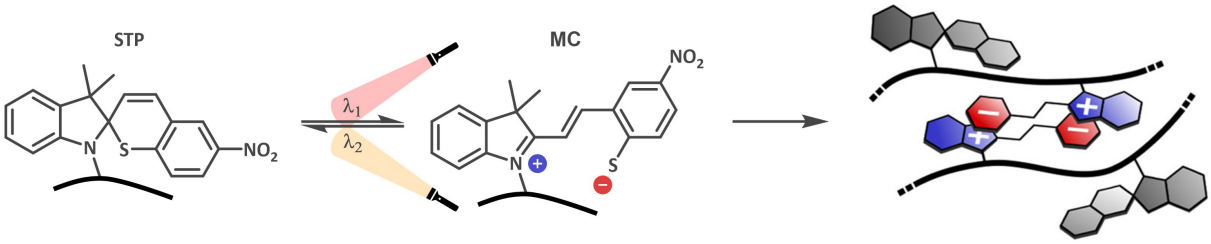

Figure 19. Two-photon activated ring-opening of spirothiopyran (STP) at 820 nm (λ_1) to its merocyanine (MC) derivative. The reverse reaction is triggered by irradiation at 640 nm (λ_2). The merocyanine form can create physical crosslinks via supramolecular interactions. Adapted with permission.[85] Copyright 2019, American Chemical Society. Adapted from Ref.[8]

In general, photoswitches provide a powerful means of achieving wavelength-dependent control over the reversible isomerization between potentially reactive and unreactive states, thereby offering a versatile toolbox for the development of antagonistic systems. Along these lines, another small-molecule antagonistic system based on the reaction of an *o*-MBA with a diarylethene photoswitch was reported by us in 2021, which was recently extended to the macromolecular crosslinking of a photoresist by our team in collaboration with the group of Campos.[8, 164, 165]

Over the past decade, the drive to surpass the diffraction limit in additive manufacturing via antagonistic photochemistry has led to numerous publications in the field. [85, 153, 158, 165] Maximizing the achievable resolution remains a highly rewarding challenge, as it would enable the precise fabrication of nanometer-scale architectures with potential applications across diverse research areas, including high-density optical data storage and 3D photonic metamaterials.[160]

2.4.2 Printing with Multiple Colors of Light

Recent developments in two-color 3D printing clearly demonstrate the substantial advantages of working with a second wavelength. Control over the printing process is enhanced by introducing another color as an additional parameter. More importantly, the use of a second color does not merely improve established manufacturing techniques but also enables fundamentally new and superior 3D printing approaches. Examples include light-sheet printing[123] (synergistic), multimaterial approaches[126] (orthogonal and cooperative) and STED-inspired fabrication with extremely high resolution[124] (antagonistic). Thus, two-color photochemistry represents a field of enormous relevance and promise for the future of 3D printing. Naturally, this raises the question of what would be possible with three, four or even more colors of light?[8]

2.4.2.1 Multi-Color Printing

Light as a spectrum offers a multitude of new opportunities that can be harnessed simultaneously to achieve distinct purposes. By introducing wavelength as an additional parameter the design of highly sophisticated systems with advanced functionalities becomes possible. At present, however, the limited versatility of materials that a single printer can process significantly restricts the commercial use of 3D printing. Enormous potential lies on the development of a multimaterial photoresist that enables the fabrication of different materials from a single cartridge by employing different wavelengths. Such an approach would allow for complex structures to be fabricated in a single step instead of producing individual parts and subsequently assembling them. For example applications in the field of biomedicine for printing organs or tissues like the retina are conceivable. Moreover, the simplicity of a universal photoresist would make it highly convenient, potentially even suitable for everyday household use. Beyond Earth, versatile 3D printing also holds immense promise for space travel, with major challenges of mass and space constraints, as well as limited resources. A “one-size-fits-all” photoresist capable of fabricating diverse structures on demand would represent a significant advantage under such conditions.[8]

Besides enhancing control over synergistic, cooperative, orthogonal, or antagonistic light-resist interactions by introducing multiple colors, the potential for combining these approaches open further opportunities. For instance, multimaterial printing could be realized at high speed by merging orthogonal and synergistic strategies, or with optimized precision by combining orthogonal with antagonistic photochemistry. Even the seemingly contradictory fusion of synergistic and antagonistic interactions may become feasible, if both processes are λ-orthogonal, and offers the potential to enable rapid fabrication of large-scale objects with extremely high resolution. At present, such

concepts remain within the realm of science fiction. To transform them into science fact, our understanding of the photochemical behavior of reactive chromophores must advance substantially, especially considering the evident mismatch between absorbance spectra and photochemical reactivity, that our group demonstrated repeatedly over the last decade.[37, 116, 118] We therefore submit that action plot measurements are of key interest for every photochemical system, since absorbance spectra alone cannot reliably predict chemical reactivity.[8]

2.4.2.2 Introduction of Stimuli Responses

Beyond the development of innovative techniques for enhanced control during fabrication, the next opportunity lies in manipulating an object after printing. This concept is termed 4D printing and refers to the programmable change of a 3D printed structure in e.g. shape and functionalities over time as a fourth dimension when exposed to certain stimuli such as temperature, pH, or light.[131, 166-169] An example is bending of a printed material, used for the motion of a gripper arm without the need for any electronic components.[170] Compared to other potential triggers, light holds a distinct advantage with its unparalleled spatiotemporal control, facilitating localized activation of structural changes even on the micro- and nanoscale.[45-47] Moreover, the spectral nature of light provides a seemingly limitless supply of wavelengths capable of triggering diverse responses. With each additional color, new functionalities can potentially be addressed, thus effectively creating a remote control with multiple buttons to regulate certain functions, such as specific robotic movements. 4D printing has gained particular interest for the fabrication of biomedical devices and drug delivery systems.[171] For designing such materials, 3D laser printing is especially powerful, enabling the fabrication of objects with tailored stimuli-responsive behavior in a straightforward manner.[172] Due to the spatiotemporal control over light, defined responses can be triggered in these structures precisely, even in highly confined regions. A theoretical vision is the creation of nanorobots with the ability to perform complex tasks, which increases with each additional wavelength, much like adding buttons to a remote control.[173] The synergy between customizable 3D printed architectures and programmed control via multiwavelength responsiveness after fabrication underscores the enormous potential of multi-color 4D printing.[8, 46]

2.4.2.3 Problems and Approaches to Solutions

At present, two-color 3D printing is still in its early stages and has not yet entered commercial use due to the inherent challenges and complex nature of multi-color photochemistry. Every additional color further amplifies the complexity for several reasons. First, it is critical to recognize that λ-orthogonal

windows are not to be determined by the absorbance spectra of a set of chromophores but by their actual wavelength-dependent reactivities, i.e. their action plots.[37] Furthermore, photochemical reactivities are not confined to single wavelengths but to spectral ranges that often overlap, ultimately compromising λ-orthogonality and thus reducing control over the process.[46] A closely related problem is that many chromophores possess overlapping reactivities within the high-energy UV region, thus preventing their selective activation.[174] Moreover, UV light entails poor penetration depth and is detrimental to biological tissues.[174, 175] Therefore, the visible spectrum holds the greatest potential for multi-color strategies. However, only a limited number of chromophores can be activated in the visible range, which significantly restricts the available toolbox.[8, 174]

These challenges naturally lead to the question of how the potential of multi-color photochemistry can be harnessed successfully. A key step is the red-shifting of photochemical reactivity into the visible spectrum, ideally without relying on catalysts, by developing and discovering new photoreactive compounds.[176, 177] Another approach relies on redesigning and tuning existing chromophores to red-shift their reactivities.[109, 174] Moreover, as emphasized above, it is critical to recognize that absorbance does not coincide with reactivity.[37] In conclusion, advancing towards sophisticated multi-color systems requires an expansion of the toolbox of chromophores activated in the visible range, combined with comprehensive action plot studies to precisely determine and harness λ-orthogonal windows.[8, 37, 174, 177, 178]

3. Motivation

Precision photochemistry has been driven forward by technological advances in light-generation techniques, enabling targeted access to nearly any wavelength and consequently wavelength-resolved insights into complex photochemical processes.[39] Transitioning from conventional broadband sources, state-of-the-art tunable lasers now provide access to diverse wavelengths, extending well beyond the visible spectrum. In parallel, compact and cost-effective alternatives such as continuous-wave (CW) lasers and narrow-disperse light-emitting diodes (LEDs) have further broadened the experimental scope. With distinct wavelengths available on demand, detailed investigations into wavelength-specific reactivities became possible. In particular photochemical action plot measurements allow for deep insights into chromophore reactivities and reveal efficiency maxima that often appear red-shifted from simple absorbance spectra.[37] Critically, such knowledge enables identification of distinct λ-orthogonal windows, thus setting the foundation for multi-color photochemistries based on diverse reaction modes, i.e. synergistic, cooperative, orthogonal and antagonistic.[8, 9]

Synergistic photochemistry is particularly powerful, as it relies on the premise that an irreversible change (e.g., bond formation) occurs only when two distinct colors of light coincide within the same volume element. The synergistic concept holds great promise for additive manufacturing, offering the potential for extremely fast and precise fabrication of complex architectures via light-sheet approaches that would otherwise not be achievable.[11, 12, 123] The commercial launch of *xolography* 3D printers,[12] which exploit synergistic two-color interplay, strikingly highlights the potential and assertiveness of such techniques.

Current implementations are based on the sequential absorption of two photons at different wavelengths by a single molecule, which then initiates radical polymerization from an excited state.[11, 12] The present study explores a novel dual-photoswitch system, where the absorption of different photons occurs at distinct sites, followed by covalent-bond formation between the activated photoswitch isomers. A similar system was reported previously by our group but was limited by insufficient reversion of the reactive photoswitches once irradiation ceased, thereby impeding synergistic efficiency.[30] Herein, a novel combination of photoswitches, i.e. DIO and SA, is investigated in detail with the intent to serve as a foundation for developing and characterizing further synergistic photochemistries. Moreover, the in-depth molecular study provides the basis for designing photoresists that translate small-molecule synergistic behavior to the macromolecular scale for application in lithographic fabrication.

4. Results and Discussion

To establish the potential of the two-color approach, first the fundamental reactivity was validated on the small-molecule scale and then the concept was systematically expanded toward macromolecular systems and lithographic applications. Accordingly, the initial focus was on the reaction shown in **Figure 20**, confirming that DIO and SA undergo covalent bond formation under two-color irradiation to yield the (3+2) cycloadduct DIOSA. Subsequently, photochemical action plot studies were performed for both photoswitches independently to identify optimal excitation wavelengths for synergistic bond formation. These investigations were followed by two-color LED kinetics to enable quantification of the synergistic efficiency of the cycloaddition.

For translation of the small-molecule model system to the macromolecular scale, a next-generation photoresist incorporating DIO and SA units was rationally designed and synthesized. The crosslinking behavior of the photoresist was then analyzed under diluted conditions (90 wt% solvent) using SEC which provided fundamental insights into the process of synergistic network formation. Finally, the applicability of the system was demonstrated through the fabrication of printed lines and two-dimensional structures using a custom-designed two-color laser lithography setup.

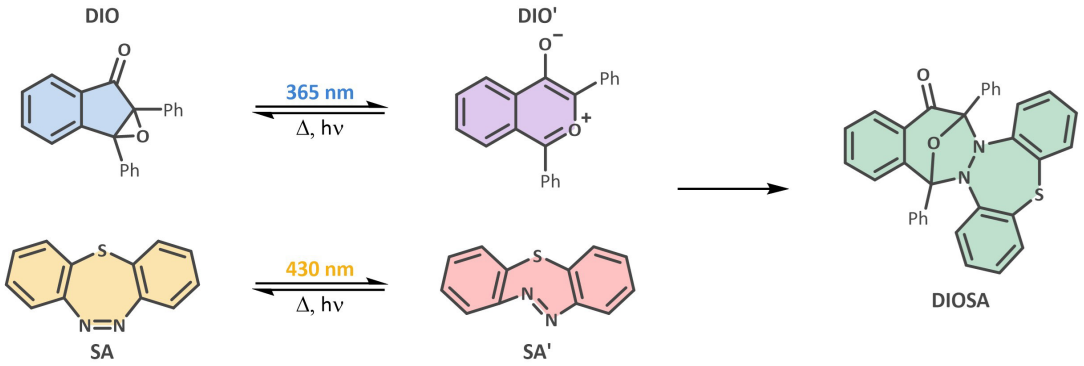

Figure 20. Light-induced photoswitching of DIO and SA to their corresponding isomers DIO' and SA' at 365 and 430 nm, respectively. These isomers possess complementary reactivities and form DIOSA as an adduct in a cycloaddition reaction. Adapted from Hobich *et al.*[31]

4.1 Two-color Covalent Bond Formation

First, the occurrence of an efficient cycloaddition between DIO and SA under dual-color irradiation was verified (**Figure 20**; it should be noted that the action plot study discussed in **Section 4.2** has served to identify the wavelengths employed herein). The selection of DIO and SA was guided by several requirements essential for synergistic photochemistry. Initially, in the dark and under ambient conditions, solely the unreactive isomers of both photoswitches, i.e. DIO and SA, are present and only

light-induced photoswitching results in the formation of the reactive isomers DIO' and SA'. Secondly, in the absence of light, the reactive species need to revert rapidly in order to enable enhanced spatiotemporal control.

SA meets the reversibility requirements as a T-type photoswitch and readily reverts once irradiation ceases, with an extremely short half-life ($t_{1/2}$) for the metastable isomer SA' (180 ms at 298 K).[34] In contrast, DIO' has a half-life of almost 50 minutes at 298 K,[33] which – although short for a photoswitch in general – is still far from instantaneous. Nevertheless, the limitation can be overcome by harnessing the photoreversion of DIO' to DIO under visible light (around 520 nm).[33] Therefore, for this combination of photoswitches, the visible light λ_2 that activates SA is also harnessed to partially deactivate DIO' and a delicate balance is required for the powers of λ_1 and λ_2 in order to reduce the half-life of DIO' without suppressing efficient reactivity under two-color conditions (**Figure 21**).

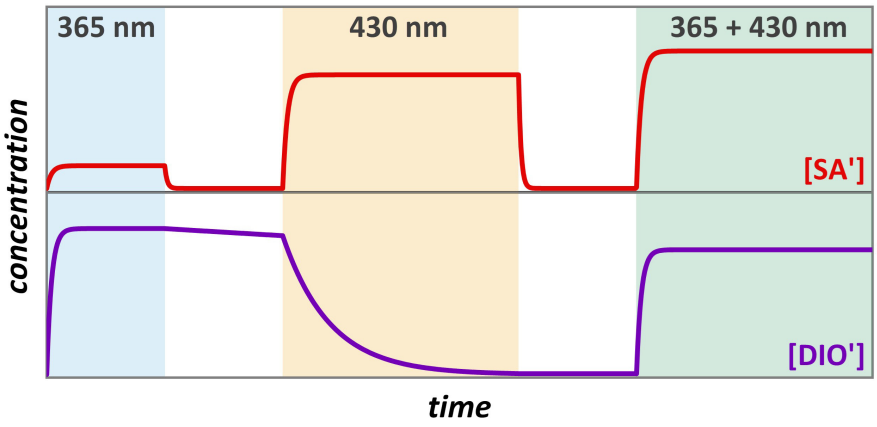

Figure 21. Schematic illustration depicting the qualitative wavelength-dependent concentrations changes of the reactive photoswitch species DIO' (violet) and SA' (red). DIO' is formed at 365 nm, deactivated at 430 nm and the thermal reversion to DIO is relatively slow ($t_{1/2}$=50 min).[33] SA' is formed at 365 and 430 nm, respectively, and undergoes almost instantaneous reversion to SA ($t_{1/2}$=180 ms)[34] in the dark. When 365 and 430 nm are applied simultaneously, the concentrations of both DIO' and SA' are relatively high. Therefore, the reaction rate increases compared to one-color irradiation and photochemical two-color synergy is achieved. Adapted from Hobich *et al.*[31]

If the first two prerequisites are met, the last important requirement is a selective and efficient covalent-bond forming reaction between the reactive isomers DIO' and SA'.[8] Meeting this criterion is especially challenging since photoswitches are usually designed to be inert in order to withstand many switching cycles without undergoing any side reactions. However, DIO and SA are both exception as photoactivation results in the formation of highly reactive metastable isomers.[33-36] In the dark, solely the inert and stable DIO is present, and upon irradiation with UV light (e.g. 365 nm)[33] ring expansion via cleavage of the epoxide C-C bond results in DIO' which readily undergoes cycloaddition reactions with ring-strained double bonds (e.g. of norbornene). SA belongs to the family of bridged azobenzenes, more specifically to the diazocines, which are locked in *cis* conformation in the dark.[75] Upon irradiation with visible light of up to 500 nm, *cis*-to-*trans* isomerization occurs and the ring strain

increases drastically.[34] Consequently, DIO and SA are an ideal match due to the complementary reactivities of their activated isomers and undergo a two-color covalent bond forming reaction to the cycloadduct DIOSA (**Figure 20**). The molecular structure of DIOSA was characterized via LC-MS and SXRD (**Figure 22**). High resolution mass spectrometry (HRMS) analysis in **Figure 22A** yielded an *m/z* value of 511.1475, in excellent agreement with the theoretically calculated value of 511.1480 for protonated DIOSA. Structure elucidation via SXRD (**Figure 22B**) further proved the successful formation of a cycloadduct and showed that the bond formation pattern matches the previously reported reactivities of the individual photoswitches, i.e. a (3+2) cycloaddition of DIO' to a strained double bond[33] which is the N=N azo bridge of SA'.[34]

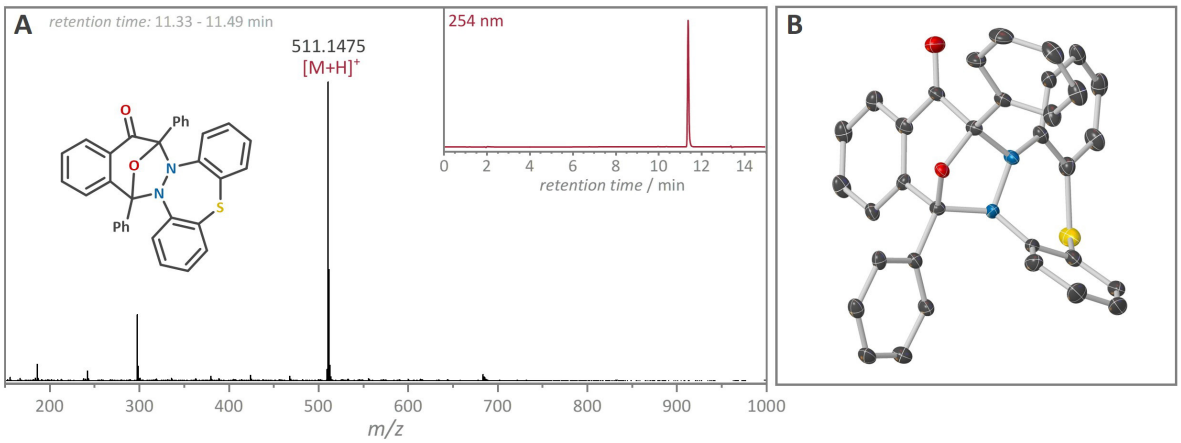

Figure 22. (**A**) Accumulated mass spectra (retention time 11.33-11.49 min) and LC traces of DIOSA in acetonitrile/water. An *m/z* of 511.1475 was obtained via HRMS for the isolated photo-adduct and matches the theoretically expected *m/z* of 511.1480 for a protonated DIOSA molecule. (**B**) Molecular structure of DIOSA obtained via SXRD. The black ellipsoids represent carbon, red for oxygen, blue for nitrogen and yellow for sulfur. For a better and clearer visualization, the hydrogen atoms have been omitted. Adapted from Hobich *et al*.[31]

SXRD confirmed the same connectivity for the cycloadduct DIOnor of a reaction between DIO' and the strained double bond of norbornene which exclusively led to the formation of the exo product (**Figure 23B**). The cycloaddition to DIOnor served as the basis for the action plot measurements of DIO, which will be further discussed in the following **Section 4.2**.

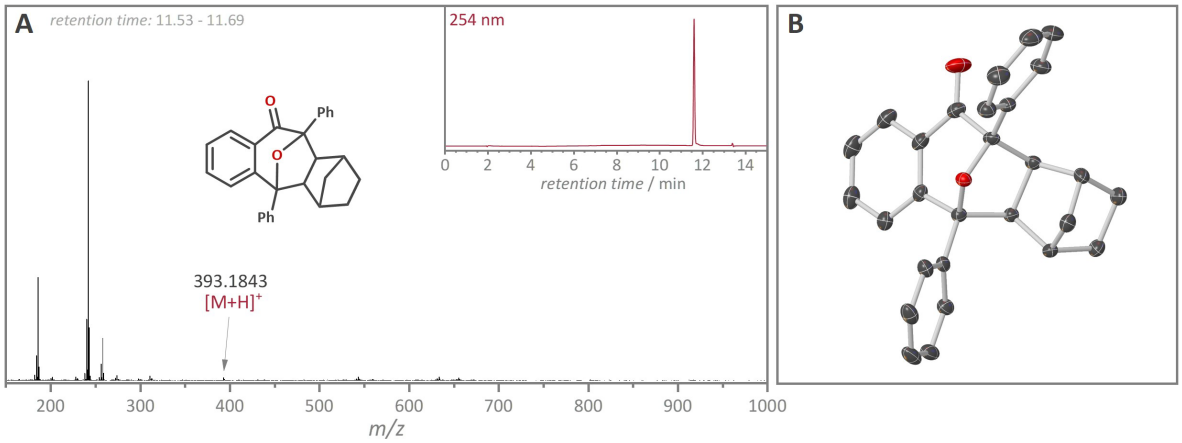

Figure 23. (**A**) Accumulated mass spectra (retention time 11.53-11.69 min) and LC traces of DIOnor in acetonitrile/water. An *m/z* of 393.1843 was obtained via HRMS for the isolated photo-adduct and matches the theoretically expected *m/z* of 393.1855 for a protonated DIOnor molecule. (**B**) Molecular structure of DIOnor obtained via SXRD. The black ellipsoids represent carbon and red for oxygen. For a better and clearer visualization, the hydrogen atoms have been omitted. Adapted from Hobich *et al*.[31]

Furthermore, to understand if the cycloaddition reaction is truly based on the reaction of DIO' and SA' in their respective ground states, a test reaction was performed where both switches were activated separately and then mixed in the dark. Under these circumstances DIOSA formation cannot occur from extremely short-lived excited state, but only from the ground states of the respective metastable photoswitches. The reaction was performed at -35 °C due to the extremely short half-life of 180 ms at 25 °C for SA'.[34] DIO (14.1 mg, 47 nmol, 1.00 eq.) and SA (10.0 mg, 47 nmol, 1.00 eq.) were each dissolved in 1 mL of acetonitrile. First, the solution of DIO was briefly irradiated at 365 nm and turned to a deep shade of violet due to the formation of DIO'. Subsequently, the solution of SA was cooled to -35 °C in an acetonitrile/dry ice bath and shortly irradiated with 430 nm, turning the solution deep red due to the formation of SA'. Finally, both solutions were combined in the dark at -35 °C and stirred for 5 minutes. When mixing both solutions the pink and red colors faded almost instantly, and LC-MS analysis (**Figure 24**) verified successful formation of DIO and confirmed that the cycloaddition occurs from the metastable ground states of the activated photoswitches.

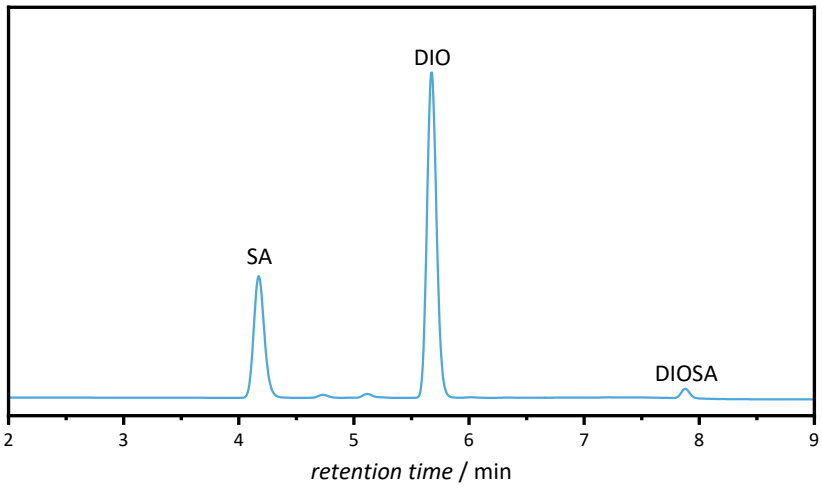

Figure 24. UV-detector LC traces at 235 nm of the reaction mixture after reaction of DIO' and SA' in the dark. Formation of DIOSA proves that the reaction occurs from the metastable ground states of the activated photoswitches. Adapted from Hobich *et al*.[31]

4.2 Understanding Reactivity and Switching Behavior via Action Plot Measurements

In order to realize advanced control over light matter interactions via precision photochemistry, it is of utmost importance to understand the wavelength-dependent reactivity of the corresponding chromophore by recording an action plot.[37, 109, 110, 179] Action plot investigations become especially relevant when multiple colors of light are employed to achieve more complex reaction modes, i.e. synergistic, antagonistic, orthogonal and cooperative. Therefore, detailed action plot studies of DIO and SA served as a basis for choosing the optimum wavelengths for the synergistic two-color covalent bond formation yielding DIOSA.[37, 116]

An action plot in general presents the wavelength-dependent reactivity of a chromophore, resulting in the formation of a particular product via covalent bond formation, cleavage or isomerization. While some light-induced reactions are irreversible, they can also be reversible, like in the case of photoswitches that can isomerize between their different (meta)stable ground states. The isomerization can occur thermally – or even more importantly photochemically – thus adding more complexity to the overall reaction processes under irradiation, which is also inherent for DIO and SA (**Figure 25**). Consequently, the activation of these photoswitches might seem to be straightforward and unidirectional, but in reality a dynamic equilibrium between both isomers is reached and the resulting action plot actually depicts the consequences of an intricate interplay between photochemical activation and deactivation.

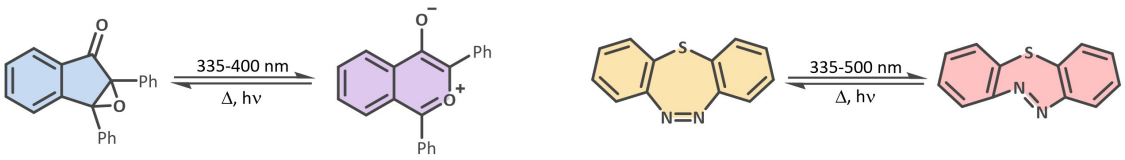

Figure 25. Reversible photoswitching reactions of DIO (left-side) and SA (right-side) to DIO' and SA', respectively. The forward reactions are light-induced while the backwards reactions proceed thermally at ambient temperature but can also be triggered by light. Adapted from Hobich *et al.*[31]

It is important to note that in the cases of DIO and SA, the activated isomers absorb and revert at longer wavelengths on the red-side of their original absorbance spectra. Consequently, only a composite action plot is obtained that constitutes the overall concentration of reactive species as a consequence of back-and-forth isomerization. Since the deactivation reactions occur at wavelengths exceeding those of the activation, any potential red-shifts of the composite action plot are suppressed and cannot be observed. However, even though a composite action plot does not resolve the intricate interplay of photochemical isomerization, which is of theoretical interest, instead, the wavelength-dependent net reactivities are obtained which is the essential data needed for any practical application. Thus, the action plots of DIO and SA in **Figure 26** provide the fundamental information for combining both photoswitches into a synergistic system.

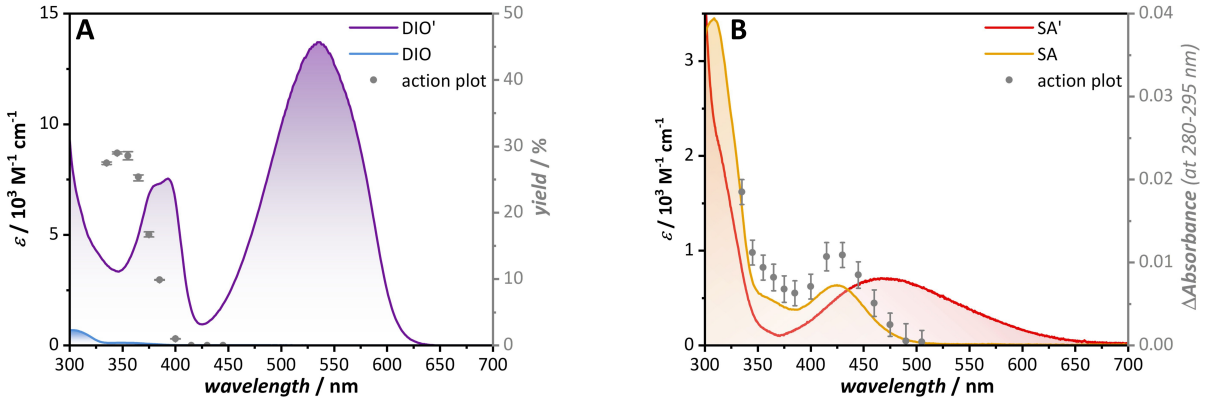

Figure 26. (**A**) UV-Vis absorbance spectra of DIO (experimental, blue line) and DIO' (theoretical, purple line, refer to **Appendix Section 7.5**) in acetonitrile and the corresponding action plot as the wavelength-dependent product formation in a reaction with norbornene. The product yield was determined by LC-MS after irradiation with 2.08 × 10^{17} photons (345 nmol) of various wavelengths from a tunable optical parametric oscillator (OPO) laser. A magnified view of the absorbance spectrum of DIO and the action plot is shown in Supporting Information Figure S5. (**B**) UV-Vis absorbance spectra of SA (experimental, orange line) and SA' (theoretical, red line, refer to **Appendix Section 7.5**) in acetonitrile and the corresponding action plot as the wavelength-dependent SA' concentration. The relative SA' concentration was obtained by measuring differences in the absorbance spectrum in the range of 280-295 nm (most notable difference between the absorbance spectra) of SA via in situ UV-Vis spectroscopy under irradiation with a constant photon flux of 7.65 × 10^{15} s^{-1} of various wavelengths from a tunable OPO. Adapted from Hobich *et al.*[31]

For DIO the action plot was determined from the product yields of the photoreaction between DIO and the strained C=C double bond of norbornene under irradiation at different wavelengths. The yields were determined via LC-MS characterization with 1,3,5-trimethoxybenzene (TMB) as a standard and a detailed description of the process can be found in the **Section 6.2.12.1**. For SA, the wavelength-

dependent change of absorbance as a consequence of photoswitching was measured via UV-Vis spectroscopy, hence providing the relative concentration of SA'. Due to the extremely short half-life of SA' it was not possible to determine the extinction coefficients of the pure compound, and no absolute concentrations could be calculated. Nevertheless, the absence of is not a problem since the essence of an action plot is of relative nature that is measured in a model system and then applied further. Another consequence of the short half-life was that the UV-Vis measurements for the action plot had to be performed in real time during laser irradiation in order to observe any differences in absorbance. The absorbance spectra of SA and SA' showed the biggest differences in the region of 280-295 nm which was used for the comparison. More details on the acquirement of the SA action plot are given in **Section 6.2.12.2**. In **Figure 27A** the action plots and absorbance spectra of the activated and deactivated isomers of both photoswitches are overlayed. While the absorbance spectra of the stable species DIO and SA were measured directly, DIO' and SA' could not be isolated so the corresponding absorbance spectra in **Figure 26** were approximated based on the UV-Vis spectra of PSS mixtures of DIO/DIO' and SA/SA' (see **Appendix Section 7.5** for a detailed explanation of the approximation).

Next, from the action plot measurements, the wavelength-dependent quantum yields for DIO and SA were calculated and shown in **Figure 27B**. For DIO the quantum yield Φ_{qy} was calculated separately for every data point according to the following formula

$$\Phi_{qy} = \frac{c \cdot V \cdot N_A \cdot \rho}{N_p \cdot (1 - 10^{-\varepsilon c l})}$$

where c is the photoswitch concentration and V the volume of the solution, N_A the Avogadro's number, ρ the product yield, N_p the number of photons deposited, ε the extinction and l the path length through the solution in the reaction vial.

Due to the relative nature of the action plot for SA, only relative quantum yields could be obtained, and the formula was adjusted accordingly by normalization.

$$\frac{\Phi_{qy}}{\Phi_{qy,max}} = \frac{\frac{\rho}{(1 - 10^{-\varepsilon c l})}}{\frac{\rho_{max}}{(1 - 10^{-\varepsilon_{max} c l})}}$$

Like the action plots, the apparent quantum yields are not solely based on the activation of DIO or SA but also depend on the photoreversion of DIO' and SA'. The relative quantum yield of SA stays mostly constant from 335-475 nm which is due to the similar trends of action plot and absorbance spectrum and is a behavior that was also previously observed for a thioindigo photoswitch.[113]

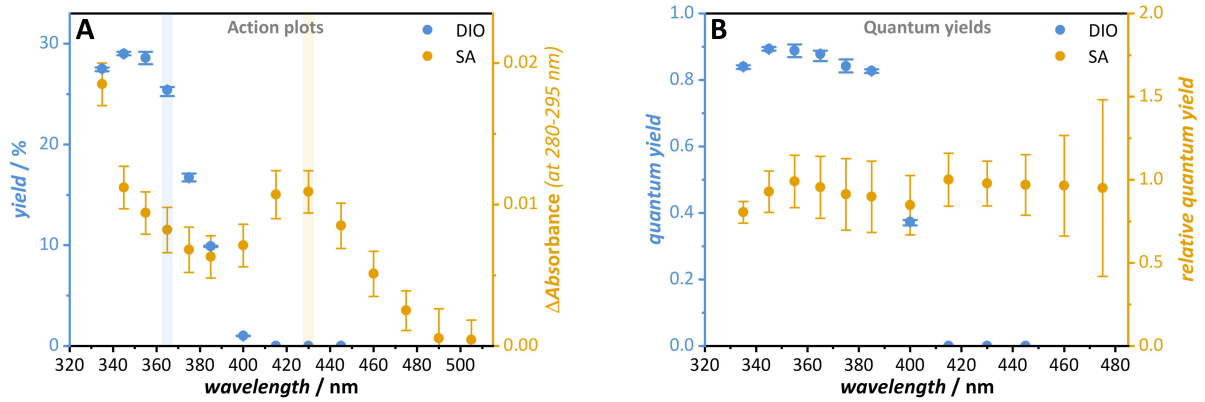

Figure 27. (**A**) Overlay of the action plots of DIO (blue) and SA (yellow) to understand the combined wavelength-dependent reactivities. (**B**) Overlay of the effective quantum yields of DIO (absolute) and SA (relative) calculated from the action plot measurements. Adapted from Hobich *et al*.[31]

Investigating the wavelength-dependent reactivities of the photoswitches is crucial in order to determine suitable λ-orthogonal windows for a two-color system, as demonstrated by overlaying the action plots of DIO and SA in **Figure 27A**. The photoreactivity of DIO has a maximum at 345 nm, sharply decreases above 365 nm and ceases completely at 415 nm. The action plot of SA shows a local minimum of SA' formation in the UV range from 375 and 385 nm and a local maximum around 415-430 nm. Deciding on 430 nm as the wavelength for SA activation proved to be straightforward since it is fully λ-orthogonal to the DIO activation and the efficiency of the reaction is comparably high at the local maximum. Furthermore, while the action plot measurements are performed with monochromatic laser light, it is preferrable to keep some buffer space to the region below 400 nm when employing commercially more viable non-monochromatic light sources such as LEDs in order to avoid any undesired activation of DIO. Employing even longer wavelengths between 430 and 500 nm is conceivable but would increasingly promote the reversion of DIO' to DIO. Choosing a wavelength for the activation of DIO proved to be more challenging due to the absence of a λ-orthogonal window. 365 nm was selected since efficiency of the photoreaction drops significantly at longer wavelengths and to avoid potential side reactions at shorter wavelengths. Additionally, 365 nm is one of the best developed and commercially available UV-LED wavelengths.[180] To summarize, 430 nm solely triggers SA, while 365 nm activates both DIO and SA, resulting in an imperfect synergy. Nevertheless, the problem can be minimized by harnessing the several orders of magnitude of difference between the half-lives of SA' (180 ms)[34] and DIO' (50 min).[33] The 365 nm LED can be operated at low powers, since even low photon fluxes can constantly keep the concentration of DIO', while the almost instantaneous thermal reversion of SA' reduces its overall concentration significantly. However, even though the undesired formation of SA' can be minimized it is not negligible and cannot be avoided completely. In the following, a parameter is introduced that enables the quantification and comparison of the imperfection across synergistic systems.

4.3 Efficiency of Photochemical Synergy

Ideally, there is no need to discuss the efficiency of a synergistic reaction and only the simultaneous irradiation with two different wavelengths triggers a reaction. However, in reality every reactive species has a certain lifetime and will at least briefly be present when irradiation ceases because it cannot revert instantly. Still, the main challenge is to identify suitable λ-orthogonal windows due to overlapping absorbances of the employed chromophores, which is especially pronounced in the UV region. Furthermore, even if optimal λ-orthogonal windows are identified they might need to be precisely addressed by monochromatic light. Besides the question of whether the wavelengths are even accessible without an extensive tunable laser system, the scope for any practical application would be limited by high expenses and impracticability.

Herein, a more realistic and practical perspective on the concept of photochemical synergy is adapted. For the combination of DIO and SA reactivities overlap at 365 nm, but a λ-orthogonal is opened by harnessing the lifetime differences between the reactive species. Furthermore, polychromatic LEDs were employed as commercially available and cost-effective light sources.[181] The problems of an imperfect λ-orthogonal window and the use of non-monochromatic light result in a deviation from perfect synergy and 365 nm alone is sufficient to trigger the formation of DIOSA. Herein, the synergistic ratio ϕ_{syn} is introduced as a new parameter for quantification of the degree of synergy resulting from the imperfect conditions and is defined by the following equation

$$\phi_{syn}(t) = \frac{Y_2(t)}{Y_1(t)}$$

where Y_1 and Y_2 are the product yields of the one- and two-color reaction, under the same conditions and after the same reaction time t, respectively. ϕ_{syn} can be understood as a factor of how much faster a reaction proceeds due to the synergistic effect when two- instead of one-color of light is applied. In the ideal scenario a reaction solely occurs under simultaneous two-color irradiation, meaning Y_1 is always 0 and ϕ_{syn} consequently infinite. Since these conditions do not apply for this work and the yields are a function of time Y_1, the synergistic ratio ϕ_{syn} is also time-dependent and changes over the course of the reaction. Therefore another parameter ϕ_{syn}^0 is introduced as the synergistic ratio at the beginning of the reaction (i.e. t=0) as a yield- and time-independent parameter for the comparison of different synergistic systems. The start of the reaction was chosen since secondary effects are minimized by comparing the initial stages of the one-and two-color kinetics. (Refer to **Section 6.2.13.2** for more details on the evaluation of the two-color reactions.)

Next, the novel insights into the photochemical synergy were investigated for the combination of the photoswitches DIO and SA. In general many variables (such as temperature, photon fluxes of the LEDs,

solvent as well as starting material concentrations and equivalents) have an impact on ϕ_{syn}. In this study, all reactions were performed with 5 mM photoswitch concentrations in acetonitrile, a common solvent for photoreactions, in which DIOSA formation proceeded efficiently. Additionally, the samples for kinetic studies were diluted and directly used for product yield characterization via acetonitrile/water eluted LC-MS. Regarding the experiment setup, stock solutions containing DIO, SA and TMB as an internal standard were prepared and for each data point 250 µL were added into a 2 mL crimped vial that was kept under argon atmosphere to avoid undesired side reactions. The vial was crimped with a magnetic cap and attached to a custom-made LED holder shown in **Figure 28** and irradiated with 365 and 430 nm. (Refer to **Section 6.2.13.1** for more details on sample preparation and reaction setup).

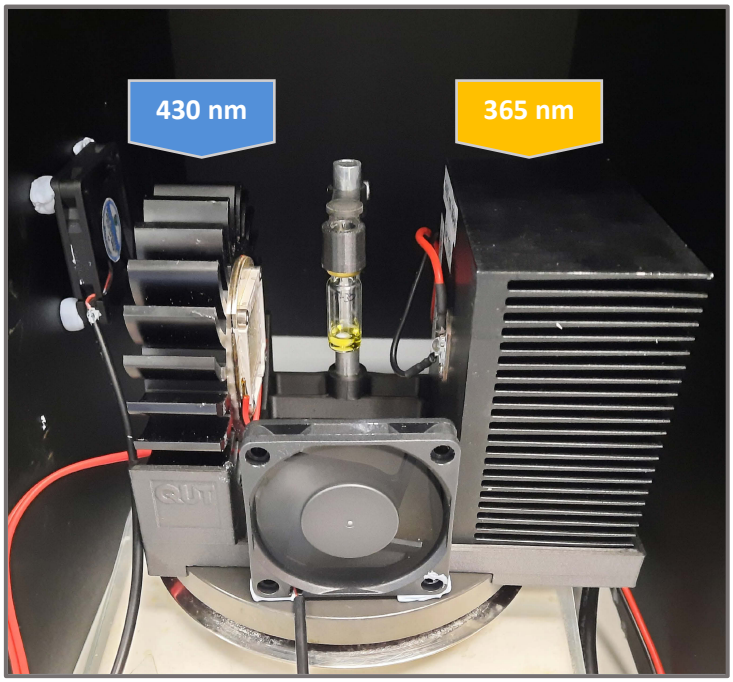

Figure 28. Setup for the photoreactions consisting of a magnetic stirrer, two LED light sources (365 and 430 nm) in a custom-made LED holder and fans for ventilation. Adapted from Hobich *et al.*[31]

To determine the optimal irradiance of the visible light LED, it was important to consider that 430 nm not only activates SA, but also partially deactivates DIO'. Therefore, a careful balance was crucial with a high concentration of SA' without significantly decreasing the DIO' concentration. The optimal photon flux was identified by performing a set of experiments under identical conditions while fixing the 365 nm photon flux at 9.63×10^{16} s^{-1} cm^{-2} and only varying the 430 nm LED current and thereby the photon flux. The synergistic ratios for the corresponding experiments are shown in **Figure 29A** with the highest efficiency at an LED current of 200 mA, i.e. a photon flux of 2.58×10^{18} s^{-1} cm^{-2}, which was then set as a standard for all following two-color reactions. When performing the reaction under 430 nm one-color conditions, trace amounts of DIOSA are formed which can be explained by a slight

overlap of the polychromatic LED emission spectrum and the action plot of DIO. Nevertheless, with a yield below 0.5% after 1 hour of irradiation (refer to **Figure 29B**) the 430 nm one-color reactivity is negligible and will not be considered for the calculations of ϕ_{syn}.

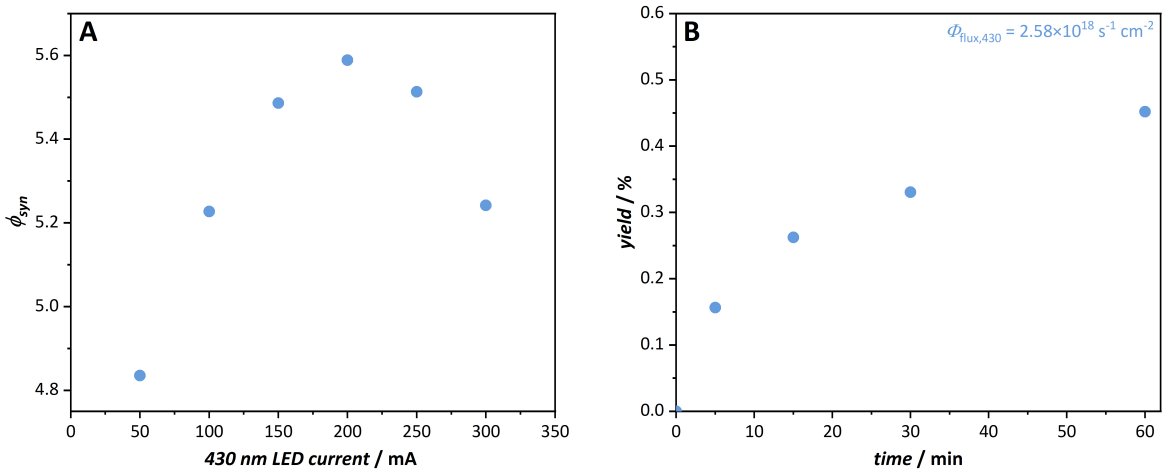

Figure 29. (**A**) Measurements of ϕ_{syn} for different 430 nm LED currents in a two-color reaction with a constant 365 nm photon flux of 9.63 × 10^{16} s^{-1} cm^{-2} and a 1:1 ratio of DIO to SA. The highest ϕ_{syn} was obtained at 200 mA, i.e. a photon flux of 2.58 × 10^{18} s^{-1} cm^{-2} and was employed for all two-color reactions. (**B**) Yield of DIOSA under 430 nm one-color irradiation with a constant photon flux of 2.58 × 10^{18} s^{-1} cm^{-2}. Since the yield was below 0.5% even after 60 minutes of irradiation, the 430 nm one-color reaction was not considered for the calculations of ϕ_{syn}. Adapted from Hobich *et al*.[31]

365 nm is the truly critical wavelength as substantial amounts of product are formed under one-color conditions. Therefore, a kinetic study was performed to understand the impact of the 365 nm photon flux on the degree of synergy. Precise control over the photon fluxed was ensured by modulating the 365 nm LED in the millisecond range while running at a constant current for all experiments. Since the reaction rate heavily depends on the photon flux, for reliable comparison, the kinetics were not performed for the same amount of time, but with the same number of 365 nm photons. **Figure 30** shows the qualitative dependence of the concentrations of DIO' and SA' (i.e. [DIO'] and [SA']) on the 365 nm photon flux ($\Phi_{flux,365}$). With an increase of $\Phi_{flux,365}$ [DIO'] increases as well and rapidly reaches a limit at the PSS where isomerization rates between [DIO] and [DIO'] are identical. At the PSS increasing the photon flux does not increase [DIO'] anymore and rather contributes to DIO undergoing unnecessary switching cycles, thus accelerating photodegradation. Due to the short half-life of SA' the thermal reversion to SA is predominant and a steady supply of photons is needed to keep [SA'] at a certain level. Since the limiting factor for SA' formation is of thermal and not photochemical nature, increasing $\Phi_{flux,365}$ steadily increases [SA'] as well. Therefore, low $\Phi_{flux,365}$ are preferential regarding the degree of synergy by enabling relatively high concentrations of [DIO'] while minimizing the formation of SA' at 365 nm.

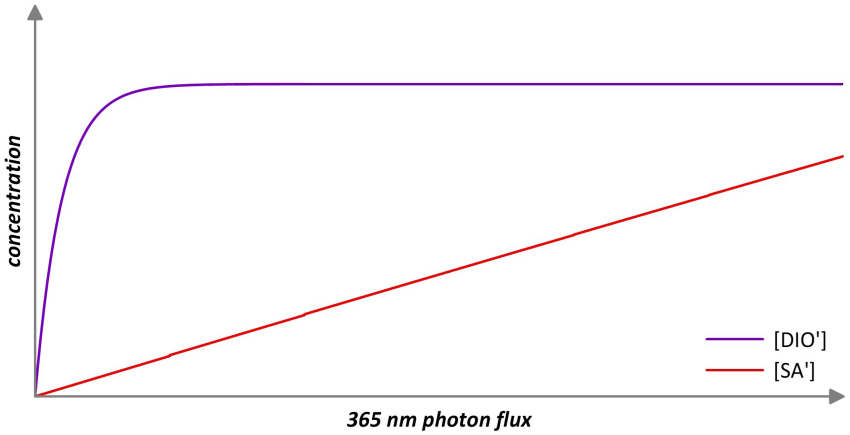

Figure 30. Qualitative dependence of [DIO'] and [SA'] on the 365 nm photon flux ($\Phi_{flux,365}$). [DIO'] increases rapidly with an increasing $\Phi_{flux,365}$ and reaches a maximum at the PSS, where the photoswitching rates between DIO and DIO' are identical. Even when increasing $\Phi_{flux,365}$, [DIO'] does not increase further. Due to the short half-life of 180 ms,[34] SA' undergoes rapid thermal reversion to SA. Therefore, a steady supply of photons is required to keep [SA'] at a certain level and increasing $\Phi_{flux,365}$ also increases [SA'] steadily. Adapted from Hobich *et al.*[31]

In **Figure 31** two exemplary sets of one- and two-color kinetics with very different synergistic efficiencies are depicted. The synergistic efficiency is much more pronounced for the kinetic in **Figure 31A** that was performed with a rather low $\Phi_{flux,365}$ of 9.63×10^{16} s^{-1} cm^{-2} and a 10 to 1 excess of DIO over SA. Almost complete conversion is achieved with a yield of 97% for the two-color reaction while the yield is only at 22% for the one in **Figure 31B** with a much higher $\Phi_{flux,365}$ of 2.41×10^{18} s^{-1} cm^{-2} and a 1 to 1 ratio of staring materials. Accordingly, even when delivering the same number of critical 365 nm photons to the samples, the synergistic efficiencies can vary significantly depending on the reaction conditions. These examples underline that the enhanced rates in the two-color reactions cannot be explained by a photoreaction that is independently fueled by 365 and 430 nm. It becomes evident that simultaneous dual-color irradiation produces an outcome greater than the sum of its parts due to a synergistic effect.

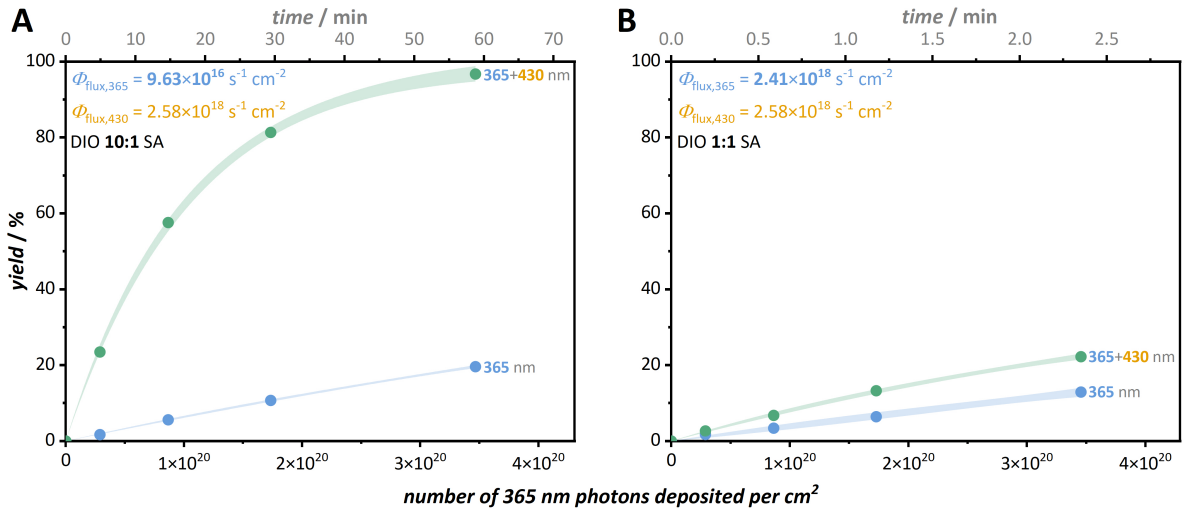

Figure 31. Reaction kinetics for one and two-color reactions with different synergistic efficiencies. In both cases the data points were collected after irradiation with the same number of 365 nm photons. (**A**) Reaction kinetics for one- and two-color reactions with a 365 nm photon flux ($\Phi_{flux,365}$) of 9.63 × 10^{16} s^{-1} cm^{-2} and a 10 to 1 ratio of starting materials DIO to SA. The 95% confidence bands of the exponential fits to the kinetics are shown in light blue and green, respectively. (**B**) Reaction kinetics for one- and two-color reactions with a $\Phi_{flux,365}$ of 2.41 × 10^{18} s^{-1} cm^{-2} and a 1 to 1 ratio of starting materials DIO to SA. The 95% confidence bands of the exponential fits to the kinetics are shown in light blue and green, respectively. Adapted from Hobich *et al.*[31]

To track the change of the synergistic effect over the course of the reaction, the time-dependent parameter $\phi_{syn}(t)$ was calculated as follows

$$\phi_{syn}(t) = \frac{Y_2(t)}{Y_1(t)} = \frac{A_2 - A_2 e^{-k_2 t}}{A_1 - A_1 e^{-k_1 t}}$$

with the exponential fit functions $Y_1(t)$ and $Y_2(t)$ for the kinetics of the one- and the two-color reactions with parameters A and k, respectively (**Section 6.2.13.2**). The irradiation times varied from 2.4 to 72 minutes in order to supply the same number of 365 nm photons while varying the photon flux. Due to significant disparities in the reaction times, a depiction of ϕ_{syn} relative to the two-color product yield facilitated comparison of the different kinetics in **Figure 32**. The conversion-independent synergistic ratio ϕ_{syn}^0 was approximated as $\phi_{syn}(t = 0.001\ \text{min})$ and served as a standard parameter for comparison of the impact of different 365 nm photon fluxes on the synergistic efficiency. With an increasing photon flux, a clear downwards trend for ϕ_{syn}^0 is visible due to an overlap of the action plots of DIO and SA at 365 nm. As previously shown in **Figure 30**, due to the relatively high lifetime of DIO', its concentration rapidly reaches a limit at the PSS when increasing the photon flux and at that point any additional 365 nm photons are excessive and cannot contribute to the desired purpose of activating DIO anymore, whereas SA' is formed indiscriminately at both 365 and 430 nm. By applying low photon fluxes the undesired activation of SA is minimized without significantly impacting the concentration of DIO'. Consequently the 365 nm photons are harnessed more efficiently for the

activation of DIO, thus increasing the overall synergistic efficiency of the reaction between DIO and SA. Nevertheless, when increasing the photon flux, while ϕ_{syn} increases, the reaction times extend as well.

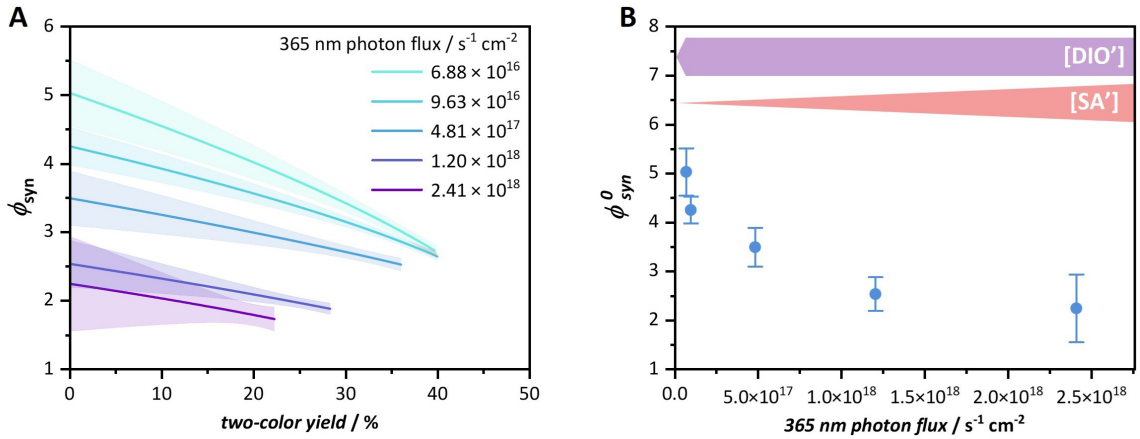

Figure 32. The synergistic ratios at different 365 nm photon fluxes. (**A**) Comparison of ϕ_{syn} under different 365 nm photon fluxes (calculated with exponential fits from kinetic measurements, refer to **Appendix Section 7.2.1**). The 95% confidence bands are shown in lighter colors for the respective ϕ_{syn}. (**B**) Dependence of ϕ_{syn}^{0} on the 365 nm photon flux. General trends of the concentrations of DIO' and SA' are illustrated in violet and orange, respectively. The concentration of the long-lived DIO' rapidly reaches a PSS even at low photon fluxes, while the concentration of the short-lived SA' continues to increase with the photon flux. The positive and negative errors on ϕ_{syn}^{0} are the values of the respective upper and lower 95% confidence bands at *t*=0.001 min. Adapted from Hobich *et al.*[31]

Furthermore, the formation of two side products from the photodegradation of DIO was observed, especially for reaction times longer than 1 hour. Inspired by previous reports of the photodegradation of DIO[33], two test reactions were performed to characterize the side products and to understand the impact factors for their formation. Two crimped vials, each containing 250 µL of a stock solution of DIO (373 µg, 1.25 nmol, 1.00 eq.) in acetonitrile were irradiated under two-color conditions with 365 nm (1.01 W cm^{-2}, $\Phi_{flux,365}$ = 1.86 × 10^{18} s^{-1} cm^{-2}) and 430 nm (1.19 W cm^{-2}, $\Phi_{flux,430}$ = 2.58 × 10^{18} s^{-1} cm^{-2}) in the reaction setup in **Figure 28**. One sample was prepared under argon atmosphere, while the other one was prepared at ambient atmosphere and after 30 minutes of irradiation the LC-MS traces were compared in **Figure 33A**. In the presence of oxygen at ambient temperature (red trace) DIO is almost fully consumed and several new signals appear due to a high sensitivity of DIO' degradation to oxygen. In comparison, only two new signals appeared under argon atmosphere which were also observed for the two-color reactions at extended reaction times above 1 hour. Main product S1 was previously reported in the literature and was characterized via HRMS (theoretical *m/z* for $[C_{21}H_{14}O_2+H]^+$: 299.1072, found 299.1065) and by comparing the crude ^{1}H NMR spectrum to a literature reference.[182] Since S1 is formed from a rearrangement under anaerobic conditions the reaction cannot be avoided even under inert atmosphere.

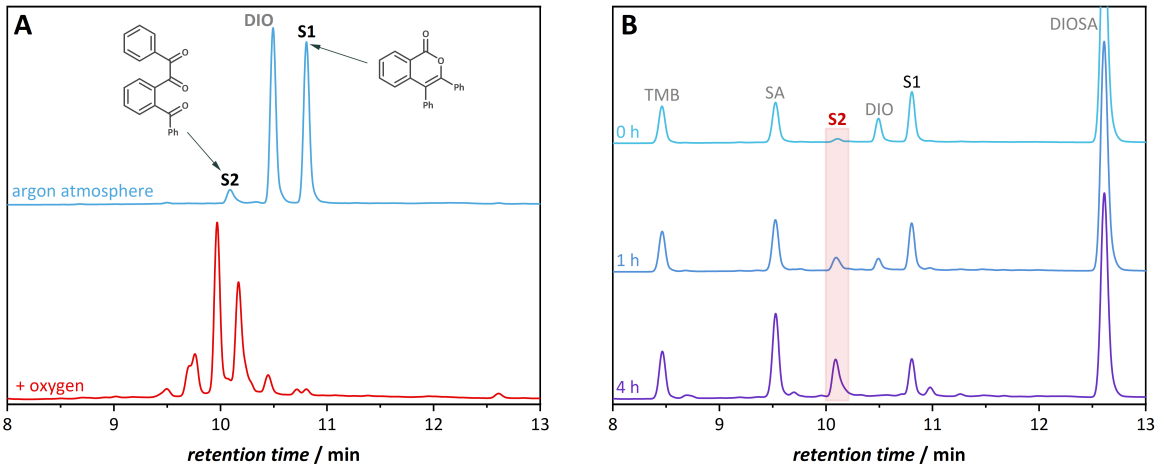

Figure 33. (**A**) UV-detector LC traces at 235 nm of the photodecomposition products of DIO (S1 and S2) under argon atmosphere (blue) and at ambient atmosphere in the presence of oxygen (red). (**B**) UV-detector LC traces at 235 nm of the side reactions occurring due to the photodecomposition of DIO (to S1 and S2) in the two-color stock solution with a DIO to SA ratio of 1:1 under initial argon atmosphere. The same irradiation conditions were applied to three samples, i.e. directly after release from the glovebox, 1 hour and 4 hours later. Diffusion of oxygen into the crimp vials over time results in an increase of the formation of S2. Adapted from Hobich *et al.*[31]

HRMS analysis of S2 gave an experimental *m/z* of 315.1014 which is in line with the molecular mass of DIO with an additional oxygen atom, i.e. 315.1021 for $[C_{21}H_{14}O_3+H]^+$. A structure for S2 is proposed, matching both the *m/z* and one of the photodegradation products mentioned by Xie *et al.*[33] To assess the influence of oxygen diffusion into the reaction vial on the formation of S2, the stock solution that was previously used for the kinetic measurements (5 mM DIO and SA in acetonitrile) was employed under the same irraditation conditions as for the previous DIO photodegradation experiment. Three crimped samples were removed from the glovebox at the same time and irradiated after 0, 1 and 4 hours, respectively. LC-MS traces of the samples (**Figure 33B**) confirm increased formation of S2 as air progressively diffused into the crimped vial over time. Therefore, long reaction times needed when working with low 365 nm photon fluxes become problematic due to the growing impact of undesired side reactions.

The problem of side-reaction becomes evident in a comparison of the end points of each kinetic in **Figure 32** with two-color yields steadily increasing from 22.3 over 36.0 to 40.0% by harnessing the 365 nm photons more efficiently at low photon fluxes. However, when the photon flux is further decreased to 6.88×10^{16} s^{-1} cm^{-2} (total reaction time of 72 minutes) the trend of increasing yields does not persist and a final yield of 39.7 is obtained which is almost identical the to the 40.0% at 9.63×10^{16} s^{-1} cm^{-2} (total reaction time 60 minutes). Additionally, when comparing these kinetics ϕ_{syn}^{0} is significantly higher for a lower photon flux (5.03 vs. 4.26) whereas the decline of ϕ_{syn} over the course of the reaction occurs more and with a steeper gradient. The steeper slope can be explained by the progressive impairment of the two-color reaction through photodegradation of DIO since all kinetics were performed with the same number of 365 nm photons, but different reaction times and therefore

very different numbers of 430 nm photons as well. Besides activation of SA, 430 nm also triggers the deactivation of DIO' which is necessary for the synergistic nature of the two-color reaction to DIOSA. An increase in the number of 430 nm photons directly induces DIO/DIO' cycling, thereby promoting side reactions for extended reaction times.

In addition to the 365 nm photon flux, the impact of the starting materials equivalent ratios (DIO to SA) on ϕ_{syn} was studied as another tunable parameter for the synergistic DIO formation (**Figure 34**). For these reaction kinetics the 365 nm photon flux was fixed at 9.63×10^{16} s^{-1} cm^{-2} and the starting materials ratios were varied while keeping the concentration at 5 mM and only adjusting the concentration of the more abundant reaction partner. Setting the 1:1 ratio as a standard for comparison, doubling the concentration of SA resulted in a decline of ϕ_{syn}^{0} from 4.25 to 2.74 while doubling the DIO concentration led to an increase to 6.62. Moreover, a ϕ_{syn}^{0} of 14.4 is reached when further increasing the excess of DIO to a 10:1 ratio and with a two-color yield of 97 % the reaction proceeds almost to completion while only 40% are achieved for an equimolar ratio under the same conditions. A higher reaction rate is expected since the maximum concentration of DIO', which is limited by the PSS, is proportional to the starting concentration of DIO. The critical influence of the educt ratio on ϕ_{syn} originates from the overlapping absorbances and reactivities of DIO and SA at 365 nm. Optimally, 365 nm should solely activate DIO and by increasing the ratio of DIO over SA, 365 nm photons are also statistically more likely to be absorbed by DIO. Furthermore, with DIO in excess, any side reactions due to photodegradation become less significant. On the other hand, at lower DIO equivalents, undesired competitive absorption leading to photoactivation of SA become more prominent, thereby diminishing the synergistic efficiency.

To summarize, the highest degrees of synergy for the two-color photoreaction between DIO and SA are obtained by employing low 365 nm photon fluxes and DIO in excess. However, employing one of the staring materials in excess might not always be feasible and lowering the photon flux necessitates longer reaction times where photodegradation of DIO' becomes a significant problem. In general, especially molecule-specific properties such as the difference in lifetimes for DIO and SA or the PSS of DIO play a critical role for the synergistic efficiency. The main challenge for the development of novel synergistic system is to identify two photoswitches with fully λ-orthogonal systems, ensuring that no product formation is possible under one-color irradiation. Accordingly, ϕ_{syn} will play a central role as a parameter for assessment and comparison of different synergistic systems.

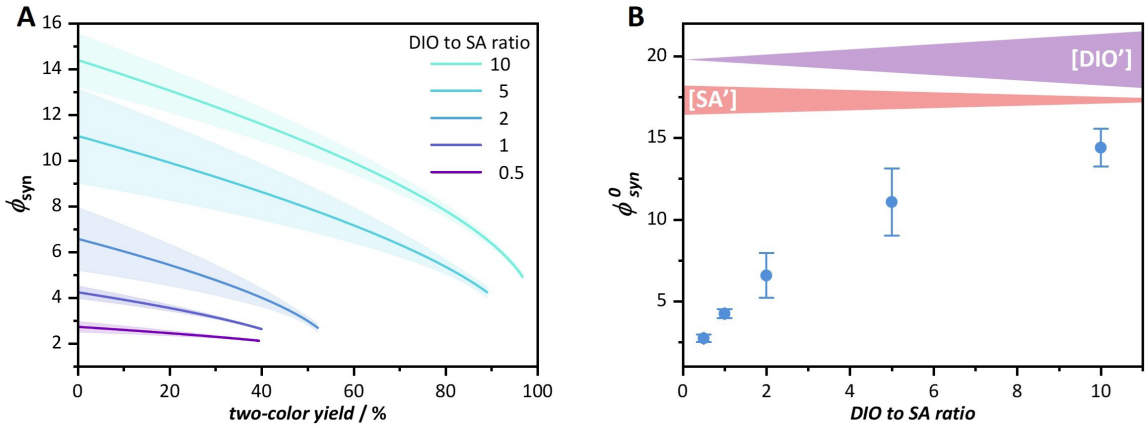

Figure 34. The synergistic ratios at different ratios of DIO and SA. (**A**) Comparison of ϕ_{syn} with different ratios of the starting materials DIO and SA (calculated with exponential fits from kinetic measurements, refer to **Appendix Section 7.2.2**). The 95% confidence bands are shown in lighter colors for the respective ϕ_{syn}. (**B**) Dependence of ϕ^0_{syn} on the ratio of starting materials DIO to SA. General trends of the concentrations of DIO' and SA' are illustrated in violet and orange, respectively. The concentration of DIO' increases with the ratio of DIO to SA, since the total amount of DIO increases. Furthermore, SA' decreases since absorbance of SA is increasingly overshadowed by DIO. The positive and negative errors on ϕ^0_{syn} are the values of the respective upper and lower 95% confidence bands at *t*=0.001 min. Adapted from Hobich *et al*.[31]

4.4 Photoresist Design

Building on the previous results of the small-molecule study (Sections 4.1 - 4.3) the next step was to transfer the photochemical synergy to the macromolecular level and harness the covalent bond formation between DIO and SA (**Figure 35A**) as a crosslinking reaction for network formation and subsequent application in lithographic fabrication.[38] The conceptual visualization of such network formation of a photoresist on the molecular scale via two-color irradiation is illustrated in **Figure 35B**.

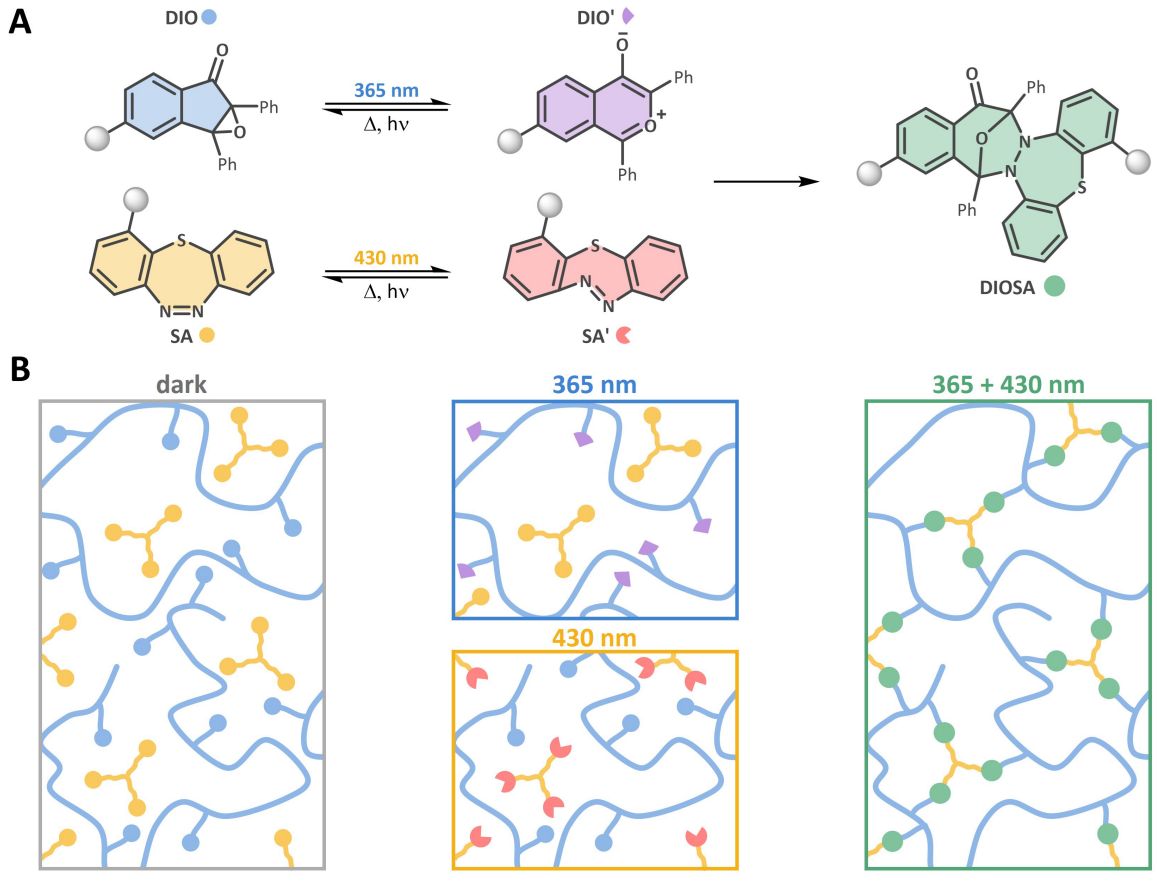

Figure 35. (**A**) Light-induced photoswitching of functionalized DIO (blue) and SA (yellow) to their corresponding isomers DIO' (violet) and SA' (red) under 365 nm and 430 nm irradiation, respectively. These activated isomers possess complementary reactivities and undergo a selective cycloaddition to form the DIOSA adduct (green). (**B**) Photoresist consisting of a polymer with multiple DIO units (blue circles) and a molecule bearing three SA functionalities (yellow circles). One-color irradiation with either 365 nm or 430 nm light reversibly and selectively switches DIO or SA to their reactive species DIO' (violet triangles) and SA' (red, three-quarter circles) respectively. Simultaneous two-color activation induces controlled crosslinking, forming a covalent network via DIOSA (green circles) formation. Color coding reflects the chemical species as defined in (A). Adapted from Hobich *et al*.[38]

First, both DIO and SA were decorated with synthetically flexible functional handles to facilitate their incorporation into macromolecular scaffolds. The previously employed DIO synthesis route[31] was modified in order to introduce an hydroxy group to the aromatic core by employing an alternative precursor (**Section 6.3.2.1**). Next, nucleophilic substitution with 6-bromohexanol yielded a DIO core moiety with a hydroxy group attached to an hexamethylene spacer (DIO-OH) with the aim to provide

enhanced solubility and molecular flexibility while minimizing steric or electronic interactions that could negatively affect the photoreactive core. Furthermore the terminal hydroxy moiety served as a strategic site for follow-up functionalization.

Design of the functional SA compound (SA-OH) was analogous to DIO-OH by adapting a new synthesis route, reported for asymmetric diazocines (**Section 6.3.2.2**).[98] Accordingly, a hydroxyhexyl moiety was attached to the core structure in *ortho* position to the thioether functionality. This site was selected in order to mitigate interference with the *cis-trans* isomerization around the azo bond or the cycloaddition to DIOSA. Similar to DIO-OH, the linker also served to increase solubility, enhance conformational flexibility and to spatially separate the SA moiety from the surrounding chemical environment.

Next, the functionalized photoswitches were tested for their photoreactivity with DIO-OH undergoing epoxide ring-opening to DIO-OH' under UV light (365 nm) and SA-OH performing *cis*-to-*trans* isomerization to SA-OH' upon visible light exposure (430 nm), resulting in the cycloaddition to a DIOSA species under simultaneous two-color irradiation. Therefore, the cycloaddition reactions of all potential combinations of DIO/DIO-OH and SA/SA-OH (shown in **Figure 36**) were performed to understand the influence of the synthetical modification on the reactivity and photochemical synergy.

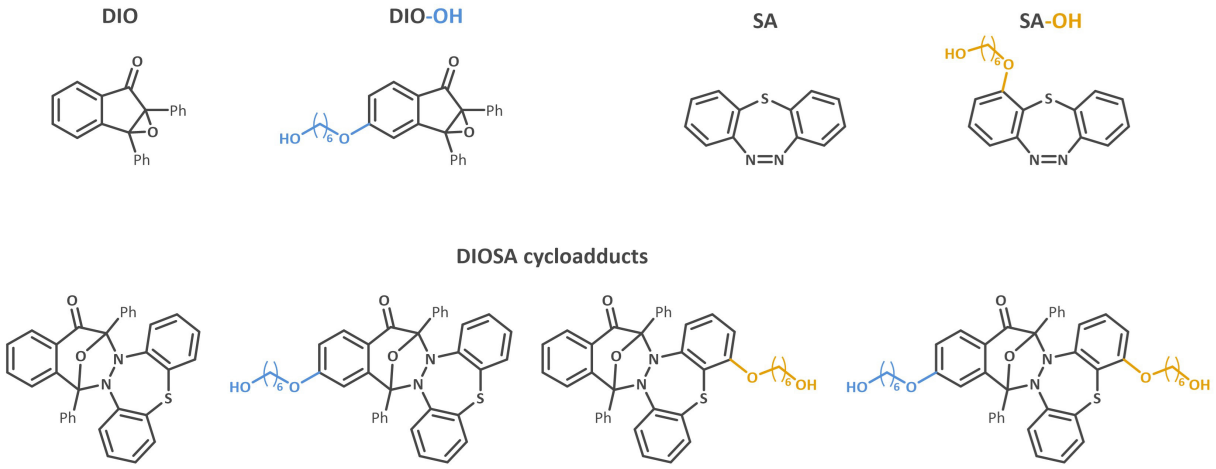

Figure 36. Schematic representation of different combinations of DIO-(top-left) and SA-derivatives (top-right) and their DIOSA cycloadducts (bottom) that were investigated herein. Adapted from Hobich *et al.*[38]

Sample preparation was adapted from previous two-color test reactions for the study of ϕ_{syn}[31] with 5 mM photoswitch stock solutions in acetonitrile and with TMB as an internal standard for LC-MS evaluation of the product yields (**Section 6.2.13.3**). Furthermore the same LED holder and LEDs were employed, i.e. 365 nm (1.69 mW cm^{-2}, 3.10×10^{15} photons s^{-1} cm^{-2}) and 430 nm (27.9 mW cm^{-2}, 6.04×10^{16} photons s^{-1} cm^{-2}). The reaction times were set to 10 minutes in order to stay within the linear range of the kinetics (below 30%), thus allowing for quantitative comparison of the impact of functional modification to the photoswitch reactivities. Since only two measurements per stock

solution were performed, extrapolating to 100% product formation as in the small-molecule study was not applicable. Therefore the product yield *Y* was indirectly determined from the LC traces at 235 nm by the consumption of SA and by the following formula

$$Y = 1 - \frac{I_{SA}}{I_{SA,0}}$$

where $I_{SA,0}$ is the integral of the SA compound at the beginning of the reaction, normalized by dividing by the integral of the internal standard TMB. I_{SA} is the normalized integral of the SA compound at the end of the reaction. Tracking the consumption of DIO compounds instead was not feasible due to the occurrence of side reactions of the activated DIO' compounds.[31] One- (365 nm) and two-color (365 + 430 nm) reactions were performed for each stock solution and the corresponding yields are shown in **Figure 37**. It becomes apparent that the reaction of DIO and SA is the most efficient while especially the substitution of SA for SA-OH leads to a decrease of the reaction rate with respective two-color yields of 20.5% and 8.1%. Nevertheless, the two-color reaction still proceeds significantly faster for the combination of DIO-OH and SA-OH than the one-color analogue, i.e. 8.1% vs. 4.5%, proving the maintenance of photochemical synergy after functionalization.

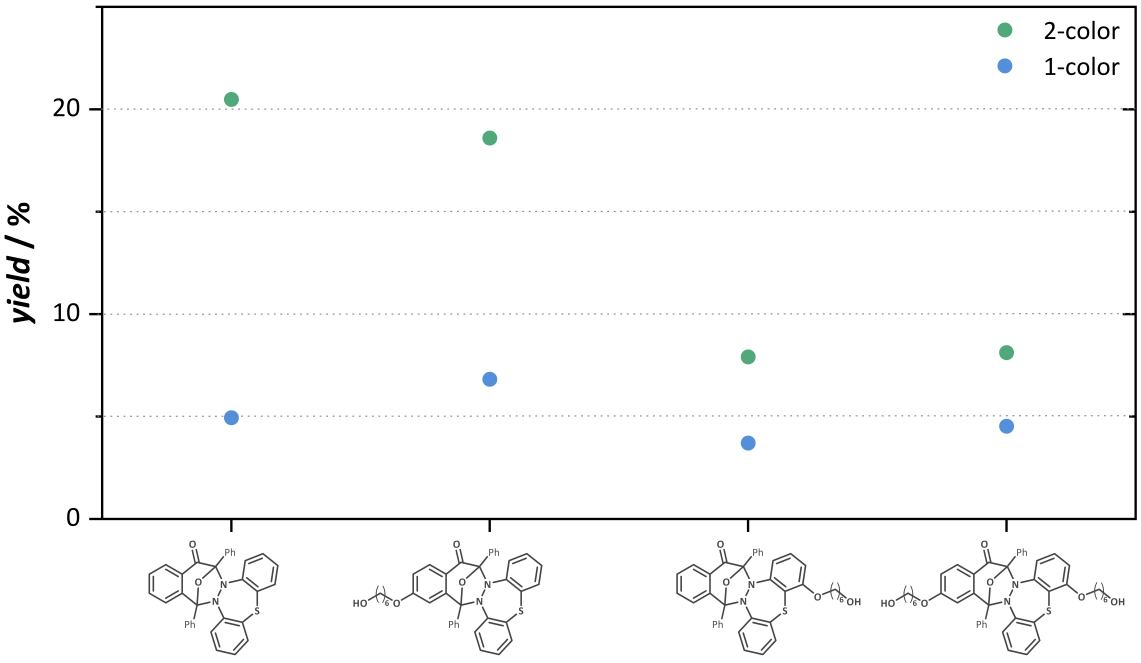

Figure 37. Comparison of the product yields for the one- and two-color reactions of different combinations of DIO/DIO-OH and SA/SA-OH. Adapted from Hobich *et al*.[38]

Additionally, a comparison of synergistic efficiencies for the different photoswitch combinations is shown in **Figure 38** that further proves the highest ϕ_{syn} for the DIO and SA core structures while dual-functionalization leads to a decrease from 4.1 to 1.8. Nevertheless, the two-color synergy was successfully transferred to the combination of functionalized photoswitches DIO-OH and SA-OH.

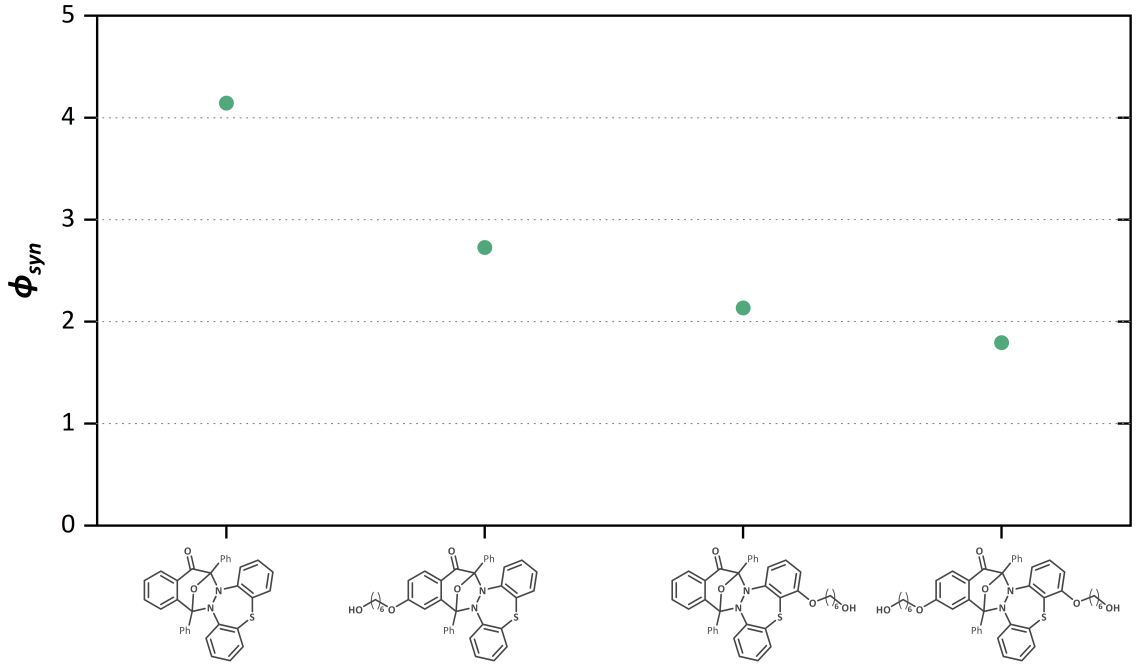

Figure 38. Comparison of the synergistic efficiencies (ϕ_{syn}) of the two-color reactions of different combinations of DIO/DIO-OH and SA/SA-OH. Adapted from Hobich *et al*.[38]

Furthermore, the successful formation of a DIOSA cycloadduct in the reaction between DIO-OH and SA-OH was proven by LC-MS (**Figure 39**). Two product peaks with identical *m/z* were observed and can be attributed to the regioisomers resulting from the reaction with an asymmetric SA moiety. The theoretical *m/z* of 743.32 for the protonated cycloadducts is in line with the experimental value of 743.3. LC-MS characterization of the cycloadducts from the other photoswitch combinations were performed as well and can be found in the **Appendix Figure S121 - Figure S123**.

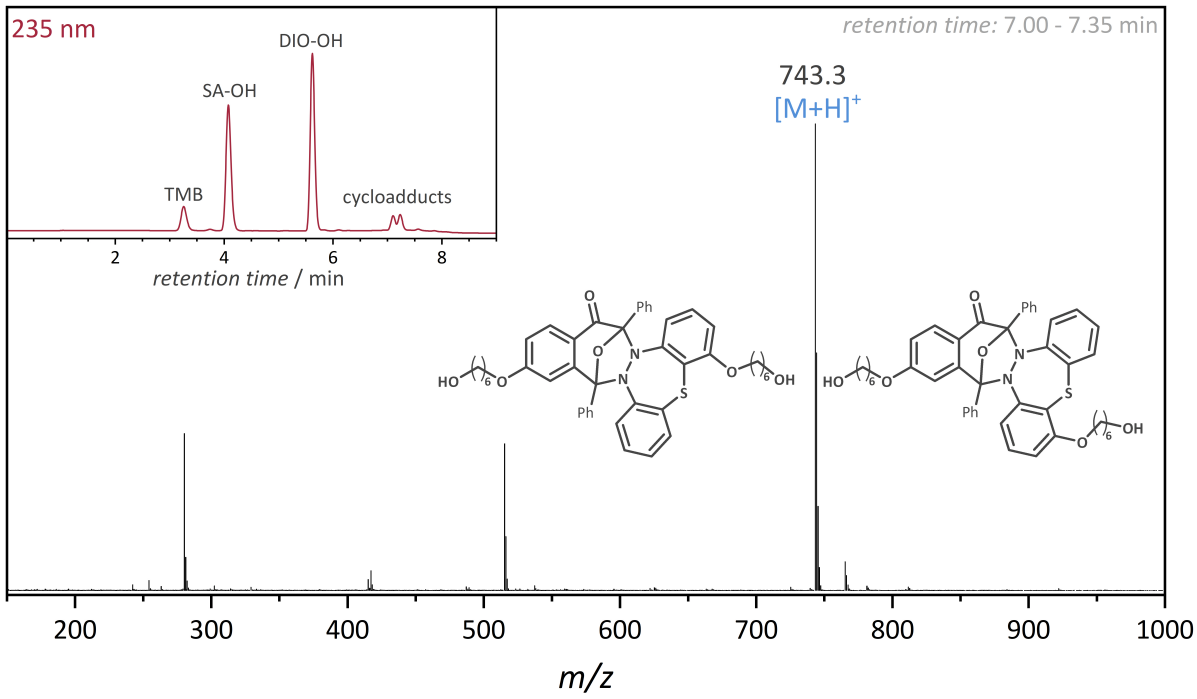

Figure 39. LC-trace (235 nm detector wavelength) of the crude mixture of the two-color photoreaction between DIO-OH and SA-OH and accumulated mass-spectra of the formed DIOSA derivatives (cycloadducts). Two product signals are present due to the formation of regioisomers. Adapted from Hobich *et al*.[38]

A key requirement for harnessing the photoinduced cycloaddition of DIO and SA moieties as a crosslinking event is the design of molecules with multiple reactive sites. For the combination of DIO and SA more than two photoswitch moieties per molecule are necessary in order to enable the formation of a crosslinked network and hence mechanically stable structures from a photoresist. Thus, tailored strategies were developed for the introduction of multiple DIO and SA units into macromolecular architectures (**Figure 40**), enabling the synergistic formation of a crosslinked polymer network.

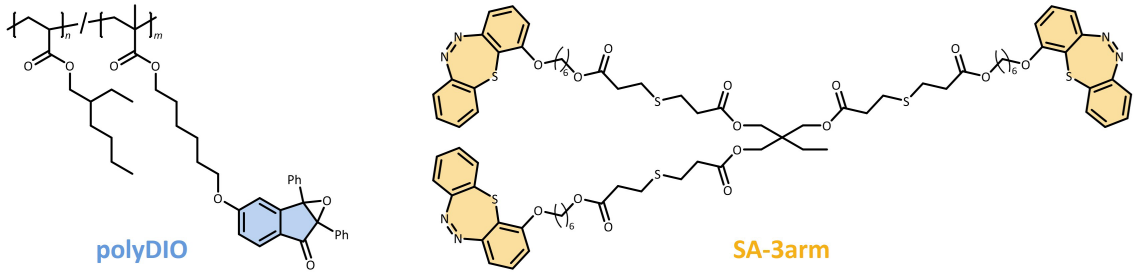

Figure 40. Chemical structures of DIO and SA moieties bearing functional handles, introduced into the molecular frameworks of polyDIO (blue) and SA-3arm (yellow), respectively, to enable synergistic network formation. Adapted from Hobich *et al*.[38]

The general strategy for designing a multi-DIO compound was the attachment of the photoswitch onto the backbone of a polymer, thus allowing for straightforward introduction of multiple DIO moieties into a polymer chain. The advantage of employing a macromolecular precursor is that less crosslinking events are needed to form a stable network. Lowering the threshold for network formation is

especially important for the reaction between DIO and SA that proceeds via a step-growth mechanism, which boosts an inherently slower kinetic compared to the radical-initiated chain growth, typically employed for photoinduced 3D printing.[183] The disparity in kinetics can be explained by the different amounts of photons needed per crosslinking event. For step-growth polymerization in the current work, one photon per photoswitch and therefore two photons per crosslink via cycloaddition are necessary. In contrast, in a radical-initiated chain growth mechanism a single photon activates a photoinitiator and consequently triggers the formation of numerous crosslinks. Consequently, by preparing polymer chains with multiple DIO functionalities, the number of crosslinking events needed for the formation of an interconnected network decreases. Furthermore, the multifunctional DIO-polymer allows for employing DIO in excess over SA which proved to increase the synergistic ratio significantly in the previous small-molecule study (refer to **Figure 34**).[31] Importantly, not every single DIO moiety must react in order to realize a high crosslinking density and to achieve structural integrity of the network.

For the preparation of a multifunctional DIO polymer, first DIO-OH was methacrylated at the terminal hydroxy group to allow for subsequent radical polymerization. For spatial separation between the DIO units on the polymer chain and enhanced solubility, 2-ethylhexyl acrylate (EHA) was employed as a comonomer. Moreover, the low glass transition temperature (T_g) of -65 °C for the EHA homopolymer[184] was expected to decrease the amount of solvent necessary for the formulation of a photoresist by enabling a soft and flexible polymer backbone and reduce brittleness. Additionally, when preparing the polymer, the desired number average molar mass (M_n) was also carefully adjusted due to the direct correlation with both T_g and viscosity.[185] Hence, it was important to maintain a delicate balance between a sufficiently high M_n for the incorporation of multiple photoreactive moieties while simultaneously being sufficiently low to allow for a favorable processing viscosity.

The methacrylated DIO monomer and EHA were dissolved in toluene (1.5 M) and copolymerized in a free radical polymerization reaction, initiated via thermal decomposition of azobisisobutyronitrile (AIBN, 0.9 mol%) in the presence of chain transfer agent 1-dodecanthiol (1.2 mol%). The final polymer (polyDIO, **Figure 40**) was obtained with a moderate M_n of 13 200 g mol^{-1} and a dispersity ($Đ$) of 1.77, as determined by SEC (**Figure 41**).

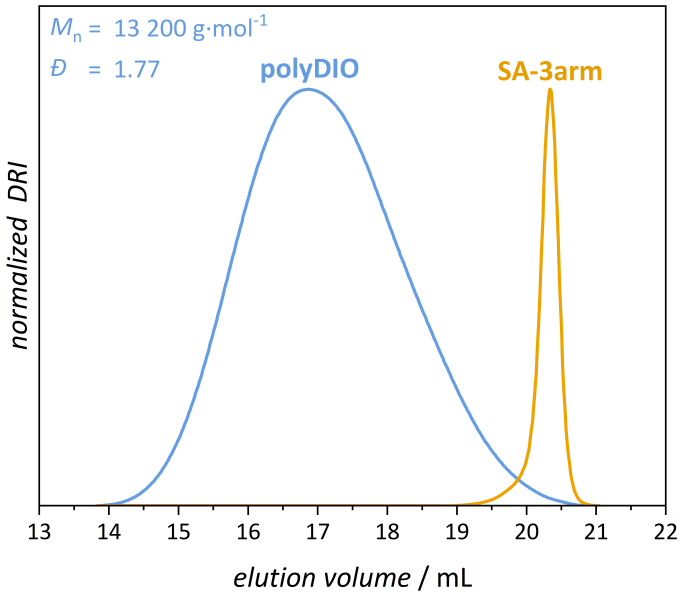

Figure 41. SEC elution traces of polyDIO (blue) and SA-3arm (yellow). For polyDIO the corresponding M_n (13 200 g mol^{-1}) and *Đ* (1.77) are shown in blue. Adapted from Hobich *et al*.[38]

The amount of integrated DIO monomers was determined via ^{1}H NMR spectroscopy (**Figure 42**) to be 13.5% (**Appendix Section 7.6**) which is in reasonable agreement with the initially employed 15% in the monomer feed. The T_g of -44 °C was obtained for polyDIO by differential scanning calorimetry (DSC) (**SI Figure S133**) which meets the formulation demands of a soft and easily processable resist material.

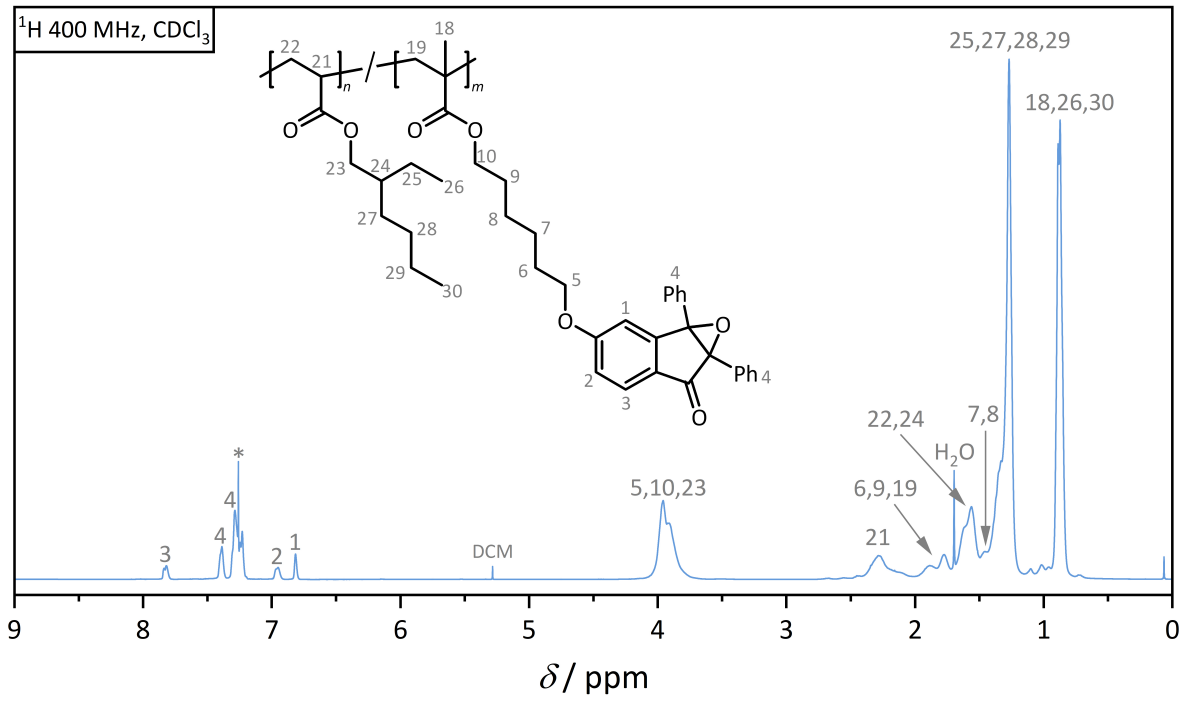

Figure 42. ^{1}H NMR (400 MHz) spectrum of polyDIO in $CDCl_3$ (*) at ambient temperature with proton assignment. Adapted from Hobich *et al*.[38]

Initially, the aim was to employ the same radical polymerization strategy for the synthesis of a multifunctional SA compound. However, polymerization was not possible under identical reaction

conditions when substituting the DIO monomer with a methacrylated SA-OH compound. Therefore, several test reactions for the homopolymerization of EHA in the presence of different amounts of unmodified SA were performed in order to understand the detrimental impact of SA on the free radical polymerization. For the test reactions EHA (284 µL, 250 mg, 1.36 mmol, 1.00 eq.) and AIBN (1.34 mg, 8.14 µmol, 0.006 eq.) were dissolved in 0.9 mL toluene. Next, three samples were prepared by adding 0, 0.5 or 5.5 mol% SA and sparging with nitrogen. Subsequently the reaction mixtures were stirred for 20 hours at 65 °C and the crude mixtures were analyzed via ^{1}H NMR spectroscopy (**Figure 43**) by tracking changes of the magnetic resonance at 4.08 ppm, belonging to the proton bound to the tertiary carbon of EHA. After polymerization this resonance shifts to lower ppm (3.93 ppm) and broadens significantly as a consequence of incorporation into a polymeric structure. For the polymerization attempt without SA the magnetic resonance at 4.08 ppm almost vanished completely (**Figure 43**, blue trace), showing almost full conversion of the monomer after 20 hours. However, in the presence of 0.5 mol% SA a more pronounced residual resonance at 4.08 ppm was observed (**Figure 43**, yellow trace), evidencing a reduced polymerization rate. Further increasing the SA content to 5.5 mol%, resulted in no significant changes of monomer consumption nor in the appearance of polymer signal at 3.93 ppm (**Figure 43**, orange trace), confirming full inhibition of polymerization and highlighting the quenching effect of SA on the radical process which is an untypical behavior regarding the fact that azobenzene photoswitches are usually not affected under radical polymerization conditions.[186] Possible explanations are the reaction of radicals with the highly ring-strained thioether or diazo moieties. Consequently, a different strategy for the synthesis of a SA-bearing compound had to be adapted without relying on radical polymerization approaches.

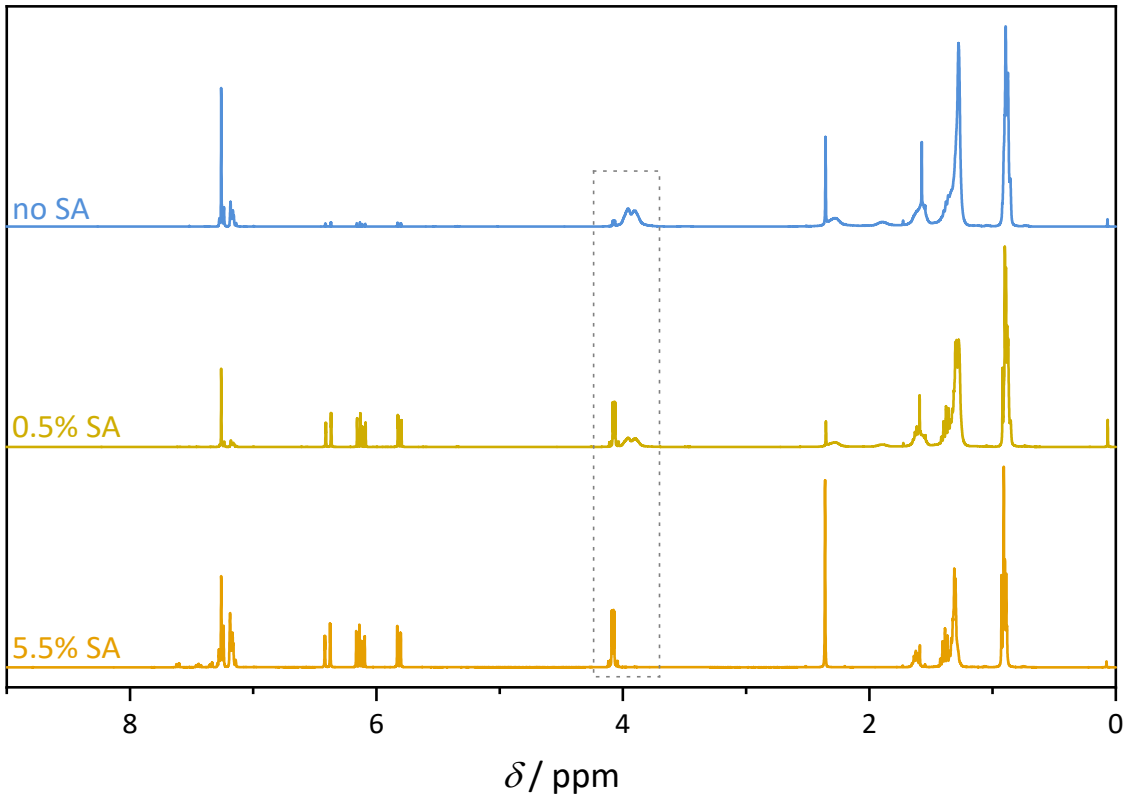

Figure 43. ^{1}H NMR spectra (400 MHz) in $CDCl_3$ of the polymerizations of EHA in toluene at 65 °C after 20 hours in the presence of 0, 0.5 and 5.5 mol% SA, showing a radical quenching by the SA moiety. Adapted from Hobich *et al.*[38]

The new design for a crosslinkable multi-SA compound was shifted to a discrete, three-armed molecule, similar to pentaerythritol triacrylate which is a widely applied crosslinker in photoresists for light-based 3D printing.[183, 187, 188] Preparation of the target molecule SA-3arm (**Figure 40**) was achieved by first, acrylating the hydroxy functionality of SA-OH, followed by base-mediated thiol-Michael addition to a trifunctional thiol in the presence of 1,8-diazabicyclo[5.4.0]undec-7-ene (DBU) as a catalyst. Successful formation of the desired product with three SA moieties per molecule was confirmed by 1 and 2D NMR spectroscopy (**Figure 44** and **Figure S106** - **Figure S110**) and SEC (**Figure 41**), thus confirming suitability for two-color synergistic crosslinking. Furthermore, successful retention of the photoswitching abilities of both polyDIO and SA-3arm were observed via UV-Vis spectroscopy (**Appendix Figure S129** and **Figure S130**).

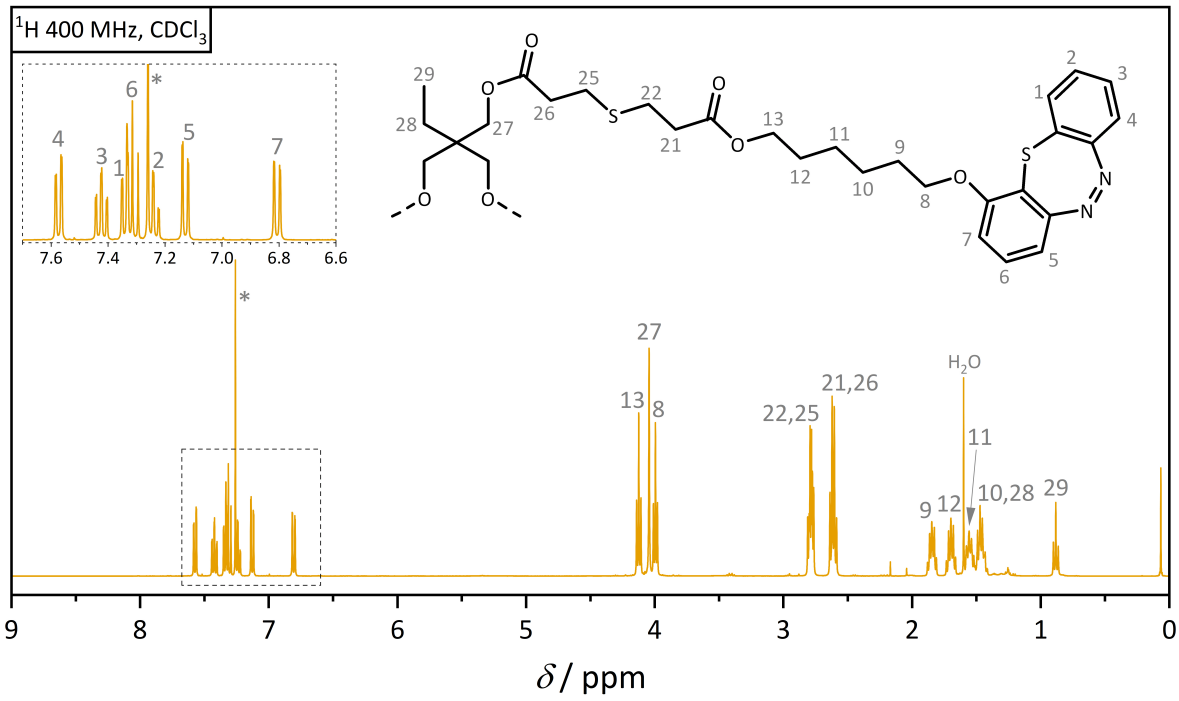

Figure 44. ^{1}H NMR (400 MHz) spectrum of SA-3arm in $CDCl_3$ (*) at ambient temperature with proton assignment. Adapted from Hobich *et al*.[38]

With both, polyDIO and SA-3arm in hand, the next step for the development of a photoresist was selection of a suitable solvent to ensure homogenous mixing of the crosslinkable species. Critical for the choice of solvent are good solubility of the photoactive compounds, photostability at the employed wavelengths (365 and 430 nm) and a high boiling point to avoid concentration changes in the photoresist over time due to evaporation in order to avoid defects such as bubble formation, phase separation or precipitation.[189] Acetophenone was selected for its high boiling point (201.7 °C)[190] and the shared polar and aromatic character with the photoswitches DIO and SA which suggests excellent solubility for the functionalized species. Moreover, acetophenone has been successfully employed as a solvent for photoresists in several comparable light-based printing setups.[151, 191-194] However, before selecting the final solvent, it was crucial to verify whether the two-color cycloaddition even proceeds in acetophenone and, further, whether the synergistic effect is retained.

To investigate the suitability of acetophenone regarding the photochemical synergy of DIOSA formation, test reactions under identical conditions to the previously discussed test reactions of different DIO/DIO-OH and SA/SA-OH combinations shown in **Figure 37**. The only differences were that reactions were performed in acetophenone instead of acetonitrile and only for the combination of the DIO and SA core structures. The reaction yields after 10 minutes were determined via LC-MS of the crude mixtures (**Figure 45**) and obtained as 2.4% for one-color and 18.0% for two-color irradiation. Consequently, a synergistic efficiency of 7.5 is determined, which is significantly higher than for the reaction under identical conditions in acetonitrile (4.1, compare **Figure 38**). The accelerated formation

of DIOSA due to a synergistic effect under two-color conditions becomes evident when comparing the product (DIOSA) integrals in the LC traces recorded after irradiation (**Figure 45**), thus validating acetophenone as the solvent of choice for preparing photoresist formulation. With the established photoreactivity, the system offers a robust basis for scaling from the molecular to the macromolecular scale, facilitating the progression toward real-world materials application.

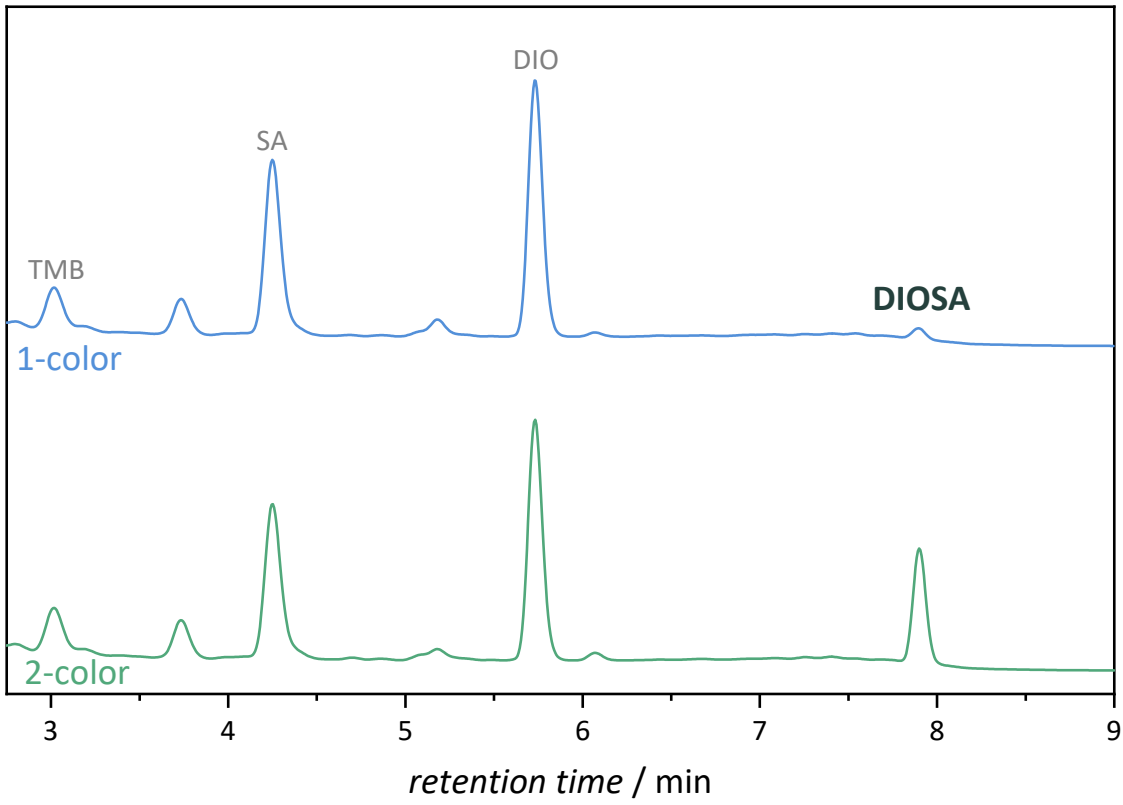

Figure 45. UV-detector LC traces at 235 nm of the reaction of DIO and SA to DIOSA in acetophenone under one- and two-color irradiation. Adapted from Hobich *et al*.[38]

4.5 Synergistic Network Formation

Based on the fundamental insights regarding the photochemistry of the functionalized photoswitches from the previous section, the next step was to expand the synergistic covalent bond formation to a synergistic network formation under conditions that are comparable to those applied for lithographic fabrication. The previous small-molecule study (Sections 4.1-4.3) allowed for detailed kinetic analyses and characterization of the two-color synergistic photochemistry on a model system.[31] Next, a series of crosslinking experiments was performed in order to serve as a bridge for the gap between the controlled, optimized reaction conditions for the model study and a more challenging environment for practical light-based lithographic application. Hence, for investigation of the synergistic network formation, polyDIO and SA-3arm were employed as crosslinkable compounds in a disparate solvent

(i.e., in acetophenone instead of acetonitrile) and at elevated concentrations to align the reaction conditions more closely with real-world lithographic fabrication. Serving as an essential validation step, this intermediate stage assessed the feasibility and reliability of synergistic two-color network formation under formulation-relevant settings.

A key demand for a photoresist is a high solid content to enable substantial crosslinking density for manufacturing stable structures. Therefore, the concentrations of DIO and SA moieties were increased from 5.0 mM (0.32 wt% solid content in acetonitrile) for the small-molecule reactions to 47.5 mM 10.0 wt% solid content in acetonitrile, **Figure S32**). For comparability purposes, the same two-color LED-setup was used (**Figure 28**) and the samples were irradiated under nitrogen atmosphere and continuous stirring for up to 3 hours. Although such extended irradiation times surpass those typically applied in practical printing, they enable a reliable assessment of the synergistic efficiency of network formation under controlled and homogeneous settings.

Contrary to the small-molecule reactions, the progress of polymeric network formation cannot be tracked via solution-state techniques, e.g. NMR spectroscopy or LC-MS, due to formation of crosslinked and insoluble structures. To address the issue of characterization, SEC was used to qualitatively monitor changes in the soluble polymer fraction during crosslinking. As the network formation proceeds, the SEC elution traces undergo a shift toward lower elution volumes, reflecting a gradual increase in molar mass (compare **Figure 46**). The M_n obtained for the polymer fraction in solution served to track the progress of crosslinking via the bond-forming reaction between polyDIO and SA-3arm into a growing polymer network.

However, it is important to note that SEC traces provide only a qualitative means to monitor the evolution of network formation. One of the reasons is that SEC provides only relative information on the molar mass of a polymer, since separation within the column is dependent on the hydrodynamic volume instead of absolute molar mass, with a calibration against narrow-disperse PMMA standards. Moreover, the SEC traces solely depict soluble fractions. As crosslink density increases, larger insoluble network structures are removed by the syringe filter during sample preparation. The removal of growing networks is experienced by the progressively higher pressure required to push the reaction mixture through the poly (tetrafluoroethylene) (PTFE) filter at longer reaction times. Despite these inherent limitations, SEC serves as a practical and effective method to monitor the relative extent of crosslinking, offering straightforward sample preparation and qualitative insights into molar mass evolution during network formation,[125] thereby enabling comparison of the synergistic efficiency across varying reaction conditions.

For better comparison, the refractive index detector (DRI) signal of the SEC traces, serving as qualitative measure of the concentration, were normalized against the signal of SA-3arm. Over the

crosslinking process, the small-molecule SA-3arm is progressively consumed, decreasing its concentration over time, whereas the amount of the network fraction in the polymer-region increases unless removed during filtration. However, the concentration of SA-3arm seems to stay constant due to the normalization while the concentration in the polymer-region appears to increase significantly. The apparent increase of concentration originates partly from the incorporation of SA-3arm into the network, but more significantly from the reduced DRI response of the normalization reference.

Furthermore, two competing effects must be considered when interpreting the shifts to lower elution volumes over time. First, the polymer molar mass increases progressively with each crosslinking event. Second, covalent crosslinking produces a more compact structure with a smaller hydrodynamic volume than a linear polymer of equivalent molar mass. As a result, the apparent molar mass obtained by comparison to linear polymer standards substantially underestimates the actual molar mass of the network, an effect that becomes increasingly pronounced as the network grows.

Kinetics under one- and two-color conditions were performed with irradiation at 365 and 430 nm with photon fluxes of 1.55×10^{16} s^{-1} cm^{-2} and 6.04×10^{16} s^{-1} cm^{-2}, respectively, under continuous stirring and inert atmosphere in the same LED setup that was previously employed for the small-molecule study **Figure 28**. For the reaction kinetics, SEC samples were measured in 30 minute intervals over the course of 3 hours with the resulting traces depicted in **Figure 46** and in more detail **Figure S10** and **Figure S11**.

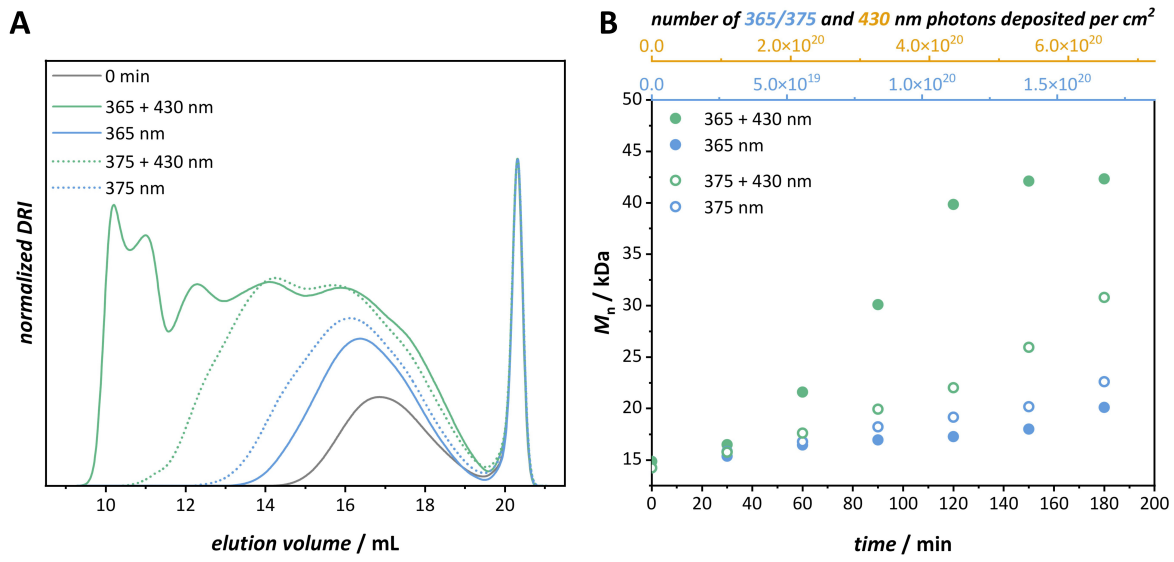

Figure 46. One- and two-color crosslinking kinetics of polyDIO and SA-3arm with comparison of 365 and 375 nm for the activation of DIO to DIO'. (**A**) SEC traces (in THF + 0.22 % w/v BHT) of the crosslinking reactions between polyDIO and SA-3arm in acetophenone before irradiation (grey), and after one- (365/375 nm, blue) and two-color (365/375 + 430 nm, green) irradiation for 3 hours, respectively. (**B**). Evolution of the polymer M_n during 3 hours of irradiation under one- (365/375 nm, blue) and two-color (365/375 + 430 nm, green) irradiation. Adapted from Hobich *et al*.[38]

In **Figure 46A** the initial SEC trace of the photoresist before irradiation is shown in grey and results from the overlay of the signals of polyDIO (broad polymer distribution from 13.5 to 19.5 mL) and SA-

3arm (narrow distribution from 19.5 to 20.8 mL). Under 365 nm one-color irradiation, M_n increases moderately from 14 900 to 20 100 g mol^{-1} while a slight shift to lower elution volumes occurs due to partial crosslinking. Contrary to that, 430 nm light exposure did not lead to any significant changes in the SEC traces even after 4 hours of irradiation (**Figure 47**), thus confirming full λ-orthogonality and suitability for synergistic two-color applications. Under dual-color 365 and 430 nm irradiation, crosslinking progressed markedly faster compared to 365 nm alone. Furthermore, the M_n increased from 14 900 to 42 300 g mol^{-1} within 3 hours, while reaching a kinetic plateau after approximately two hours (**Figure 46B**). The apparent stagnation in crosslinking is likely due to the growing network becoming largely insoluble beyond a certain point, a notion further supported by the significantly increased filtration resistance observed during SEC sample preparation. These results confirm that the synergistic reactivity observed at the molecular level was successfully introduced to the macromolecular scale, allowing synergistic two-color network formation.

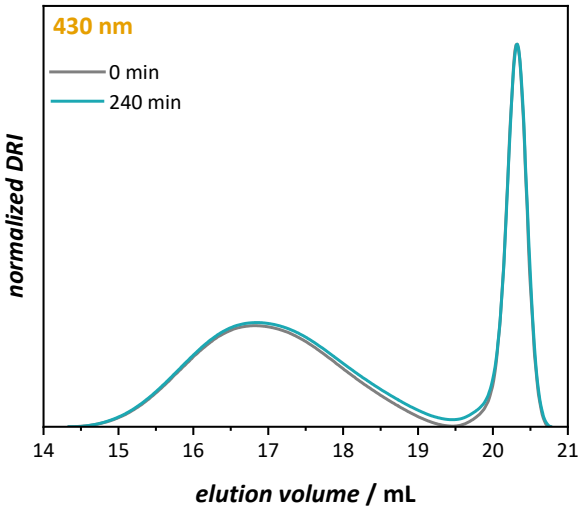

Figure 47. SEC traces (in THF + 0.22 % w/v BHT) of the photoresist composed of polyDIO and SA-3arm in acetophenone before (grey) and after 4 hours of one-color irradiation at 430 nm (turquoise), showing no significant shift. Adapted from Hobich *et al*.[38]

For the implementation of a lithography setup based on laser light instead of LEDs, the UV wavelength of 365 nm had to be substituted. Even though we possess a nanosecond (ns) pulsed OPO, i.e. a tunable laser, that was employed to generate 430 nm laser light, simultaneously achieving 365 nm was not possible. Moreover, the acquisition of a second tunable laser to match the ns-pulsed delivery of photons would be prohibitively expensive. To overcome the laser-based limitations, a continuous-wave (CW) 375 nm laser – readily available and cost-effective – was selected as the closest functional alternative for lithographic application.

To understand what impact the wavelength substitution has on the synergistic network formation, SEC kinetics under one- and two-color conditions were performed by switching the 365 nm LED with a 375 nm LED, that was operated with the same photon flux (1.55 × 10^{16} photons s^{-1} cm^{-2}). Interestingly,

comparison of the SEC kinetics revealed that the one-color reaction at 375 nm led to a higher degree of crosslinking compared to the 365 nm analog (M_n = 22 600 vs. 20 100 g mol^{-1}). Meanwhile, the synergistic effect was clearly retained for the two-color reaction under simultaneous 375 and 430 nm irradiation even though the M_n of 30 800 g mol^{-1} after 3 hours was lower than that for the combination of 365 and 430 nm (42 300 g mol^{-1}).

The difference in the progress of crosslinking for the one-color reactions was unexpected and is contrary to previous action plot studies (**Figure 26**), since the reactivities of both photoswitches were lower at 375 nm compared to 365 nm.[31] However, this discrepancy may be attributed to several factors, such as different solvents (acetonitrile vs. acetophenone), an almost ten-fold increase in the concentrations of the photoswitches (5 mM vs. 47.5 mM) and the introduction of auxochromic ether groups to the chromophores. Additional explanations are the wavelength-specific variations in penetration depth and the enhanced complexity of photochemical interactions between DIO and SA during network formation. Although the exact contribution of each variable remains unclear, their interplay most likely accounts for the unexpectedly enhanced reactivity observed for the one-color light exposure at 375 nm compared to 365 nm.

Although employment of 375 nm narrows the degree of synergy, the synergistic enhancement of the reactivity is clearly preserved as simultaneous irradiation with 375 and 430 nm yielded a significant increase in molar mass compared to irradiation with 375 nm alone. These results confirm the viability of synergistic polymer network formation after the substitution of the UV wavelength. Considering the availability and technical limitations regarding the laser sources, the combination of 375 and 430 nm was employed for all subsequent lithography experiments as the best compromise between instrumental feasibility and photochemical performance.

4.6 Synergistic Two-Color Lithography

The lithography project was performed in cooperation with Dr. Xingyu Wu who built the laser lithography setup, performed the lithography experiments, recorded the optical microscopy images and prepared the figures in this section. I prepared the photoresists and designed the general laser setup and lithography experiments together with Dr. Xingyu Wu.

To realize lithographic fabrication via synergistic two-color photochemistry, two wavelengths need to be delivered simultaneously while enabling independent control over the photon fluxes. Based on the successful synergistic network formation under dual-LED irraditation at 375 and 430 nm (**Figure 46**) a readily available and cost-effective 375 nm CW laser was integrated into our custom-made Mono LISA 3D printer[151] to achieve synergistic two-color lithography. The Mono LISA relies on a tunable, ns-

pulsed laser that was employed to generate 430 nm laser light. It should be noted that while the tunable laser provides the selection of a broad wavelength range (210-2400 nm), two wavelengths cannot be emitted simultaneously. Alternatively, it would also be possible to generate 375 or even the optimal 365 nm with the tunable laser in combination with a 430 nm CW laser. However, due to the inherent one-color photoreactivities of DIO and SA in the UV range, using a ns-pulsed tunable laser with extremely short energy spikes would necessitate either a comparably strong 430 nm CW laser or a second tunable laser to match the photon fluxes during the pulse – an approach that is prohibitively expensive, if realizable at all.

In the lithography setup the laser beams are combined by reflecting the 375 nm CW laser at a beam splitter and passing the 430 nm pulsed laser through as illustrated in **Figure 48**. Subsequently, the beams are guided onto a two-axis Galvo mirror system (X and Y axes) and delivered with a 45° mirror and a focusing lens onto the printing stage. G-code files defining the coordinates and travel speed were imported into a customized software and processed to control the printing path and velocity via the motion of the Galvo mirror. More details on the specifications of the optical components, laser configurations, and the two-color lithography sample preparation and mechanism are provided in **Appendix 7.13.1**.

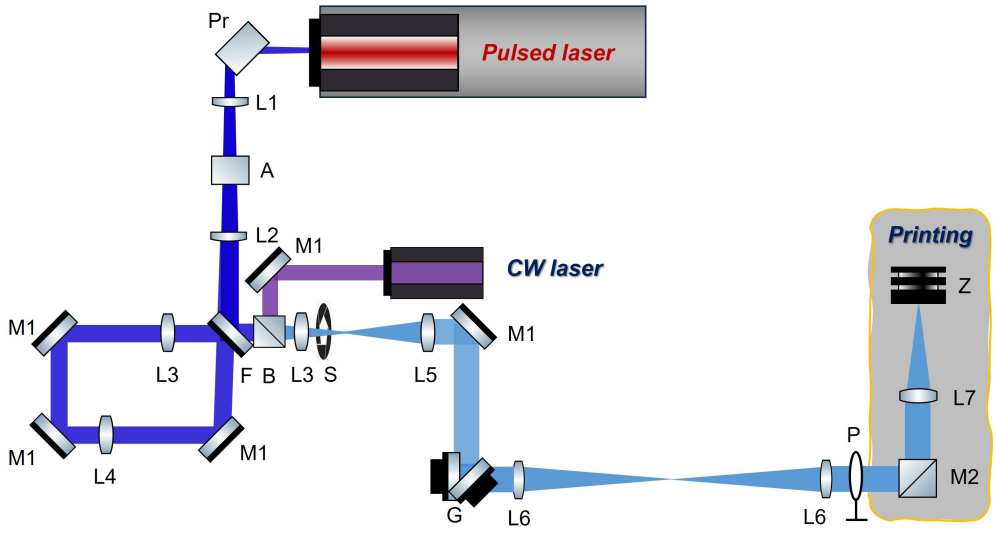

Figure 48. Schematic of the two-color lithography setup, showing the beam path and various components. Adapted from Hobich *et al*.[38]

The expanded Mono LISA printing setup offered versatility and enabled simultaneous delivery of 375 nm CW and ns-pulsed tunable laser irradiation with a broad range of adjustable printing speeds and laser powers. The synergistic photoresist for lithography was prepared with equimolar DIO and SA concentrations (70.5 mM, **Figure S33**) by dissolving polyDIO (22.7 wt%) and SA-3arm (7.4 wt%) in acetophenone. First, lithographic writing of a resist containing only polyDIO or SA-3arm was tested for 375 and 430 nm one-color or 375 + 430 nm dual-color exposure in order to understand if crosslinking

processes besides the targeted cycloaddition to DIOSA play a role. For the incomplete photoresists no fabrication of structures was observed under any accessible printing speeds or laser powers, proving that network formation can only occur in the presence of both DIO and SA. Exposure of the synergistic two-component photoresist to the 430 nm pulsed laser alone yielded the same results, confirming full λ-orthogonality for this wavelength which is in line with the action plot of DIO[31] (**Figure 27A**) and previous LED experiments (refer to **Figure 29B** and **Figure 47**). Next, the optimal conditions for synergistic efficiency in two-color lithographic fabrication were evaluated by systematically varying the printing speeds and the laser powers at 375 and 430 nm.

Printing with the photoswitch-based photoresist was readily achievable as seen in the microscopy images in **Figure 49** of structures in the millimeter-range with feature sizes down to of 48 µm. By variation of the printing speed at fixed laser powers for 375 nm (5 mW) and 430 nm (10 mW) it became evident that the fabrication window broadened significantly under these experimental conditions when employing two-colors (**Figure 49A**, bottom) instead of only one (**Figure 49A**, top). Specifically under one-color exposure, the fabrication window ended at 0.40 mm s^{-1} whereas dual-color irradiation enabled the formation of well-defined lines at even higher printing speeds of 0.45, 0.50 and 0.55 mm s^{-1}. An expansion of the fabrication window was also observed for different 375 nm laser powers (i.e. 1, 2.5 and 15 mW) as summarized in **Table S9**. When fixing the printing speed (0.6 mm s^{-1}) and 430 nm laser power (10 mW) while screening the 375 nm laser powers (from 3 to 13 mW), one-color irradiation did not produce well-defined structures at 5.0, 5.5, 6.0, and 6.5 mW (**Figure 49B**, top), whereas dual-wavelength exposure yielded clear lines at these power levels (**Figure 49B**, bottom). The findings are consistent with the results in **Figure 49A**, regarding the fact that the fabrication window mainly depends on the 375 nm photon flux that can be adjusted by either varying printing speed or laser power. Therefore, an increase of the 375 nm photon flux led to a broadening of the fabrication window for both one- and two-color lithography (**Table S9**) and linewidths increased as well (**Figure 49**). It is anticipated that higher photon flux, achieved through elevated laser power or reduced printing speed, enhances the rate of cycloaddition between DIO and SA. The resulting increase in DIOSA crosslinks leads to the formation of wider lines that remain intact after development in acetone to remove the soluble residuals.

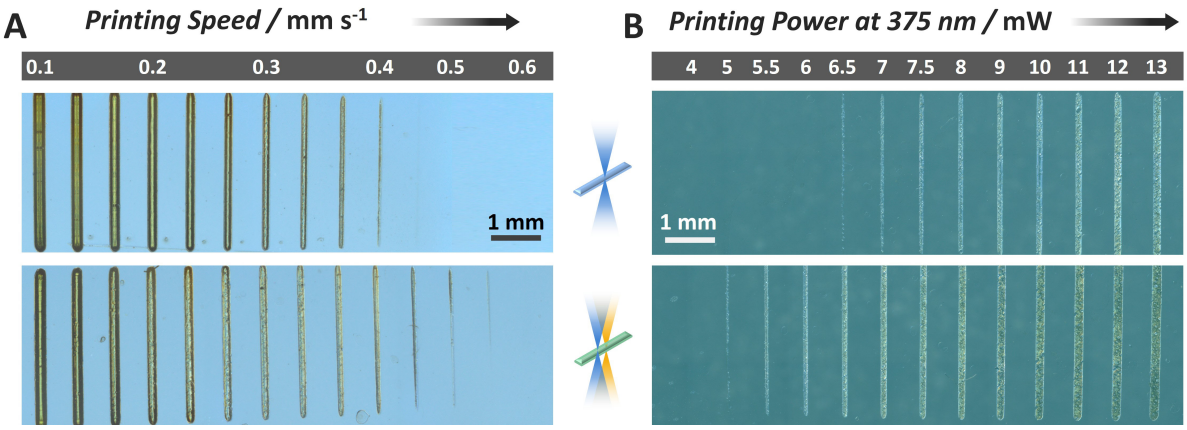

Figure 49. Optical microscopy images of lines printed with one- or two-color exposure. Top lines were printed with one color, while bottom lines were printed using two colors as illustrated by the schematic in the middle. (**A**) Lines printed at fixed laser powers at 375 nm (5 mW) and 430 nm (10 mW, bottom lines) with varying printing speeds. (**B**) Lines printed at a fixed printing speed (0.6 mm s^{-1}) and a 430 nm laser power (10 mW, bottom lines) with varying laser powers at 375 nm. Adapted from Hobich *et al*.[38]

Next, the impact of the 430 nm laser power was investigated by fixing the printing speed (0.55 mm s^{-1}) and 375 nm laser power (5 mW). Interestingly, the linewidths were not significantly affected (**Figure 50**) by changes in the 430 nm laser power which is probably due to the pulsed delivery of the 430 nm photons. As previously discussed it is expected that delivery of both wavelengths in the same mode, i.e. either CW or simultaneously pulsed, enhances the synergistic efficiency – a configuration that is not feasible at the current stage. Still, the ability to fabricate lines under dual-color exposure at specific printing speeds and laser powers, that is not retained for 375 or 430 nm single-color exposure, underlines the successful integration of synergistic two-color network formation experiments to lithographic fabrication.

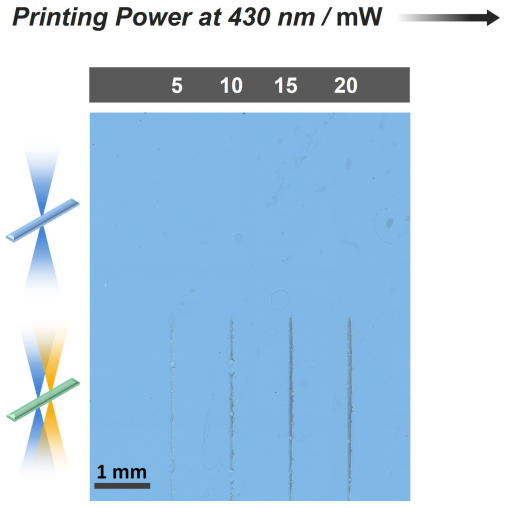

Figure 50. Optical microscopy images of lines printed with one- or two-color exposure. Top lines were printed with one color (375 nm, 5 mW, 0.55 mm s^{-1}), while bottom lines were printed using two colors with varying laser powers at 430 nm (375 nm at 5 mW, 0.55 mm s^{-1}) as illustrated by the schematic on the left. Adapted from Hobich *et al*.[38]

After exploring the optimal printing conditions regarding the photochemical synergy in the line tests, the following step was the fabrication of more intricate structures. A set of ring patterns was printed in which segments of 100, 75, 50, 25, and 0%, respectively, were exposed to 375 nm only, while the complementary parts were irradiated with 375 and 430 nm simultaneously. G-codes for the ring series and their trajectories are detailed in **Figure S137**. Lithography was performed under the optimized conditions of a printing speed of 0.45 mm s^{-1} and laser powers of 5 mW and 10 mW for 375 and 430 nm exposure, respectively. As shown in **Figure 51** and **Figure S138**, the fabrication of well-defined ring segments only occurred under dual-wavelength irradiation, whereas single-wavelength exposure did not yield any discernible structures. The two-color dependency is further reflected in the progressive emergence of 0, 25, 50, 75, and 100% rings from left to right, highlighting the critical role of synergistic activation for successful solidification via network formation.

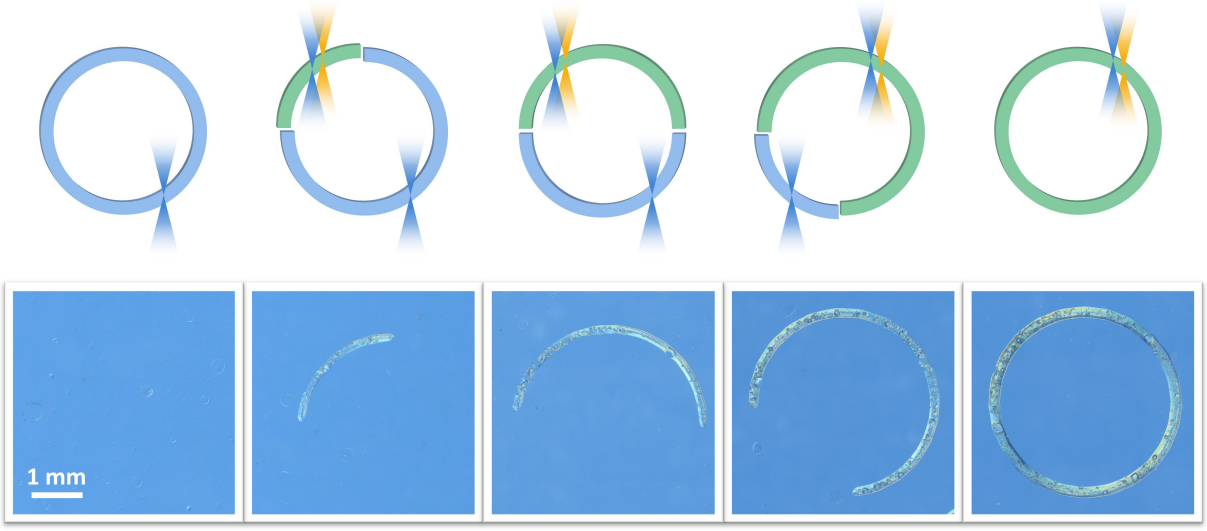

Figure 51. Optical microscopy images of a series of rings with varying fractions (100%, 75%, 50%, 25% and 0% from left to the right) printed using one-color exposure (375 nm, 5 mW, 0.45 mm s^{-1}). The remaining portions of each ring were printed using two-color irradiation (375 nm at 5 mW and 430 nm at 10 mW, 0.45 mm s^{-1}). The schematic at the top illustrates the segments irradiated with one- and two-colors of light. Adapted from Hobich *et al.*[38]

To further demonstrate the versatility of the lithography setup in combination with the photoresist, a more sophisticated butterfly structure was fabricated under optimized printing conditions (375 nm at 5 mW and 430 nm at 10 mW, 0.45 mm s^{-1}). As shown in **Figure 52**, reliable structure formation was only achieved for the left side of the butterfly, which was exposed to dual-color irradiation, whereas the right side, irradiated solely at 375 nm, failed to print properly. The resulting butterfly structure highlights the excellent synergistic printability of the photoresist under two-color irradiation. The G-code and trajectory of the butterfly design are provided in **Figure S139**. Microscopic inspection revealed a slightly rough surface texture of the printed structures. While polyDIO and SA-3arm are readily miscible in acetophenone, they may form micelle-like assemblies in solution that persist despite

filtration of the ink. Such intrinsic nanoscale heterogeneity likely caused light scattering during printing, leading to surface irregularities.

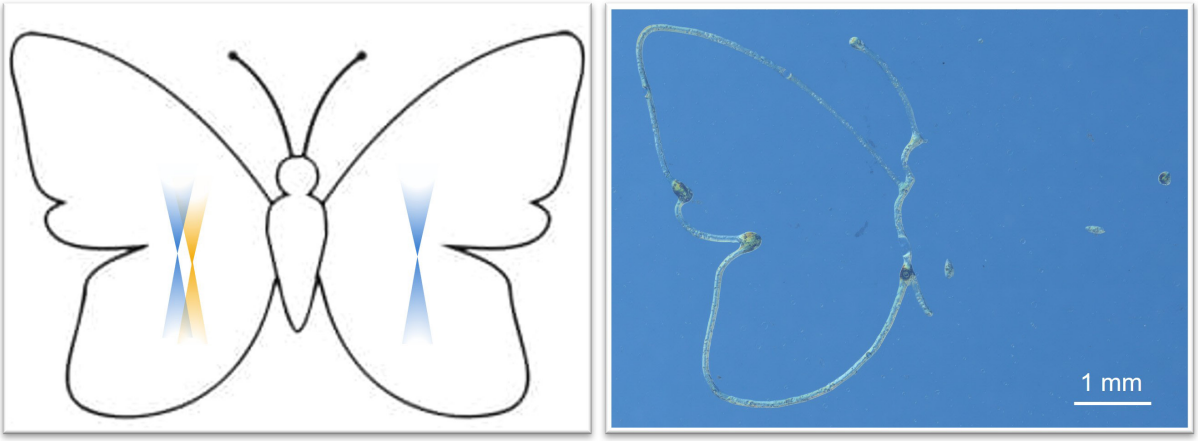

Figure 52. Butterfly structure, with the left half fabricated using two colors and the right half using only one color. **Left:** Schematic representation of the whole butterfly structure and the corresponding single- and dual-irradiation applied. **Right:** Optical microscopy image of the butterfly with the left half fabricated using two colors (375 nm at 5 mW and 430 nm at 10 mW, 0.45 mm s^{-1}) and the right half using only one color (375 nm at 5 mW, 0.45 mm s^{-1}). Adapted from Hobich *et al.*[38]

For future investigations, synergistic two-color printing presents opportunities for fabrication of hollow and complex structures that remain challenging, if even possible, by employing conventional 3D printing methods like DLP or SLA.[11, 12] This advantage comes from the distinctive requirement that network formation occurs only under simultaneous irradiation with both wavelengths, thereby enabling rapid construction of intricate architectures with high spatial precision and resolution.

5. Conclusion and Outlook

5.1 Conclusion

Upon simultaneous irradiation at 365 and 430 nm, the photoswitch combination of diarylindenone epoxide (DIO) and strained azobenzene (SA) undergoes synergistic covalent bond formation to generate the cycloadduct DIOSA. The structure of DIOSA was elucidated via SXRD and further confirmed by LC-MS analysis. Subsequent photochemical action plot studies of the separate photoswitches revealed their wavelength-dependent reactivities and provided the basis for identifying the optimal wavelength combination for λ-orthogonal activation of DIO and SA. While 430 nm exclusively activates SA, both photoswitches isomerize at 365 nm, resulting in partial reactivity under 365 nm single-wavelength exposure. Consequently, a systematic evaluation of two-color synergy under varied reaction conditions was conducted. The investigations revealed that, due to significant differences in the half-lives of the two photoswitches, undesired one-color reactivity can be attenuated by either reducing the 365 nm photon flux or employing a higher DIO-to-SA ratio. However, complete suppression of the one-color reaction is not feasible – a common occurrence, as most chromophores exhibit overlapping absorbances and reactivities, particularly in the UV region.

To quantify the efficiency of two-color synergy, the synergistic ratio ϕ_{syn} was introduced as a new parameter. As the ratio decreases with increasing conversion, ϕ_{syn}^{0} was proposed as a conversion-independent metric for comparing different synergistic systems. Essentially, ϕ_{syn} directly measures the acceleration of product formation under dual-wavelength irradiation compared to single-wavelength conditions. Values of up to 14.4 for ϕ_{syn}^{0} were achieved under conditions of low 365 nm photon flux (9.63×10^{16} s^{-1} cm^{-2}) and a tenfold excess of DIO relative to SA. These findings establish a general framework for the development and systematic characterization of novel synergistic photochemistries, with particular promise for applications in lithographic fabrication and 3D additive manufacturing.

The next step was to translate the insights gained from the small-molecule model system of DIO and SA to the macromolecular level by developing a photoresist for two-color synergistic lithography. To enable dual-wavelength-gated crosslinking, DIO and SA were decorated with versatile functional handles and covalently incorporated into a defined multifunctional polymer architecture (polyDIO) and a trifunctional compound (SA-3arm), respectively. The photoresist was prepared by dissolving polyDIO and SA-3arm with equimolar chromophore ratios in acetophenone. To bridge the gap between model study and lithography, the identical dual-color LED setup and comparable reaction conditions were applied to the diluted photoresist. Crosslinking progress was monitored qualitatively by SEC and

systematic kinetic studies revealed substantially accelerated network formation under two-color (365 + 430 nm) compared to one-color (365 nm) irradiation, demonstrating successful integration of photochemical synergy at the macromolecular level.

Because acquiring a 365 nm CW laser for the lithography setup was not feasible, and 375 nm is the closest viable alternative, the kinetic study was repeated for the combination of 375 and 430 nm. Although the degree of synergy decreased upon substituting the UV wavelength, a pronounced synergistic effect persisted, underscoring the great potential for additive manufacturing. Implementation in a customized dual-color (375 + 430 nm) laser lithography setup enabled the fabrication of intricate geometries, such as asymmetric designs and ring segments, under specifically optimized combinations of laser powers and printing speeds. The intrinsic dual-gate mechanism offers an effective means of suppressing undesired crosslinking, thereby paving the way for rapid, high-precision, high-resolution printing. Overall, synergistic two-color lithography emerges as a promising strategy for next-generation additive manufacturing, integrating molecular-level photochemical control into practical lithographic fabrication.

5.2 Outlook

The current thesis introduces a novel synergistic dual-photoswitch system with the primary aim of establishing a foundation for future real-world applications by first exploring the underlying photochemistry on a molecular scale and subsequently transferring it to lithographic fabrication as a proof of principle. The next challenge lies in optimizing the synergistic efficiency of the cycloaddition between photoactivated DIO and SA, thereby expanding the scope from 2D to 3D fabrication and enabling light-sheet printing techniques. A critical step toward widening the synergistic operation window will be to match the photon delivery patterns of both wavelengths, either through adapting two CW or pulsed lasers operating on the same timescale. The use of two ns-pulsed tunable lasers would, for example, allow fabrication at 365 nm, which is not yet feasible with CW lasers, while also enabling direct investigation of synergistic efficiencies across different wavelength combinations in the real, combined system rather than through separate chromophore action plot studies. Such a setup would markedly enhance versatility and facilitate the screening of various wavelength combinations to optimize reaction conditions.

Further progress may be achieved by structurally tuning the photoswitches, particularly DIO, to shift photoactivation into the visible region, thereby avoiding complications associated with UV irradiation and enabling CW laser compatibility. In addition, tailoring and broadening λ-orthogonal windows represents a key strategy to enhance synergy. With an optimized and finely tuned dual-color response

of DIO and SA, the ultimate aspiration is the rapid and precise fabrication of complex architectures via light-sheet printing. Beyond this, the in-depth characterization of one of the first synergistic photochemistries is intended to serve as a roadmap and inspiration for the development of novel systems, providing both conceptual guidance and practical tools for quantifying and improving synergistic efficiency, thus serving as foundation for transformative advances in light-based additive manufacturing.

When applying the dual-photoswitch concept, several conditions must be fulfilled to approach the ideal case where ϕ_{syn} converges toward infinity. First, both photoswitches should exist exclusively in their unreactive, stable isomers in the dark and at ambient temperature. Next, photoisomerization should proceed in a fully λ-orthogonal manner with high quantum yields to ensure efficient conversion. Furthermore, low extinction coefficients at the incident wavelengths are advantageous to enhance irradiation homogeneity within a photoresist, for instance in a light-sheet setup. In addition, the metastable isomers should exhibit extremely short half-lives (on the millisecond timescale or shorter) but high PSS values at the incident wavelength to achieve high concentrations of reactive species within short time frames. The photoisomerization should be purely T-type to avoid additional complexity arising from photochemical reversion at the irradiation wavelengths. All photoswitch isomers should be insensitive to oxygen and display high cycling stability to minimize side reactions and photobleaching. Ideally, the synthesis should require minimal effort and rely on inexpensive starting materials to ensure feasibility. Finally, both photoswitches should be well-matched, and only their metastable isomers should react selectively with each other, resulting in the irreversible formation of covalent bonds between the two compounds.

Current approaches to achieve photochemical two-color synergy rely on either two-step absorption of two photons[11] or photoisomerization with subsequent photon absorption,[12] both followed by radical initiation, or on separate photoisomerization of two distinct photoswitches followed by covalent bond formation.[31, 38] These approaches illustrate that increasing complexity through the addition of a second wavelength simultaneously expands the conceptual toolbox, enabling novel and creative strategies to achieve synergy. The key characteristic of any synergistic system is reversibility: all photochemical processes must revert fully and rapidly, depending on the incident wavelength, while only dual-color exposure should yield an irreversible outcome. Reversibility can be achieved in two different ways – either thermally or photochemically. Thermal reversion can occur via excited-state relaxation or reversion of a T-type photoswitch, whereas photochemical reversion requires at least one additional, independent, and λ-orthogonal wavelength.

Several exciting concepts based on the fundamental principle of reversibility can be envisioned. For instance, a straightforward strategy would be to broaden the dual-photoswitch approach by

incorporating compounds with reactive excited states. Promising candidates exhibiting selective and efficient photoreactivities include *ortho*-methyl benzaldehydes (*o*-MBA)[110, 195] and 9,10-phenanthrenequinones.[196, 197] Furthermore, instead of relying on excited states and switchable reactivities, one could exploit conformational changes of a photoswitch in combination with a second photoreaction that leads to crosslinking exclusively from one of the two isomers. Inspiration for this concept arises from a functionalized stiff-stilbene, which forms intramolecular hydrogen bonds in its *cis*-isomer, whereas the *trans*-isomer engages in intermolecular hydrogen bonding, resulting in supramolecular polymerization.[198]

In all these concepts, light is employed as a direct stimulus to induce changes within a system. However, it can also act as an indirect trigger by influencing another stimulus that subsequently enables a reaction. For example, photoacids or -bases (e.g., water-soluble merocyanine compounds)[199] can reversibly alter the pH, which in turn can be exploited to control pH-dependent photoreactions such as the [2+2] cycloaddition of styrylquinoxalines.[200]

Another concept draws on the idea of a “sunscreen” that absorbs most incident photons without reacting and must be switched off to enable efficient crosslinking. Since photoswitches typically isomerize upon photon absorption and would therefore only serve as temporary screens, this approach needs to be combined with a compound whose absorbance profile can be modulated by another stimulus. For instance, a photoacid in combination with a pH indicator could be employed to either block or open specific wavelength ranges.

From these diverse examples it becomes evident that synergistic photochemistry offers a creative playground, enabling a myriad of different approaches and inviting exciting ideas and novel concepts with the potential to substantially advance the fields of two-color photochemistry and 3D printing.

6. Experimental Section

In the following materials and methods that were employed for the small-molecule study of the synergistic ratio[31] will be referred to as “Small-molecule study” and the ones for the preparation and lithographic fabrication of a photoresists[38] as “Macromolecular study”.

6.1 Materials

6.1.1 Small-molecule study

The following chemicals were used as received without further purification:

1-Bromo-2-nitrobenzene (98%, Sigma Aldrich), 2-bromobenzaldehyde (98%, TCI), diphenylacetylene (99%, Thermo Fisher Scientific), norbornene (99%, Alfa Aesar), thiourea (99%, Chem-Supply), 1,3,5-trimethoxybenzene (99%, Sigma Aldrich), ammonium chloride (99%, Carl Roth), copper(I) iodide (99.5%, Sigma Aldrich), palladium(II) acetate (99.9%, Acros Organics), potassium carbonate (99%, Chem-Supply), sodium acetate (99%, Acros Organics), sodium hydroxide (98%, Chem-Supply), sodium sulfate (99%, Thermo Fisher Scientific), tetrabutylammonium chloride (98%, TCI), zinc powder (99.9%, -100 mesh, Thermo Fisher Scientific), hydrogen peroxide 30% (Thermo Fisher Scientific), acetonitrile (HPLC grade, RCI Labscan), chloroform (99%, VWR), cyclohexane (reagent grade, Merck), dichloromethane (99.8%, Thermo Fisher Scientific), dry dimethylformamide (99.8%, Thermo Fisher Scientific), dry dimethyl sulfoxide (99.9%, Sigma Aldrich), ethanol (99.5%, Thermo Fisher Scientific), ethyl acetate (99.5%, Thermo Fisher Scientific), isopropanol (99%, VWR), acetonitrile-d_3 (99.8%D, Eurisotop), chloroform-d (99.8%D, Eurisotop).

6.1.2 Macromolecular study

The following chemicals were used as received without further purification:

Acryloyl chloride (96%, Alfa Aesar), 2-Aminothiophenol (98%, Thermo Fisher Scientific), Ammonium chloride (99%, Carl Roth), 2-Bromo-3-nitrophenol (98%, BLD Pharm), 6-Bromohexan-1-ol (98.2%, BLD Pharm), 2-Bromo-4-hydroxybenzaldehyde (98.2%, Ambeed), 1,8-Diazabicyclo[5.4.0]undec-7-ene (98%, Merck), Diphenylacetylene (99.9%, BLD Pharm), 1-Dodecanethiol (98%, Alfa Aesar), Hydrogen peroxide (30%, Carl Roth), Iron(III) chloride hexahydrate (99%, Carl Roth), Methacryloyl chloride (97%, Sigma Aldrich), Palladium(II) acetate (99.9%, BLD Pharm), Potassium carbonate (99%, Alfa Aesar), Potassium hydroxide (85%, Carl Roth), Sodium acetate (99%, Acros Organics), Sodium bicarbonate (99%, Carl Roth), Sodium hydroxide (98%, Carl Roth), Sodium sulfate (99%, Carl Roth), Tetrabutylammonium chloride (95%, BLD Pharm), Triethylamine (99%, Sigma Aldrich), Trimethylolpropane tris(3-mercaptopropionate) (95%, Sigma Aldrich), Zinc powder (99.9%, Thermo

Fisher Scientific), Acetonitrile (HPLC grade, VWR), Acetophenone (99%, Sigma Aldrich), Dichloromethane (99%, GPR Rectapur), Dimethylformamide (99.8%, anhydrous, Thermo Fisher Scientific), Ethanol (99.5%, GPR Rectapur), Tetrahydrofuran (99.9%, anhydrous, Thermo Fisher Scientific), Tetrahydrofuran (HPLC grade, Carl Roth), Cyclohexane (reagent grade, VWR), Ethyl acetate (reagent grade, VWR), Toluene (HPLC grade, Carl Roth), CD_3CN (99.8%, Eurisotop), $CDCl_3$ (99.5%, Eurisotop), DMSO-d_6 (99.8%, Eurisotop).

6.2 Methods

6.2.1 Nuclear magnetic resonance (NMR) spectroscopy

6.2.1.1 Small-molecule study and Macromolecular study

^{1}H- and ^{13}C-NMR spectra of the compounds were recorded on a *Bruker* AM 400, equipped with a 5 mm BBO-Probe, (^{1}H: 400 MHz, ^{13}C: 101 MHz). The δ-scale was normalized relative to the magnetic resonance arising from the residual solvent signal of $CDCl_3$ (δ = 7.26 ppm), CD_3CN (δ = 1.94 ppm) and DMSO-d_6 (δ = 2.50 ppm) for ^{1}H spectra, and $CDCl_3$ (δ = 77.16 ppm), CD_3CN (δ = 118.26 ppm) and DMSO-d_6 (δ = 39.52 ppm) for ^{13}C spectra, respectively.[201] The multiplicities were reported using the following abbreviations: s for singlet, d for doublet, t for triplet, q for quartet, p for pentet, m for multiplet and br for broad signal.

6.2.1.2 Small-molecule study – Two-color stock solutions

^{1}H and ^{13}C-NMR spectra of the compounds were recorded on a *Bruker* System 600 Ascend LH, equipped with a BBO-Probe (5 mm), (^{1}H: 600 MHz). The δ-scale was normalized relative to the magnetic resonance of the residual solvent signal CH_3CN for ^{1}H spectra.

6.2.2 Liquid chromatography-mass spectrometry (LC-MS)

6.2.2.1 Action plot (DIO) and Macromolecular study

LC-MS measurements for the DIO action plot were performed on an *Agilent* 1260 Infinity II system consisting of a quaternary pump (GB7111B), autosampler (G7129A, 100 µL sample loop), a temperature-controlled column oven (G7114A) and a variable UV-Vis detector (G7114A, VWD, flow cell G7114A 018, d = 10 mm, V = 14 µL). Separation was performed on a C18 HPLC column (*Agilent* Poroshell 120 EC-C18 4.6x100 mm, 2.7 µm) operating at 40 °C. A gradient of acetonitrile : H_2O 45:55 – 100:0 (v/v) (additive 10 mmol L^{-1} ammonium formate) at a flow rate of 1 mL min^{-1} during 9 minutes was used as the eluting solvent. The flow was directed into an *Agilent* MSD (G613BA, AP-ESI ion source). The instrument was calibrated in the *m*/*z* range 118-2121 in positive mode and 113-2233 in

the negative mode, using a premixed calibration solution (*Agilent*). The following parameters were used: spray chamber flow: 12 L min^{-1} , drying temperature: 350 K, Capillary Voltage: 3000 V, Fragmentor Voltage: 100 V.

6.2.2.2 Small-molecule study – Synthesized compounds and two-color reactions

LC-MS measurements of the synthesized molecules and for the two-color reactions were performed on an UltiMate 3000 UHPLC System (*Dionex*, Sunnyvale, CA, USA) consisting of a pump (LPG 3400SZ), autosampler (WPS 3000TSL) and a temperature-controlled column compartment (TCC 3000). Separation was performed on a C18 HPLC column (*Phenomenex* Luna 5 µm, 100 Å, 250 × 2.0 mm) operating at 40 °C. Water (containing 5 mmol L^{-1} ammonium acetate) and acetonitrile were used as eluents. A gradient of acetonitrile: H_2O, 5:95 to 100:0 (v/v) in 7 minutes at a flow rate of 0.40 mL min^{-1} was applied. The flow was split in a 9:1 ratio, where 90% of the eluent was directed through a DAD UV-detector (VWD 3400, *Dionex*) and 10% was infused into the electrospray source. Spectra were recorded on an LTQ Orbitrap Elite mass spectrometer (*Thermo Fisher Scientific*, San Jose, CA, USA) equipped with a HESI II probe. The instrument was calibrated in the *m/z* range 74-1822 using premixed calibration solutions (*Thermo Scientific*). A constant spray voltage of 3.5 kV, a dimensionless sheath gas, and a dimensionless auxiliary gas flow rate of 5 and 2 were applied, respectively. The capillary temperature was set to 300 °C, the S-lens RF level was set to 68, and the aux gas heater temperature was set to 100 °C.

6.2.3 Size-exclusion chromatography (SEC)

The SEC measurements were conducted on a *PSS* SECurity2 system containing a *PSS* SECurity Degasser, *PSS* SECurity TCC6000 Column Oven (35 °C for THF), *PSS* SDV Column Set (8x50 mm 5 µm precolumn, 8x300 mm 5 µm analytical columns, 100000 Å and 1000 Å) and an *Agilent* 1260 Infinity II Isocratic Pump, Agilent 1260 Infinity II Standard Autosampler, *Agilent* 1260 Infinity II Diode Array and Multiple Wavelength Detector, *Agilent* 1260 Infinity II Refractive Index Detector (35 °C). HPLC grade THF was used as eluting solvents at a flow rate of 1 mL min^{-1}. Narrow disperse linear poly(methyl methacrylate) (PMMA) standards (M_n 831 g mol^{-1} to 1.89×10^6 g mol^{-1}, PSS ReadyCal) were used as a calibrant. Molecular weight and dispersity analyses were performed via the PSS WinGPC UniChrom software (version 8.2). The polymer samples were dissolved in THF (~2 mg mL^{-1}) at ambient temperature and filtered through a 0.2 µm PTFE syringe filter.

6.2.4 Ultraviolet-visible (UV-Vis) spectroscopy

6.2.4.1 Small-molecule study

UV-Vis spectra were recorded on a *Shimadzu* UV-2700 spectrophotometer equipped with a CPS-100 electronic temperature control cell positioner. Samples were prepared in acetonitrile and measured in *Hellma Analytics* quartz high precision cells with a path length of 10 mm at 20 °C.

6.2.4.2 Macromolecular study

a) UV-Vis spectra for SA-OH, DIO-OH and polyDIO were recorded on an *Agilent* Cary 5000 UV-VIS-NIR spectrophotometer. Measurements were performed at ambient temperature using a *Hellma Analytics* quartz high precision cell (*108-F-10-40*) with a path length of 10 mm. Samples were prepared in acetonitrile or acetophenone, filtered through a 0.2 µm PTFE syringe filter and measured at ambient temperature.

b) UV-Vis spectra of the photoswitching of SA-3arm were recorded with a different setup due to the extremely short half-life times of the SA species in the millisecond range.[34] An *Ocean Insight* DH-2000 UV-VIS-NIR Light Source was coupled via optic fibers (*P400-025-SR*) to an *Ocean Insight* Ocean-FX spectrometer, sensitive from 200 to 850 nm, via an *Ocean Insight Square One* cuvette holder. Measurements were performed at ambient temperature using a *Hellma Analytics* quartz high precision cell (*108-F-10-40*) with a path length of 10 mm. Samples were prepared in acetophenone, filtered through a 0.2 µm PTFE syringe filter and measured at ambient temperature.

6.2.5 Attenuated total reflectance infrared spectroscopy (ATR-IR)

All IR measurements were performed on a *Bruker* Alpha II ATR-IR from 400-4000 cm^{-1} at ambient temperature.

6.2.6 Thermogravimetric analysis (TGA)

TGA measurements were carried out on the *TA* Instruments TGA 5500 under nitrogen atmosphere using platinum TGA sample pans and with a heating rate of 10 K min^{-1} over a temperature range from 25 to 600 °C.

6.2.7 Differential scanning calorimetry (DSC)

Thermal properties were measured on a *TA* DSC 2500 with a heating rate of 20 K min^{-1} from -90 °C and 100 °C in *TA* Tzero sample holder. The glass transition temperature T_g was determined in the second heating run to eliminate possible interference from the polymer's thermal history.

6.2.8 Flash column chromatography

Flash column chromatography was performed on a CombiFlash Rf+ (*Teledyne ISCO*). Factions were collected based on a UV detector (254, 280 nm and detection of the full UV-Vis spectrum). *Interchim* Puriflash 15 and 30 µm Silica-HP columns were used for the separations. The raw products were deposited on Celite® 565 by dissolving, mixing and evaporation off the volatiles under reduced pressure. Subsequently, the Celite® was transferred into a Teledyne plunger pre-column filled to 1/3 with aspherical silica gel 35-60 µm.

6.2.9 Optical microscopy

2D images were acquired by digital optical microscope DSX1000 (Olympus) with a 10×long working distance objective. The feature sizes of structures were analyzed with DSX software.

6.2.10 Single crystal X-ray diffraction (SXRD)

Single crystal X-ray diffraction data of **DIOSA** and **DIOnor** were collected on a STOE STADI VARI diffractometer with monochromated Ga Kα (1.34143 Å) radiation at low temperature. Using Olex2,[202] the structures were solved with the ShelXT[203] structure solution program using Intrinsic Phasing and refined with the ShelXL[204] refinement package using Least Squares minimization. Refinement was performed with anisotropic temperature factors for all non-hydrogen atoms; hydrogen atoms were calculated on idealized positions.

6.2.11 Light emitting diode (LED) characterization

6.2.11.1 Small-molecule study

For the photoreactions a 365 nm LED by *Boston Photonics* (2850 mW, Product Number: VC2X2C45L9-365) and a 430 nm LED by *Lumixtar* (30 W, Product Number: WL-P30EP4545UV140-430) were employed.

LED output energies were recorded using a *Thorlabs* S401C thermopile sensor, with an active area of 100 mm^2 and a wavelength range of 190 nm – 20 µm, connected to a *Thorlabs* PM400 energy meter console. The emitted power from each LED was measured for 60 seconds at the same distance from the sensor as in the photoreaction from the center of the crimp vial, after which the mean and standard deviation of the emission could be determined. LEDs were cooled during measurement to minimize any thermal effects on the emission power or sensor performance.

LED emission spectra (**Figure S1**) were recorded using an *Ocean Optics* FLAME-T-UV-VIS spectrometer, with an active range of 200-850 nm, an integration time of 50 ms and averaging over 10 scans.

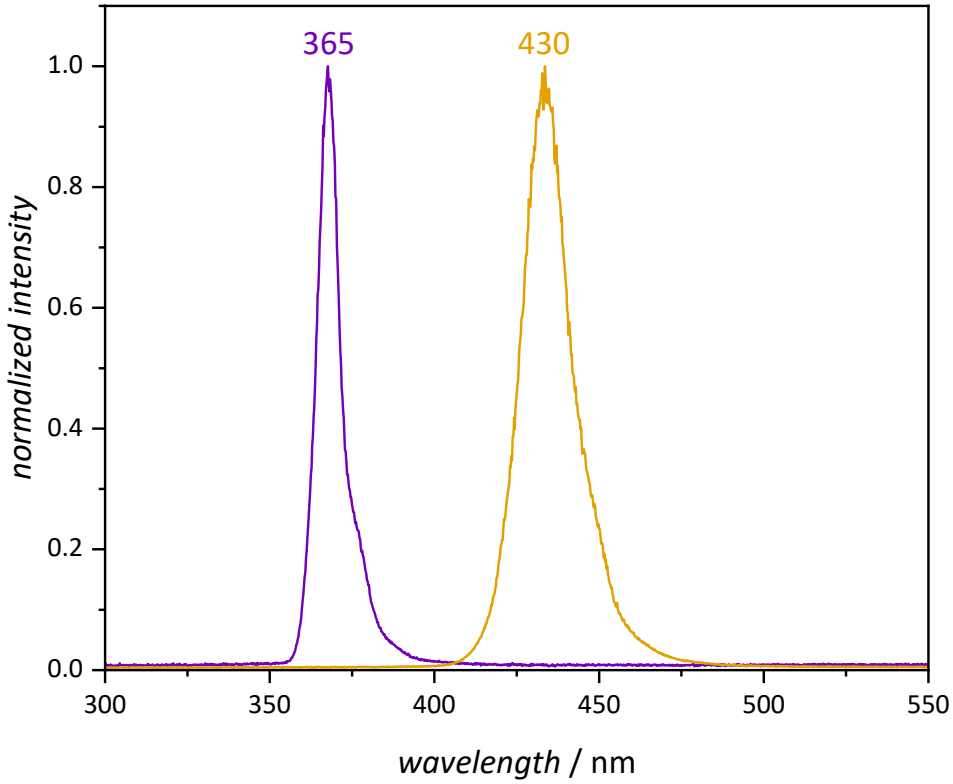

Figure S1. Emission spectra of LED light employed for irradiation, i.e. 365 nm (purple) and 430 nm (blue).

6.2.11.2 Macromolecular study

For the photoreactions a 365 nm LED by *Boston Photonics* (2850 mW, Product Number: VC2X2C45L9-365), a 375 nm LED by *Boston Photonics* (3300 mW, Product Number: VC2X2C45L9-375) and a 430 nm LED by *Lumixtar* (30 W, Product Number: WL-P30EP4545UV140-430) were employed.

LED emission spectra (**Figure S2**) and output energies were recorded using an *Opsytec Dr. Gröbel* Spectroradiometer SR600 at the same distance (30 mm) from the sensor as in the photoreactions from

the center of the crimp vial. LEDs were cooled during measurement to minimize any thermal effects on the emission power or sensor performance.

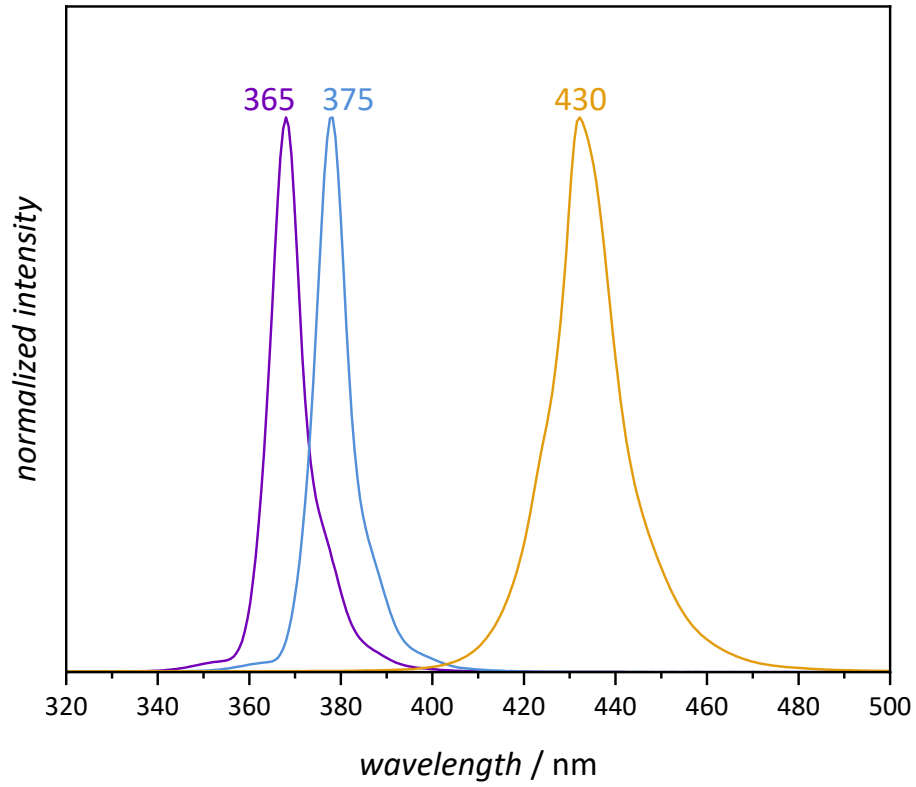

Figure S2. Emission spectra of LED light employed for irradiation, i.e., 365 nm (purple), 375 nm (blue) and 430 nm (yellow).

6.2.12 Photochemical action plot measurements

6.2.12.1 Kinetics and Action plot of DIO

Action plots were recorded using the methodology outlined in our recent overview article.[37] **Figure S3** shows the experimental setup used to conduct the photochemical action plots. An *Innolas* SpitLight 600 optical parametric oscillator (OPO) tunable laser system with a full width half maximum of 7 ns and a repetition rate of 10 Hz. The beam passes through an electronic shutter and is directed upwards using a prism. Finally, the beam enters the sample, suspended in an aluminum block, from below. The laser energy deposited into the sample was measured above the aluminum block before and after experiments using a *Coherent* EnergyMax thermopile sensor (J-25MB-LE) to account for any power fluctuations during irradiation.

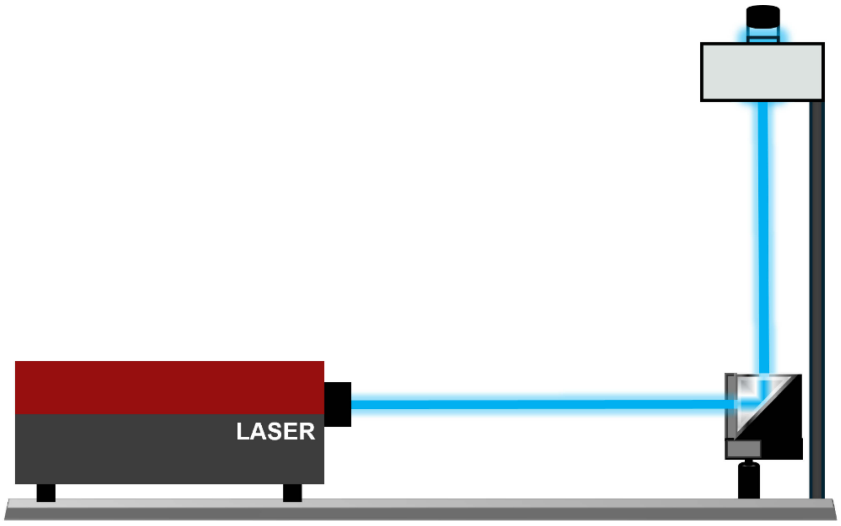

Figure S3. Schematic representation of the setup used to conduct the photochemical action plots.

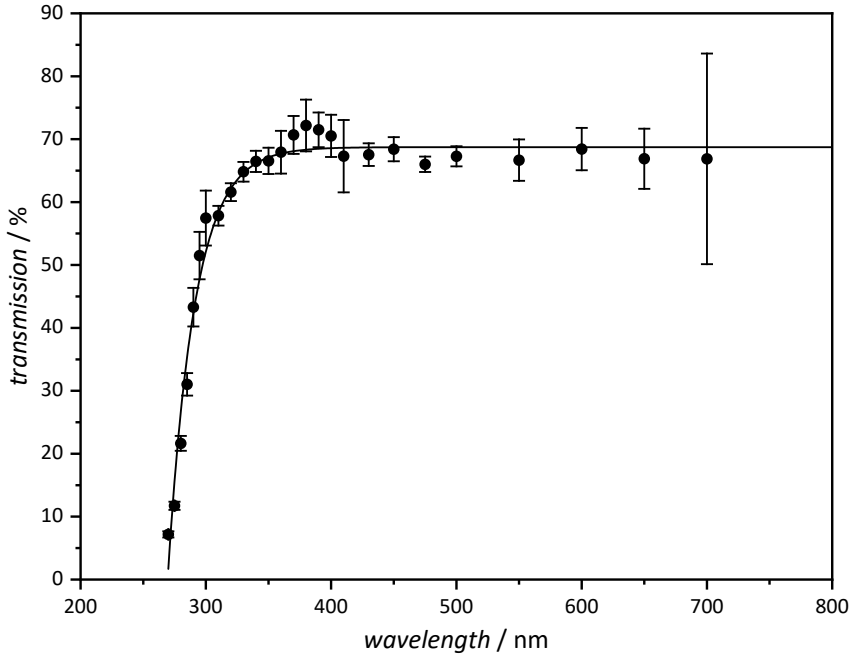

Figure S4. Transmission (%) of laser vials used in this study as a function of wavelength (nm).

For laser measurements, all samples were prepared in 0.7 mL glass crimp vials by *Thermo Fisher* (Clear Glass Vial, 7x40 mm, Flat Bottom, Product Number: C4008-741) capped with a rubber/PTFE septum. The wavelength dependent glass transmittance, essential for quantitative measurements, is presented in **Figure S4**. Precise photons numbers N_p were determined from the laser pulse energy using the following relation

$$N_p = \frac{E_{pulse}\lambda f_{rep} t}{hc[\frac{T_\lambda}{100}]}$$

where E_{pulse} is the measured pulse energy above the aluminum block, λ is the wavelength of the incident radiation, f_{rep} is the laser repetition rate, t is the irradiation time, h is Planck's constant, c is

the speed of light and T_λ is the wavelength dependent glass transmission presented in **Figure S4**. Once an initial measurement is completed and the required photon number is known, the required energies at other wavelengths can be found by rearranging the previous equation to give

$$E_{pulse} = \frac{N_p hc[\frac{T_\lambda}{100}]}{\lambda f_{rep} t}$$

To prepare the samples, a stock solution of 1 mM DIO (4.48 mg, 15.0 µmol, 1.0 eq.) and norbornene (141 mg, 1.50 mmol, 100 eq.) in acetonitrile (15 mL) was prepared and sparged by passing through a stream of nitrogen for 20 min. Excess of norbornene was employed in order to have DIO' directly react and thus keep its concentration at a minimum. If DIO' was not directly trapped by norbornene the results would be invalid, since DIO' competes with DIO for absorption of the photons, leading to partial deactivation of DIO. Each laser vial contained 150 µL of the stock solution and the headspace of the vial was purged with nitrogen for 3 minutes before irradiation. After irradiation, the solvent and norbornene were evaporated under reduced pressure at ambient temperature. Then the sample was redissolved in 450 µL of a 0.5 mM stock solution of 1,3,5-trimethoxybenzene (TMB, internal standard) in acetonitrile and analyzed via LC-MS. The reaction yield *Y* was obtained with the following formula

$$Y = \frac{I_{DIOnor}/I_{TMB}}{I_{DIOnor,max}/I_{TMB,max}}$$

Where I_{DIOnor} and I_{TMB} are the integrals of the DIOnor and TMB signals respectively, while $I_{DIOnor,max}$ and $I_{TMB,max}$ are the integrals at full conversion of DIO to DIOnor. All integrals were calculated from the UV-detector LC traces at 235 nm.

Initially, a kinetic study of the photoreaction at 365 nm was performed (**Figure S5**) in order to estimate the number of photons needed to keep the yield in the linear regime below 30%. With an exponential fit, the number of photons needed for 25% conversion was calculated to be approximately 2.08×10^{17} (345 nmol).

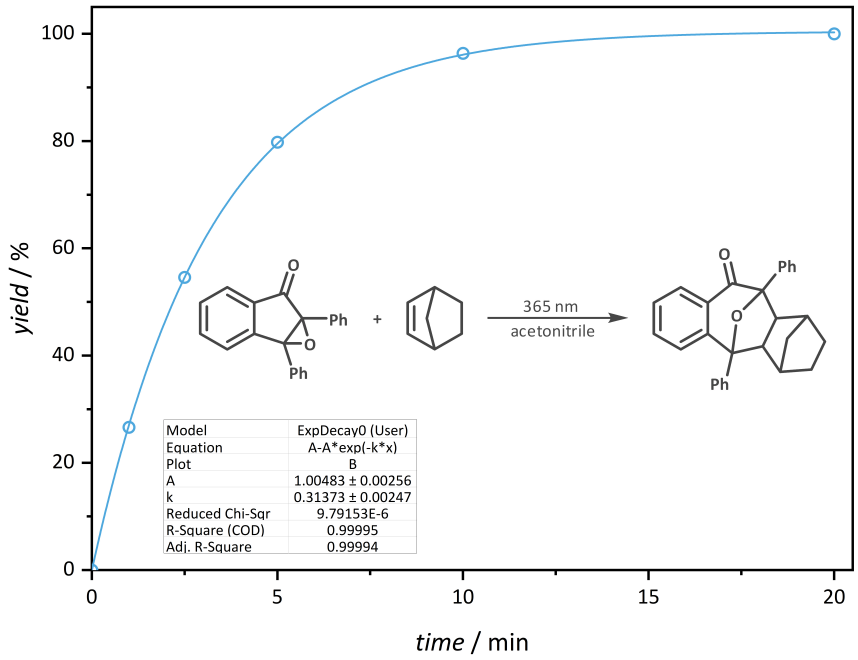

Figure S5. Kinetic study of the photoreaction of DIO with norbornene to DIOnor. An exponential fit was added to determine the number of photons needed for a specific yield.

For the photochemical action plot, all irradiation experiments were carried out for 2 minutes and the power was adjusted using a polarizer to achieve the same number of photons at each wavelength. Negative and positive error bars were obtained by taking triplicate measurements for each wavelength and represent the highest and lowest yield measured.

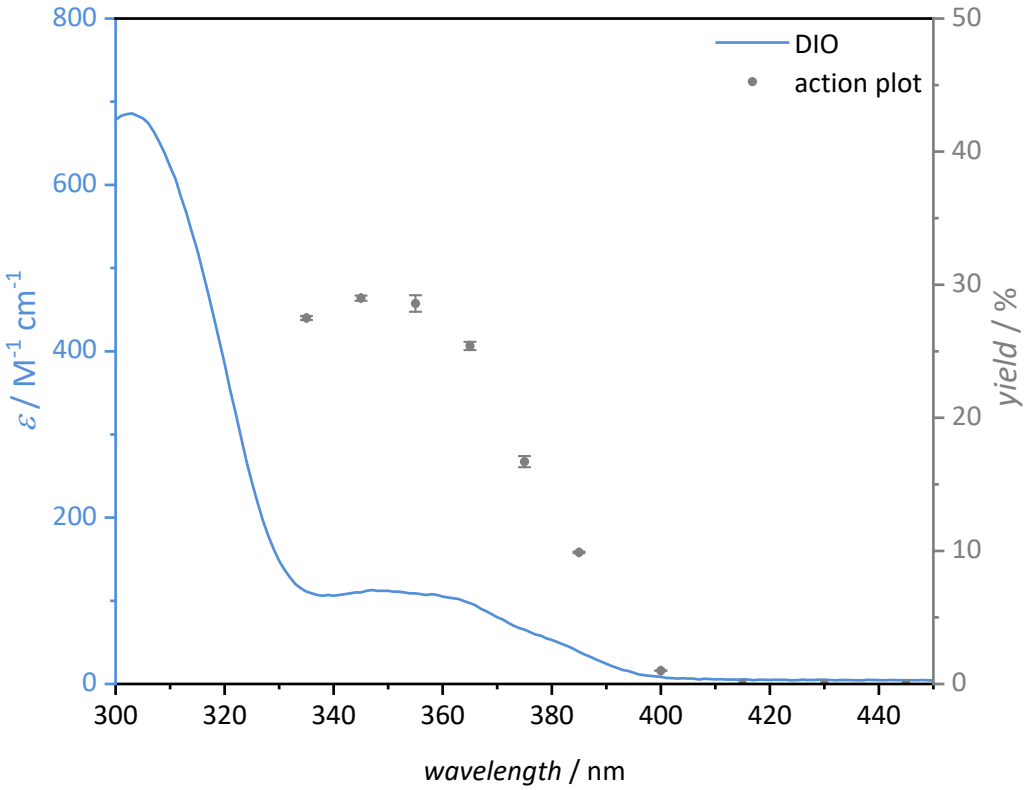

Figure S6. Absorbance spectrum and action plot of DIO. The action plot was obtained by tracking the wavelength-dependent product formation of a reaction between DIO and norbornene.

6.2.12.2 UV-Vis Action plot of SA

Due to the short lifetime of the activated photoswitch SA',[33] only real-time monitoring of the switching during irradiation allows for measuring an action plot of SA. The on-line tracking of absorbance spectra during irradiation was conducted using an in-situ UV-Vis spectrometer depicted in **Figure S7**. An *Analytical Instrument Systems* DT 1000 CE UV-Vis Light Source was coupled via optic fibers (P400-025-SR) to an *Ocean Optics* FLAME-T-UV-VIS spectrometer, sensitive from 200 to 850 nm, via a cuvette holder. A custom designed cuvette holder enabled laser irradiation into the bottom of the cuvette, while simultaneously measuring absorbance through the side of the cuvette. An *Opolette* HE 355 LD tunable OPO, emitting 5 ns pulses from 210-2400 nm at a repetition rate of 20 Hz, was directed upwards into the bottom of a quartz fluorescence (*Hellma Analytics* quartz high precision cell). The laser energy deposited into the sample was measured above the sample holder before and after experiments using a *Coherent* EnergyMax thermopile sensor (J-25MB-LE) to account for any power fluctuations during irradiation.

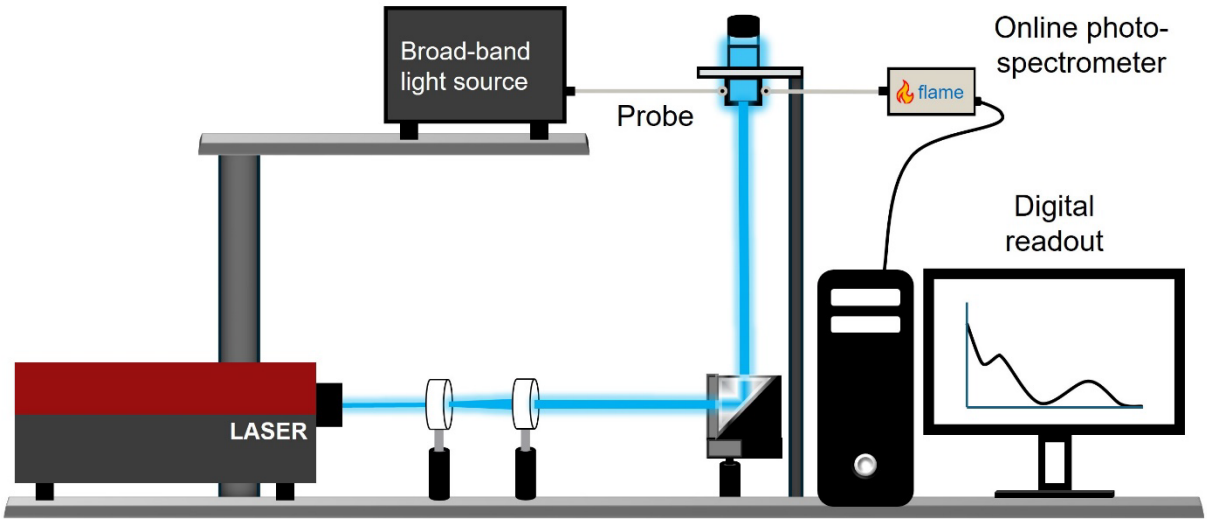

Figure S7. Schematic diagram of experimental apparatus for the photophysical studies. The tunable OPO output is passed through beam expansion optics before being incident on the bottom of a quartz fluorescence cuvette. Perpendicular, fiber-coupled white light is passed through the cuvette, and the absorbance spectrum is captured on a fiber coupled spectrometer.

For every action plot datapoint, first a spectrum of the sample (0.5 mM SA in acetonitrile) was measured as a blank. Subsequently, the sum of absorbances (280-295 nm) was recorded every 500 ms (50 ms integration time, 10 scan average) while the laser was off for 20 s, then on for 20 s (repeated 5 times) ending with another off period for 20 s. An example of the measurement at 430 nm is shown in **Figure S8**. By calculating the differences in absorbance with and without laser irradiation, the qualitative wavelength-dependent degree of switching was obtained for the action plot of SA. In order to avoid any errors from unprecise timing of switching the irradiation on and off, 1 s before and after

every switch were not included in the calculations. All data processing was performed in Matlab®. The standard deviations of the data points were calculated at all wavelengths and are shown as error bars in the action plot.

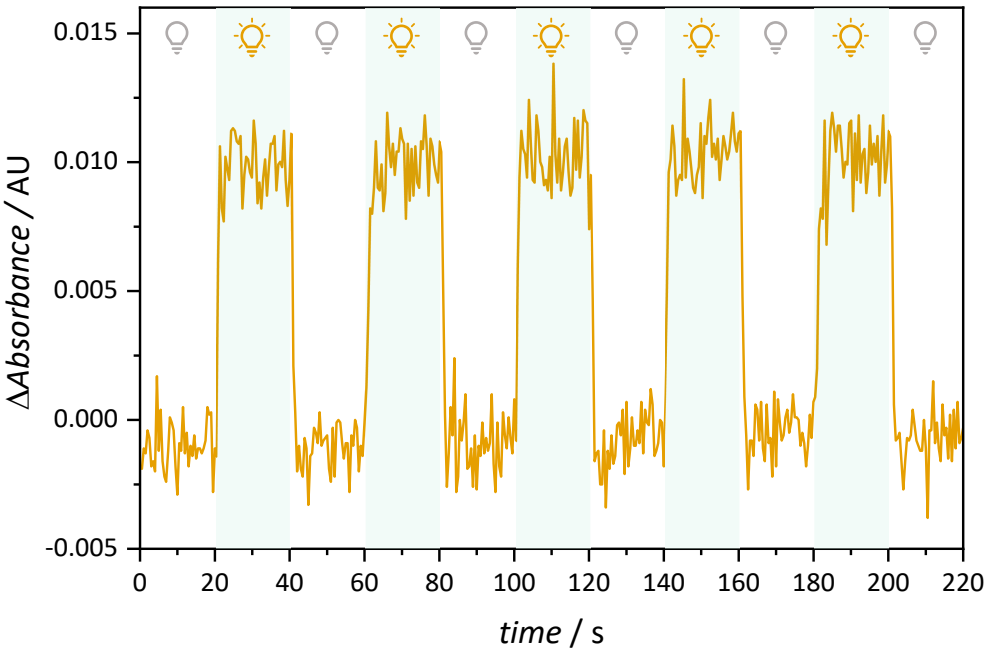

Figure S8. UV-Vis measurement for the SA action plot data point at 430 nm. A white background represents an "irradiation off" phase, while a light green background represents an "irradiation on" phase.

6.2.13 Two-color photoreactions using LED lamps

6.2.13.1 Small-molecule study – Sample preparation and reaction setup

A 5 mM stock solution of DIO, SA and TMB in HPLC grade acetonitrile (20 mL) was prepared, purged by bubbling with argon and freeze-pump-thawed to remove any leftover oxygen in the solution. Subsequently, the solution was placed into a glovebox to prepare the samples under argon atmosphere. For each sample, a stirring bar and 250 µL of the stock solution, containing DIO (373 µg, 1.25 nmol, 1.00 eq.), SA (265 µg, 1.25 nmol, 1.00 eq.) and TMB (105 µg, 0.625 nmol, 0.50 eq.) were added into a 2 mL crimp vial by *LabCo Scientific* (Clear Glass Vial, 12x32 mm, Flat Bottom, Product Number: 355.100.100). Stock solutions for non-equimolar educt ratios were prepared by keeping the concentration of the less abundant photoswitch at 5 mM and increasing the equivalents of the other one. TMB concentrations were identical, i.e. 2.5 mM, for all stock solutions. The educt ratios of DIO to SA were confirmed via ^{1}H NMR spectroscopy (see **Section 7.3**). The vial was crimped with a magnetic cap to facilitate attachment to the custom-made LED holder shown in **Figure 28** and irradiated with 365 nm (1.31 W cm^{-2}, 2.41 × 10^{18} s^{-1} cm^{-2}) and 430 nm (1.19 W cm^{-2}, 2.58 × 10^{16} s^{-1} cm^{-2}) while stirring at 500 rpm. Both heat sinks were fixed on opposing sides with a distance of 35 mm to the center of the reaction vial. Different irradiances at 365 nm were realized by pulsing the LED on the millisecond

timescale (i.e. a 10 ms LED pulse and varying times between pulses), thus achieving precise control over low irradiances.

6.2.13.2 Small-molecule study – Evaluation of the two-color reactions

After the photoreaction, 50 µL of the sample were diluted with 950 µL acetonitrile and passed through a syringe filter (0.2 µm, PTFE) into an LC-MS vial. In the LC traces for an absorbance at 235 nm, the peak integrals of TMB, SA and DIOSA were calculated. The yield of a reaction was determined according to the following formula

$$Y = \frac{I_{DIOSA}}{I_{DIOSA,max}}$$

where I_{DIOSA} is the integral of DIOSA, normalized by dividing by the integral of the internal standard TMB. $I_{DIOSA,max}$ is the normalized integral at full conversion of the educts and could theoretically be obtained by either performing a reaction to full conversion as a reference, or by tracking the educt conversions in relation to I_{DIOSA}. Due to the fact that side reactions occur to DIO under irradiation (see **Figure 33**), performing a reaction to full conversion or tracking the DIO conversion is not applicable. Furthermore, tracing the conversion of SA is very prone to errors at low conversions (<10%) since even small shifts of the integration borders have a significant influence on the resulting calculated yield. Tracking the integral of DIOSA instead gives much more consistent results, even at low conversions. Therefore, the normalized integral of DIOSA was plotted against the conversion of SA in each measurement. Consequently, $I_{DIOSA,max}$ was predicted via linear regression (refer to **Section 7.1**).

To determine the synergistic efficiencies for the different reaction conditions, reaction kinetics for a one- and two-color reaction were measured for each set of conditions. Since oxygen contamination severely impacts the degradation of DIO, instead of taking multiple samples from a single reaction vial after different irradiation times, one reaction was performed per data point. The yield as a function of time $Y_1(t)$ for each kinetic was obtained by introducing an exponential fit and the synergistic ratio $\Phi(t)_{\mathrm{syn}}$ was calculated according to the following relation

$$\phi_{syn}(t) = \frac{Y_2(t)}{Y_1(t)} = \frac{A_2 - A_2 e^{-k_2 t}}{A_1 - A_1 e^{-k_1 t}}$$

where $Y_1(t)$ and $Y_2(t)$ are exponential fit functions with parameters A and k for the kinetics of the 365 nm one- and the two-color reactions, respectively. All fit functions with 95% confidence bands for kinetic measurements were calculated with Origin® and can be found in **Section 7.2**. The upper $Y_{upper}(t)$ and lower $Y_{lower}(t)$ 95% confidence bands represent the error ΔY which is identical for both bands and is given by the following formula

$$\Delta Y = Y(t) - Y_{lower}(t) = -(Y(t) - Y_{upper}(t))$$

The error $\Delta\phi_{syn}(t)$ was calculated for every data point according to the following formula

$$\Delta\phi_{syn}(t) = \phi_{syn}(t) \cdot \sqrt{\frac{\Delta Y_1(t)}{Y_1(t)} + \frac{\Delta Y_2(t)}{Y_2(t)}}$$

The conversion-independent synergistic ratio ϕ_{syn}^0 cannot be obtained exactly at the start of the reaction, i.e. at $t = 0$ since

$$Y_1(0) = Y_2(0) = 0$$

and consequently $\phi_{syn}(0)$ cannot be calculated. Therefore, ϕ_{syn}^0 was obtained as $\phi_{syn}(0.001\ min)$ with the respective relative error $\Delta\phi_{syn,rel}(0.001\ min)$.

6.2.13.3 Macromolecular study – Sample preparation and reaction setup

The reaction setup and sample preparation for the two-color test reactions were identical to the set-up employed for the small-molecule study in **Section 6.2.13.1**.[31]

Stock solutions of the DIO/DIO-OH and SA/SA-OH combinations with 1,3,5-trimethoxybenzene (TMB) as an internal standard were prepared in 2 mL crimp vials by *LabCo Scientific* (Clear Glass Vial, 12x32 mm, Flat Bottom, Product Number: 355.100.100) under nitrogen atmosphere. The vial was crimped with a magnetic cap to facilitate attachment to the custom-made LED holder shown in **Figure S9** and irradiated with 365 nm (1.69 mW cm^{-2}, 3.10 × 10^{15} photons s^{-1} cm^{-2}) and 430 nm (27.9 mW cm^{-2}, 6.04 × 10^{16} photons s^{-1} cm^{-2}) while stirring at 500 rpm. Both heat sinks were fixed on opposing sides with a distance of 35 mm to the center of the reaction vial. Different irradiances at 365 nm were realized by pulsing the LED on the millisecond timescale (i.e., a 10 ms LED pulse and varying times between pulses), thus achieving precise control over low irradiances. All reactions were performed under one-color irradiation with 365 nm only and under two-color irradiation with 365 + 430 nm for comparison of the synergistic efficiencies.

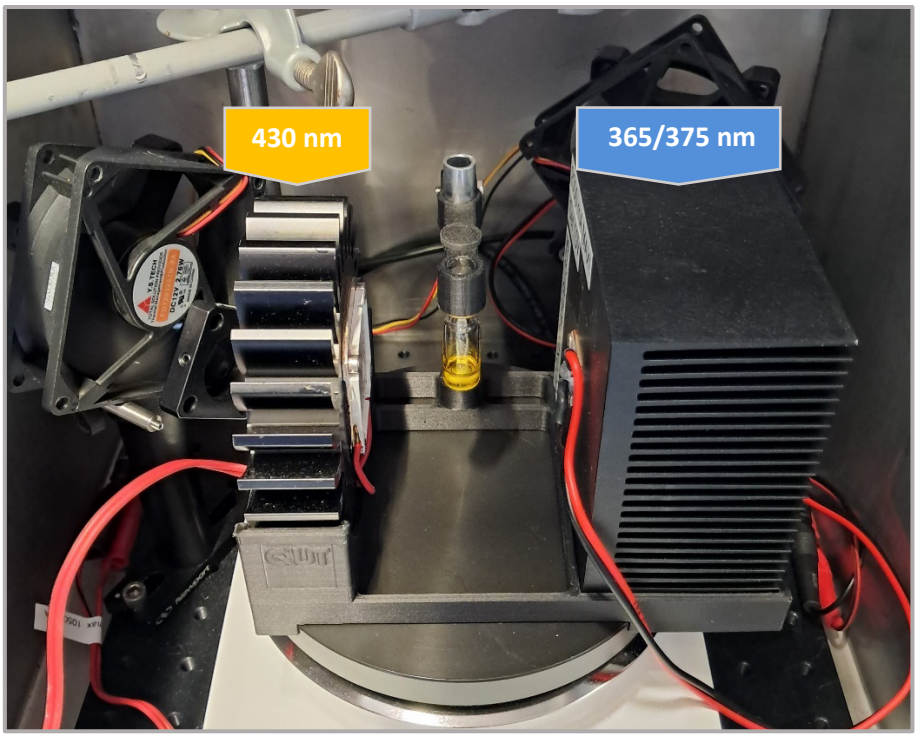

Figure S9. Representative setup for the photoreactions consisting of a magnetic stirrer, two LED light sources (365/375 and 430 nm) in a custom-made LED holder and fans for cooling.

After the photoreactions, 50 µL of the sample were diluted with 950 µL acetonitrile and passed through a syringe filter (0.2 µm, PTFE) into an LC-MS vial. In the LC traces for an absorbance at 235 nm, the peak integrals of TMB, SA and DIOSA were calculated. The yield Y of a reaction was determined according to the following formula

$$Y = 1 - \frac{I_{SA}}{I_{SA,0}}$$

where $I_{SA,0}$ is the integral of the SA compound at the beginning of the reaction, normalized by dividing by the integral of the internal standard TMB. I_{SA} is the normalized integral of the SA compound at the end of the reaction. Due to the fact that side reactions occur to DIO under irradiation,[31] tracking the DIO conversion to calculate the reaction yield is not applicable.

The synergistic ratio ϕ_{syn} was calculated via the following formula

$$\phi_{syn} = \frac{Y_2}{Y_1}$$

where Y_1 is the reaction yield of a one-color reaction, and Y_2 is the yield of the corresponding two-color reaction.

6.2.13.4 Macromolecular study – Sample preparation for Network Formation

For the SEC tracked crosslinking of polyDIO (184 mg, 100 µmol, 1.00 eq) and SA-3arm (51.1 mg, 100 µmol, 1.00 eq.), a stock solution in 2.1 mL acetophenone (90 wt%, 47.5 mM) was prepared and purged by bubbling with nitrogen (amount of substance, equivalents and concentration are given in regard to the photoswitching moieties). For each sample, a stir bar and 400 µL of the stock solution were added into a 2 mL crimp vial by *LabCo Scientific* (Clear Glass Vial, 12x32 mm, Flat Bottom, Product Number: 355.100.100) under nitrogen atmosphere. The vial was crimped with a magnetic cap and irradiated in the same reaction setup that was used for the small-molecule test reactions (**SI Section 6.2.13.3**). Photon fluxes of 1.55×10^{16} s^{-1} cm^{-2} for 365 and 375 nm and 6.04×10^{16} s^{-1} cm^{-2} for 430 nm were employed. Samples were taken every 30 minutes for 180 minutes and measured via SEC to investigate the qualitative differences in the increase of M_n during irradiation between one- (365/375 nm) and two-color (365/375 + 430 nm) reactions (**Figure S10** and **Figure S11**).

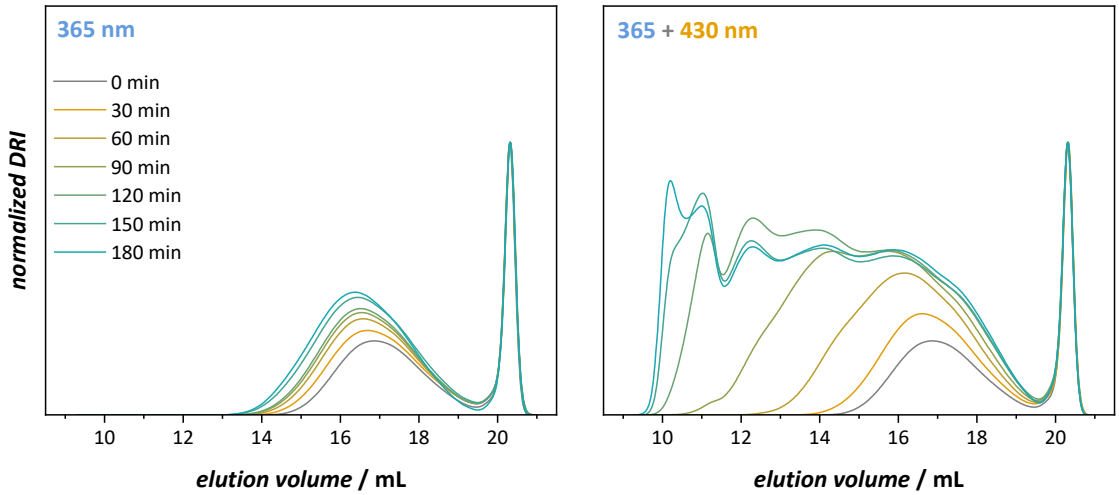

Figure S10. Evolution of SEC traces for the photoresist composed of polyDIO and SA-3arm in acetophenone under one-color (365 nm, left) and two-color (365 + 430 nm, right) irradiation over 180 minutes. Samples were taken every 30 minutes to monitor the progression of the crosslinking reaction.

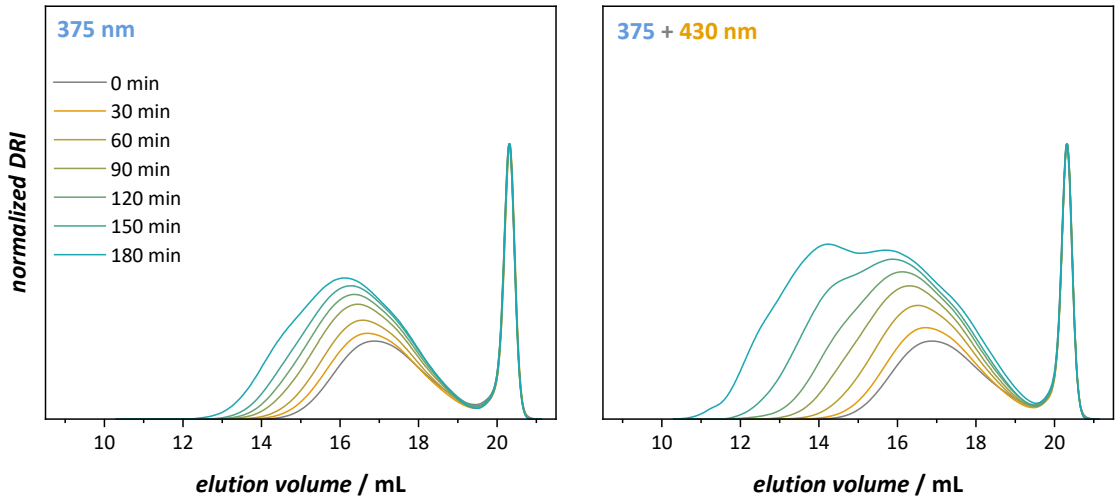

Figure S11. Evolution of SEC traces for the photoresist composed of polyDIO and SA-3arm in acetophenone under one-color (375 nm, left) and two-color (375 + 430 nm, right) irradiation over 180 minutes. Samples were taken every 30 minutes to monitor the progression of the crosslinking reaction.

6.3 Synthesis

6.3.1 Small-molecule study

2,3-Diphenyl-1*H*-inden-1-one (preDIO)

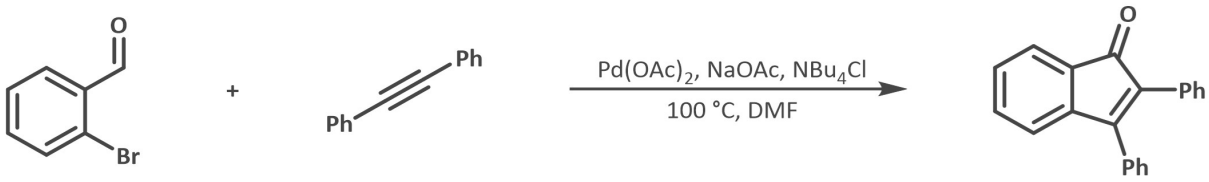

The synthesis procedure was adapted from Xie *et al*.[33]

2-Bromobenzaldehyde (946 µL, 1.50 g, 8.11 mmol, 1.00 eq.), diphenylacetylene (2.17 g, 12.2 mmol, 1.50 eq.), sodium acetate (NaOAc, 2.66 g, 32.4 mmol, 4.00 eq.), tetrabutylammonium chloride (NBu_4Cl, 2.25 g, 8.11 mmol, 1.00 eq.) and palladium(II) acetate ($Pd(OAc)_2$, 91.0 mg, 0.41 mmol, 0.05 eq.) were suspended in dry dimethylformamide (DMF) (50 mL) and purged with inert gas (i.e., nitrogen) for 15 minutes. The reaction mixture was heated to 100 °C under continuous stirring for 48 h, subsequently water (100 mL) was added after cooling to ambient temperature in order to quench the reaction. The aqueous phase was extracted with ethyl acetate (EA) (2 × 50 mL), washed with saturated $NH_4Cl_{(aq.)}$ (3 × 100 mL) and dried over Na_2SO_4. After removal of the organic solvent, the crude product was purified via flash column chromatography (cyclohexane 95:5 EA, *v/v*). The product was obtained as a red crystalline solid (1.40 g, 61%).

^{1}H NMR (400 MHz, $CDCl_3$): δ (ppm) = 7.60 – 7.56 (m, 1H), 7.42 – 7.33 (m, 6H), 7.30 – 7.22 (m, 6H), 7.14 (m, *J* = 7.3 Hz, 1H).

MS (*m/z*): calculated for $[C_{21}H_{14}O+H]^+$: 283.1123, found 283.1116.

1a,6a-Diphenyl-1a,6a-dihydro-6*H*-indeno[1,2-*b*]oxiren-6-one (DIO)

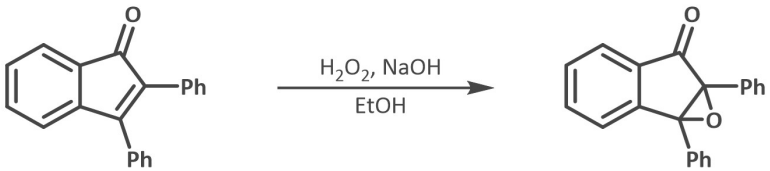

The synthesis procedure was adapted from Xie *et al*.[33]

2,3-Diphenyl-1-indenone (1.00 g, 3.54 mmol, 1.00 eq.) was dissolved in a small amount of dichloromethane (DCM) and added to ethanol (EtOH) (300 mL) under stirring. Then, 30% $H_2O_{2(aq.)}$ (5 mL) was added to the reaction mixture, followed by dropwise addition of 4 M $NaOH_{(aq.)}$ (10 mL). The reaction mixture was stirred at ambient temperature for 2 hours. Over the reaction time, the orange solution turned colorless due to the oxidation and a white solid precipitated (NaOH). Subsequently,

water was added which first dissolved the white solid and precipitated another white solid upon further addition. The suspension was left standing in the dark for sedimentation, followed by filtration and washing with water and then ice-cold ethanol. After removal of the solvent under vacuum the product was obtained as a white solid (873 mg, 83%) and used without further purification.

^{1}H NMR (400 MHz, MeCN-d_3): δ (ppm) = 7.88 (dt, *J* = 7.4, 1.0 Hz, 1H), 7.68 (td, *J* = 7.5, 1.3 Hz, 1H), 7.61 (td, *J* = 7.5, 1.1 Hz, 1H), 7.49 – 7.43 (m, 2H), 7.40 (dt, *J* = 7.5, 0.9 Hz, 1H), 7.39 – 7.33 (m, 5H), 7.33 – 7.28 (m, 3H).

^{13}C NMR (101 MHz, MeCN-d_3): δ (ppm) = 197.3, 149.9, 135.9, 135.8, 131.1, 130.8, 129.8, 129.6, 129.5, 129.3, 129.0, 129.0, 128.8, 126.3, 126.0, 73.4, 72.5.

MS (*m/z*): calculated for $[C_{21}H_{14}O_2+H]^+$: 299.1072, found 299.1063.

Bis(2-nitrophenyl)sulfane (preSA)

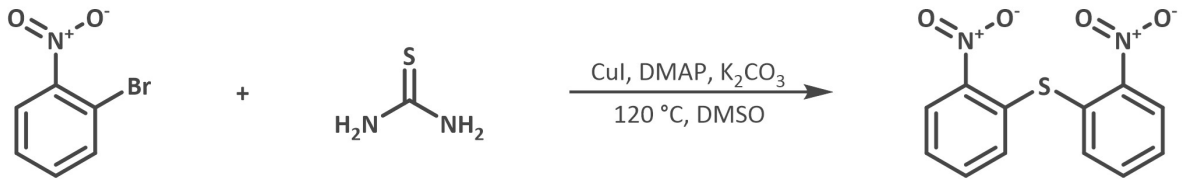

The synthesis procedure was adapted from Roy *et al*.[205]

1-Bromo-2-nitrobenzene (2.00 g, 9.90 mmol, 1.00 eq.) and thiourea (452 mg, 5.94 mmol, 0.60 eq.) were dissolved in dry dimethyl sulfoxide (DMSO) (10 mL) under argon atmosphere. Then, copper(I) iodide (CuI, 94.2 mg, 0.50 mmol, 0.05 eq.), 4-dimethylaminopyridine (DMAP, 241 mg, 2.00 mmol, 0.20 eq.) and K_2CO_3 (1.37 g, 9.90 mmol, 1.00 eq.) were added, and the reaction mixture was heated at 120 °C for 20 hours under argon atmospheres (balloon). After cooling to ambient temperature, water (100 mL) was added to quench the reaction, and the solution was extracted with DCM (2 × 100 mL). Subsequently, the combined organic phases were washed with water (2 × 200 mL) and dried over Na_2SO_4. After removal of the solvent, the crude product was purified via flash column chromatography (cyclohexane 90:10 EA, *v/v*). The product was obtained as a yellow solid (915 mg, 67%).

^{1}H NMR (400 MHz, $CDCl_3$): δ (ppm) = 8.12 (dd, *J* = 7.9, 1.6 Hz, 2H), 7.57 – 7.44 (m, 4H), 7.29 (dd, *J* = 7.8, 1.5 Hz, 2H).

MS (*m/z*): calculated for $[C_{12}H_8N_2O_4S+NH_4]^+$: 294.0549, found 294.0548.

Dibenzo[*b,f*][1,4,5]thiadiazepine (SA)

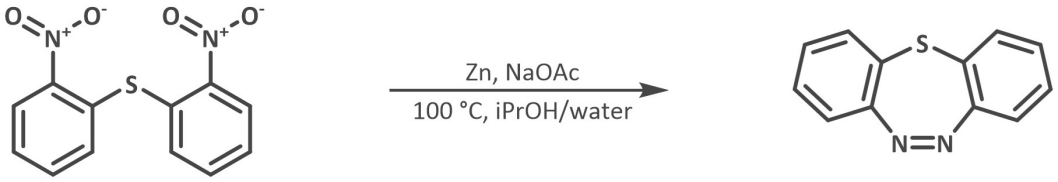

Bis(2-nitrophenyl)sulfane (1.01 g, 3.65 mmol, 1.00 eq.), zinc powder (Zn, 1.20 g, 18.2 mmol, 5.00 eq.) and sodium acetate (NaOAc, 1.50 g, 18.2 mmol, 5.00 eq.) were suspended in a mixture of isopropanol (^{i}PrOH) (100 mL) and water (50 mL) and the mixture was refluxed for 2 h. Over this time period, the color of the solution changed from yellow to purple to white. Vigorous stirring was continued at ambient temperature and atmosphere for 12 hours to promote oxidation with ambient oxygen of the reaction intermediate to the desired product. During this process, the color changed from white to yellow-brown. Subsequently, the solvent was removed, the crude mixture was dissolved in DCM and the solution filtrated to remove the residual zinc and sodium acetate. Upon the removal of the solvent, the product was purified via flash column chromatography (cyclohexane 95:5 EA, *v/v*) to yield an impure product. To fully remove all impurities, the contaminated product was dissolved in chloroform (10 mL) and irradiated at 365 nm for 10 minutes, which led to a darkening of the previously yellow solution. The solvent was removed, and the mixture was redissolved in a small amount of DCM and flushed over a short plug of silica with DCM. The pure product was obtained as a yellow solid (98.0 mg, 13%).

^{1}H NMR (400 MHz, $CDCl_3$): δ (ppm) = 7.61 (dd, *J* = 7.9, 1.1 Hz, 2H), 7.44 (td, *J* = 7.8, 1.4 Hz, 2H), 7.34 (dd, *J* = 7.8, 1.3 Hz, 2H), 7.27 (td, *J* = 7.7, 1.3 Hz, 2H).

^{13}C NMR (101 MHz, $CDCl_3$): δ (ppm) = 152.0, 131.9, 131.2, 129.8, 129.3, 127.7.

MS (*m/z*): calculated for $[C_{12}H_8N_2S+H]^+$: 213.0486, found 213.0480.

5,10-diphenyl-5,5a,6,7,8,9,9a,10-octahydro-11*H*-5,10-epoxy-6,9-methanodibenzo[*a,d*][7]annulen-11-one (DIOnor)

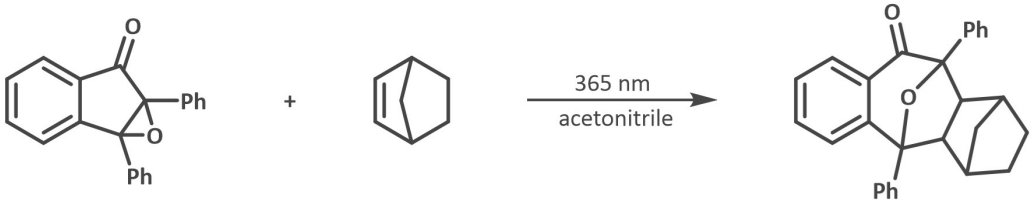

DIO (100 mg, 335 µmol, 1.00 eq.) and norbornene (94.6 mg, 1.00 mmol, 3.00 eq.) were dissolved in HPLC grade acetonitrile (10 mL) and purged by bubbling with nitrogen for 15 minutes. The mixture was stirred and irradiated with an LED at 365 nm (0.11 W cm^{-2}) for 4 hours until DIO was fully consumed

(*Note to the reader*: no pink color of the switched DIO was observed anymore). During the reaction, the product started to precipitate as a white snowy solid and afterwards the mixture was placed in the freezer overnight to increase the amount of the precipitate. The solid was isolated by decantation, washed with a small amount of acetonitrile, and subsequently dried under vacuum at 40 °C. An additional amount of product was obtained from the mother liquor. The product was obtained as a combination of the white solids (97.8 mg, 74%).

^{1}H NMR (400 MHz, $CDCl_3$): δ (ppm) = 8.11 (dd, *J* = 7.6, 1.6 Hz, 1H), 7.77 – 7.71 (m, 4H), 7.54 (t, *J* = 7.7 Hz, 2H), 7.49 – 7.31 (m, 6H), 7.19 (dd, *J* = 7.8, 1.3 Hz, 1H), 2.66 (dd, *J* = 7.2, 1.5 Hz, 1H), 2.58 – 2.51 (m, 1H), 2.39 – 2.32 (m, 1H), 2.12 – 2.06 (m, 1H), 1.44 (dt, *J* = 10.0, 2.0 Hz, 1H), 1.41 – 1.29 (m, 2H), 1.19 – 1.03 (m, 2H), 0.50 (dt, *J* = 10.0, 1.5 Hz, 1H).

^{13}C NMR (101 MHz, $CDCl_3$): δ (ppm) = 194.1, 150.3, 139.4, 135.9, 133.6, 128.9, 128.5, 128.1, 128.1, 127.9, 127.7, 127.5, 127.4, 127.3, 124.0, 91.6, 88.1, 59.1, 53.8, 39.1, 39.1, 33.1, 29.1, 28.2.

MS (*m/z*): calculated for $[C_{28}H_{24}O_2+H]^+$: 393.1855, found 393.1843.

5,17-Diphenyl-5*H*-5,17-epoxydibenzo[*b,f*]benzo[4,5][1,2]diazepino[1,2-*d*][1,4,5]thiadiazepin-18(17*H*)-one (DIOSA)

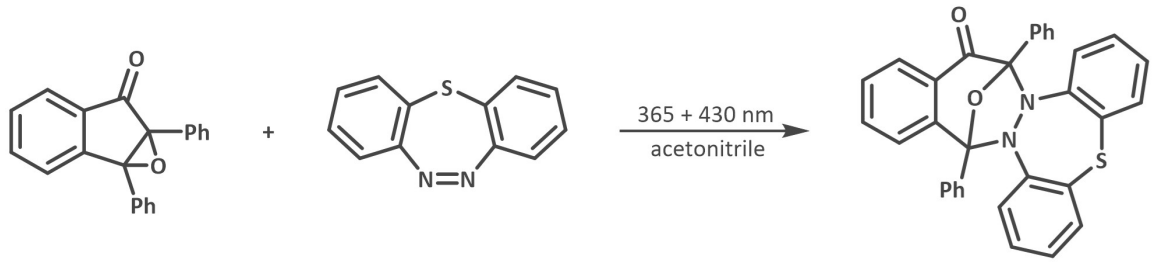

DIO (140 mg, 470 µmol, 1.00 eq.) and **SA** (100 mg, 470 µmol, 1.00 eq.) were dissolved in HPLC grade acetonitrile (10 mL) and purged by bubbling with nitrogen for 15 minutes. The mixture was stirred and irradiated with two LEDs at 365 nm (1.01 W cm^{-2}) and 430 nm (2.96 W cm^{-2}), respectively, for 2.5 hours until DIO was fully consumed (no pink color of the switched DIO was observed anymore). During the reaction, the product started to precipitate as a yellow solid and afterwards the mixture was placed in the freezer overnight to increase the amount of precipitate. The solid was isolated by decantation and washed with a small amount of acetonitrile. Subsequently, the solid was dissolved in a mixture of acetonitrile and DCM and crystallized during slow evaporation of the solvent under ambient conditions. After washing with a small amount of acetonitrile and then drying under vacuum the product was obtained as yellow crystals (170.2 mg, 71%).

^{1}H NMR (400 MHz, $CDCl_3$): δ (ppm) = 8.03 (dd, *J* = 7.6, 1.4 Hz, 1H), 7.71 (s, 1H), 7.60 (d, *J* = 7.5 Hz, 1H), 7.48 – 7.12 (m, 13H), 7.05 (t, *J* = 7.1 Hz, 1H), 6.79 (t, *J* = 7.5 Hz, 1H), 6.72 (td, *J* = 8.5, 7.9, 1.5 Hz, 1H), 6.65 – 6.53 (m, 2H), 6.23 (d, *J* = 8.3 Hz, 1H).

^{13}C NMR (101 MHz, $CDCl_3$): δ (ppm) = 191.5, 149.3, 143.5, 143.2, 135.7, 134.0, 133.0, 131.5, 131.4, 131.2, 129.7, 129.4, 129.2, 128.8, 128.3, 128.1, 127.4, 126.9, 126.8, 126.5, 119.8, 119.0, 113.5, 99.2, 96.7.

MS (*m/z*): calculated for $[C_{33}H_{22}N_2O_2S+H]^+$: 511.1480, found 511.1475.

6.3.2 Macromolecular Study

6.3.2.1 polyDIO

5-Hydroxy-2,3-diphenyl-1*H*-inden-1-one (1)

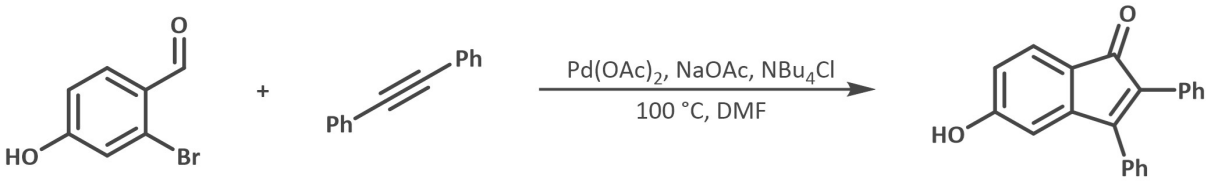

2-Bromo-4-hydroxy-benzaldehyde (4.00 g, 19.9 mmol, 1.00 eq.), diphenylacetylene (3.90 g, 21.9 mmol, 1.10 eq.), sodium acetate (NaOAc, 6.53 g, 79.6 mmol, 4.00 eq.), tetrabutylammonium chloride (NBu_4Cl, 5.53 g, 19.9 mmol, 1.00 eq.) and palladium(II) acetate ($Pd(OAc)_2$, 223 mg, 995 µmol, 0.05 eq.) were suspended in anhydrous dimethylformamide (DMF, 50 mL) and purged with nitrogen for 15 minutes. The reaction mixture was heated to 100 °C under continuous stirring for 48 h. Subsequently, water (100 mL) was added after cooling to ambient temperature in order to quench the reaction. The aqueous phase was extracted with ethyl acetate (EA, 2 × 200 mL), washed with saturated $NH_4Cl_{(aq.)}$ (200 mL), diluted $NaOH_{(aq.)}$ (3 × 200 mL) and diluted $HCl_{(aq.)}$ (200 mL), and dried over Na_2SO_4. After removal of the organic solvent, the crude product was purified via flash column chromatography (cyclohexane 70:30 EA, *v/v*). The product was obtained as a dark red crystalline solid (1.92 g, 32%).

^{1}H NMR (400 MHz, DMSO-d_6): δ (ppm) = 10.50 (s, 1H), 7.50 – 7.43 (m, 3H), 7.41 (d, *J* = 7.9 Hz, 1H), 7.38 – 7.33 (m, 2H), 7.31 – 7.23 (m, 3H), 7.21 – 7.14 (m, 2H), 6.64 (dd, *J* = 7.9, 2.0 Hz, 1H), 6.56 (d, *J* = 2.0 Hz, 1H).

^{13}C NMR (101 MHz, DMSO-d_6): δ (ppm) = 194.2, 163.2, 152.8, 147.8, 132.9, 132.2, 130.8, 129.7, 129.3, 128.9, 128.3, 128.0, 127.7, 125.2, 120.7, 113.5, 110.5.

5-((6-Hydroxyhexyl)oxy)-2,3-diphenyl-1*H*-inden-1-one (2)

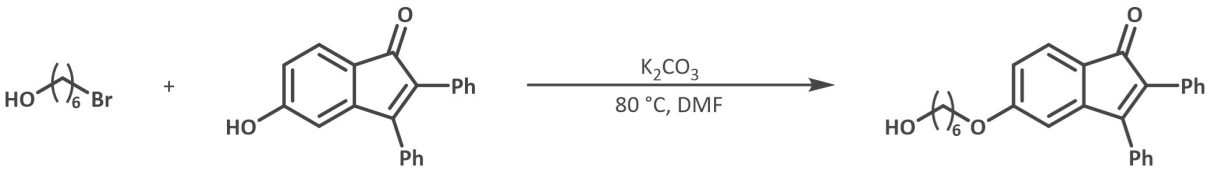

1 (1.92 g, 6.43 mmol, 1.00 eq.), 6-bromohexan-1-ol (2.33 g, 1.32 mL, 12.9 mmol, 2.00 eq.) and potassium carbonate (1.78 g, 12.9 mmol, 2.00 eq.) were dispersed in anhydrous dimethylformamide (DMF, 50 mL). The reaction mixture was stirred at 80 °C for 48 hours, then ethyl acetate (EA, 150 mL) was added. The organic phase was washed with brine (3 × 200 mL) and water (200 mL), and the solvent removed under reduced pressure. The product was purified via flash column chromatography (cyclohexane 50:50 EA, *v/v*) and obtained as an orange solid (1.75 g, 68%).

^{1}H NMR (400 MHz, DMSO-d_6): δ (ppm) = 7.50 (d, *J* = 8.0 Hz, 1H), 7.45 (dd, *J* = 5.0, 1.9 Hz, 3H), 7.40 – 7.33 (m, 2H), 7.31 – 7.24 (m, 3H), 7.20 – 7.14 (m, 2H), 6.82 (dd, *J* = 8.1, 2.1 Hz, 1H), 6.59 (d, *J* = 2.1 Hz, 1H), 4.35 (t, *J* = 5.2 Hz, 1H), 4.01 (t, *J* = 6.4 Hz, 2H), 3.38 (td, *J* = 6.4, 5.1 Hz, 2H), 1.69 (p, *J* = 6.7 Hz, 2H), 1.46 – 1.24 (m, 6H).

^{13}C NMR (101 MHz, DMSO-d_6): δ (ppm) = 194.1, 163.7, 153.0, 147.2, 133.2, 131.9, 130.6, 129.7, 129.4, 128.9, 128.3, 128.0, 127.8, 124.9, 122.2, 111.6, 110.4, 68.2, 60.6, 32.4, 28.5, 25.3, 25.2.

3-((6-Hydroxyhexyl)oxy)-1a,6a-diphenyl-1a,6a-dihydro-6*H*-indeno[1,2-*b*]oxiren-6-one (DIO-OH)

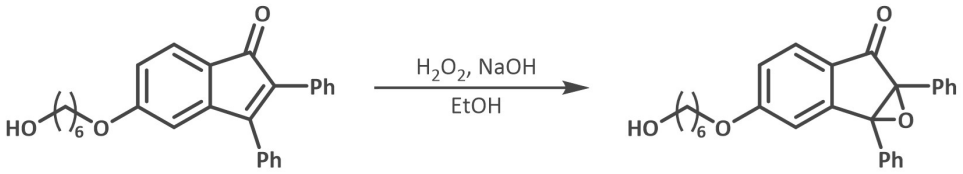

2 (1.75 g, 4.39 mmol, 1.00 eq.) was dissolved in a small amount of dichloromethane (DCM) and added to ethanol (200 mL) under stirring. Next, 30% $H_2O_{2(aq.)}$ (6.3 mL) was added, followed by dropwise addition of 4 M $NaOH_{(aq.)}$ 13.2 mL). The reaction mixture was stirred at ambient temperature for 1 hour. Over time, the orange solution turned colorless due to the oxidation and a white solid precipitated (NaOH). The solvent was removed under reduced pressure, and subsequently, water and ethyl acetate were added to the suspension until all solids were dissolved. The product was extracted with ethyl acetate (1 × 100 mL), washed with brine (2 × 200 mL), water (200 mL) and dried over Na_2SO_4. After removal of the solvent under reduced pressure, the product DIO-OH was obtained as a yellowish viscous liquid (1.67 g, 92%) and used without further purification.

^{1}H NMR (400 MHz, MeCN-d_3): δ (ppm) = 7.80 (d, *J* = 8.4 Hz, 1H), 7.49 – 7.40 (m, 2H), 7.37 – 7.25 (m, 8H), 7.05 (dd, *J* = 8.4, 2.3 Hz, 1H), 6.85 (d, *J* = 2.2 Hz, 1H), 4.01 (t, *J* = 6.6 Hz, 2H), 3.48 (td, *J* = 6.4, 5.2 Hz, 2H), 2.53 (t, *J* = 5.3 Hz, 1H), 1.73 (dt, *J* = 8.0, 6.5 Hz, 2H), 1.54 – 1.31 (m, 6H).

^{13}C NMR (101 MHz, MeCN-d_3): δ (ppm) = 195.7, 165.8, 152.7, 130.9, 129.8, 129.8, 129.5, 129.3, 129.0, 129.0, 128.8, 128.3, 128.1, 117.2, 112.3, 72.9, 72.9, 69.8, 62.5, 33.5, 29.6, 26.4, 26.3.

MS (*m/z*): calculated for $[C_{27}H_{16}O_4+H]^+$: 415.19, found 415.2.

3-((6-Hydroxyhexyl)oxy)-1a,6a-diphenyl-1a,6a-dihydro-6*H*-indeno[1,2-*b*]oxiren-6-one (3)

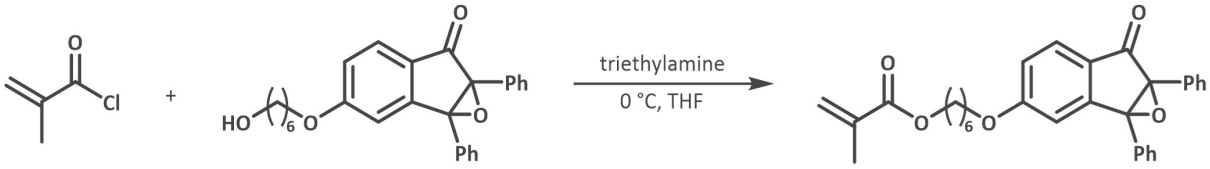

DIO-OH (809 mg, 1.95 mmol, 1.00 eq.) was dissolved in anhydrous tetrahydrofuran (THF, 20 mL) under nitrogen atmosphere and cooled to 0 °C with an ice bath. Triethylamine (988 mg, 1.36 mL, 9.76 mmol, 5.00 eq.) was added, followed by methacryloyl chloride (953 µL, 1.02 g, 9.76 mmol, 5.00 eq.) in a dropwise manner. The reaction mixture was stirred for 3 days. To quench the reaction, methanol (5 mL) was added and stirred for 5 minutes. The solvents were removed under reduced pressure and the crude product redissolved in ethyl acetate (EA) (100 mL). Subsequently, the organic phase was washed with saturated $NaHCO_{3(aq.)}$ (2 × 200 mL) and water (200 mL) and dried over Na_2SO_4. After removal of the organic solvent, the crude product was purified via flash column chromatography (cyclohexane 85:15 EA, *v/v*). The product was obtained as a yellowish viscous liquid (704 mg, 75%).

^{1}H NMR (400 MHz, MeCN-d_3): δ (ppm) = 7.80 (d, *J* = 8.4 Hz, 1H), 7.48 – 7.41 (m, 2H), 7.37 – 7.26 (m, 8H), 7.05 (dd, *J* = 8.5, 2.3 Hz, 1H), 6.85 (d, *J* = 2.2 Hz, 1H), 6.02 (dt, *J* = 1.8, 1.0 Hz, 1H), 5.57 (p, *J* = 1.6 Hz, 1H), 4.10 (t, *J* = 6.5 Hz, 2H), 4.03 (t, *J* = 6.5 Hz, 2H), 1.89 (t, *J* = 1.3 Hz, 3H), 1.80 – 1.71 (m, 2H), 1.70 – 1.61 (m, 2H), 1.52 – 1.35 (m, 4H).

^{13}C NMR (101 MHz, MeCN-d_3): δ (ppm) = 195.7, 168.0, 165.7, 152.7, 137.8, 131.0, 129.9, 129.8, 129.5, 129.3, 129.0, 129.0, 128.8, 128.3, 128.1, 125.6, 117.2, 112.3, 72.9, 79.7, 65.3, 29.5, 29.2, 26.3, 26.2, 26.2, 18.5.

MS (*m/z*): calculated for $[C_{31}H_{30}O_5+H]^+$: 483.22, found 483.3.

Poly(DIO-*co*-EHA) copolymer (polyDIO)

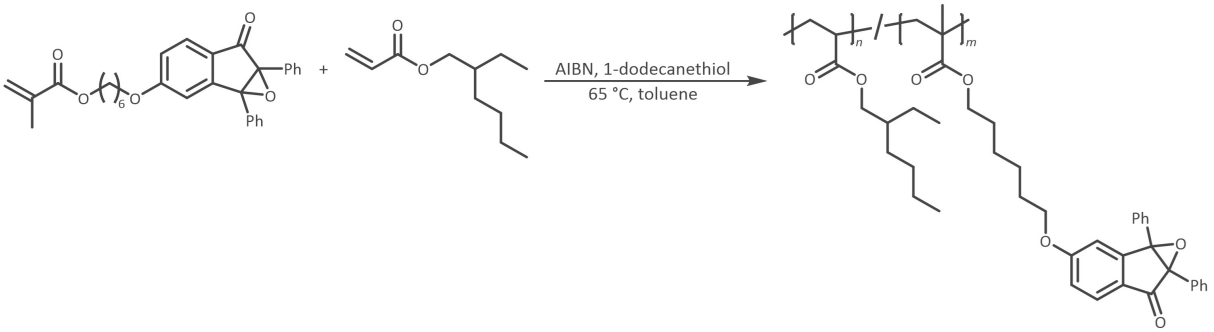

3 (1.61 g, 3.34 mmol, 1.00 eq.) and 2-ethylhexyl acrylate (EHA, 3.97 mL, 3.49 g, 18.9 mmol, 5.67 eq.) were prepared in a 25 mL round bottom flask under nitrogen atmosphere. Azobisisobutyronitrile (AIBN, 32.9 mg, 200 µmol, 0.06 eq.) and 1-dodecanethiol (54.1 mg, 64.0 µL, 267 µmol, 0.08 eq.) were

dissolved in toluene (15 mL) and added to the comonomers. Next, the solution was bubbled with a slow stream of nitrogen flow for 15 minutes, sealed and stirred at 65 °C for 4 hours. The solvent was removed under reduced pressure, and the polymer was isolated by adding 20 mL methanol and stirring for 10 minutes at 40 °C and decanting the solvent. This washing process was repeated 5 times to remove leftover residual small molecules. Subsequently, the residual solvent was removed under reduced pressure, and the product was obtained as a colorless, slightly turbid viscous liquid (4.54 g, 89%, M_n = 12 600 g mol^{-1}, $Đ$ = 1.72).

^{1}H NMR (400 MHz, $CDCl_3$): δ (ppm) = 7.83 (d, *J* = 5.9 Hz, 1H), 7.40 (d, *J* = 6.5 Hz, 2H), 7.33 – 7.21 (m, 8H), 6.96 (d, *J* = 8.3 Hz, 1H), 6.82 (s, 1H), 4.10 – 3.70 (m), 2.59 – 0.55 (m, aliphatic protons).

^{13}C NMR (101 MHz, $CDCl_3$): δ (ppm) = 194.9, 174.6, 164.7, 151.7, 130.1, 128.7, 128.6, 128.4, 128.4, 128.1, 128.1, 127.9, 127.8, 127.6, 115.7, 111.7, 72.0, 71.8, 68.7, 67.1, 64.8, 45.4, 41.7, 38.7, 35.6, 30.3, 29.8, 29.5, 29.0, 28.7, 25.8, 23.7, 23.1, 14.2, 10.9.

6.3.2.2 SA-3arm

6-(4-Bromo-3-nitrophenoxy)hexan-1-ol (4)

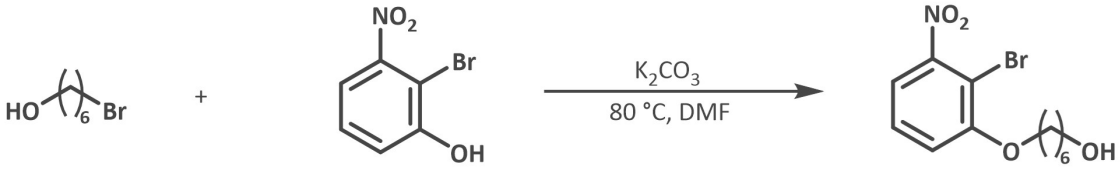

2-Bromo-3-nitro-phenol (9.83 g, 45.1 mmol, 1.00 eq.), 6-bromohexan-1-ol (8.85 mL, 12.2 g, 67.6 mmol, 1.50 eq.) and potassium carbonate (12.5 g, 90.2 mmol, 2.00 eq.) were dispersed in anhydrous dimethylformamide (DMF, 50 mL). The reaction mixture was stirred at 80 °C for 48 hours and then ethyl acetate (EA, 150 mL) was added. The organic phase was washed with brine (3 × 200 mL) and water (200 mL), and the solvent removed under reduced pressure. The product was obtained as a deep red-purple viscous liquid (12.7 g, 88%). The product was used in the next step without further purification.

^{1}H NMR (400 MHz, DMSO-d_6): δ (ppm) = 7.55 (t, *J* = 8.1 Hz, 1H), 7.49 (dd, *J* = 8.1, 1.5 Hz, 1H), 7.38 (dd, *J* = 8.2, 1.6 Hz, 1H), 4.35 (t, *J* = 5.2 Hz, 1H), 4.14 (t, *J* = 6.3 Hz, 2H), 3.39 (td, *J* = 6.4, 5.1 Hz, 2H), 1.75 (dt, *J* = 8.2, 6.4 Hz, 2H), 1.51 – 1.31 (m, 6H).

^{13}C NMR (101 MHz, DMSO-d_6): δ (ppm) = 156.1, 151.5, 129.7, 116.5, 116.0, 102.8, 69.6, 60.6, 32.5, 28.4, 25.3, 25.1.

6-(2-((2-Aminophenyl)thio)-3-nitrophenoxy)hexan-1-ol (5)

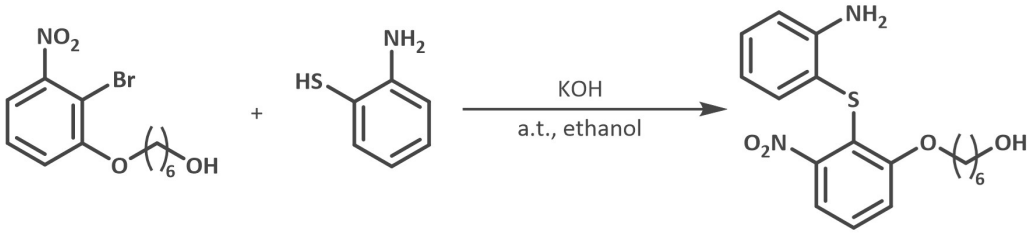

4 (12.7 g, 39.8 mmol, 1.00 eq.) was dissolved in ethanol (100 mL) and the solution was bubbled with nitrogen for 15 minutes. Next, potassium hydroxide (4.47 g, 79.6 mmol, 2.00 eq.) and 2-aminothiophenol (8.52 mL, 9.97 g, 79.6 mmol, 2.00 eq.) were added, and the reaction mixture was stirred for 20 hours at ambient temperature. The solvent was removed under reduced pressure, and the residuals redissolved in ethyl acetate (100 mL), washed with brine (2 × 300 mL) and water (300 mL) and dried over Na_2SO_4. After removal of the organic solvent, the crude product was purified via flash column chromatography (cyclohexane 40:60 EA, *v/v*). The product was obtained as a viscous orange oil that solidified to an orange-red waxlike solid (12.5 g, 84%).

^{1}H NMR (400 MHz, DMSO-d_6): δ (ppm) = 7.50 (t, *J* = 8.2 Hz, 1H), 7.43 (dd, *J* = 8.1, 1.2 Hz, 1H), 7.28 (dd, *J* = 8.3, 1.3 Hz, 1H), 7.03 – 6.92 (m, 2H), 6.67 (dd, *J* = 8.1, 1.4 Hz, 1H), 6.45 (td, *J* = 7.5, 1.4 Hz, 1H), 5.23 (s, 2H), 4.34 (t, *J* = 5.1 Hz, 1H), 3.93 (t, *J* = 6.4 Hz, 2H), 3.37 (td, *J* = 6.5, 5.1 Hz, 2H), 1.57 – 1.45 (m, 2H), 1.44 – 1.33 (m, 2H), 1.32 – 1.16 (m, 4H).

^{13}C NMR (101 MHz, DMSO-d_6): δ (ppm) = 158.9, 154.1, 148.7, 133.3, 130.4, 129.2, 116.6, 115.7, 115.1, 114.9, 114.8, 114.7, 69.2, 60.7, 32.4, 28.2, 25.2.

4-Bromo-3-nitrobenzoate 6-(dibenzo[*b*,*f*][1,4,5]thiadiazepin-1-yloxy)hexan-1-ol (SA-OH)

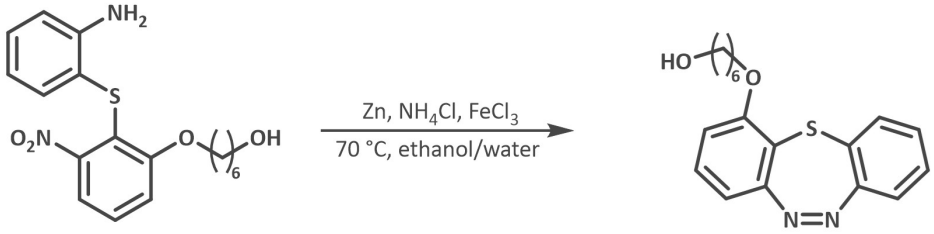

5 (2.50 g, 6.90 mmol, 1.00 eq.) was dissolved in ethanol (175 mL) and heated to 70 °C. Next, an aqueous 2 M ammonium chloride solution (31.6 mL) and zinc powder (1.71 g, 26.2 mmol, 3.80 eq.) were added, and stirred for 20 minutes at 70 °C. The reaction mixture was hot-filtered, and the filtrate directly poured into a solution of $FeCl_3 \cdot 6\ H_2O$ (3.73 g, 13.8 mmol, 2.00 eq.) in water (200 mL) and ice (200 g). While stirring for an additional 15 minutes, the color of the reaction mixture slowly turned black. Subsequently, acetic acid (100 mL) was added and stirring continued for 20 hours at ambient temperature. The acidic solution was neutralized with $NaHCO_3$ and NaOH, and then extracted with

ethyl acetate (EA, 2 × 200 mL), followed by washing with water/brine (3 × 400 mL). The organic phase was dried over Na_2SO_4 and the solvent removed under reduced pressure. The product was purified via flash column chromatography (cyclohexane 50:50 EA, *v/v*) and obtained as a yellow-brownish viscous liquid (681 mg, 30%).

^{1}H NMR (400 MHz, MeCN-d_3): δ (ppm) = 7.55 (dd, *J* = 7.9, 1.6 Hz, 1H), 7.50 (td, *J* = 7.9, 7.5, 1.5 Hz, 1H), 7.40 (d, *J* = 8.1 Hz, 2H), 7.34 – 7.28 (m, 1H), 7.08 (dd, *J* = 8.0, 1.2 Hz, 1H), 6.95 (dd, *J* = 8.2, 1.2 Hz, 1H), 4.03 (t, *J* = 6.4 Hz, 2H), 3.51 (td, *J* = 6.5, 5.4 Hz, 2H), 1.79 (dq, *J* = 8.3, 6.4 Hz, 2H), 1.58 – 1.46 (m, 4H), 1.46 – 1.37 (m, 2H).

^{13}C NMR (101 MHz, MeCN-d_3): δ (ppm) = 157.7, 153.7, 153.3, 133.2, 132.1, 130.9, 130.7, 127.7, 120.7, 119.0, 113.6, 70.5, 62.5, 33.6, 29.7, 26.6, 26.3.

MS (*m/z*): calculated for $[C_{18}H_{20}N_2O_2S+H]^+$: 329.13, found 329.2.

4-bromo-3-nitrobenzoate 6-(dibenzo[*b,f*][1,4,5]thiadiazepin-1-yloxy)hexyl acrylate (6)

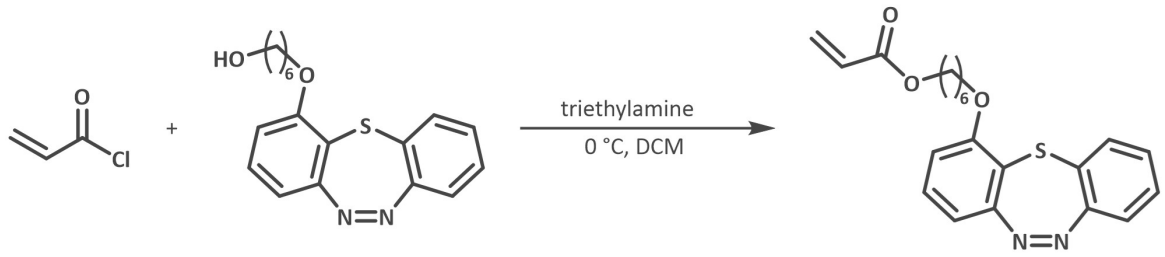

SA-OH (814 mg, 2.48 mmol, 1.00 eq.) was dissolved in DCM (70 mL) under nitrogen atmosphere and cooled to 0 °C with an ice bath. Triethylamine (1.04 mL, 752 mg, 7.44 mmol, 3.00 eq.) was added and lastly acryloyl chloride (604 µL, 673 mg, 7.44 mmol, 3.00 eq.) in a dropwise manner. The reaction mixture was stirred for 24 hours and washed with saturated $NaHCO_{3(aq.)}$ (2 × 100 mL) and water (100 mL) and dried over Na_2SO_4. After removal of the organic solvent, the crude product was purified via flash column chromatography (cyclohexane 70:30 EA, *v/v*). The product was obtained as a yellow-orange viscous liquid (402 mg, 42%).

^{1}H NMR (400 MHz, $CDCl_3$): δ (ppm) = 7.58 (dd, *J* = 7.9, 1.4 Hz, 1H), 7.43 (td, *J* = 7.6, 1.4 Hz, 1H), 7.36 – 7.29 (m, 2H), 7.27 – 7.21 (m, 1H), 7.14 (dd, *J* = 7.9, 1.2 Hz, 1H), 6.81 (dd, *J* = 8.2, 1.2 Hz, 1H), 6.40 (dd, *J* = 17.3, 1.5 Hz, 1H), 6.13 (dd, *J* = 17.3, 10.4 Hz, 1H), 5.82 (dd, *J* = 10.4, 1.5 Hz, 1H), 4.19 (t, *J* = 6.7 Hz, 2H), 4.00 (t, *J* = 6.3 Hz, 2H), 1.90 – 1.81 (m, 2H), 1.74 (p, *J* = 6.9 Hz, 2H), 1.64 – 1.43 (m, 4H).

^{13}C NMR (101 MHz, $CDCl_3$): δ (ppm) = 166.5, 156.8, 153.1, 152.6, 132.4, 131.7, 130.7, 129.6, 129.4, 129.3, 128.7, 127.5, 120.6, 119.1, 112.3, 69.5, 64.6, 29.1, 28.8, 25.9, 25.8.

MS (*m/z*): calculated for $[C_{21}H_{22}N_2O_3S+H]^+$: 383.14, found 383.2.

SA-3arm

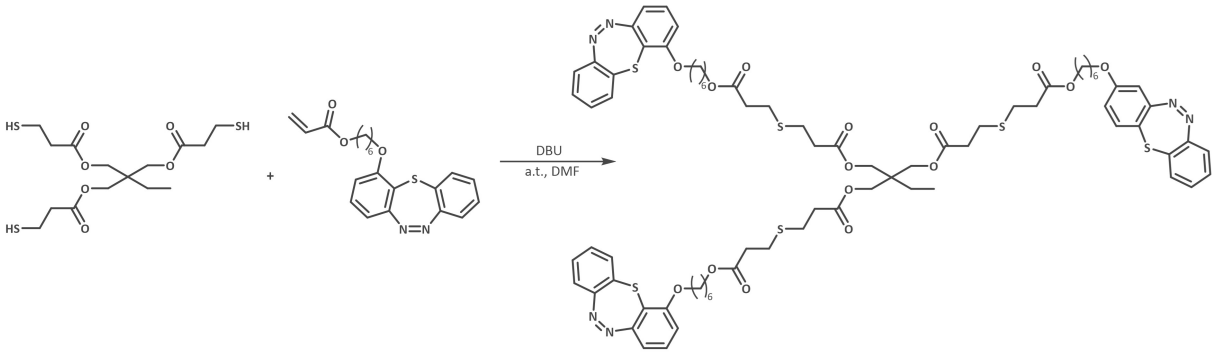

The acrylated photoswitch **6** (708 mg, 1.85 mmol, 1.00 eq.) and trimethylolpropane tris(3-mercaptopropionate) (152 µL, 184 mg, 463 µmol, 0.25 eq.) were dissolved in dimethylformamide (DMF, 10 mL). 1,8-Diazabicyclo [5.4.0]undec-7-ene (DBU, 13.8 µL, 14.1 mg, 92.6 µmol, 0.05 eq.) was added as a catalyst and the reaction mixture was stirred for 30 minutes. Then, ethyl acetate (EA, 100 mL) was added, and the organic phase was washed with brine (2 × 200 mL), then water (200 mL) and dried over Na_2SO_4. The solvent was removed under reduced pressure, and the product was purified via flash column chromatography (cyclohexane 30:70 EA, *v/v*) and obtained as a very viscous, yellow liquid (568 mg, 79%). The excess starting material **6** was recovered from the flash column chromatography as well.

^{1}H NMR (400 MHz, $CDCl_3$): δ (ppm) = 7.57 (dd, *J* = 7.9, 1.4 Hz, 3H), 7.42 (td, *J* = 7.6, 1.4 Hz, 3H), 7.36 – 7.29 (m, 6H), 7.26 – 7.21 (m, 3H), 7.13 (dd, *J* = 8.0, 1.2 Hz, 3H), 6.81 (dd, *J* = 8.2, 1.2 Hz, 3H), 4.12 (t, *J* = 6.7 Hz, 6H), 4.04 (s, 6H), 4.00 (t, *J* = 6.3 Hz, 6H), 2.82 – 2.76 (m, 12H), 2.61 (q, *J* = 6.8 Hz, 12H), 1.90 – 1.79 (m, 6H), 1.70 (p, *J* = 6.9 Hz, 6H), 1.59 – 1.52 (m, 6H), 1.50 – 1.41 (m, 8H), 0.88 (t, *J* = 7.5 Hz, 3H).

^{13}C NMR (101 MHz, $CDCl_3$): δ (ppm) = 172.0, 171.6, 156.7, 153.1, 152.6, 132.4, 131.6, 129.6, 129.4, 129.3, 127.5, 120.5, 119.1, 112.3, 69.5, 64.9, 64.0, 40.9, 34.9, 34.7, 29.1, 28.7, 27.2, 27.1, 25.9, 25.8, 23.1, 7.5.

7. Appendix

7.1 Linear regression to predict $I_{DIOSA,max}$

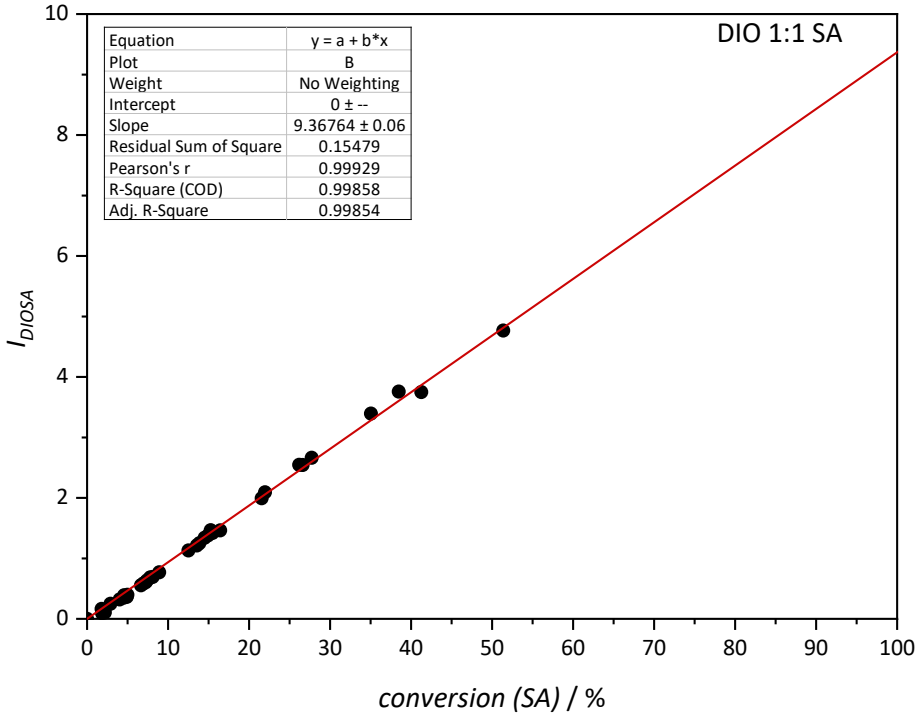

Figure S12. Linear regression of the SA conversion against I_{DIOSA} to predict $I_{DIOSA,max}$ at 100% conversion of SA for the stock solution with a DIO:SA ratio of 1:1. $I_{DIOSA,max}$ was calculated to be 9.37.

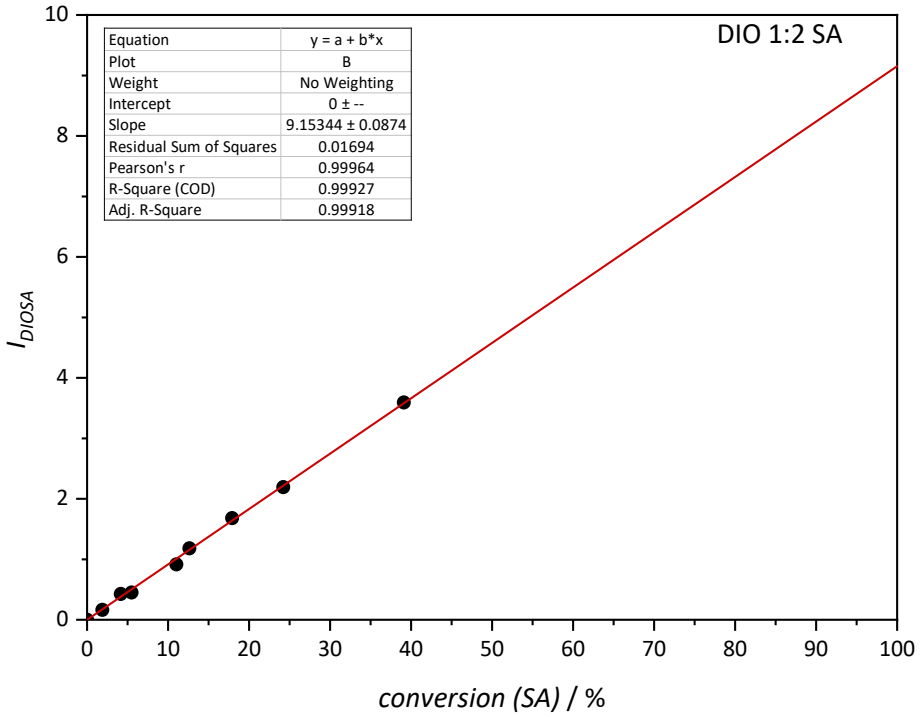

Figure S13. Linear regression of the SA conversion against I_{DIOSA} to predict $I_{DIOSA,max}$ at 100% conversion of SA for the stock solution with a DIO:SA ratio of 1:2. $I_{DIOSA,max}$ was calculated to be 9.15.

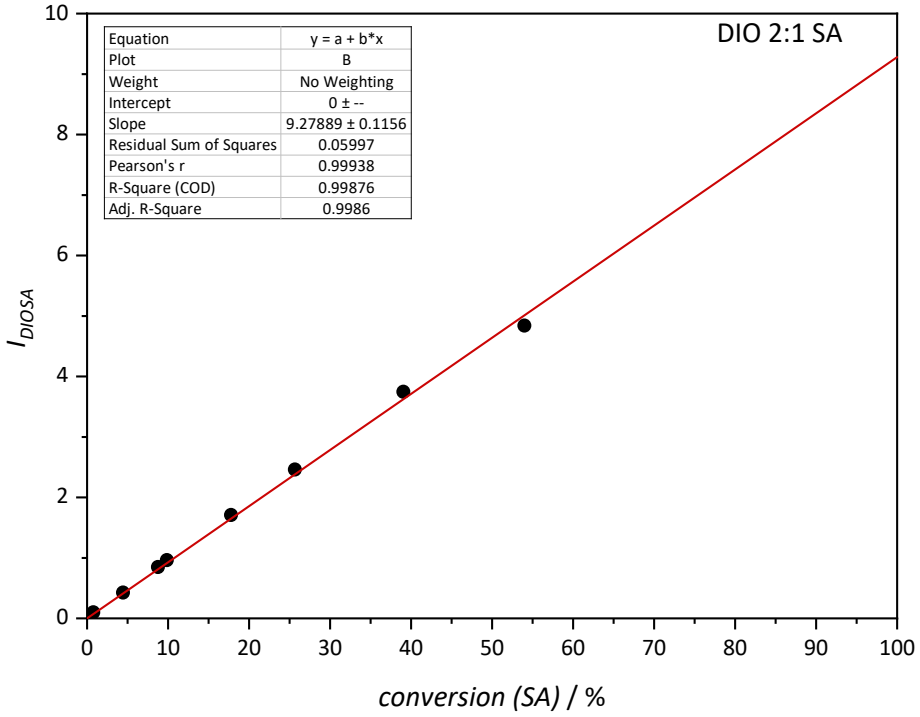

Figure S14. Linear regression of the SA conversion against I_{DIOSA} to predict $I_{DIOSA,max}$ at 100% conversion of SA for the stock solution with a DIO:SA ratio of 2:1. $I_{DIOSA,max}$ was calculated to be 9.28.

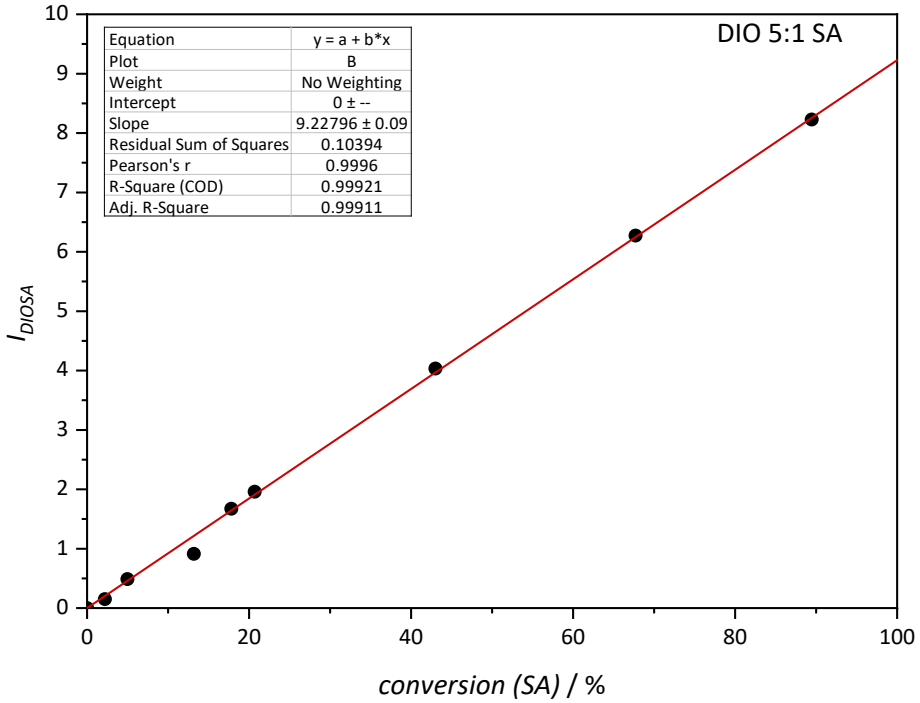

Figure S15. Linear regression of the SA conversion against I_{DIOSA} to predict $I_{DIOSA,max}$ at 100% conversion of SA for the stock solution with a DIO:SA ratio of 5:1. $I_{DIOSA,max}$ was calculated to be 9.23.

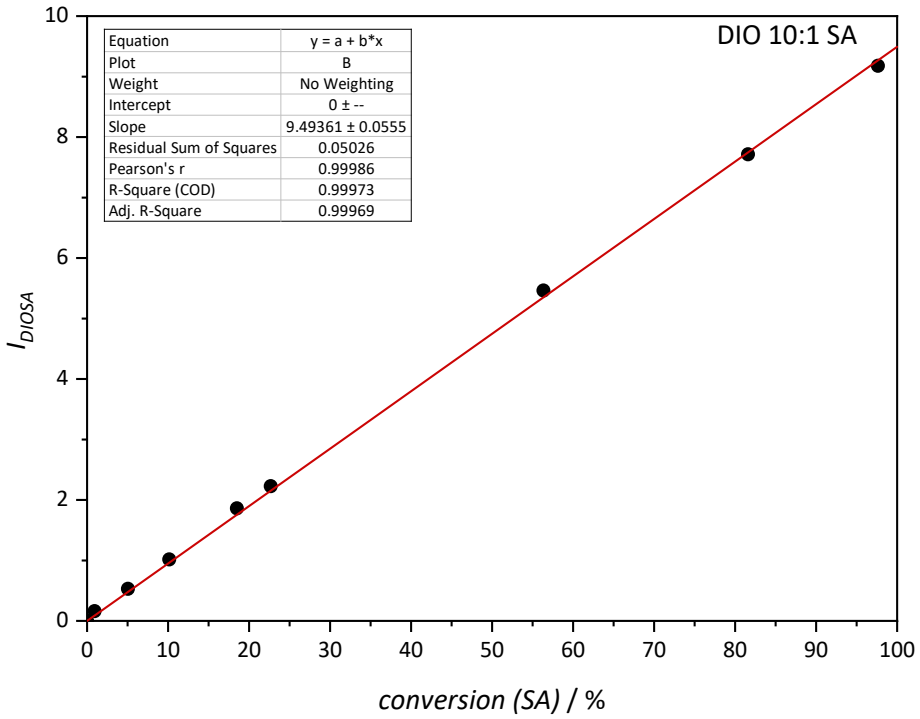

Figure S16. Linear regression of the SA conversion against I_{DIOSA} to predict $I_{DIOSA,max}$ at 100% conversion of SA for the stock solution with a DIO:SA ratio of 10:1. $I_{DIOSA,max}$ was calculated to be 9.49.

7.2 Kinetic fits

7.2.1 Variation of the 365 nm photon flux

Table S1. Product yields for the one- and two-color reaction kinetics with a 1:1 ratio of DIO to SA and under irradiation with a constant 365 nm photon flux of 2.41 × 10^{18} s^{-1} cm^{-2}.

time / min	Y_1 / %	Y_2 / %
0	0	0
0.2	1.76	2.66
0.6	3.42	6.76
1.2	6.42	13.28
2.4	12.90	22.23

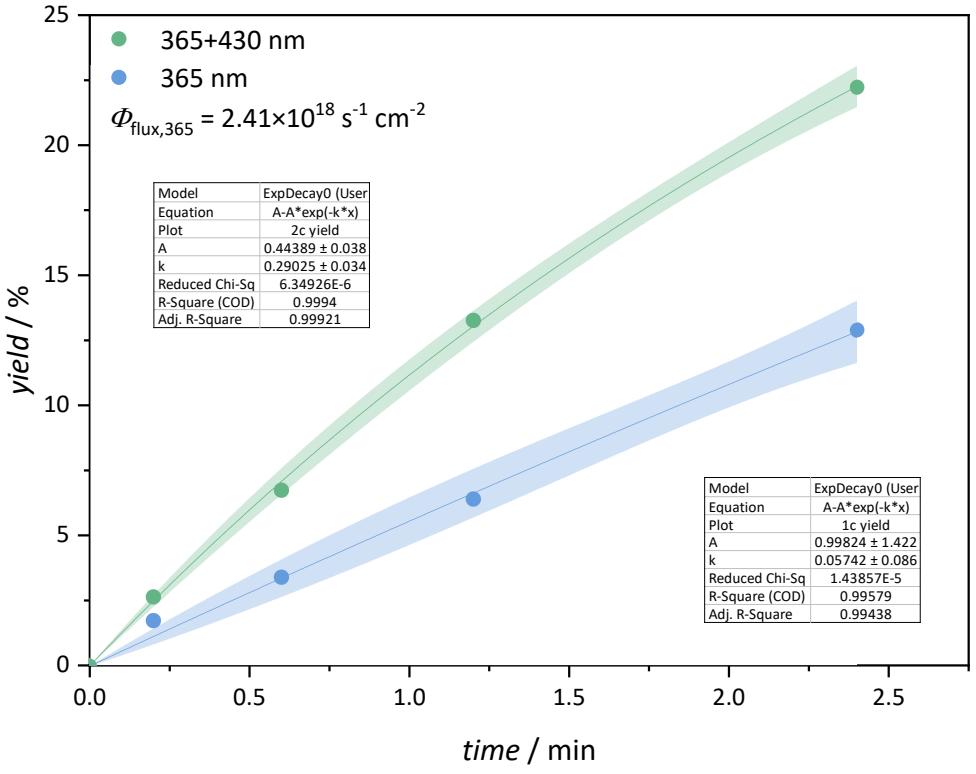

Figure S17. Exponential fits and 95% confidence bands for the one- and two-color reaction kinetics, irradiated with a constant 365 nm photon flux of 2.41 × 10^{18} s^{-1} cm^{-2} and a 1:1 ratio of DIO to SA.

Table S2. Product yields for the one- and two-color reaction kinetics with a 1:1 ratio of DIO to SA and under irradiation with a constant 365 nm photon flux of 1.20×10^{18} s^{-1} cm^{-2}.

time / min	Y_1 / %	Y_2 / %
0	0	0
0.4	0.95	2.95
1.2	3.81	9.08
2.4	7.59	16.27
4.8	15.02	28.35

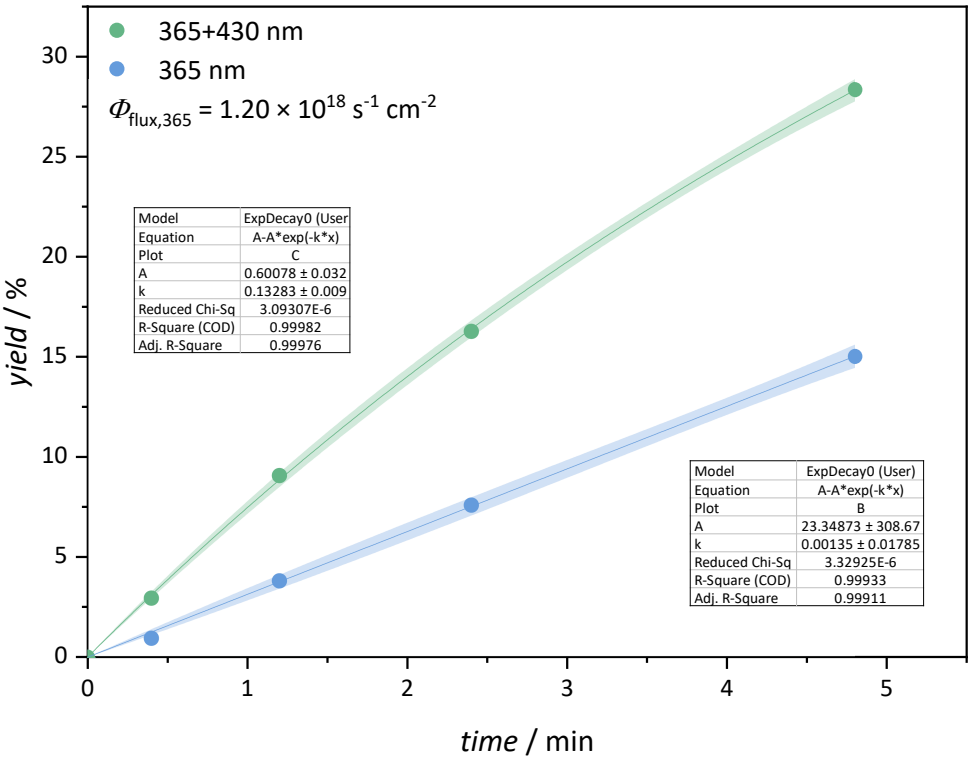

Figure S18. Exponential fits and 95% confidence bands for the one- and two-color reaction kinetics, irradiated with a constant 365 nm photon flux of 1.20×10^{18} s^{-1} cm^{-2} and a 1:1 ratio of DIO to SA.

Table S3. Product yields for the one- and two-color reaction kinetics with a 1:1 ratio of DIO to SA and under irradiation with a constant 365 nm photon flux of 4.81×10^{17} s^{-1} cm^{-2}.

time / min	Y_1 / %	Y_2 / %
0	0	0
1	0.99	4.23
3	3.73	12.04
6	7.29	21.21
12	14.24	36.08

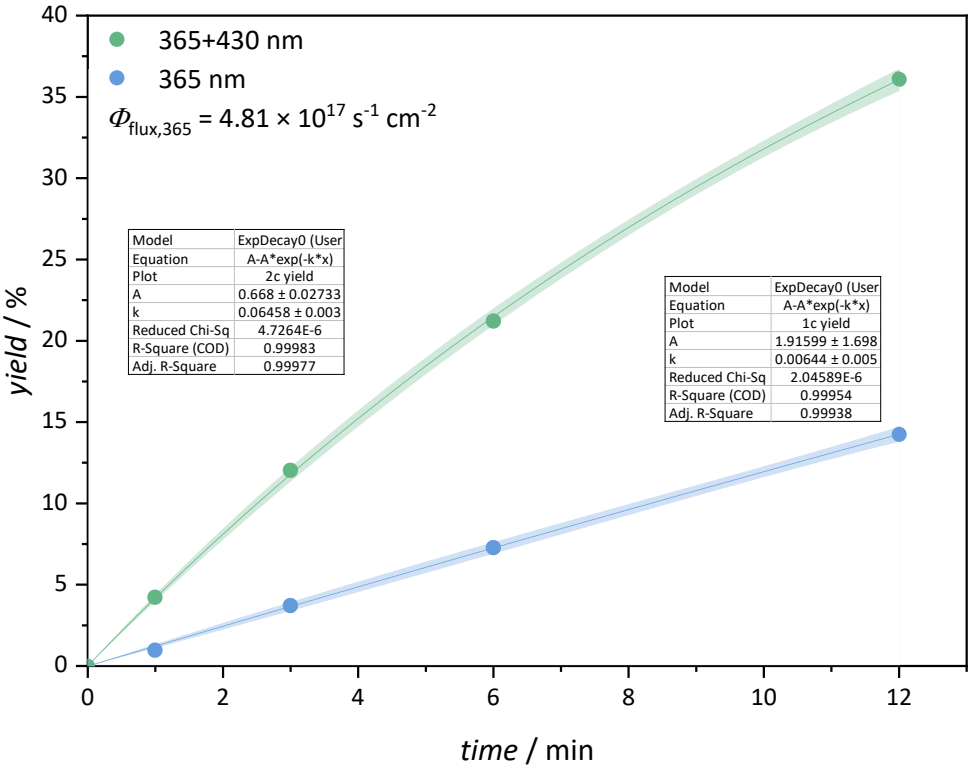

Figure S19. Exponential fits and 95% confidence bands for the one- and two-color reaction kinetics, irradiated with a constant 365 nm photon flux of 4.81×10^{17} s^{-1} cm^{-2} and a 1:1 ratio of DIO to SA.

Table S4. Product yields for the one- and two-color reaction kinetics with a 1:1 ratio of DIO to SA and under irradiation with a constant 365 nm photon flux of 9.63×10^{16} s^{-1} cm^{-2}.

time / min	Y_1 / %	Y_2 / %
0	0	0
5	1.57	5.90
15	4.16	15.58
30	8.19	27.07
60	15.11	39.94

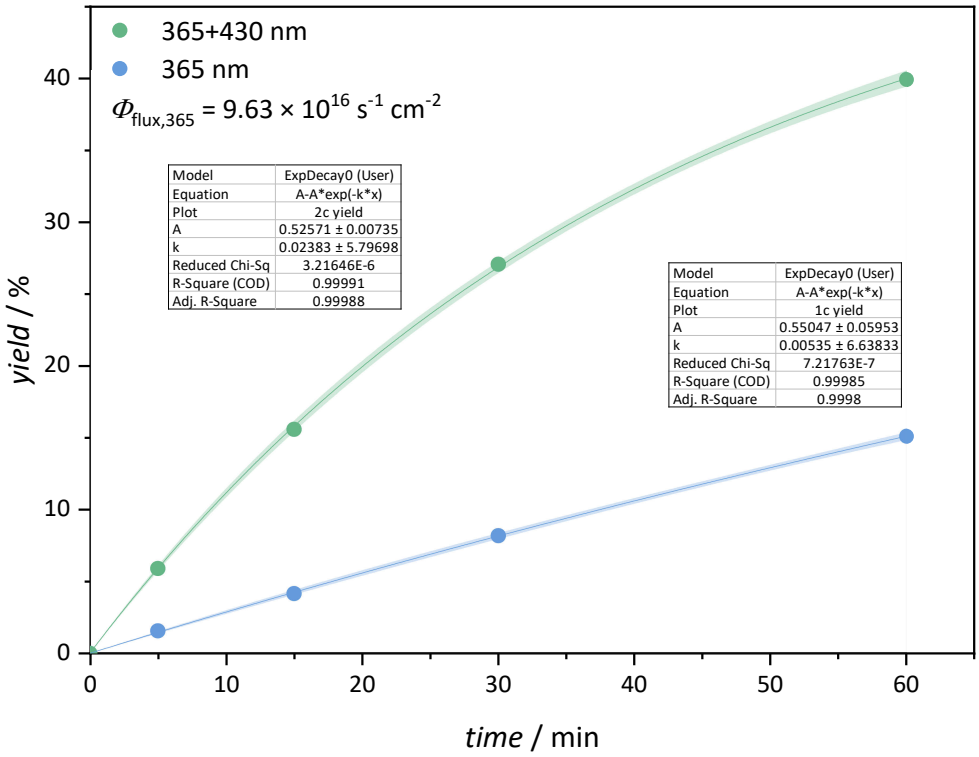

Figure S20. Exponential fits and 95% confidence bands for the one- and two-color reaction kinetics, irradiated with a constant 365 nm photon flux of 9.63×10^{16} s^{-1} cm^{-2} and a 1:1 ratio of DIO to SA.

Table S5. Product yields for the one- and two-color reaction kinetics with a 1:1 ratio of DIO to SA and under irradiation with a constant 365 nm photon flux of 6.88×10^{16} s^{-1} cm^{-2}.

time / min	Y_1 / %	Y_2 / %
0	0	0
6.8	1.12	6.21
20.4	3.88	15.55
40.8	7.36	27.05
81.6	14.69	39.85

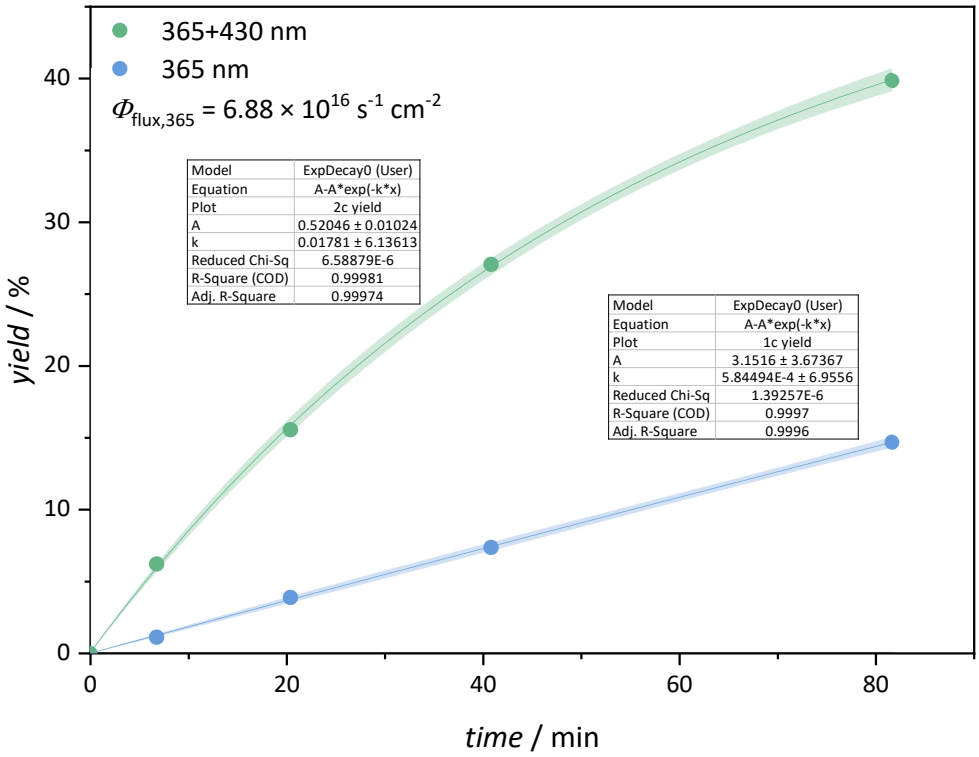

Figure S21. Exponential fits and 95% confidence bands for the one- and two-color reaction kinetics, irradiated with a constant 365 nm photon flux of 6.88×10^{16} s^{-1} cm^{-2} and a 1:1 ratio of DIO to SA.

7.2.2 Variation of the DIO to SA ratio

Table S6. Product yields for the one- and two-color reaction kinetics with varying DIO to SA ratios and under irradiation with a constant 365 nm photon flux of 9.63×10^{16} s^{-1} cm^{-2}.

	DIO 1:2 SA		DIO 1:1 SA		DIO 2:1 SA		DIO 5:1 SA		DIO 10:1 SA	
time / min	Y_1 / %	Y_2 / %	Y_1 / %	Y_2 / %	Y_1 / %	Y_2 / %	Y_1 / %	Y_2 / %	Y_1 / %	Y_2 / %
0	0.00	0.00	0.00	0.00	0.00	0.00	0.00	0.00	0.00	0.00
5	1.81	4.68	1.57	5.90	1.22	10.00	1.65	18.13	1.70	23.48
15	4.92	12.92	4.16	15.58	5.04	26.57	5.31	43.72	5.61	57.56
30	10.02	23.97	8.19	27.07	10.49	40.43	9.90	67.97	10.73	81.31
60	18.37	39.28	15.11	39.94	19.29	52.22	21.23	89.16	19.61	96.73

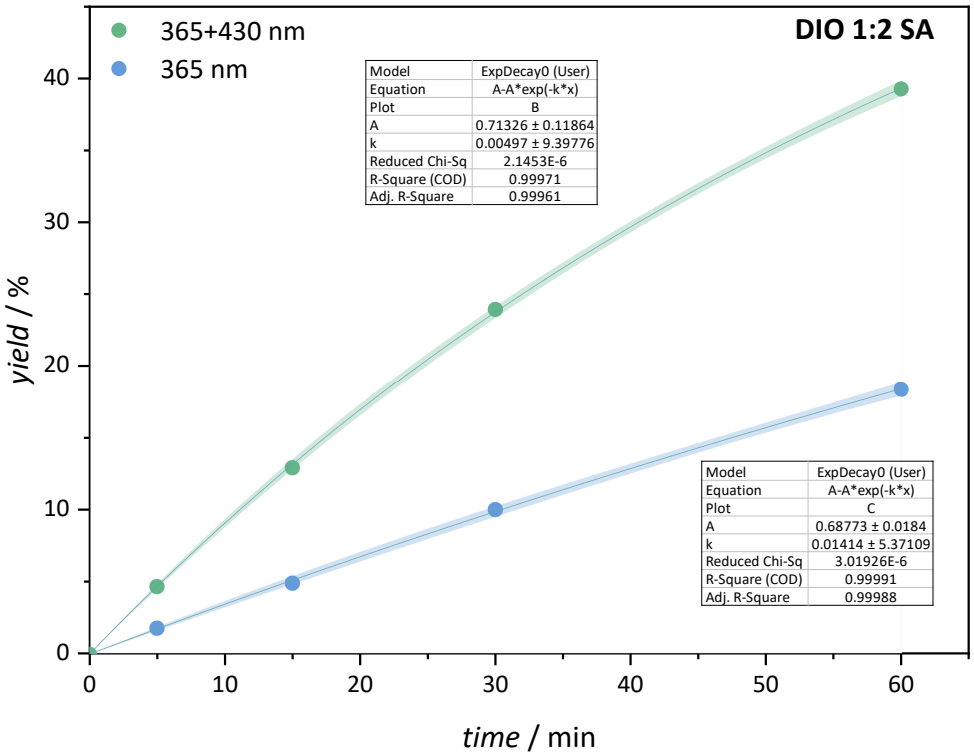

Figure S22. Exponential fits and 95% confidence bands for the one- and two-color reaction kinetics, irradiated with a constant 365 nm photon flux of 9.63×10^{16} s^{-1} cm^{-2} and a 1:2 ratio of DIO to SA.

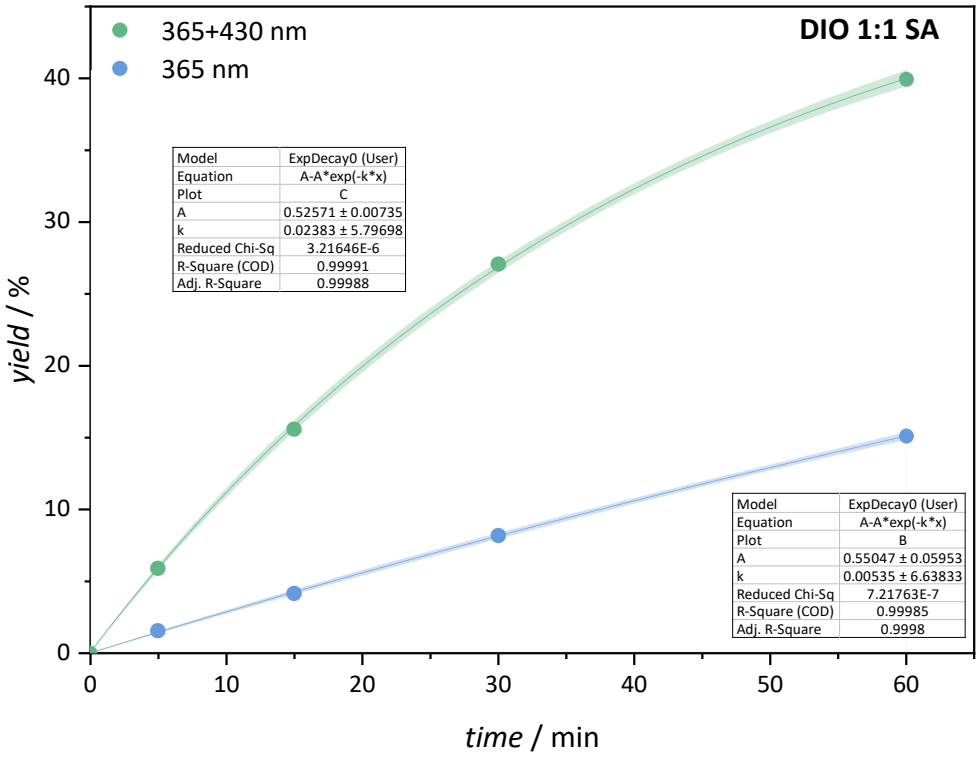

Figure S23. Exponential fits and 95% confidence bands for the one- and two-color reaction kinetics, irradiated with a constant 365 nm photon flux of 9.63×10^{16} s^{-1} cm^{-2} and a 1:1 ratio of DIO to SA.

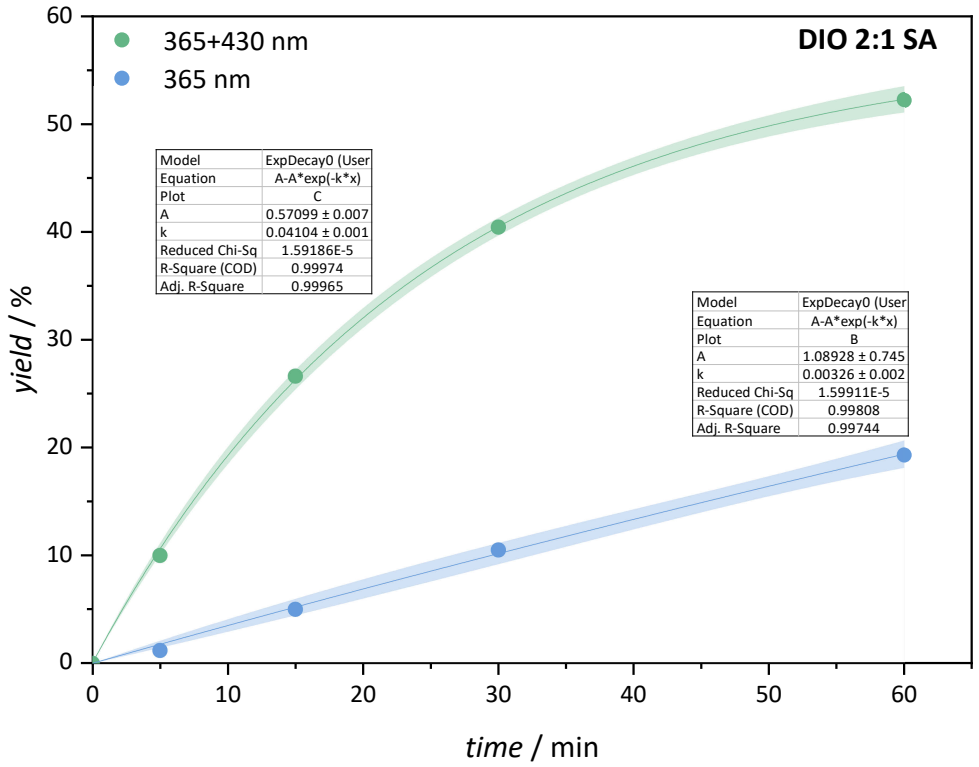

Figure S24. Exponential fits and 95% confidence bands for the one- and two-color reaction kinetics, irradiated with a constant 365 nm photon flux of 9.63×10^{16} s^{-1} cm^{-2} and a 2:1 ratio of DIO to SA.

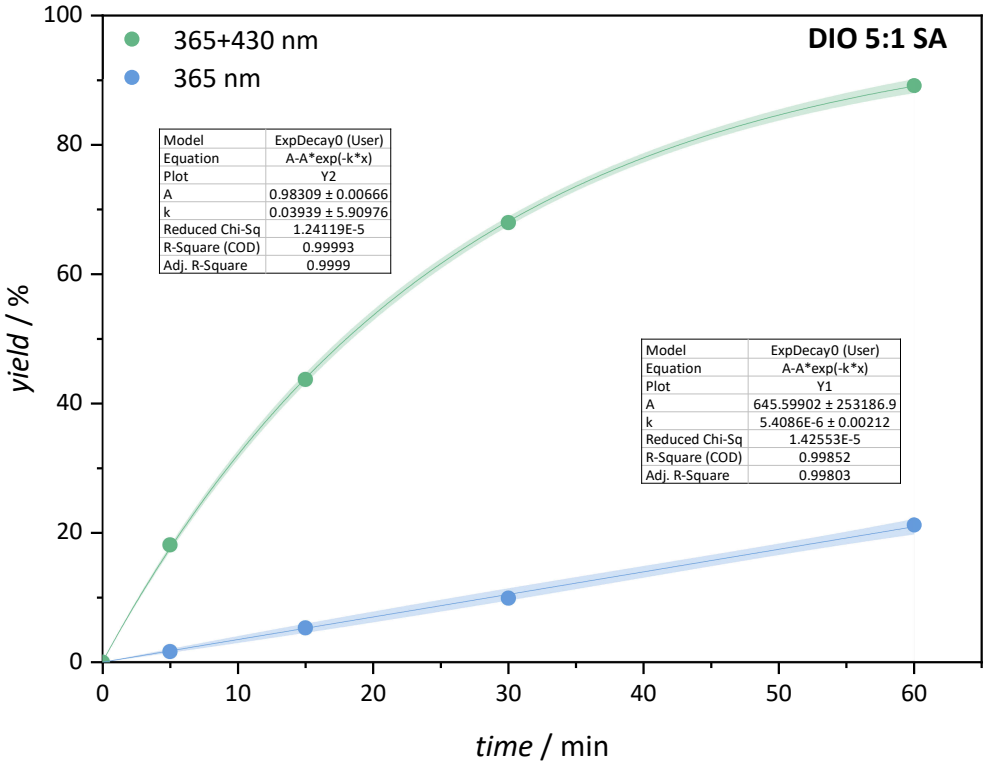

Figure S25. Exponential fits and 95% confidence bands for the one- and two-color reaction kinetics, irradiated with a constant 365 nm photon flux of 9.63×10^{16} s^{-1} cm^{-2} and a 5:1 ratio of DIO to SA.

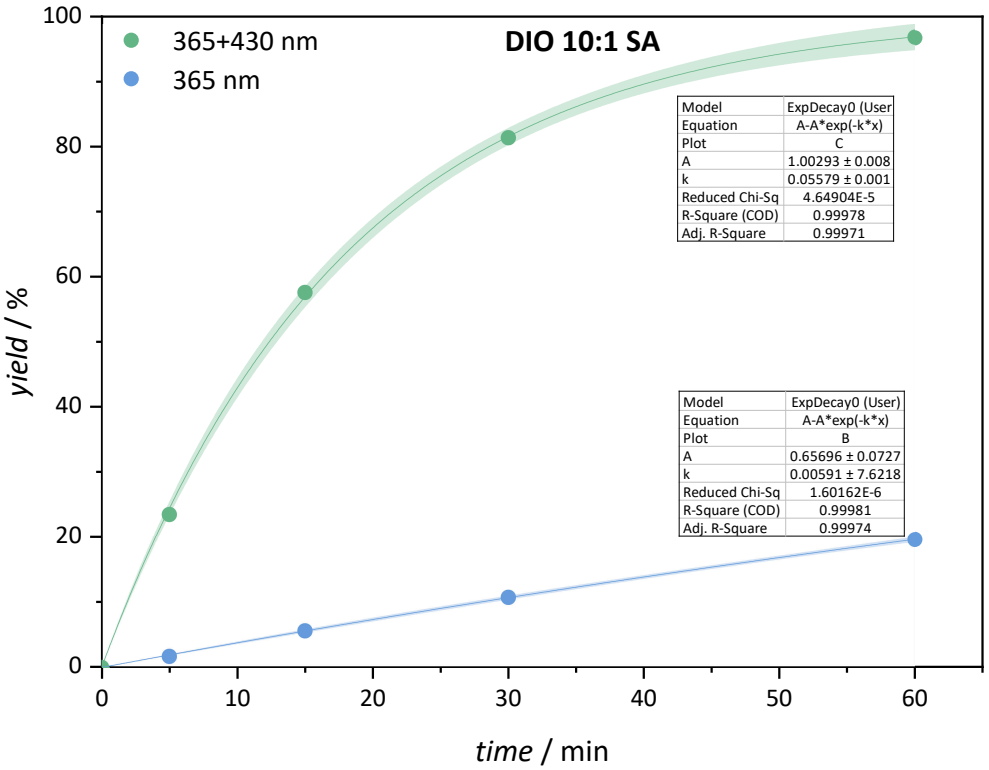

Figure S26. Exponential fits and 95% confidence bands for the one- and two-color reaction kinetics, irradiated with a constant 365 nm photon flux of 9.63×10^{16} s^{-1} cm^{-2} and a 10:1 ratio of DIO to SA.

7.3 Small-molecule study – NMR spectra of the stock solutions

DIO 1:1 SA

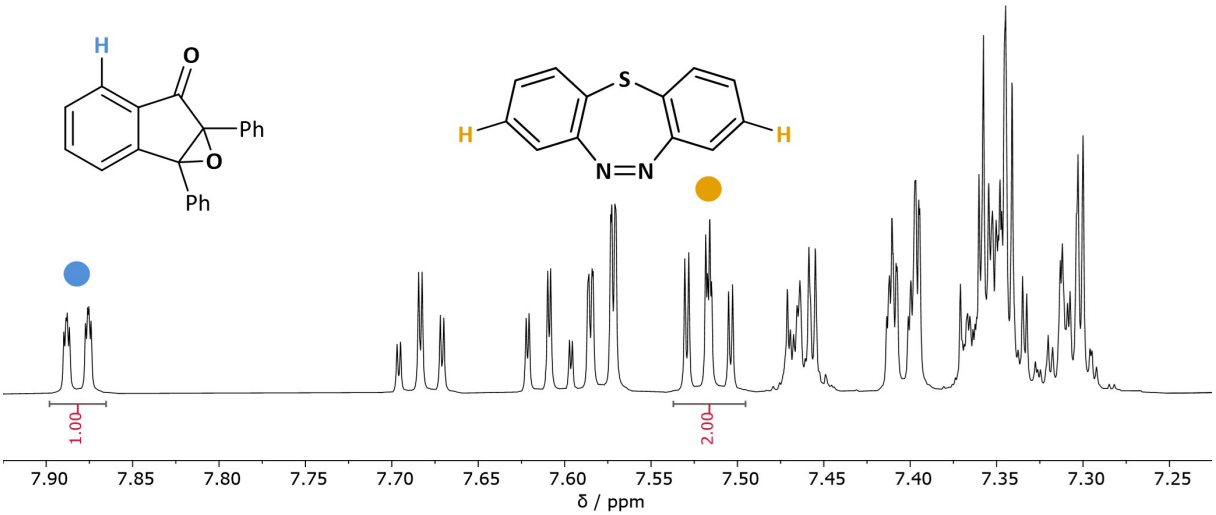

Figure S27. ^{1}H NMR (600 MHz) spectrum in MeCN-d_3 at ambient temperature of the stock solution for the two-color reactions with a DIO:SA ratio of 1:1 ([DIO]=5 mM, [SA]=5 mM).

DIO 1:2 SA

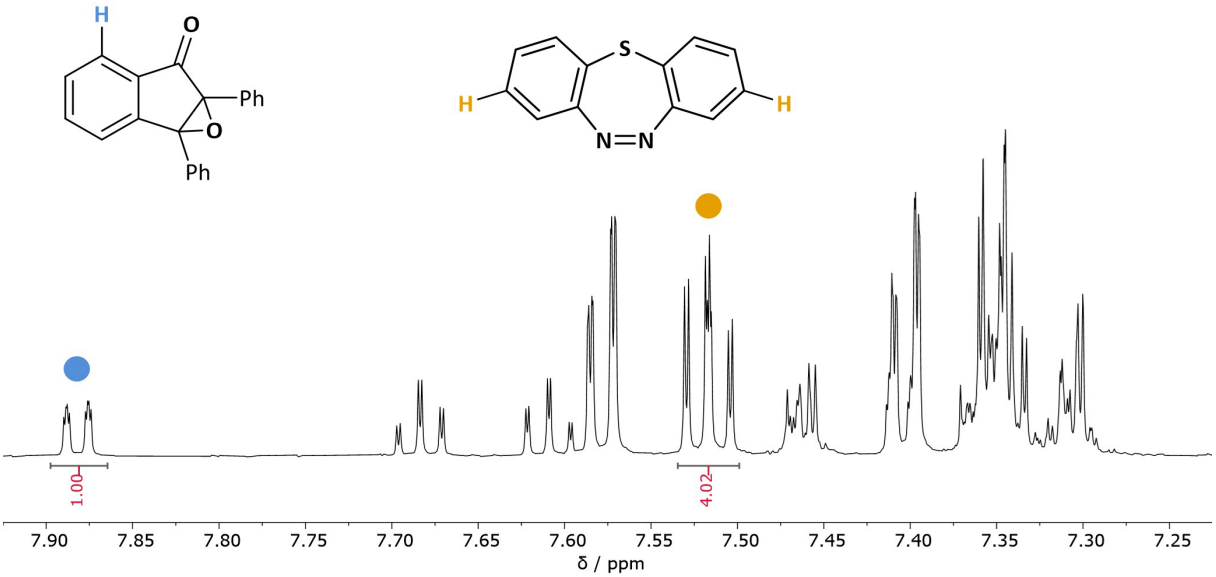

Figure S28. ^{1}H NMR (600 MHz) spectrum in MeCN-d_3 at ambient temperature of the stock solution for the two-color reactions with a DIO:SA ratio of 1:2 ([DIO]=5 mM, [SA]=10 mM).

DIO 2:1 SA

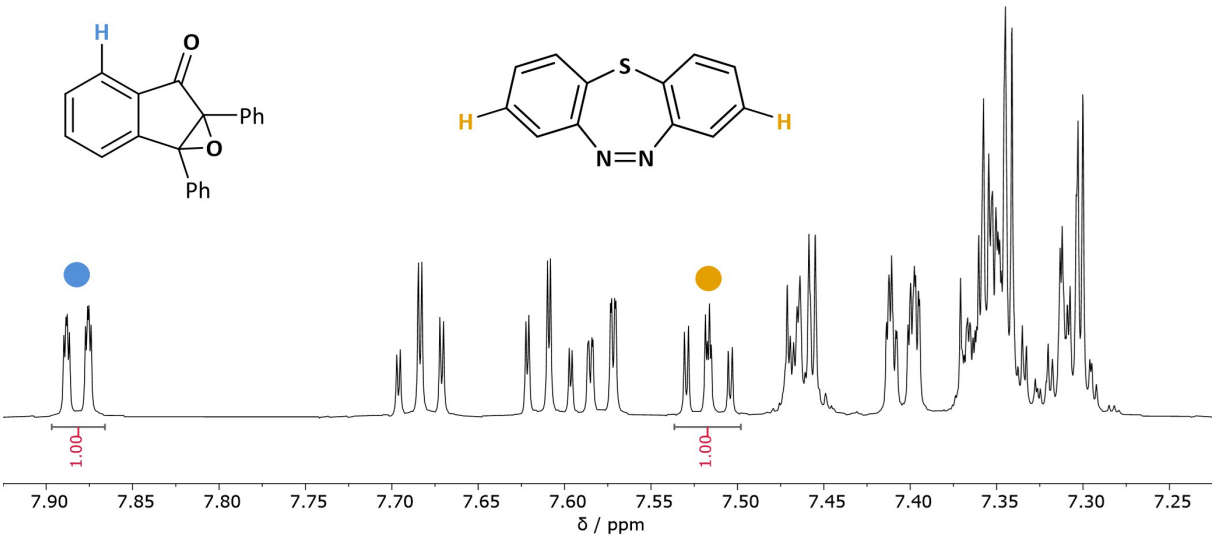

Figure S29. ^{1}H NMR (600 MHz) spectrum in MeCN-d_3 at ambient temperature of the stock solution for the two-color reactions with a DIO:SA ratio of 2:1 ([DIO]=10 mM, [SA]=5 mM).

DIO 5:1 SA

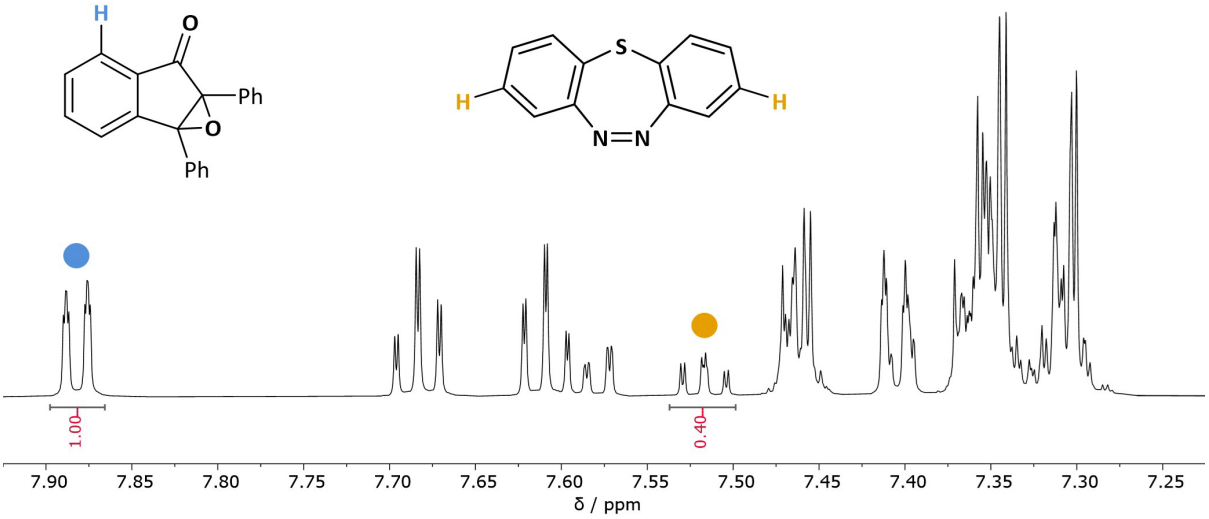

Figure S30. ^{1}H NMR (600 MHz) spectrum in MeCN-d_3 at ambient temperature of the stock solution for the two-color reactions with a DIO:SA ratio of 5:1 ([DIO]=25 mM, [SA]=5 mM).

DIO 10:1 SA

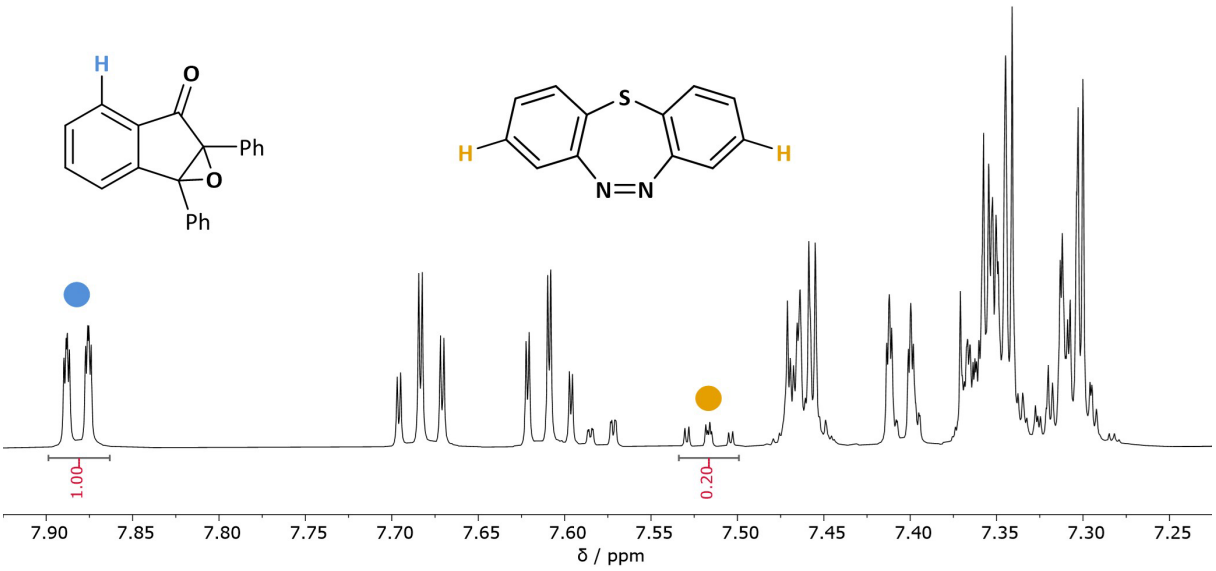

Figure S31. ^{1}H NMR (600 MHz) spectrum in MeCN-d_3 at ambient temperature of the stock solution for the two-color reactions with a DIO:SA ratio of 10:1 ([DIO]=50 mM, [SA]=5 mM).

7.4 Macromolecular study – NMR spectra of the photoresists

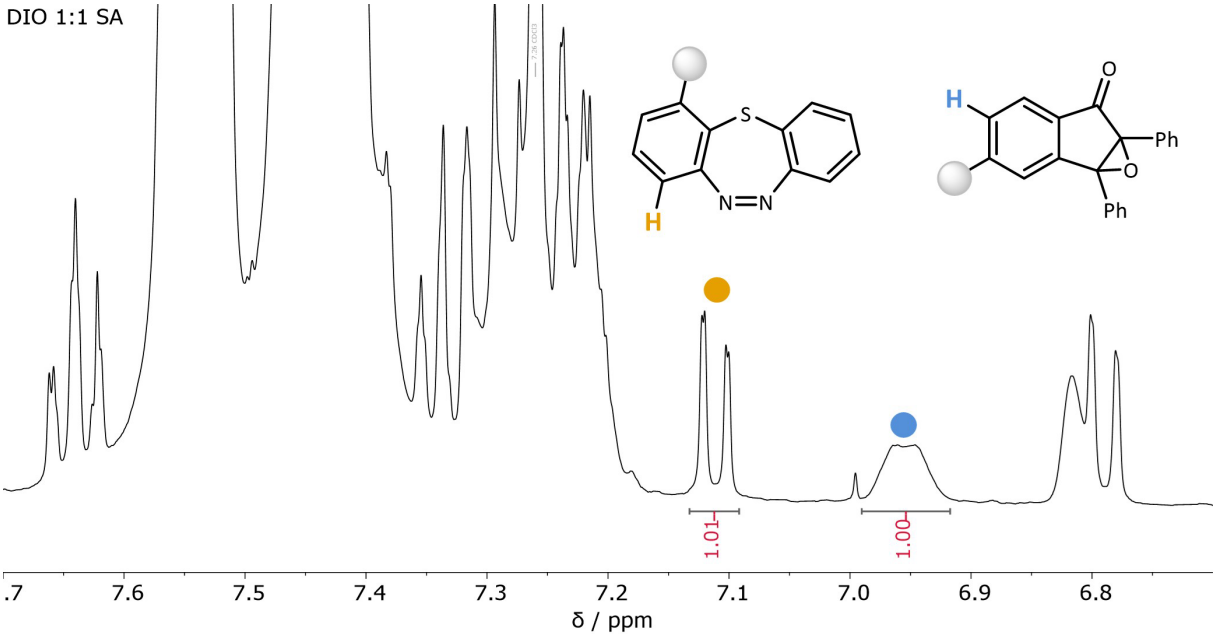

Figure S32. ^{1}H NMR (400 MHz) spectrum in $CDCl_3$ at ambient temperature of the photoresist formulation in acetophenone for the two-color SEC crosslinking tests, with a DIO:SA ratio of 1:1 ([DIO] = 47.5 mM, [SA] = 47.5 mM).

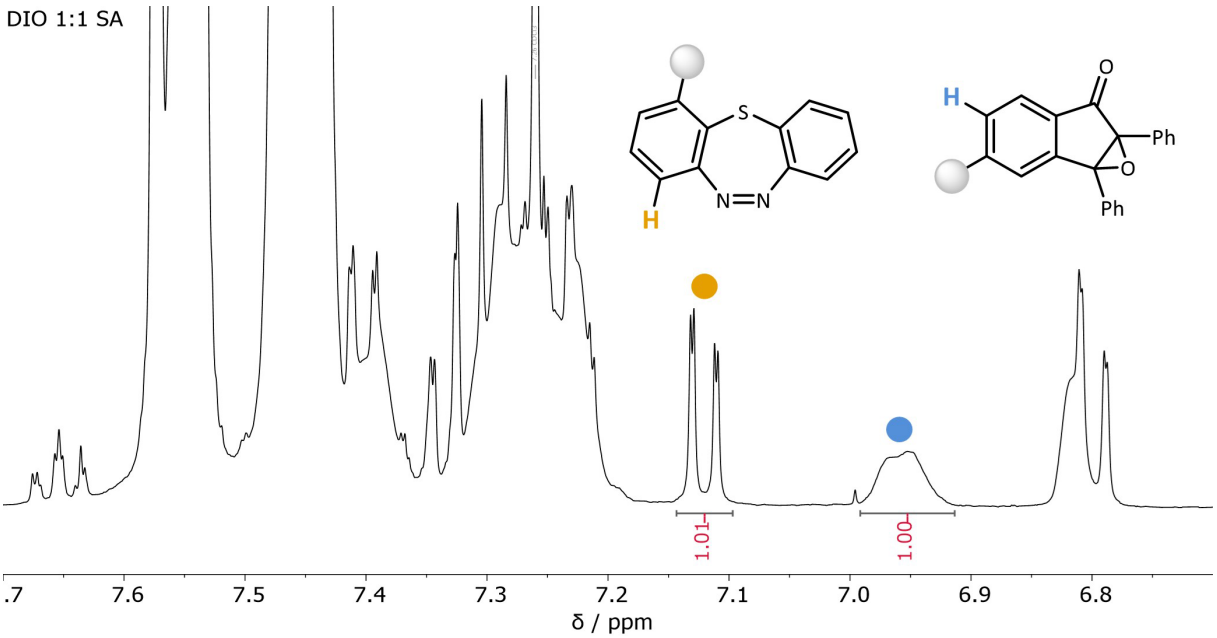

Figure S33. ^{1}H NMR (400 MHz) spectrum in $CDCl_3$ at ambient temperature of the photoresist formulation in acetophenone for two-color lithography with a DIO:SA ratio of 1:1 ([DIO] = 70.5 mM, [SA] = 70.5 mM).

7.5 Estimation of theoretical UV-Vis spectra of DIO' and SA'

The datapoints for all wavelengths of the theoretical UV-Vis spectrum of DIO' were calculated by measuring UV-Vis spectra of pure DIO and the DIO/DIO' mixture in the photostationary state (PSS) at 365 nm and with the following formula

$$\varepsilon_{DIO'} = \varepsilon_{DIO} + \frac{\varepsilon_{PSS} - \varepsilon_{DIO}}{x}$$

where $\varepsilon_{DIO'}$ is the wavelength-dependent extinction of DIO', ε_{DIO} of DIO and ε_{PSS} of the DIO/DIO' mixture at the PSS and x is the fraction of DIO' at the PSS. The fraction of DIO in the PSS at 365 nm was reported to be 11% DIO'.[33]

The same measurements and calculations were made for SA (by substituting DIO and DIO' with SA and SA' respectively in the formula). The fraction of SA' in the PSS mixture was estimated to be 30%. Only an estimation was made in order to give a qualitative understanding of the absorbance spectrum of SA', since its short half-life complicates a precise measurement of the SA/SA' distribution under exactly the same conditions as during the UV-Vis measurement.

7.6 Incorporation ratio of DIO in polyDIO

The incorporation ratio x_{DIO} of DIO to EHA in polyDIO was calculated via integration of magnetic resonance 1 for DIO and of the overlapping resonances 5, 10 and 23 for EHA (**Figure S34**) according to the following formula

$$x_{DIO} = \frac{I_1}{(I_{5,10,23} - 4 * I_1)/(2 * I_1)} = \frac{1}{(18.85 - 4)/(2)} = 13.5\%$$

where I_1 and $I_{5,10,23}$ are the integrated values of the corresponding magnetic resonances 1 and 5, 10, 23, respectively.

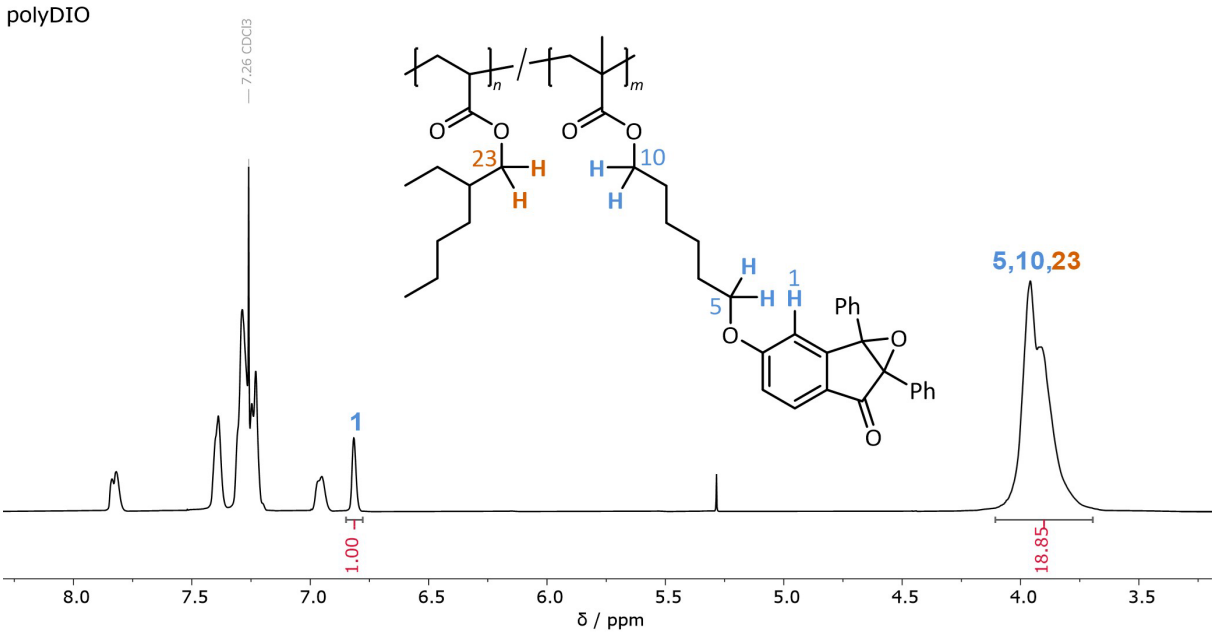

Figure S34. ^{1}H NMR (400 MHz) spectrum of polyDIO in $CDCl_3$ at ambient temperature. Highlighted in orange are the magnetic resonances of the EHA units and in blue of the DIO units that were used to calculate the DIO ratio.

7.7 NMR spectra

7.7.1 Small-molecule study

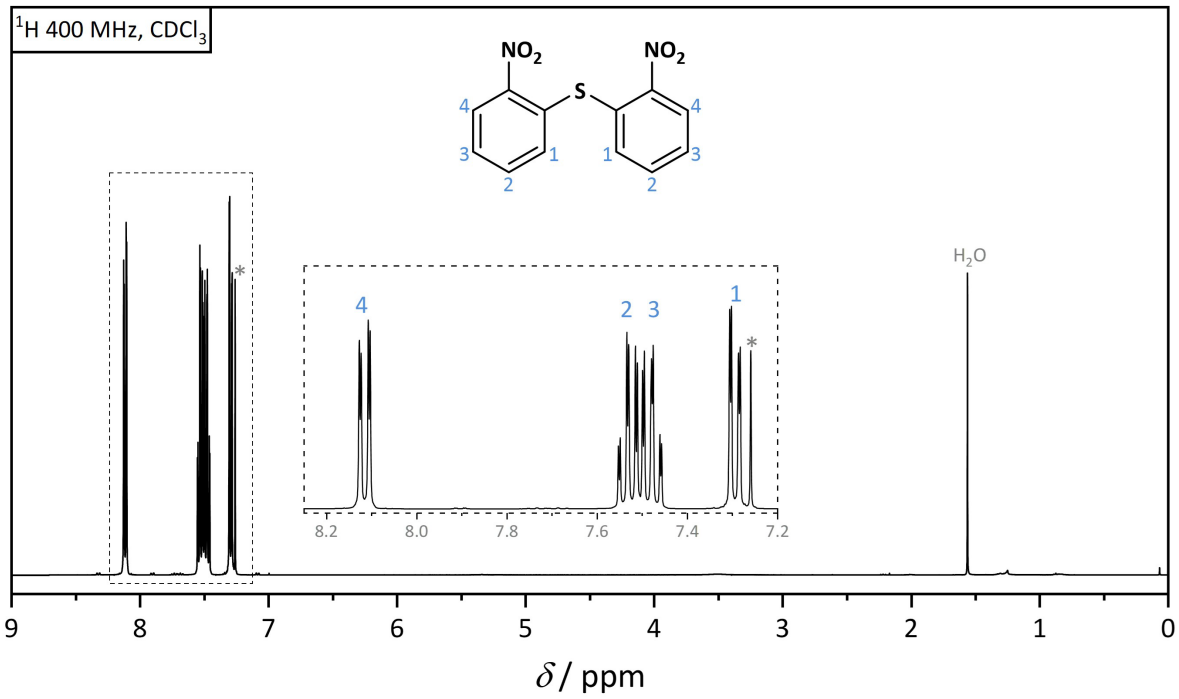

Figure S35. ^{1}H NMR (400 MHz) spectrum of **preSA** in $CDCl_3$ (*) at ambient temperature.

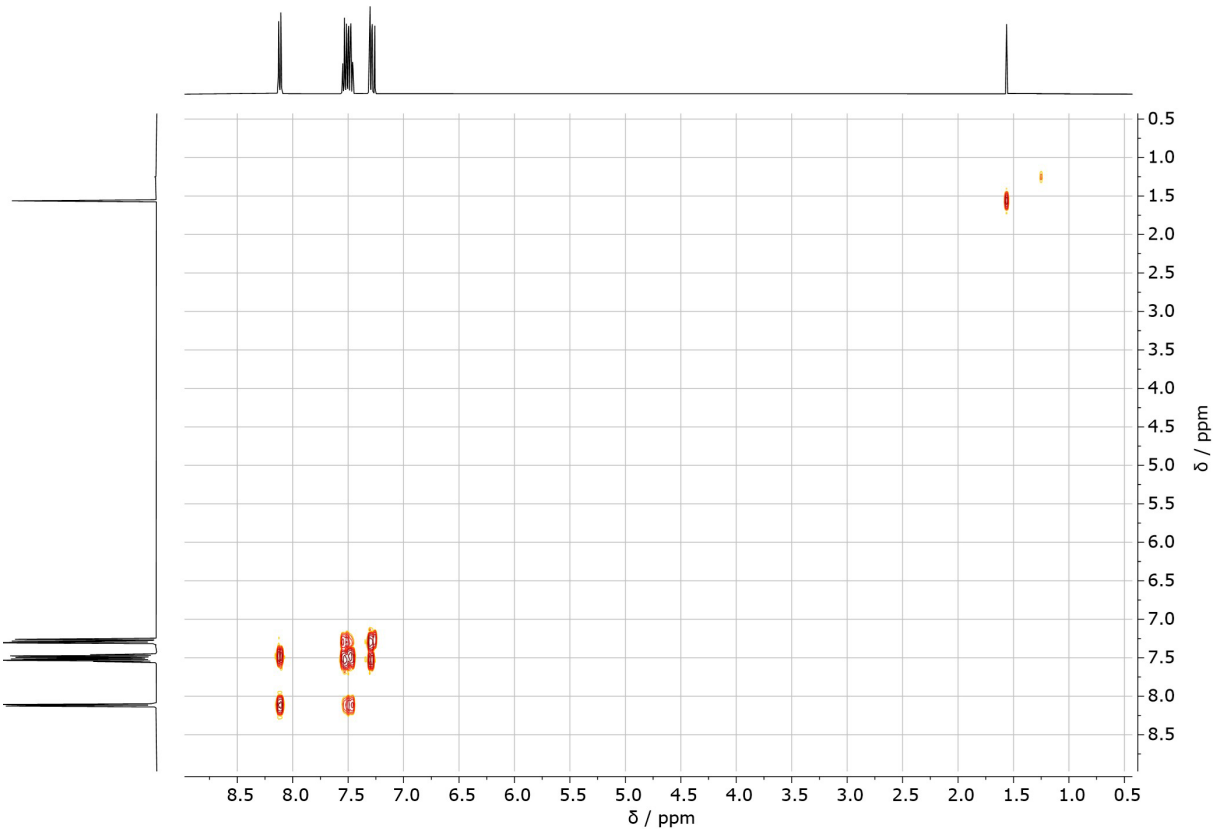

Figure S36. ^{1}H-^{1}H COSY (400 MHz) spectrum of **preSA** in $CDCl_3$ (*) at ambient temperature.

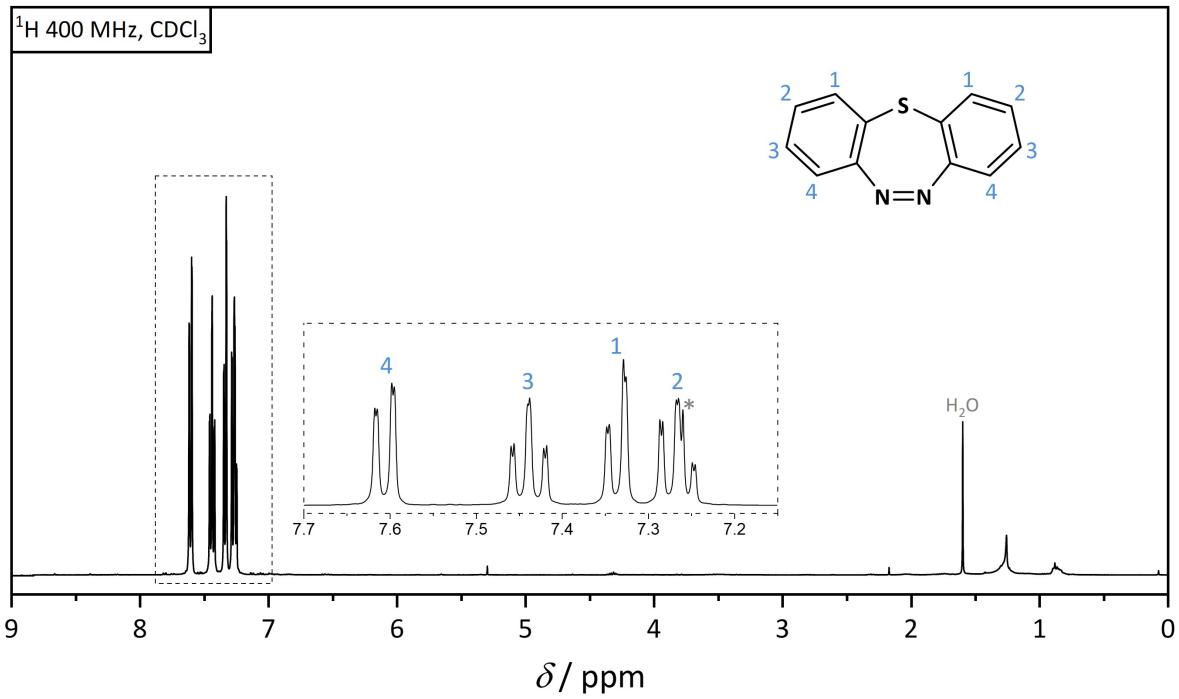

Figure S37. ^{1}H NMR (400 MHz) spectrum of **SA** in $CDCl_3$ (*) at ambient temperature.

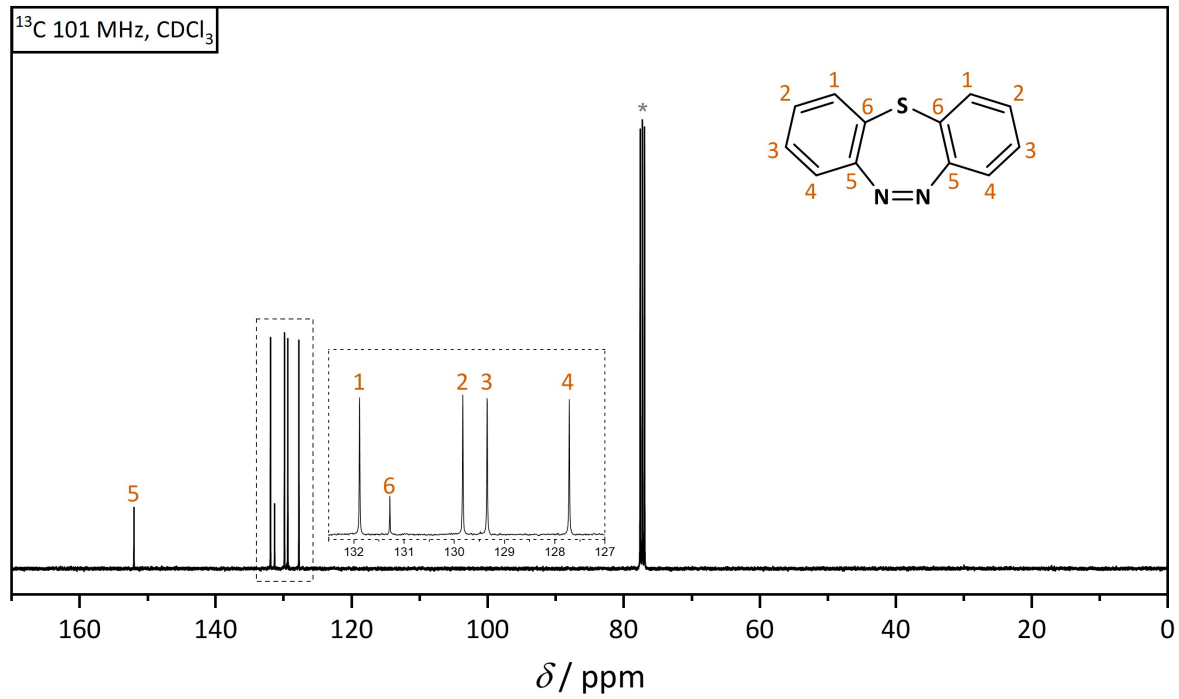

Figure S38. ^{13}C NMR (101 MHz) spectrum of **SA** in $CDCl_3$ (*) at ambient temperature.

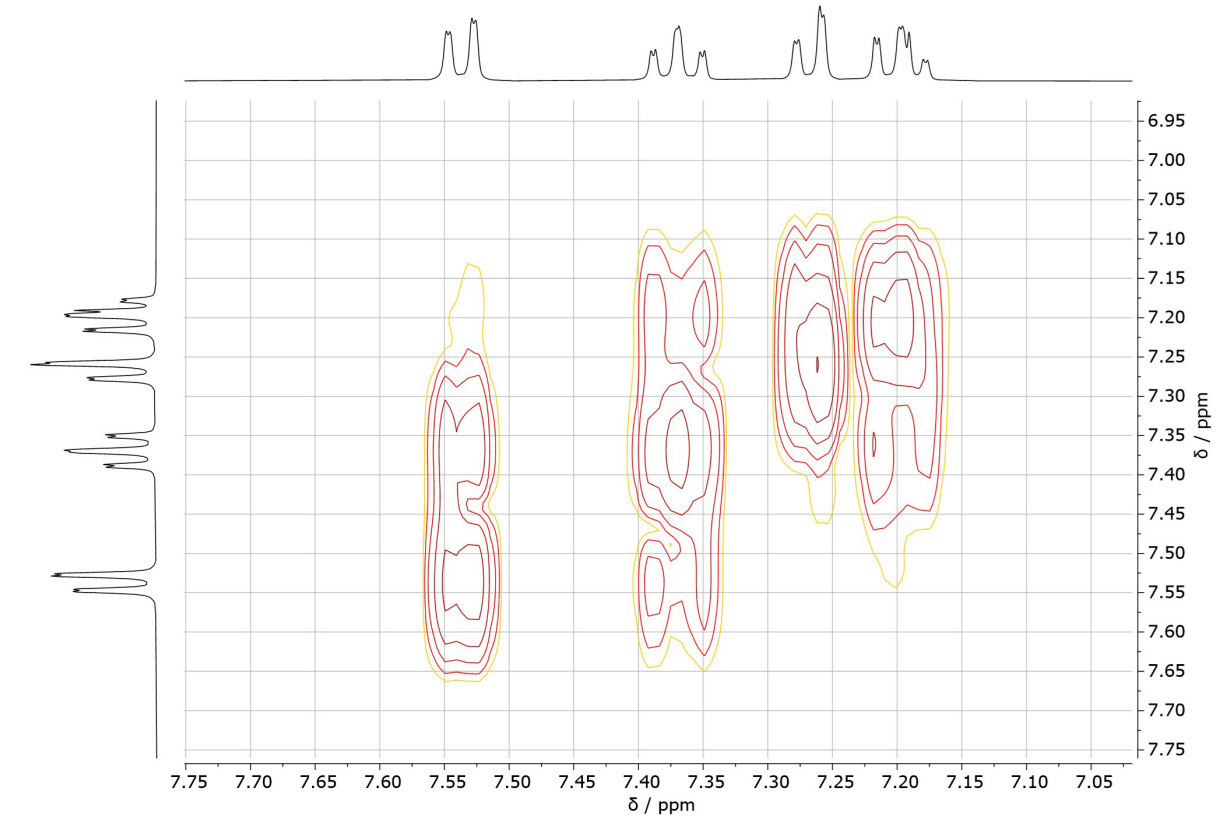

Figure S39. ^{1}H-^{1}H COSY (400 MHz) spectrum of **SA** in $CDCl_3$ (*) at ambient temperature.

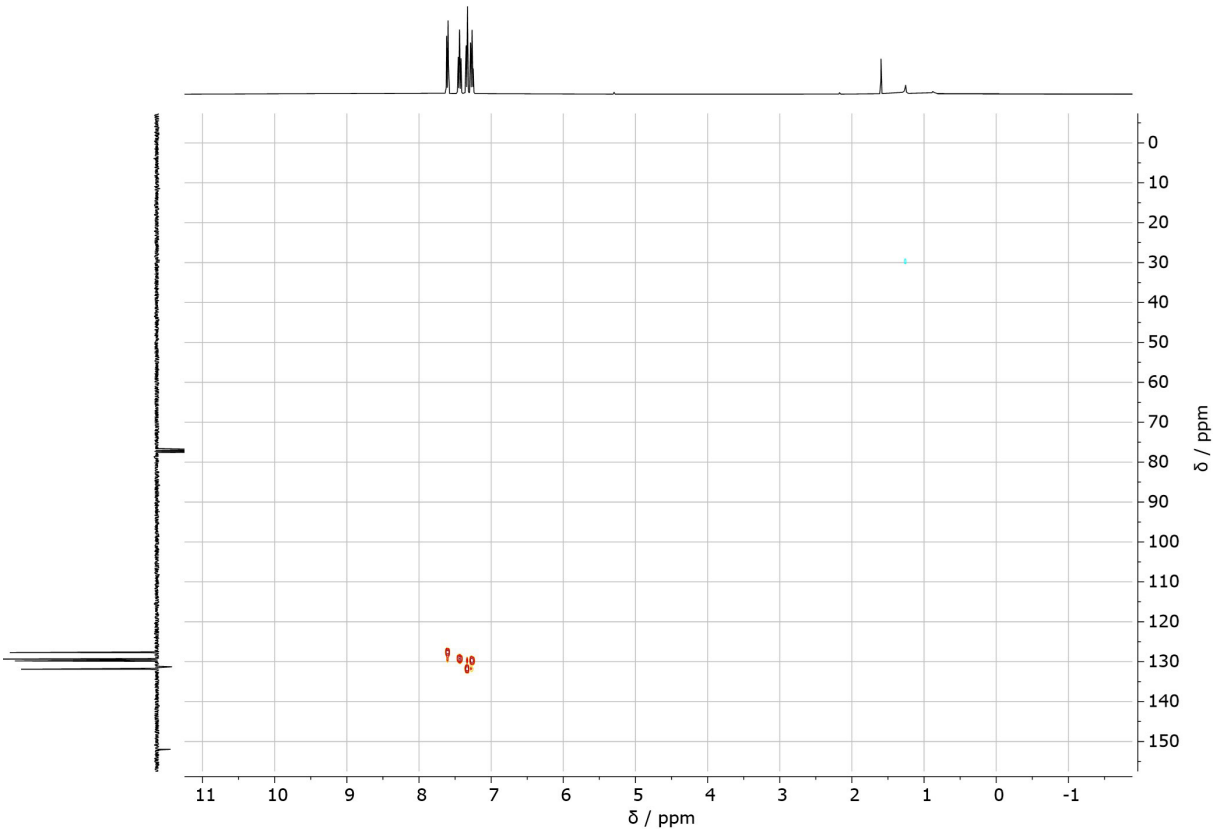

Figure S40. ^{1}H (400 MHz) - ^{13}C (101 MHz) HSQC spectrum of **SA** in $CDCl_3$ (*) at ambient temperature.

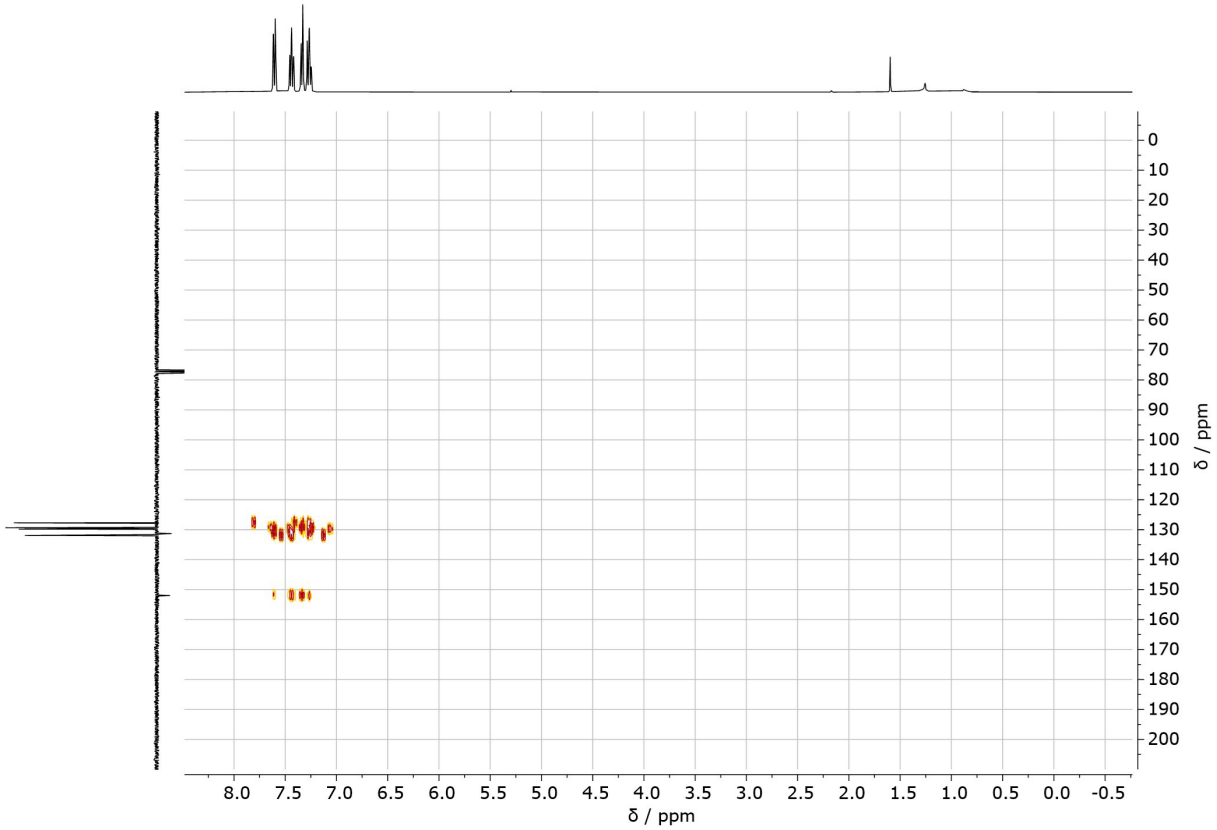

Figure S41. ^{1}H (400 MHz) - ^{13}C (101 MHz) HMBC spectrum of **SA** in $CDCl_3$ (*) at ambient temperature.

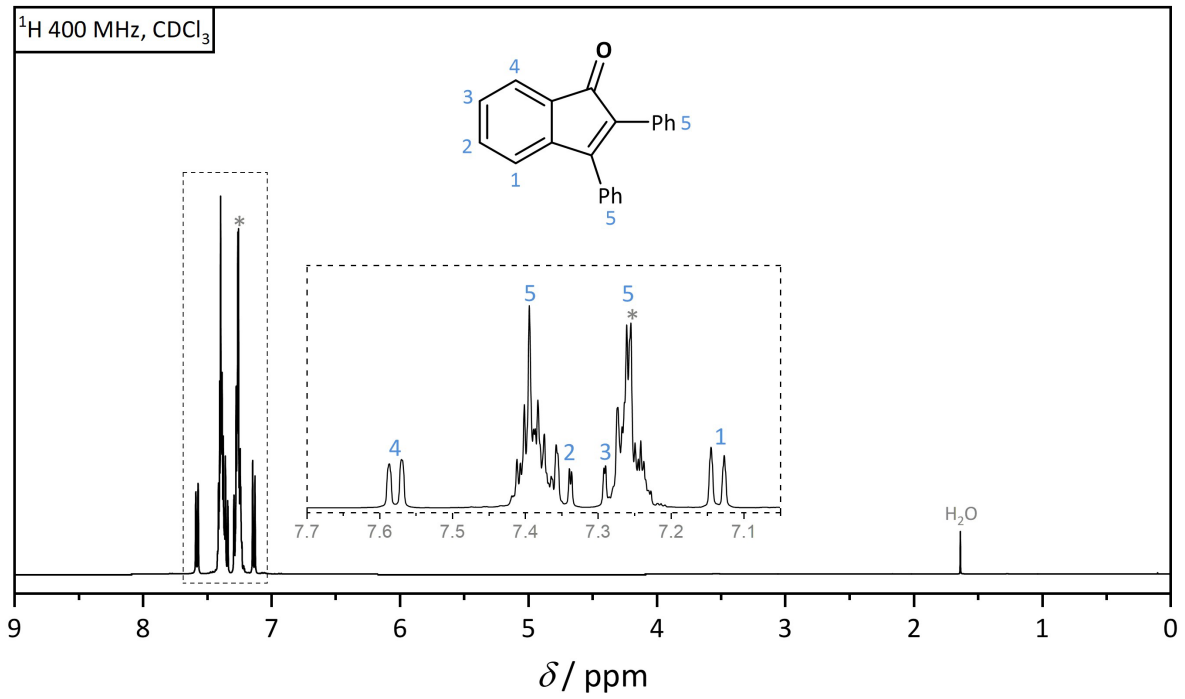

Figure S42. ^{1}H NMR (400 MHz) spectrum of **preDIO** in $CDCl_3$ (*) at ambient temperature.

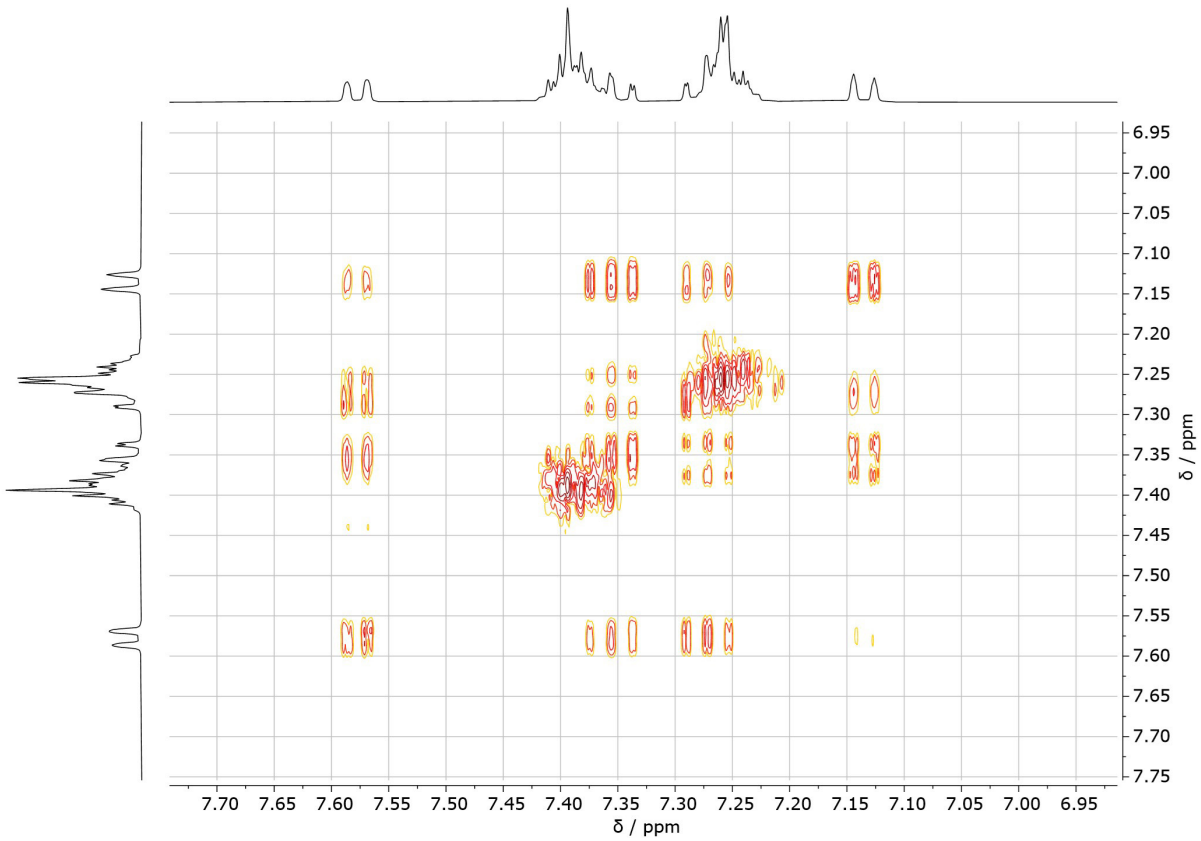

Figure S43. ^{1}H-^{1}H COSY (400 MHz) spectrum of **preDIO** in $CDCl_3$ (*) at ambient temperature.

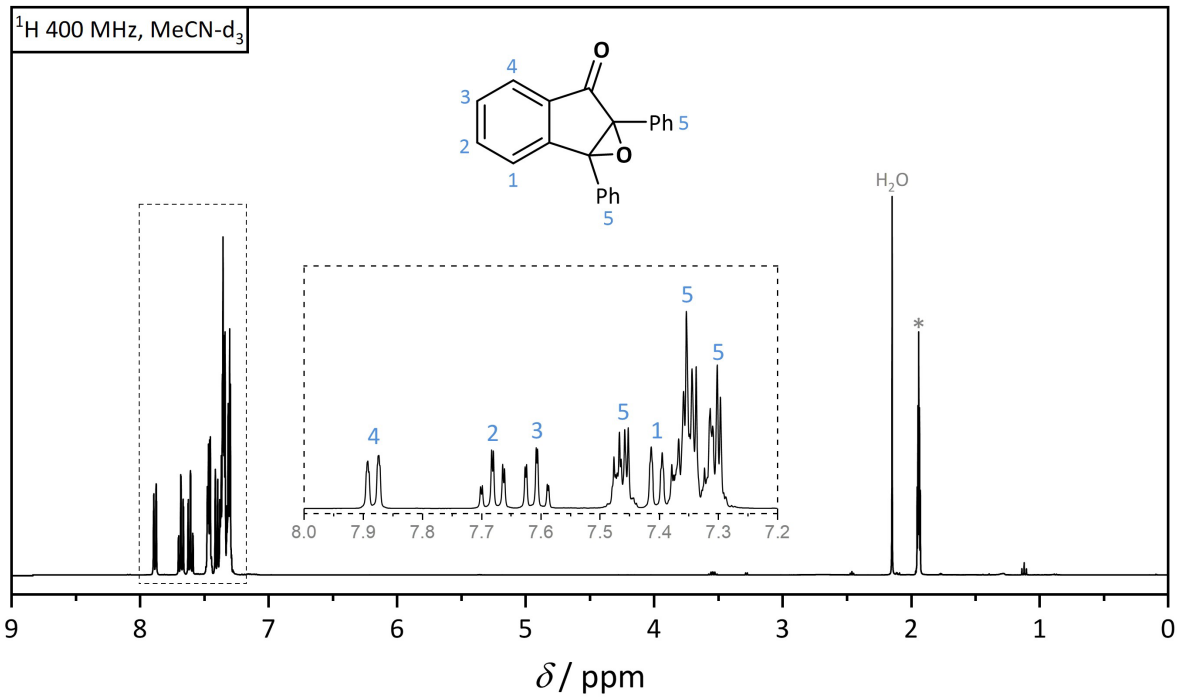

Figure S44. ^{1}H NMR (400 MHz) spectrum of **DIO** in MeCN-d$_3$ (*) at ambient temperature.

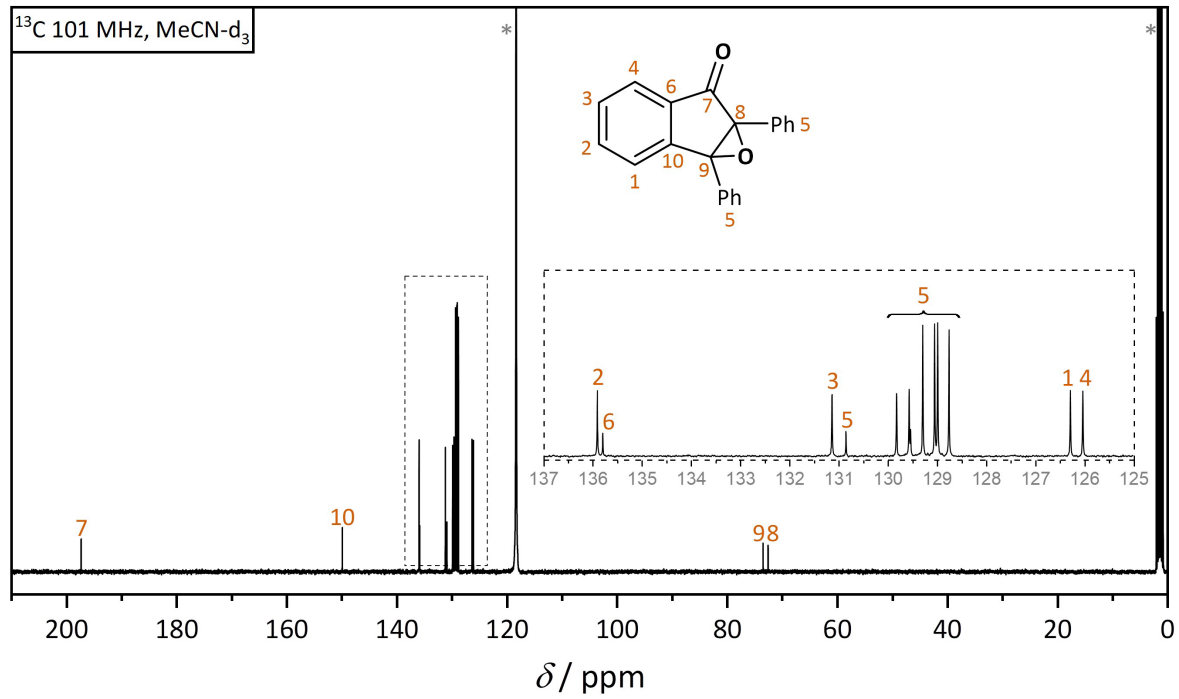

Figure S45. ^{13}C NMR (101 MHz) spectrum of **DIO** in MeCN-d$_3$ (*) at ambient temperature.

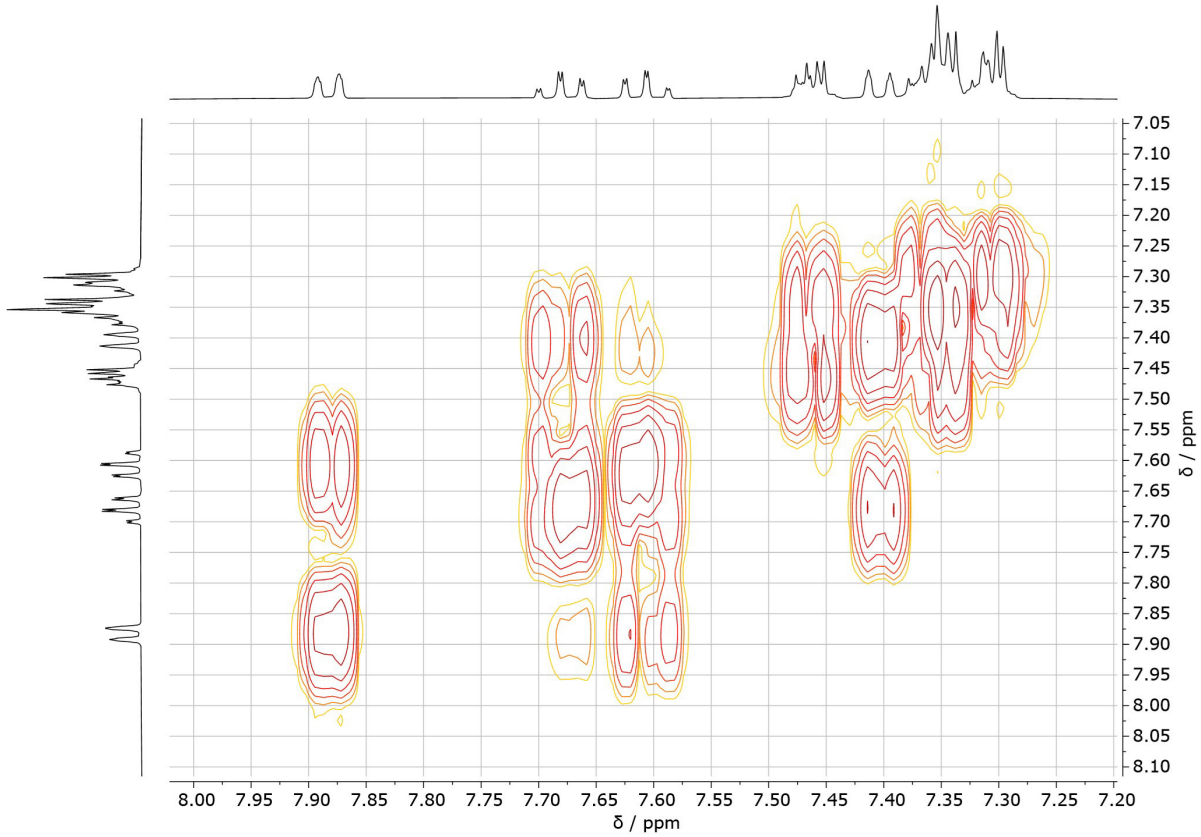

Figure S46. ^{1}H-^{1}H COSY (400 MHz) spectrum of **DIO** in MeCN-d_3 (*) at ambient temperature.

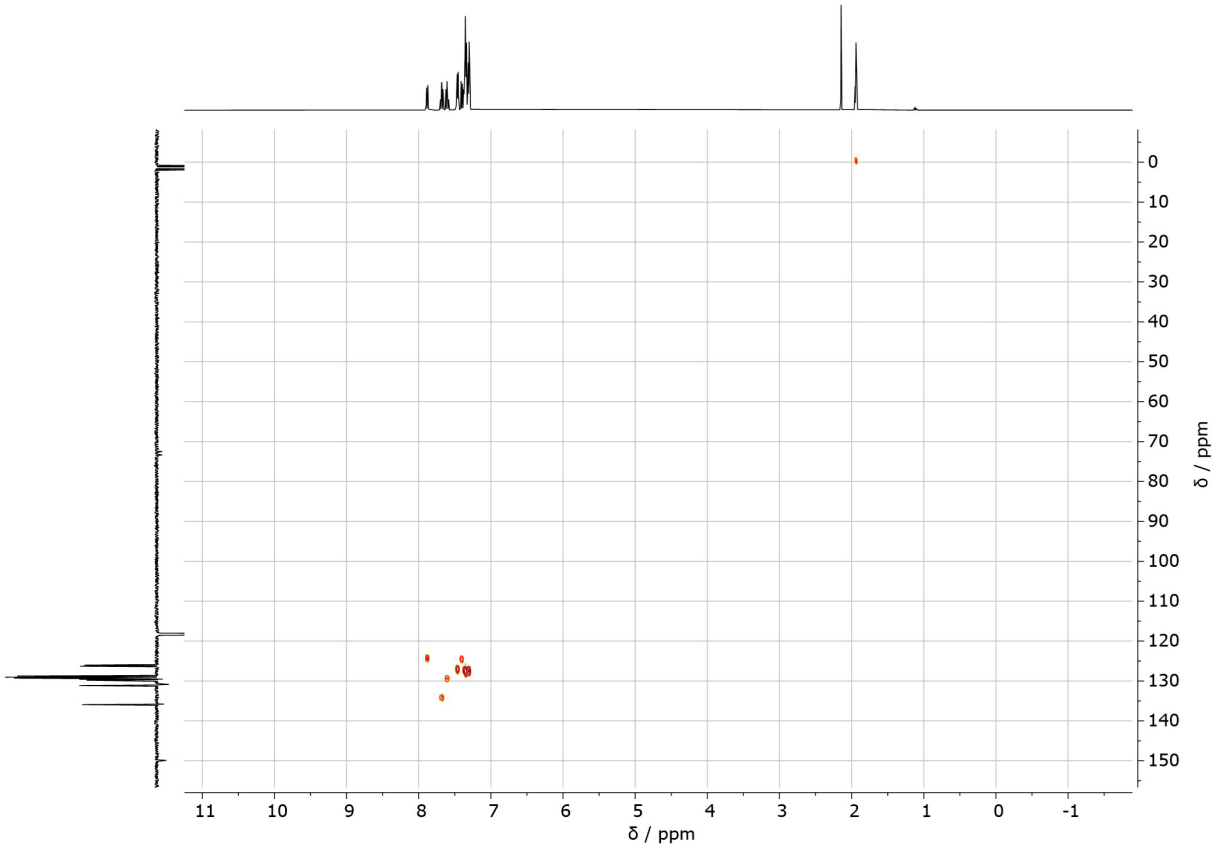

Figure S47. ^{1}H (400 MHz) - ^{13}C (101 MHz) HSQC spectrum of **DIO** in MeCN-d_3 (*) at ambient temperature.

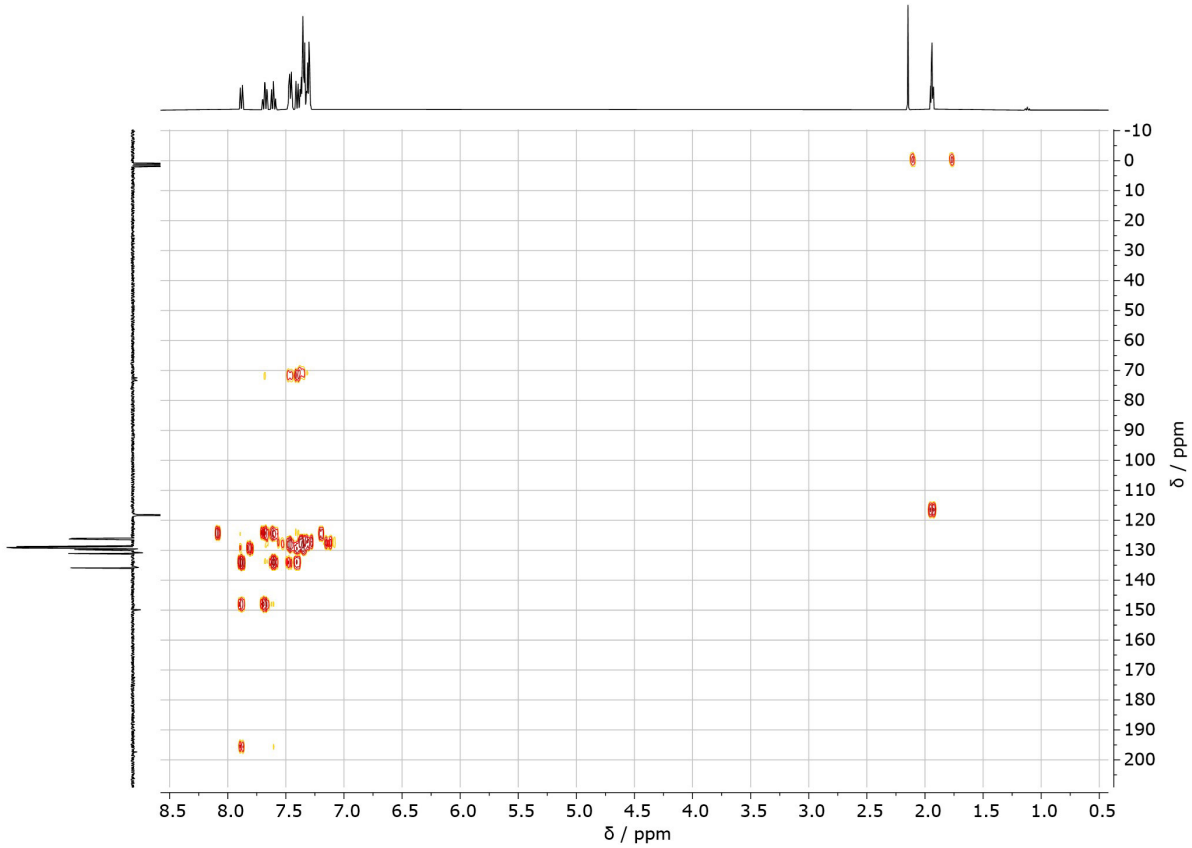

Figure S48. ^{1}H (400 MHz) - ^{13}C (101 MHz) HMBC spectrum of **DIO** in MeCN-d_3 (*) at ambient temperature.

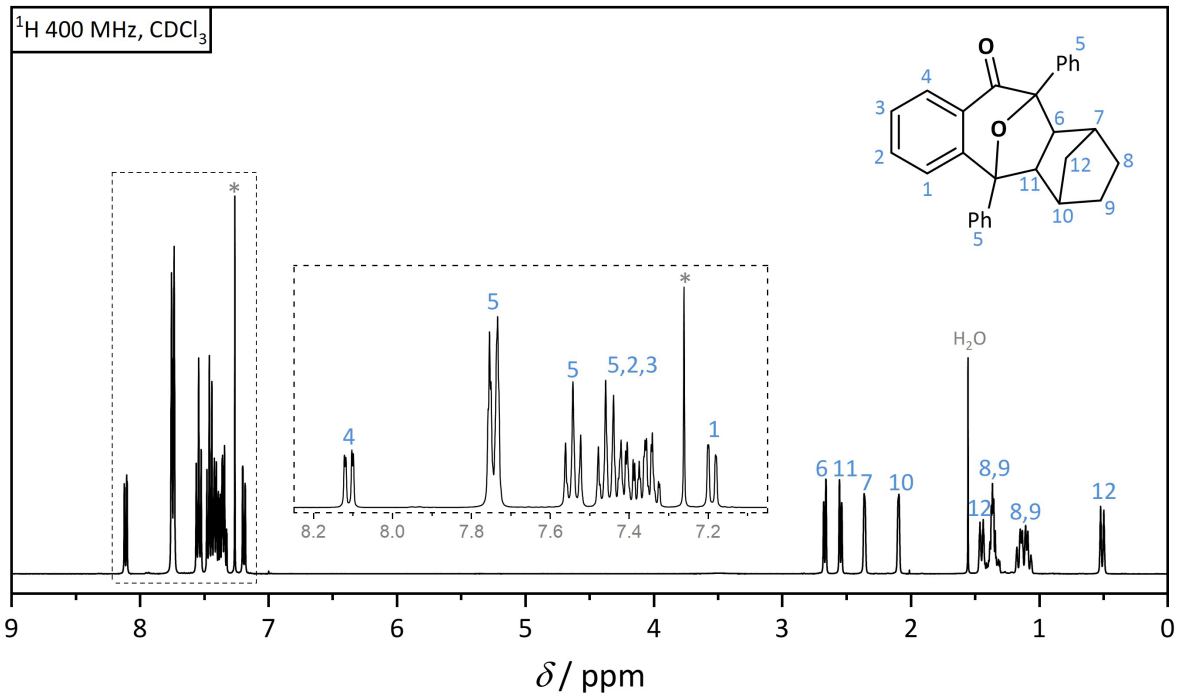

Figure S49. ^{1}H NMR (400 MHz) spectrum of **DIOnor** in $CDCl_3$ (*) at ambient temperature.

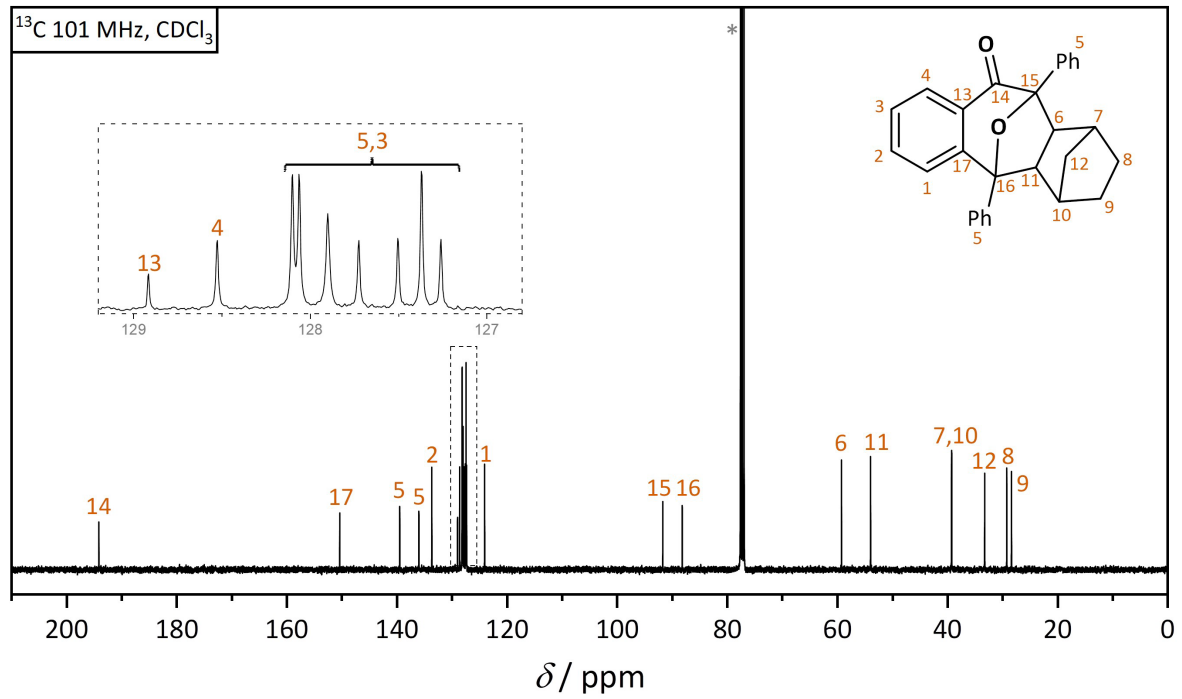

Figure S50. ^{13}C NMR (101 MHz) spectrum of **DIOnor** in $CDCl_3$ (*) at ambient temperature.

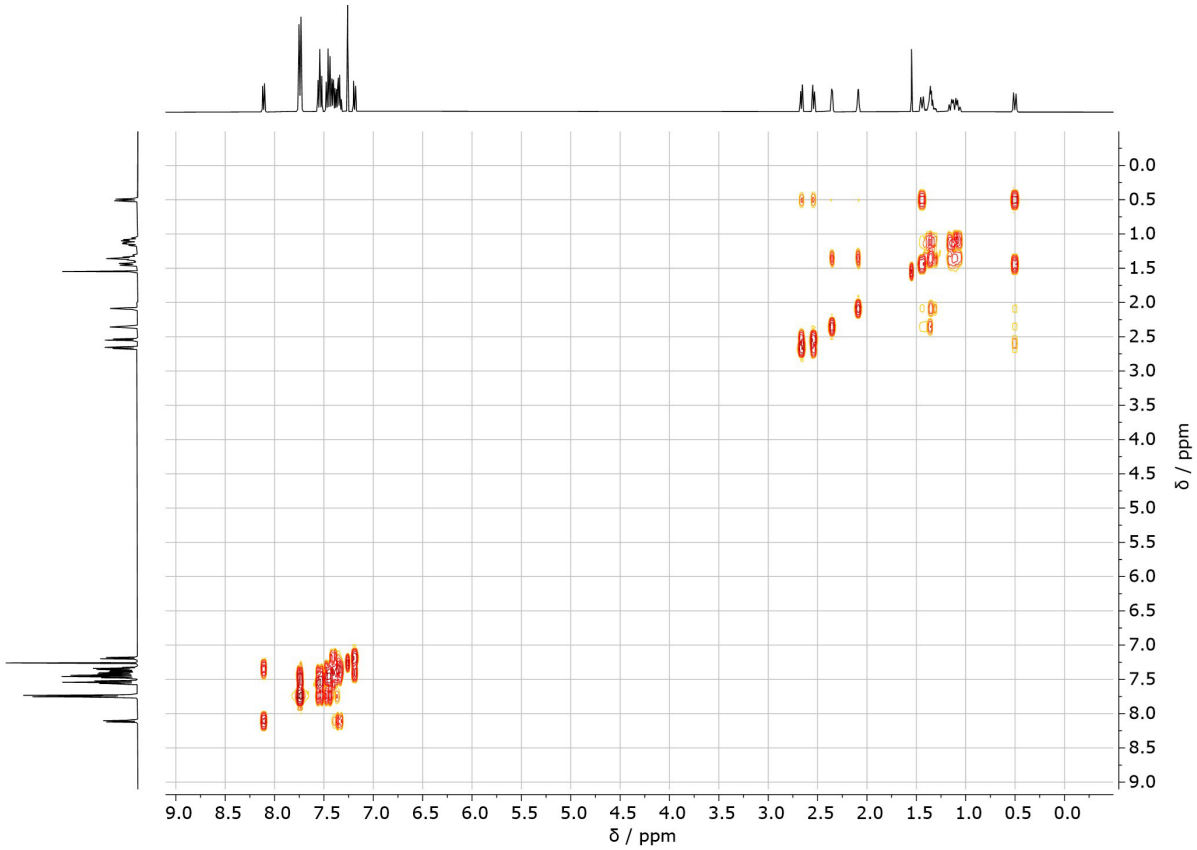

Figure S51. ^{1}H-^{1}H COSY (400 MHz) spectrum of **DIOnor** in $CDCl_3$ (*) at ambient temperature.

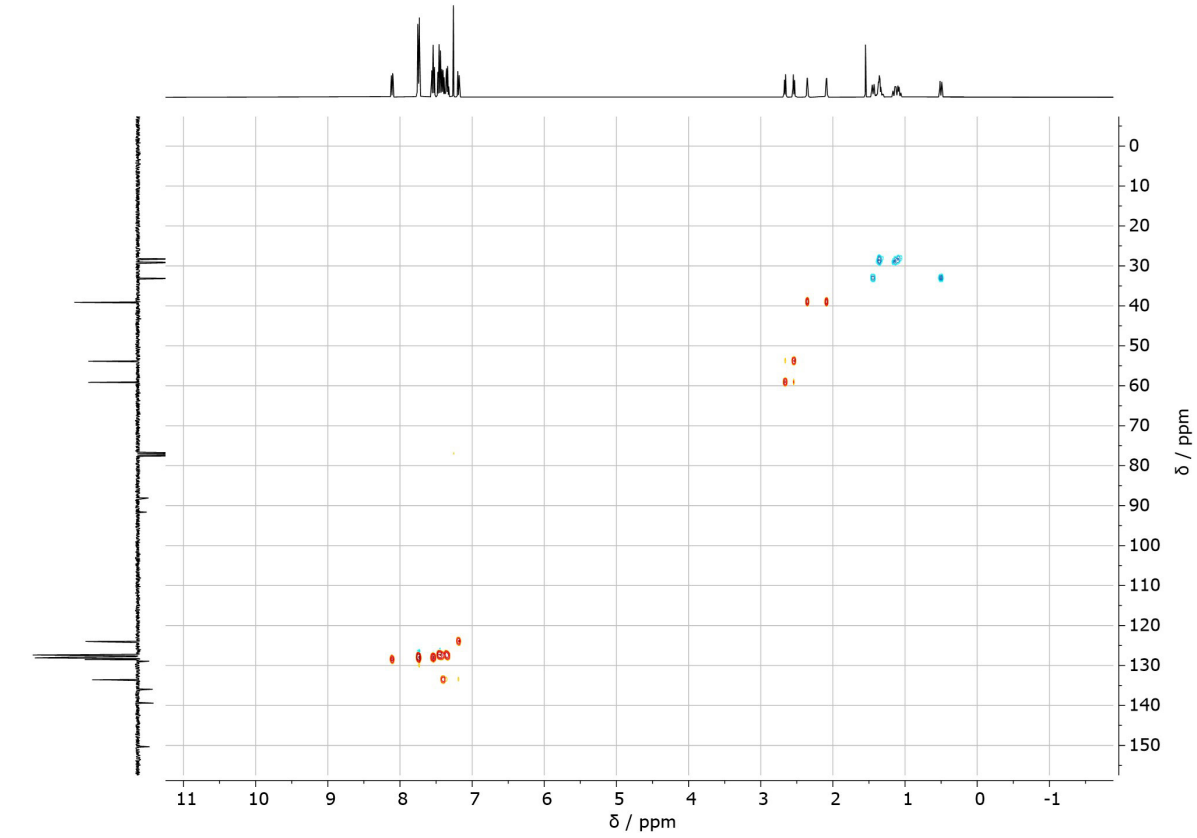

Figure S52. ^{1}H (400 MHz) - ^{13}C (101 MHz) HSQC spectrum of **DIOnor** in $CDCl_3$ (*) at ambient temperature.

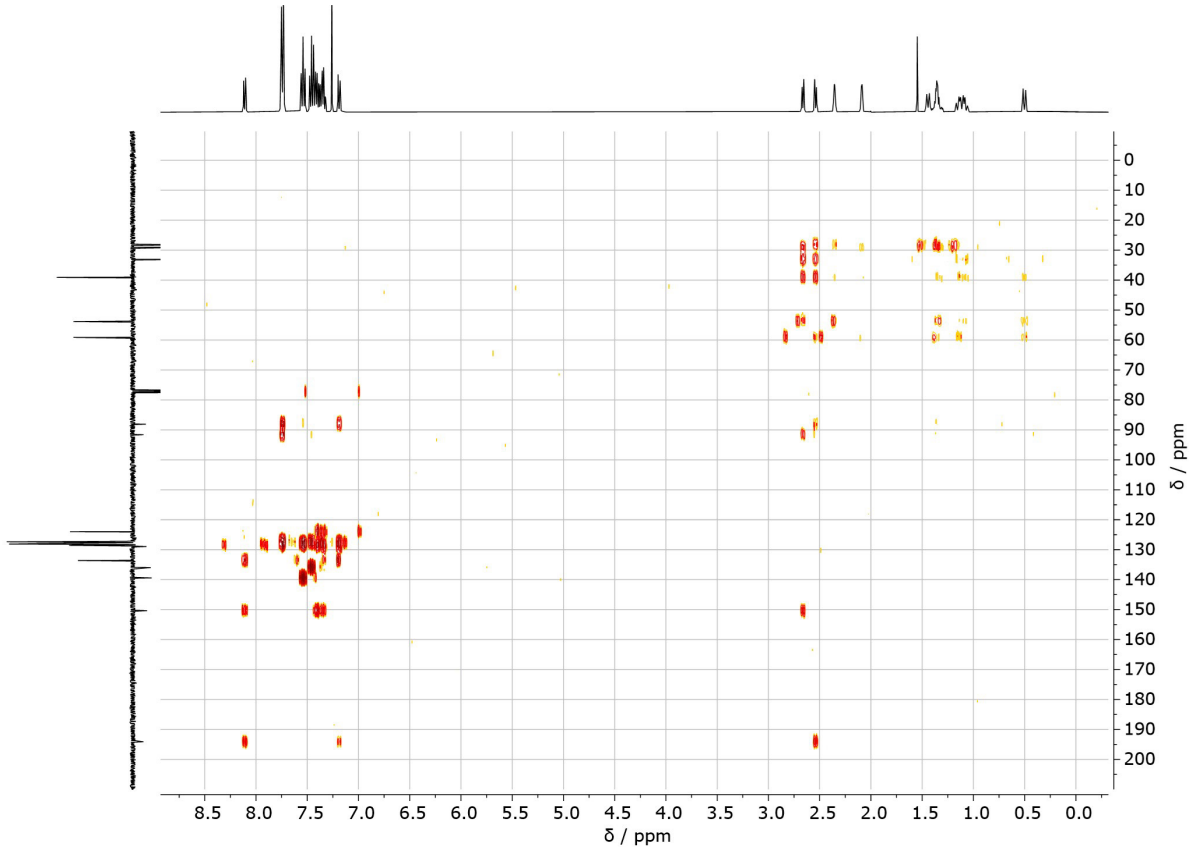

Figure S53. ^{1}H (400 MHz) - ^{13}C (101 MHz) HMBC spectrum of **DIOnor** in $CDCl_3$ (*) at ambient temperature.

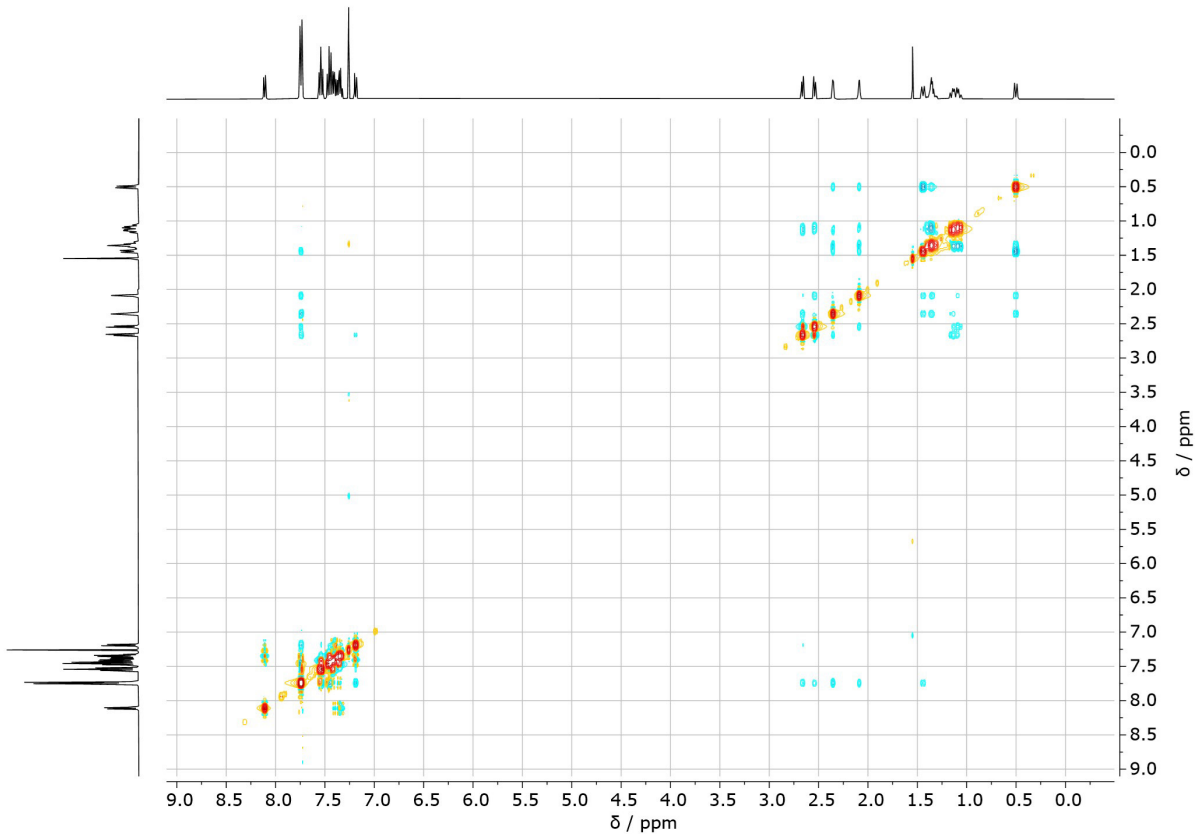

Figure S54. ^{1}H (400 MHz) - ^{13}C (101 MHz) NOESY spectrum of **DIOnor** in $CDCl_3$ (*) at ambient temperature.

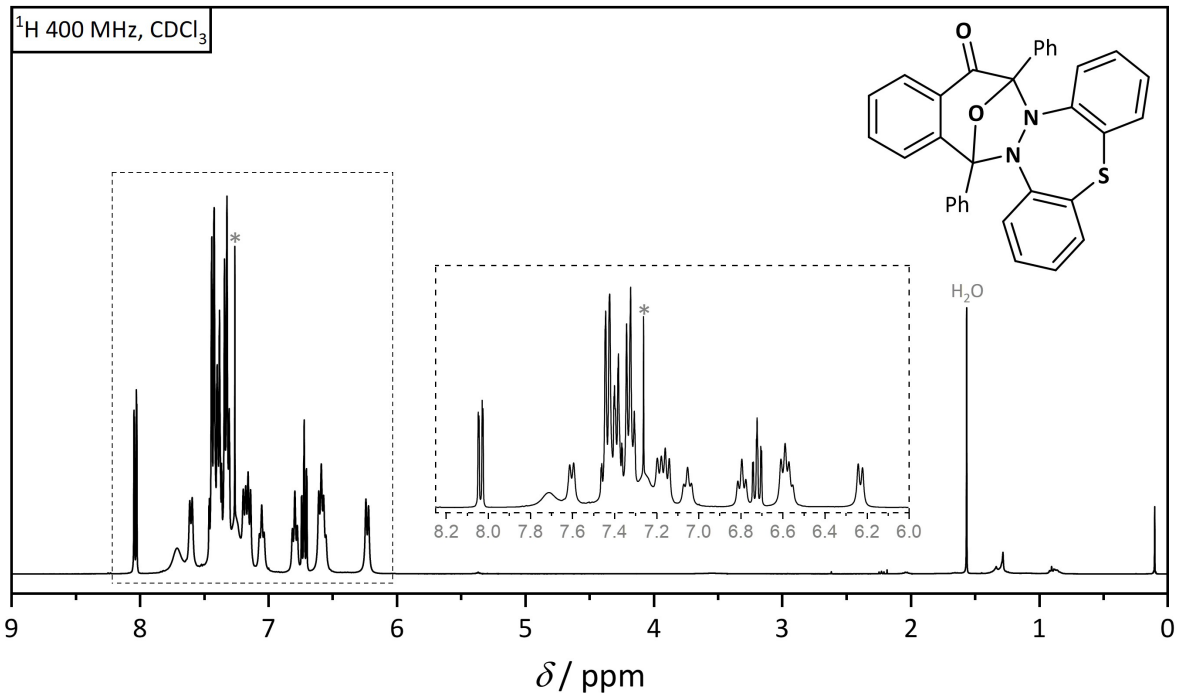

Figure S55. ^{1}H NMR (400 MHz) spectrum of **DIOSA** in $CDCl_3$ (*) at ambient temperature.

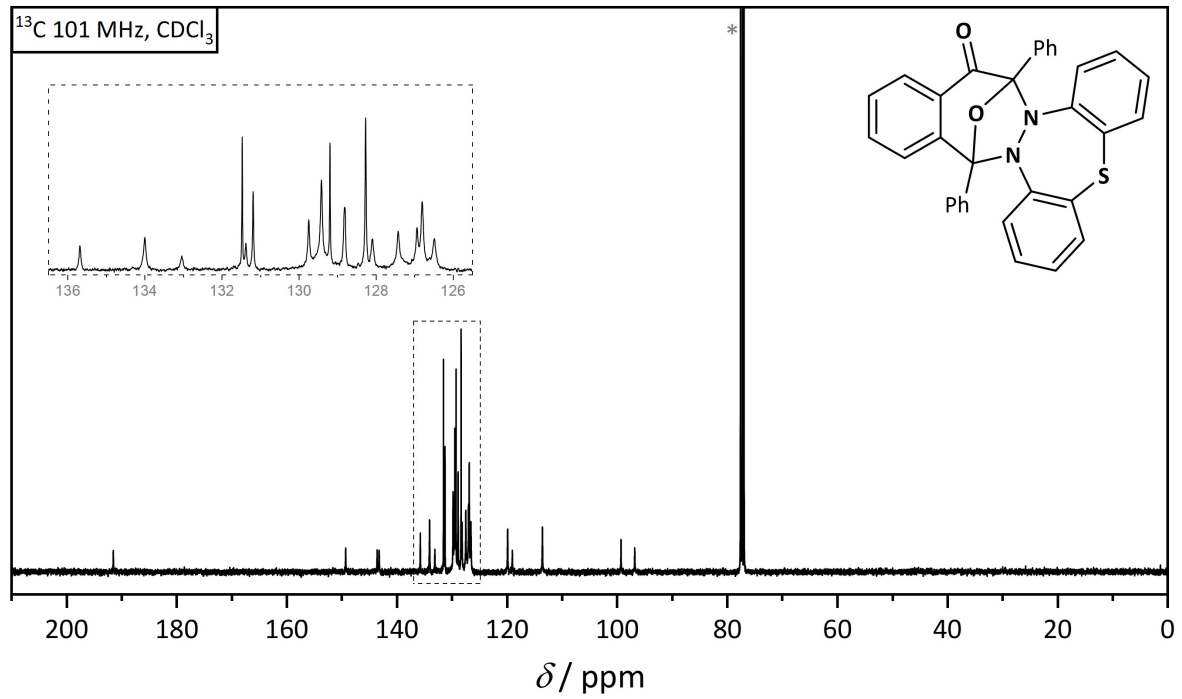

Figure S56. ^{13}C NMR (101 MHz) spectrum of **DIOSA** in $CDCl_3$ (*) at ambient temperature.

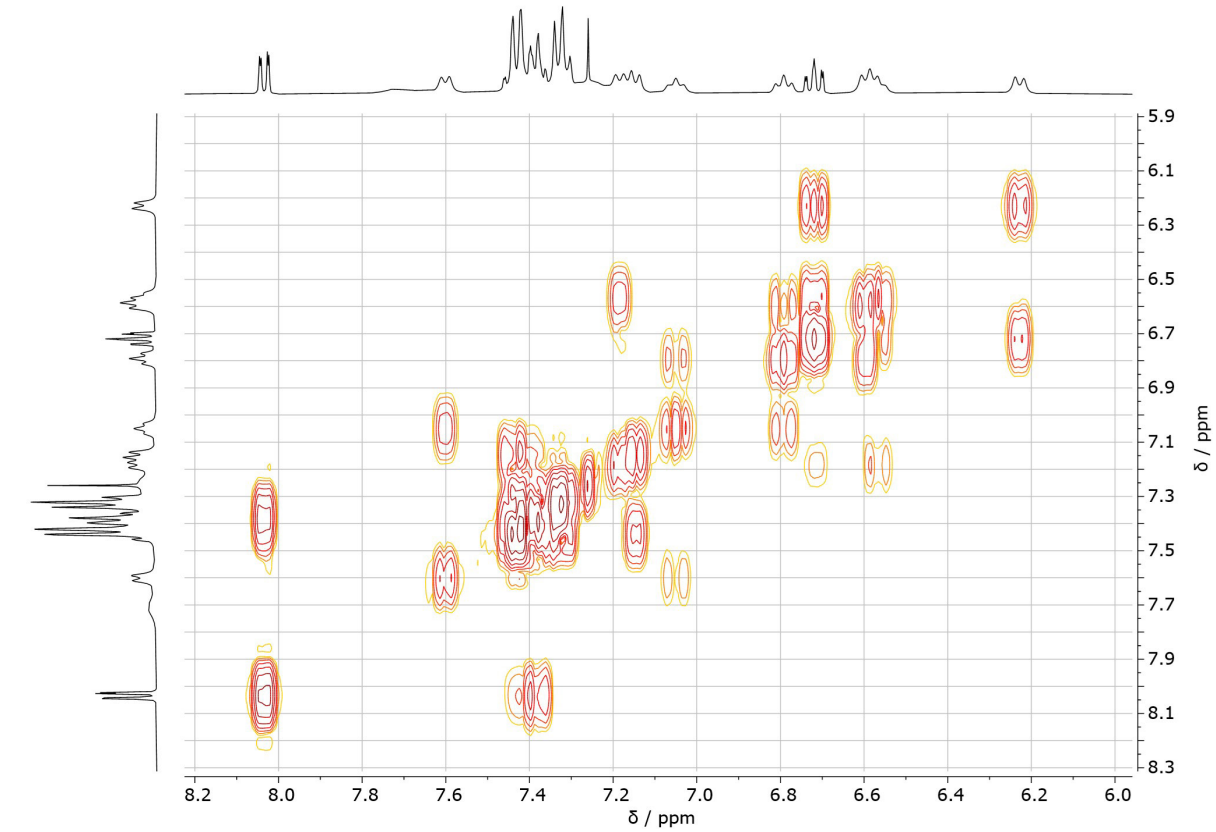

Figure S57. ^{1}H-^{1}H COSY (400 MHz) spectrum of **DIOSA** in $CDCl_3$ (*) at ambient temperature.

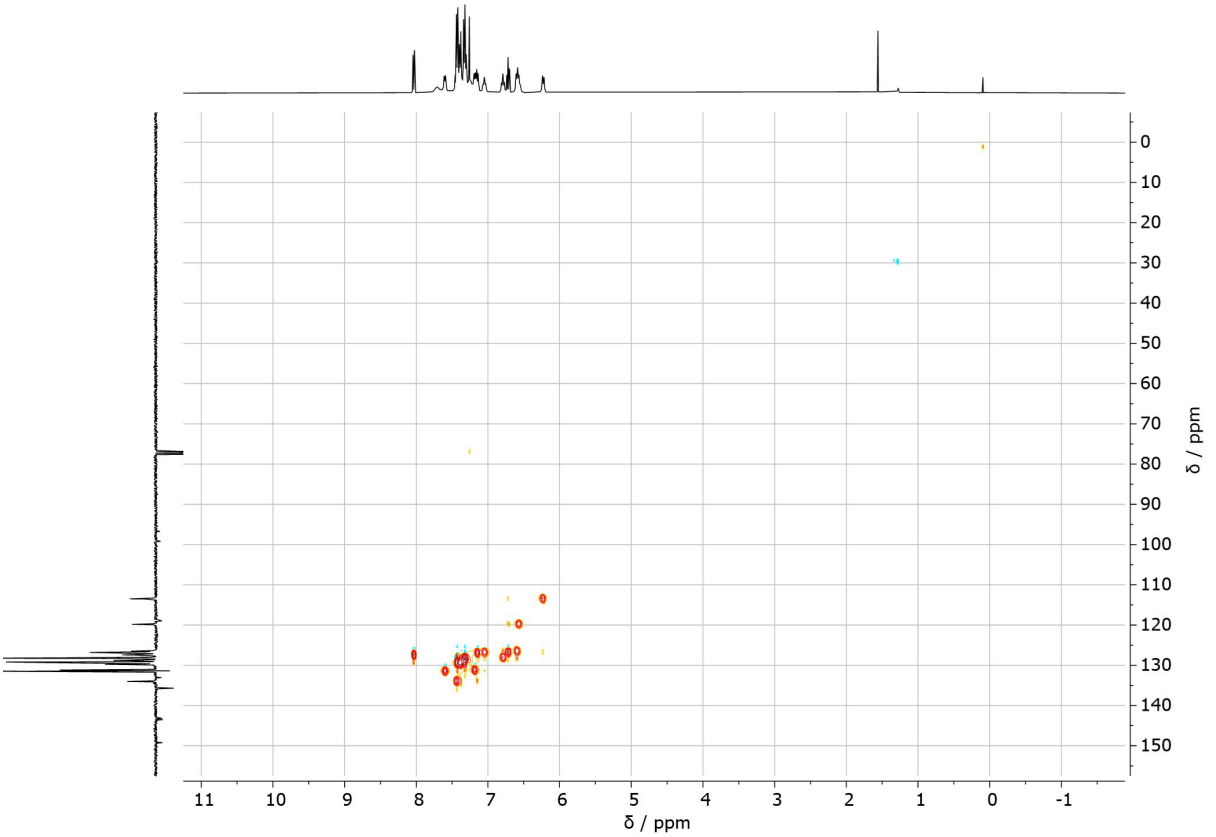

Figure S58. ^{1}H (400 MHz) - ^{13}C (101 MHz) HSQC spectrum of **DIOSA** in $CDCl_3$ (*) at ambient temperature.

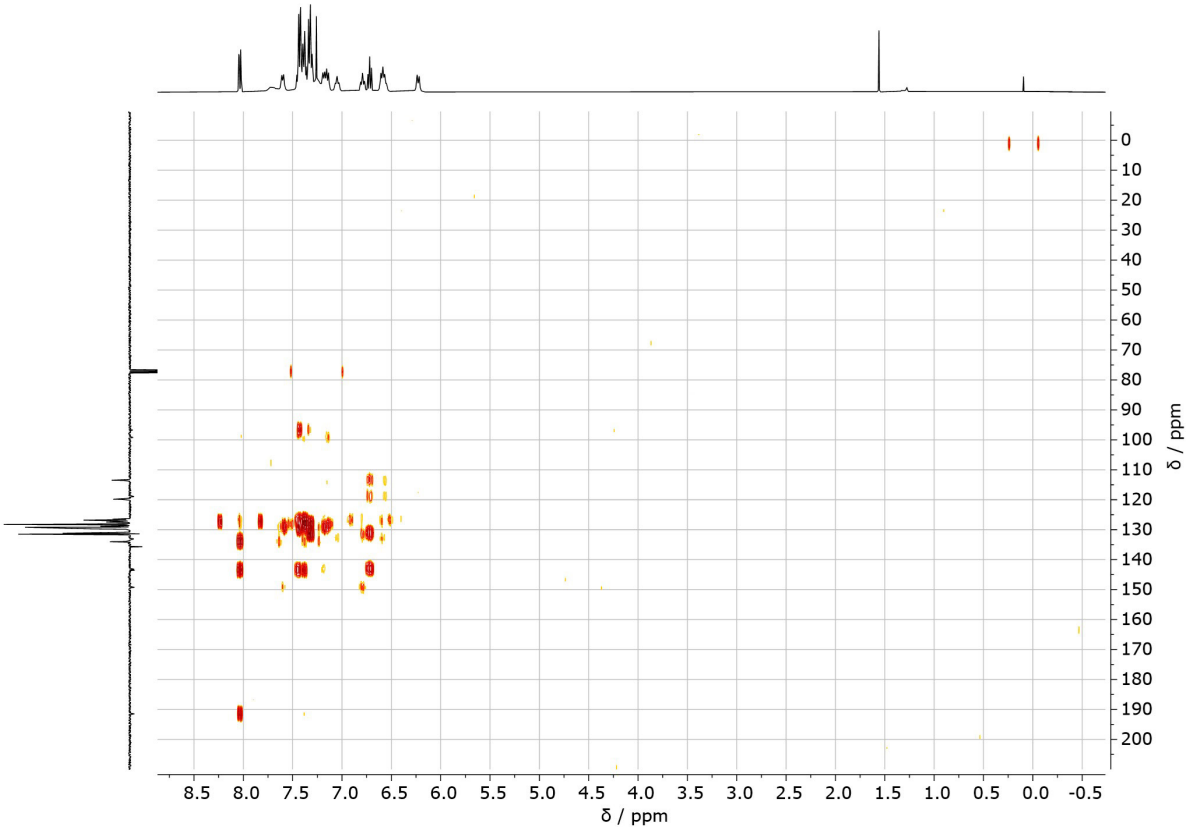

Figure S59. ^{1}H (400 MHz) - ^{13}C (101 MHz) HMBC spectrum of **DIOSA** in $CDCl_3$ (*) at ambient temperature.

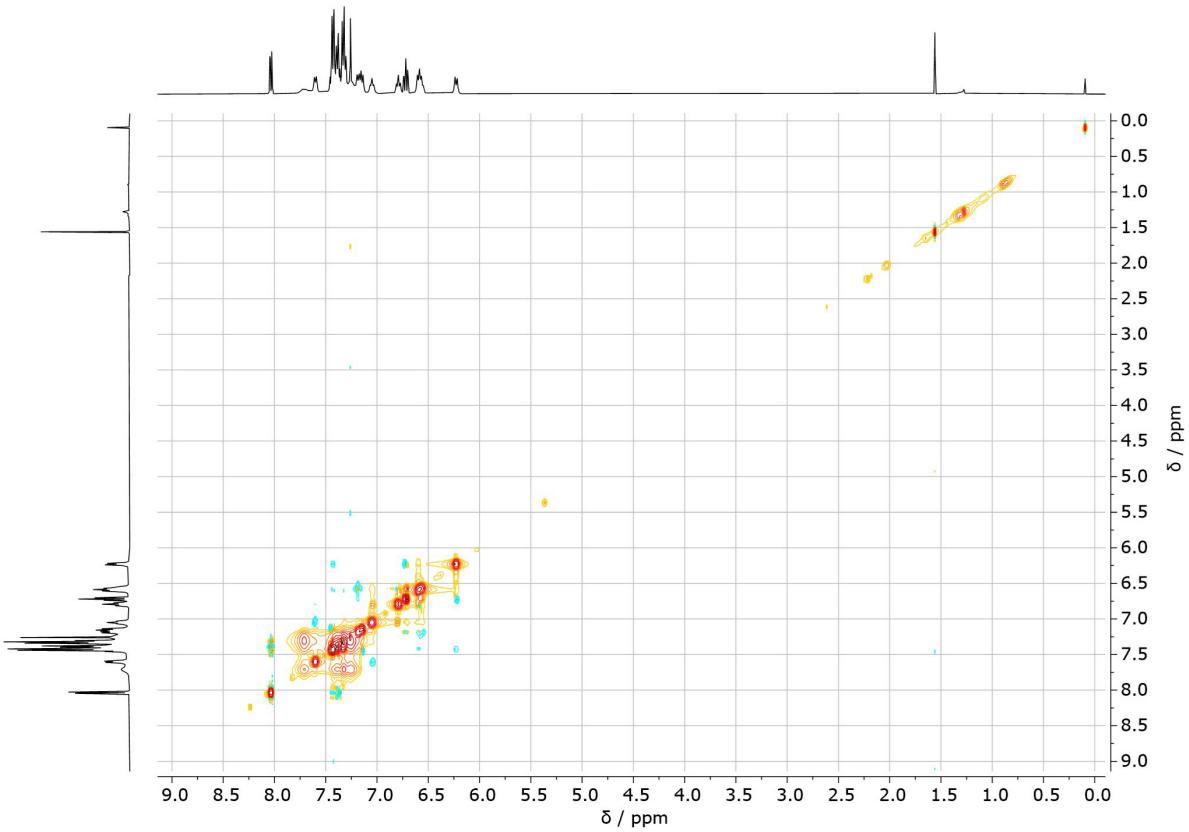

Figure S60. ^{1}H (400 MHz) - ^{13}C (101 MHz) NOESY spectrum of **DIOSA** in $CDCl_3$ (*) at ambient temperature.

7.7.2 Macromolecular study

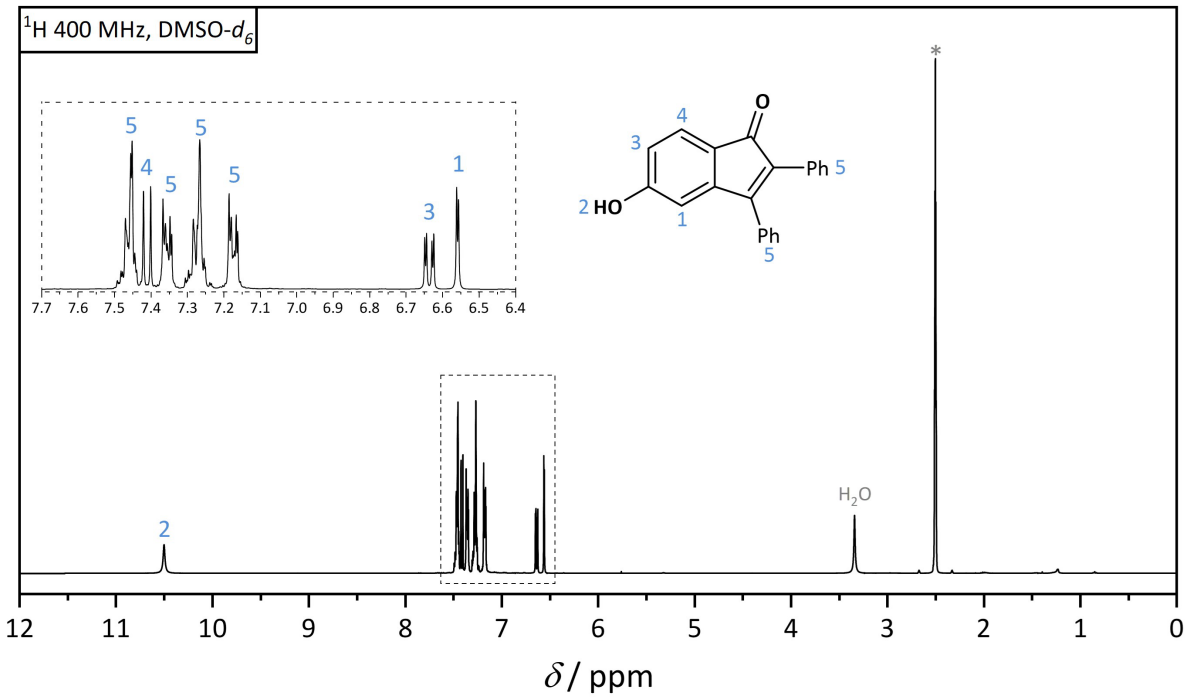

Figure S61. ^{1}H NMR (400 MHz) spectrum of **1** in DMSO-d_6 (*) at ambient temperature.

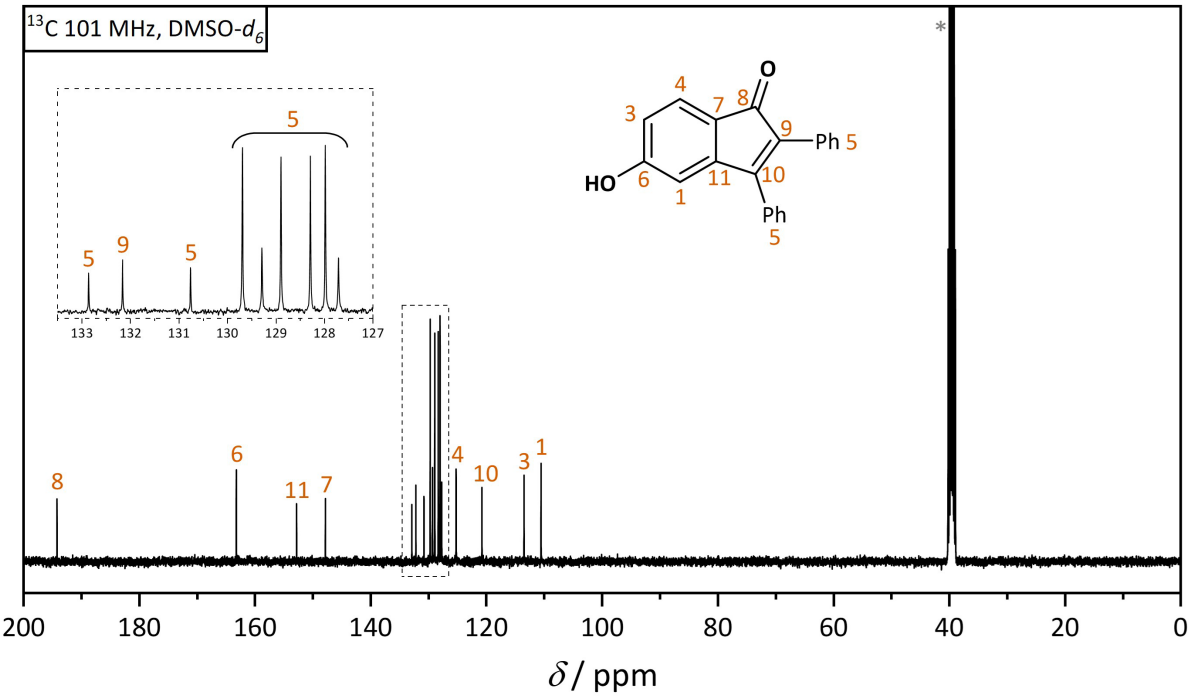

Figure S62. ^{13}C NMR (101 MHz) spectrum of **1** in DMSO-d_6 (*) at ambient temperature.

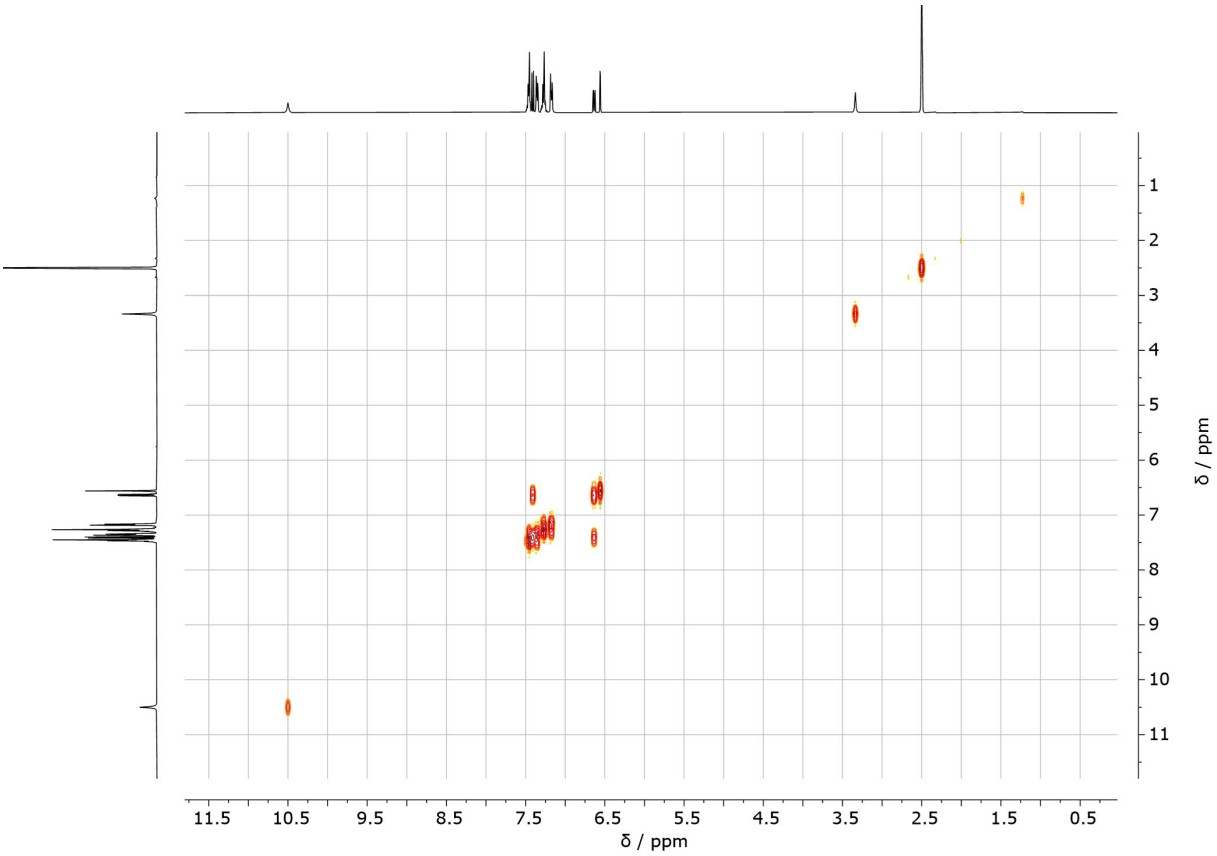

Figure S63. ^{1}H-^{1}H COSY (400 MHz) spectrum of **1** in DMSO-d_6 at ambient temperature.

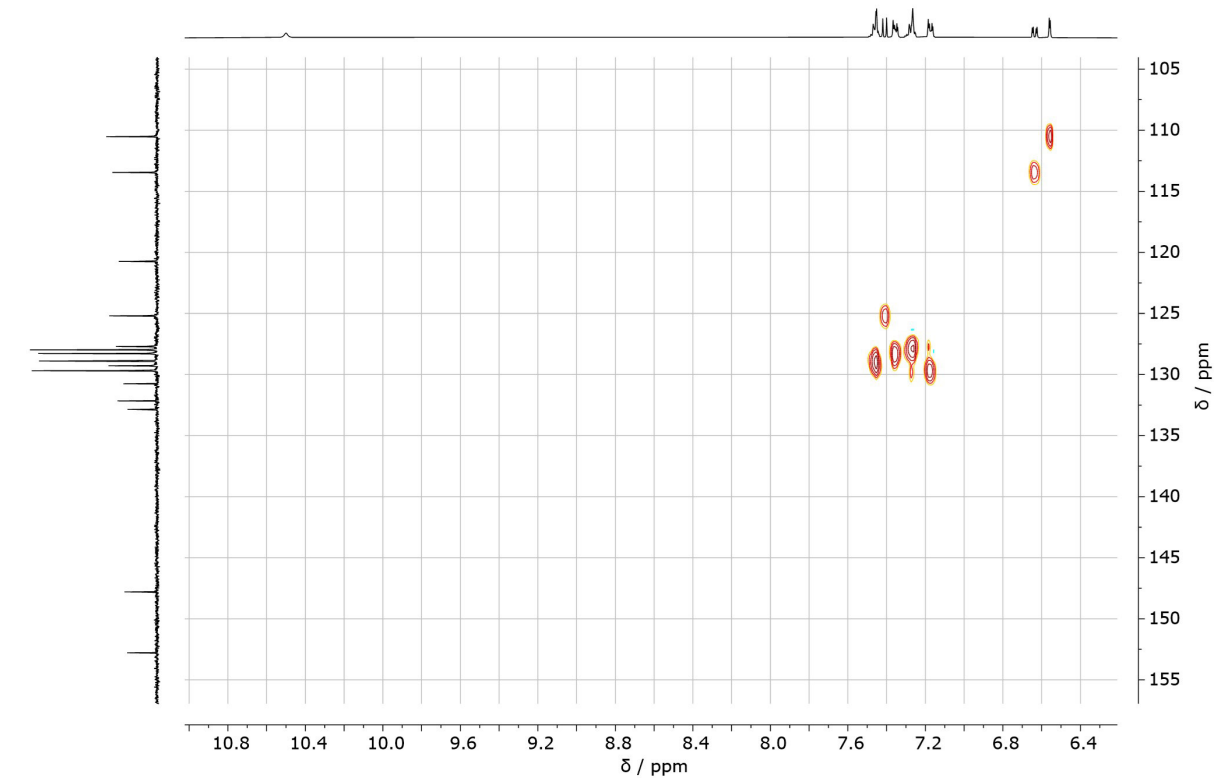

Figure S64. ^{1}H (400 MHz) - ^{13}C (101 MHz) HSQC spectrum of **1** in DMSO-d_6 at ambient temperature.

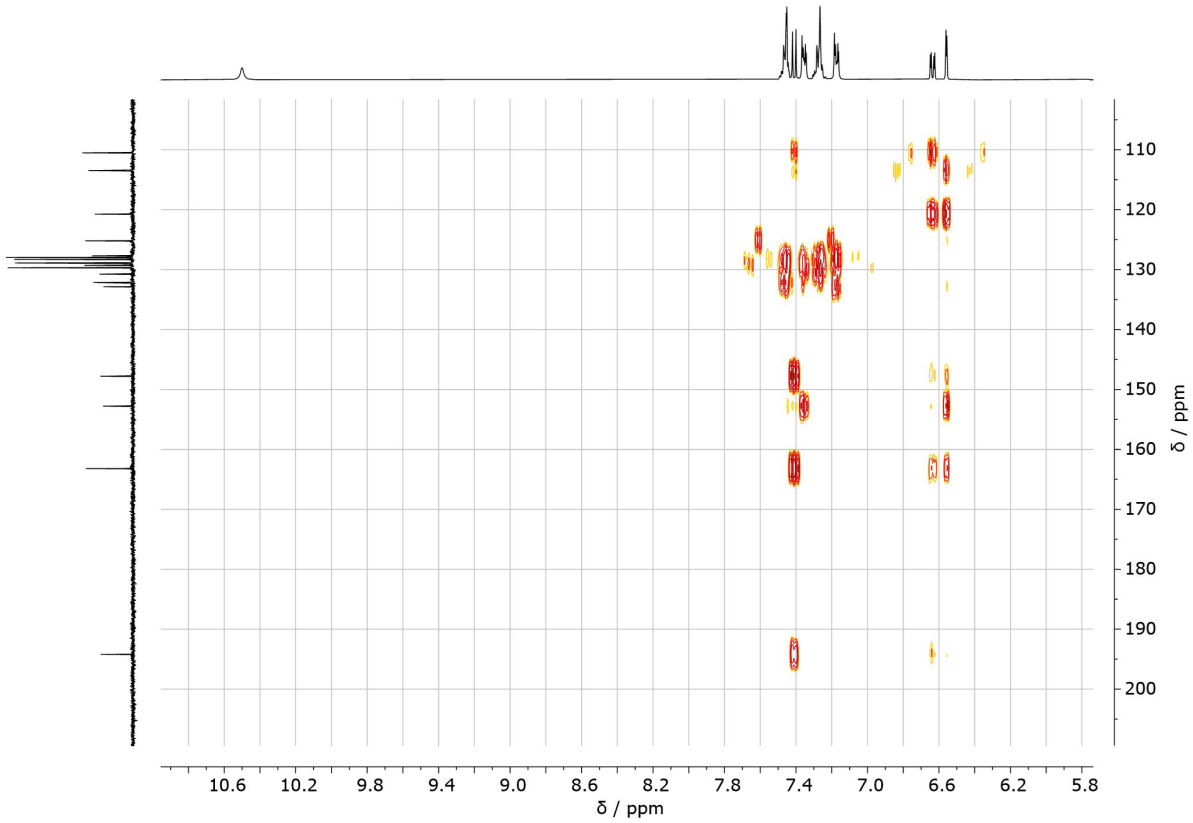

Figure S65. ^{1}H (400 MHz) - ^{13}C (101 MHz) HMBC spectrum of **1** in DMSO-d_6 at ambient temperature.

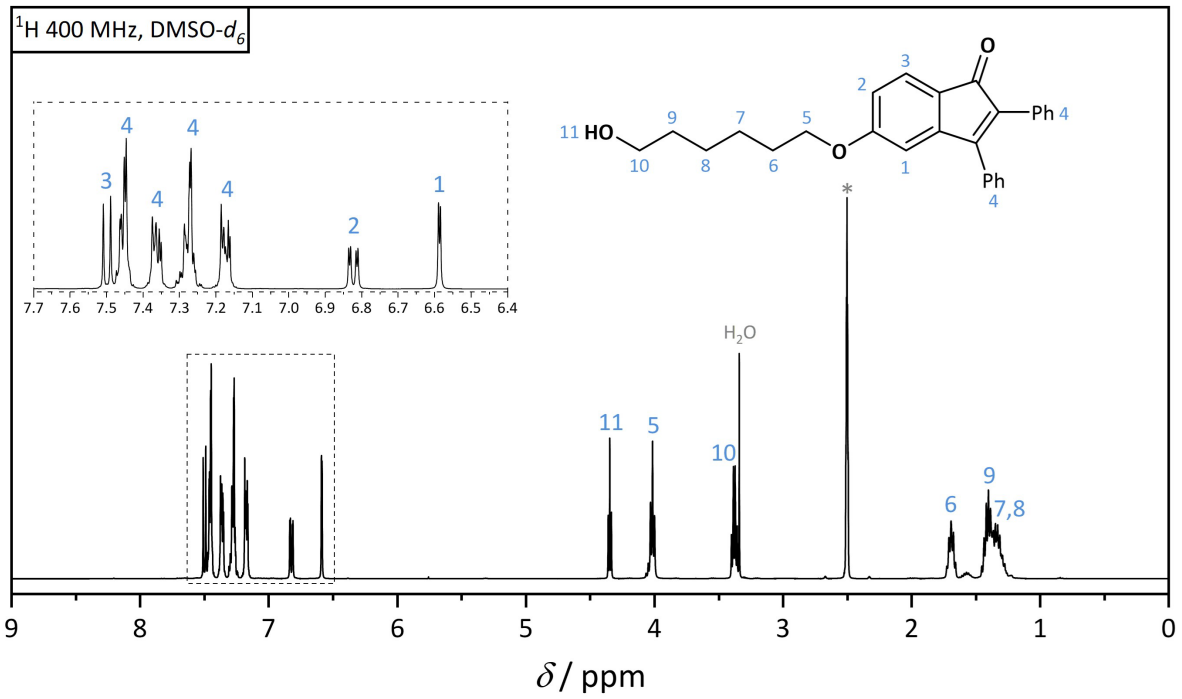

Figure S66. ^{1}H NMR (400 MHz) spectrum of **2** in DMSO-d_6 (*) at ambient temperature.

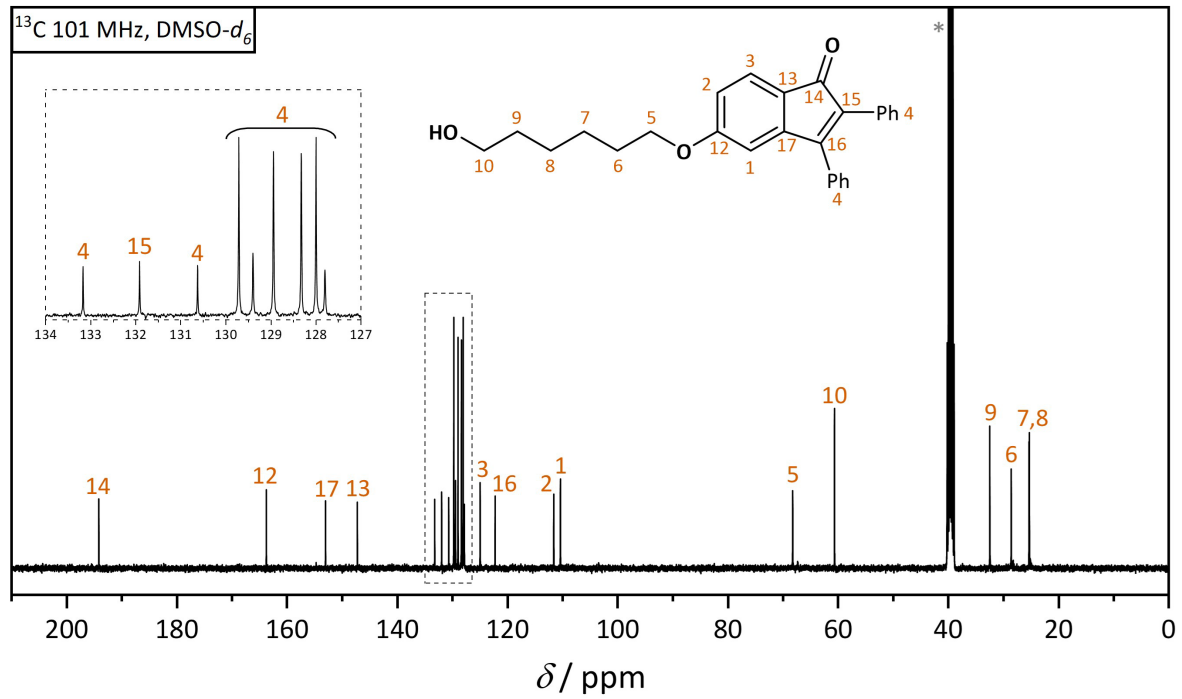

Figure S67. ^{13}C NMR (101 MHz) spectrum of **2** in DMSO-d_6 (*) at ambient temperature.

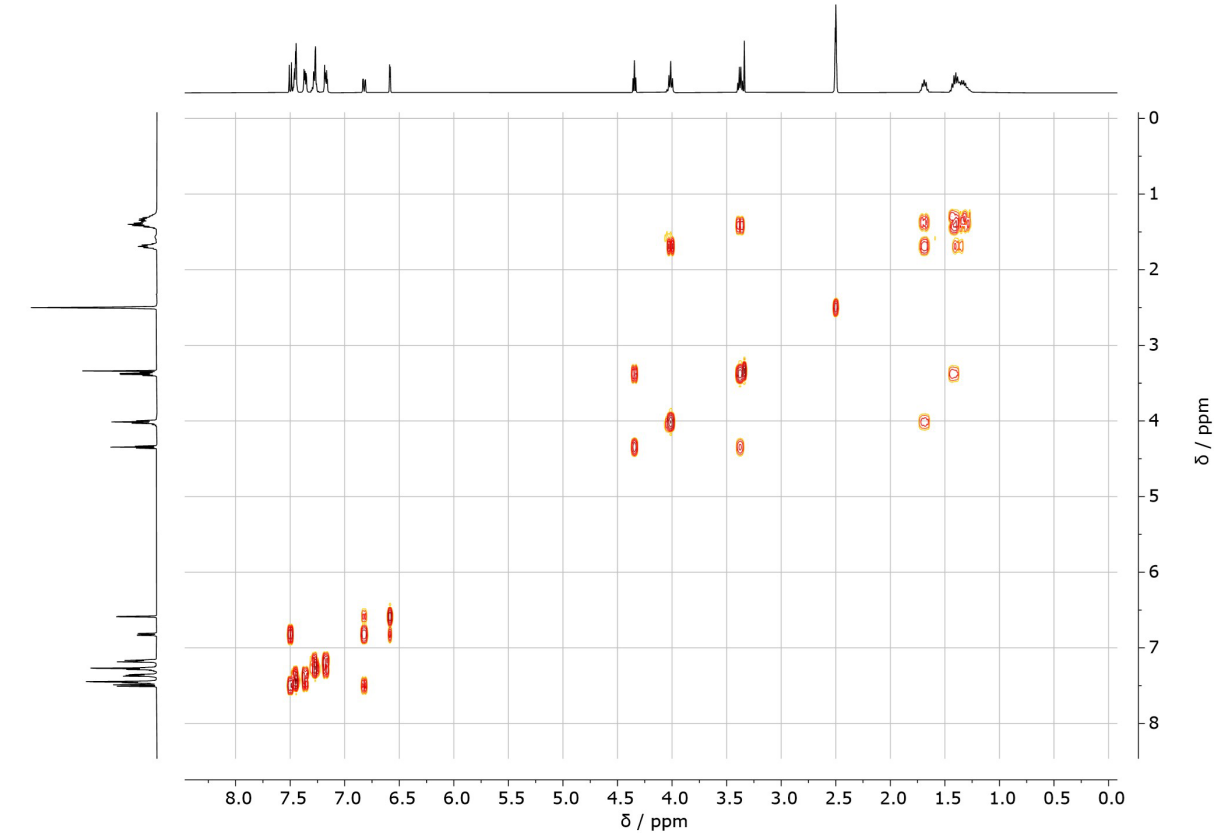

Figure S68. ^{1}H-^{1}H COSY (400 MHz) spectrum of **2** in DMSO-d_6 at ambient temperature.

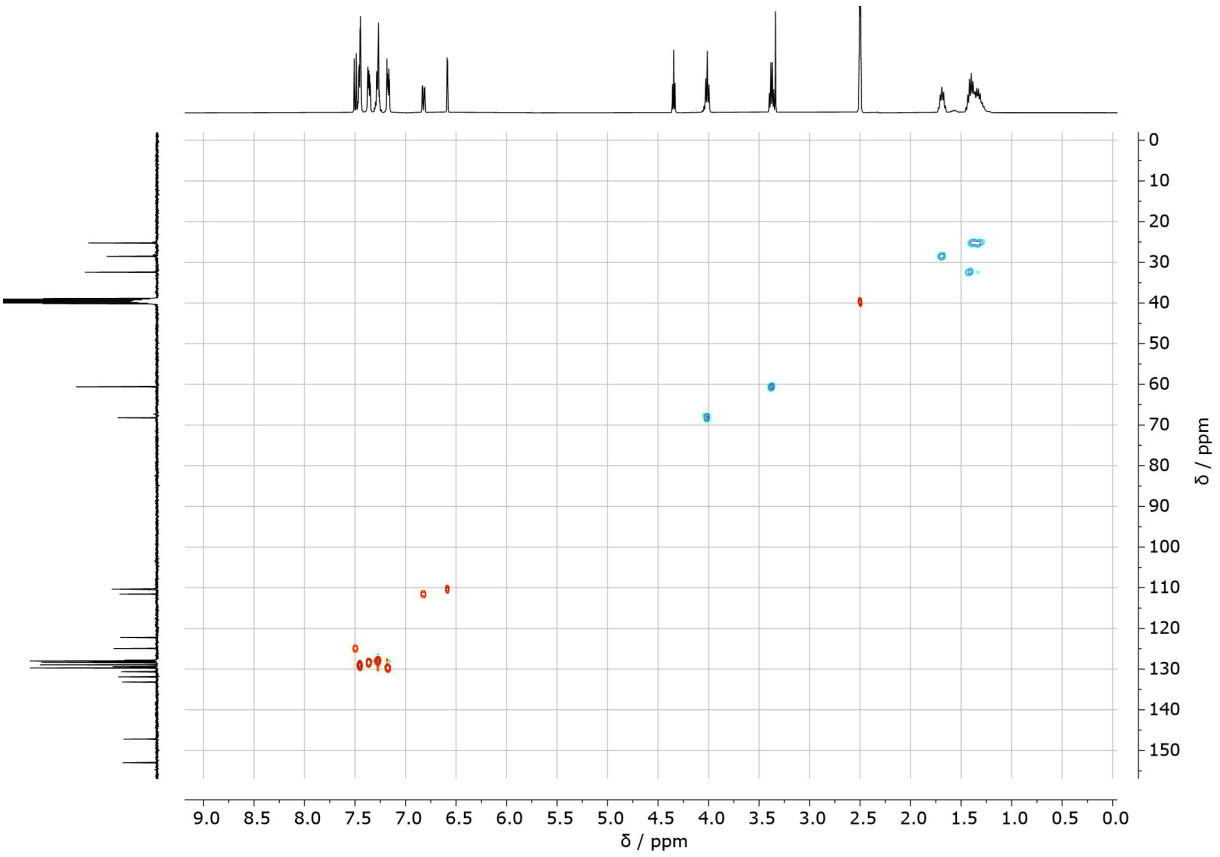

Figure S69. ^{1}H (400 MHz) - ^{13}C (101 MHz) HSQC spectrum of **2** in DMSO-d_6 at ambient temperature.

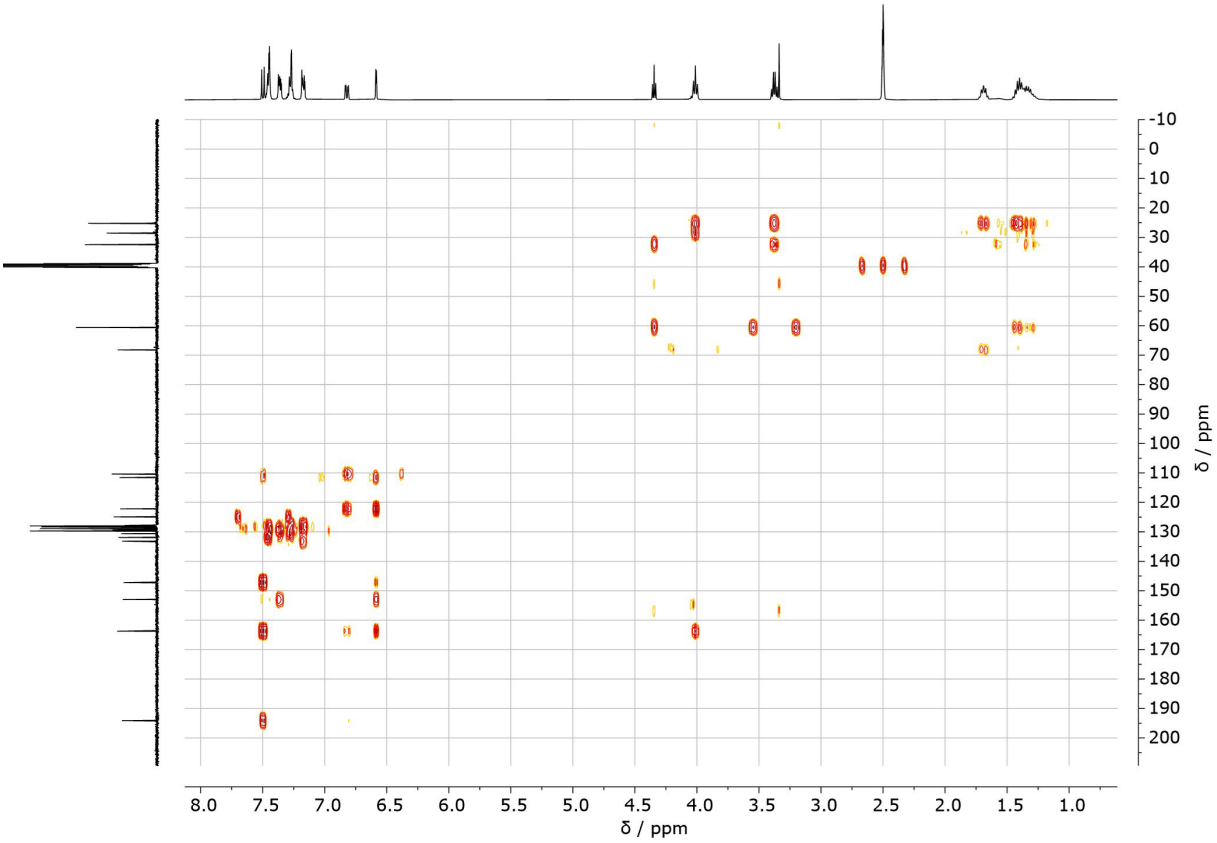

Figure S70. ^{1}H (400 MHz) - ^{13}C (101 MHz) HMBC spectrum of **2** in DMSO-d_6 at ambient temperature.

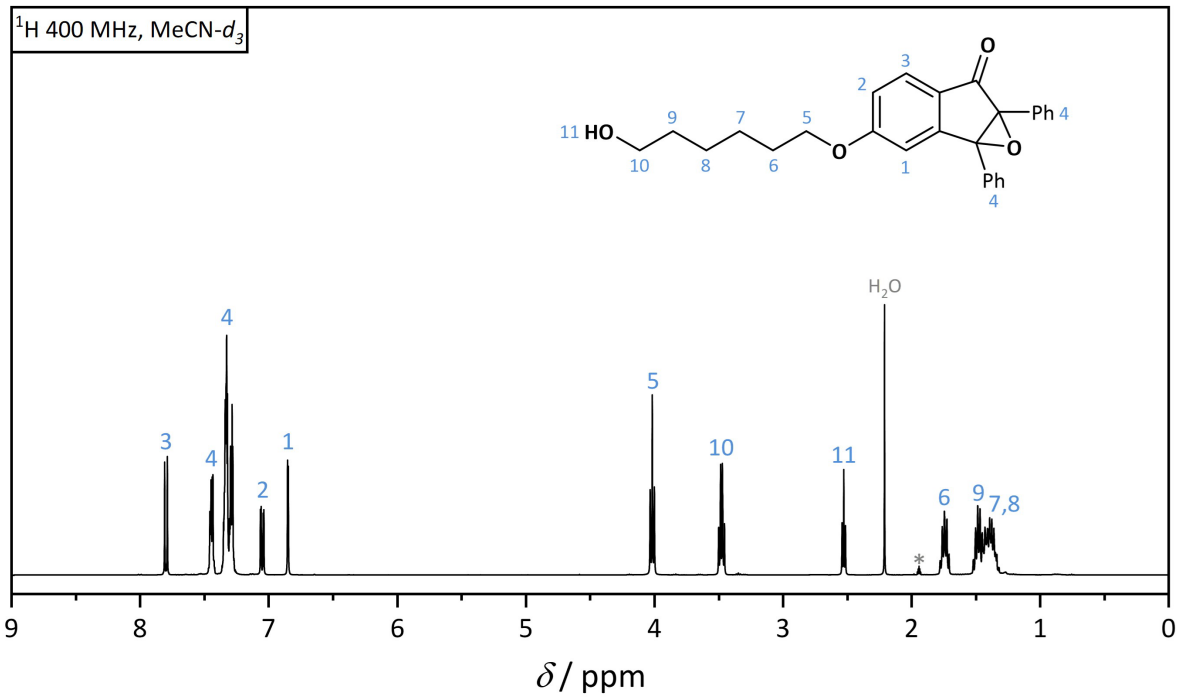

Figure S71. ^{1}H NMR (400 MHz) spectrum of **DIO-OH** in MeCN-d_3 (*) at ambient temperature.

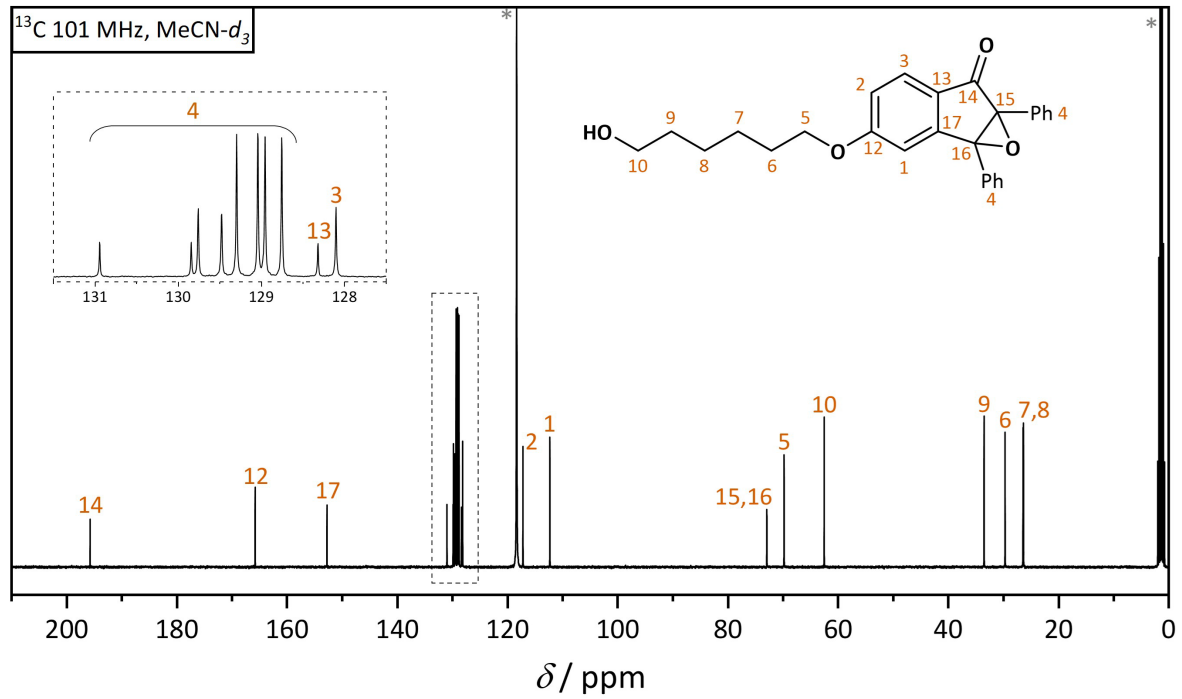

Figure S72. ^{13}C NMR (101 MHz) spectrum of **DIO-OH** in MeCN-d_3 (*) at ambient temperature.

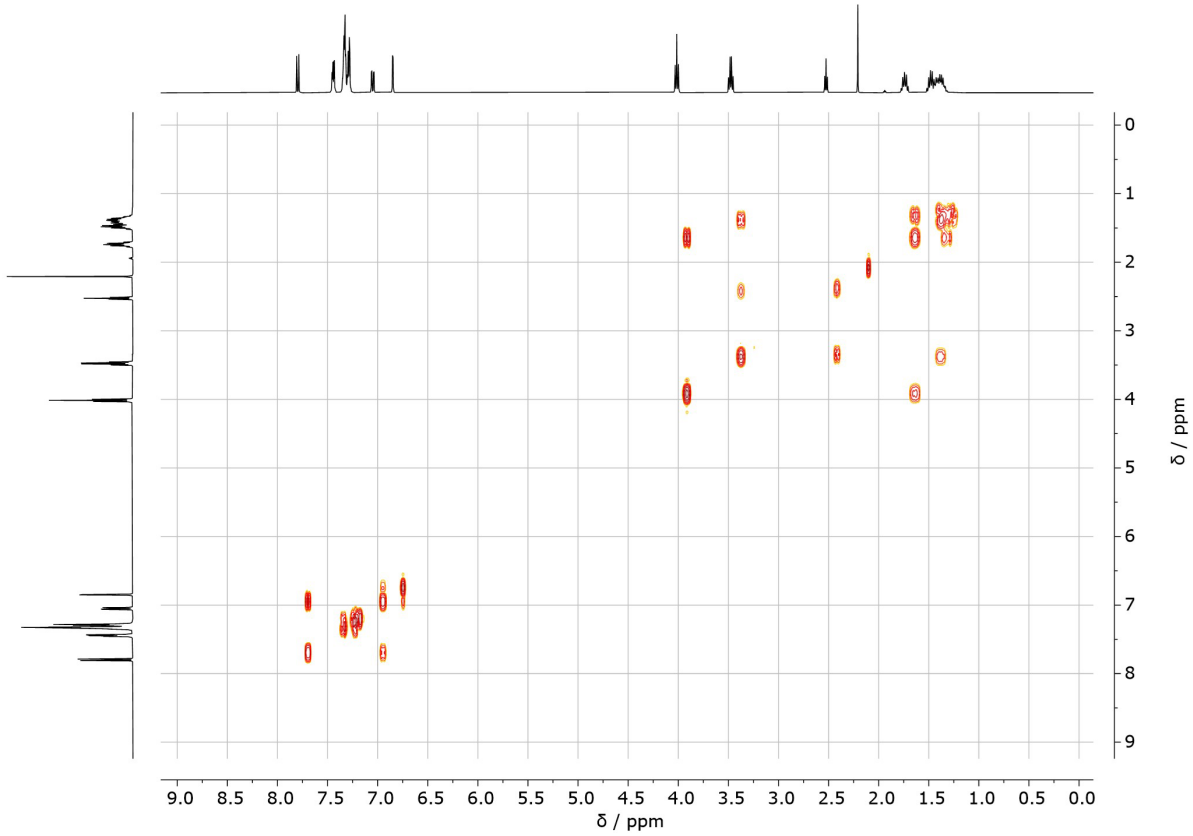

Figure S73. ^{1}H-^{1}H COSY (400 MHz) spectrum of **DIO-OH** in MeCN-d_3 at ambient temperature.

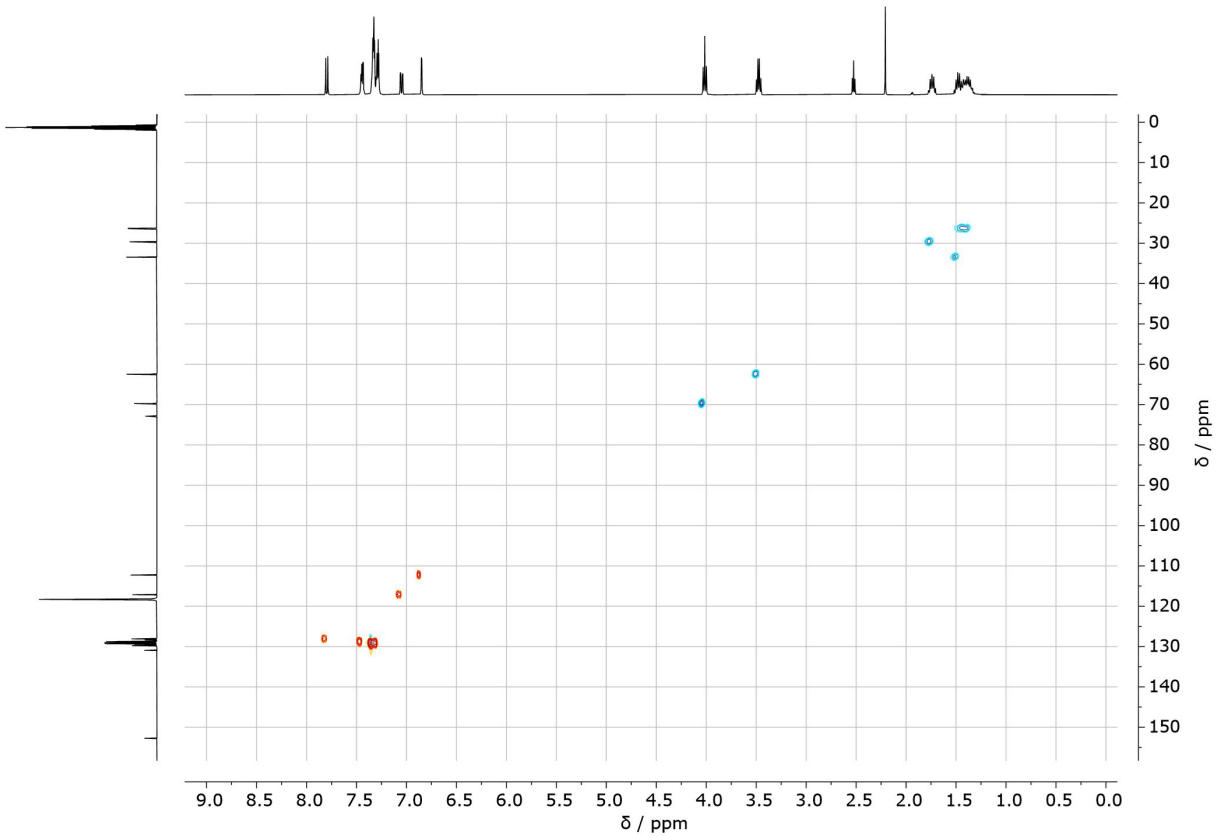

Figure S74. ^{1}H (400 MHz) - ^{13}C (101 MHz) HSQC spectrum of **DIO-OH** in MeCN-d_3 at ambient temperature.

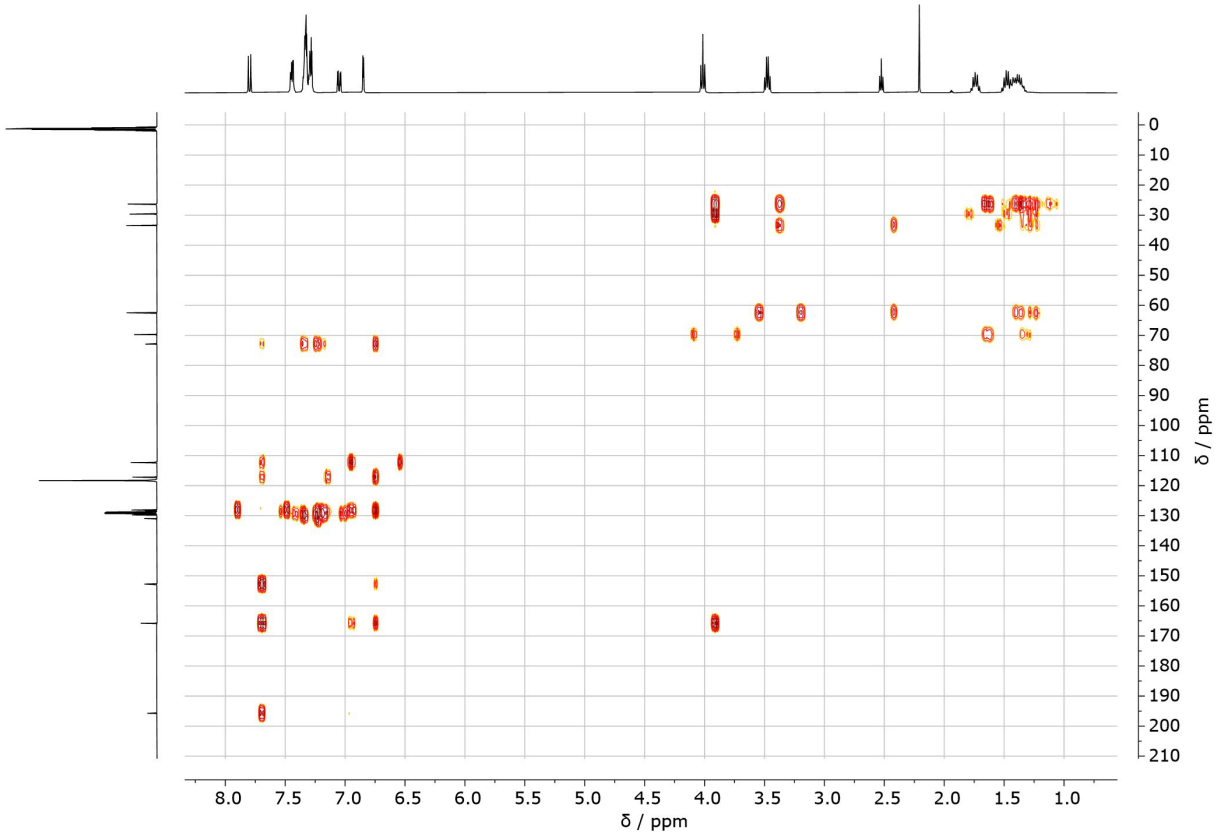

Figure S75. ^{1}H (400 MHz) - ^{13}C (101 MHz) HMBC spectrum of **DIO-OH** in MeCN-d_3 at ambient temperature.

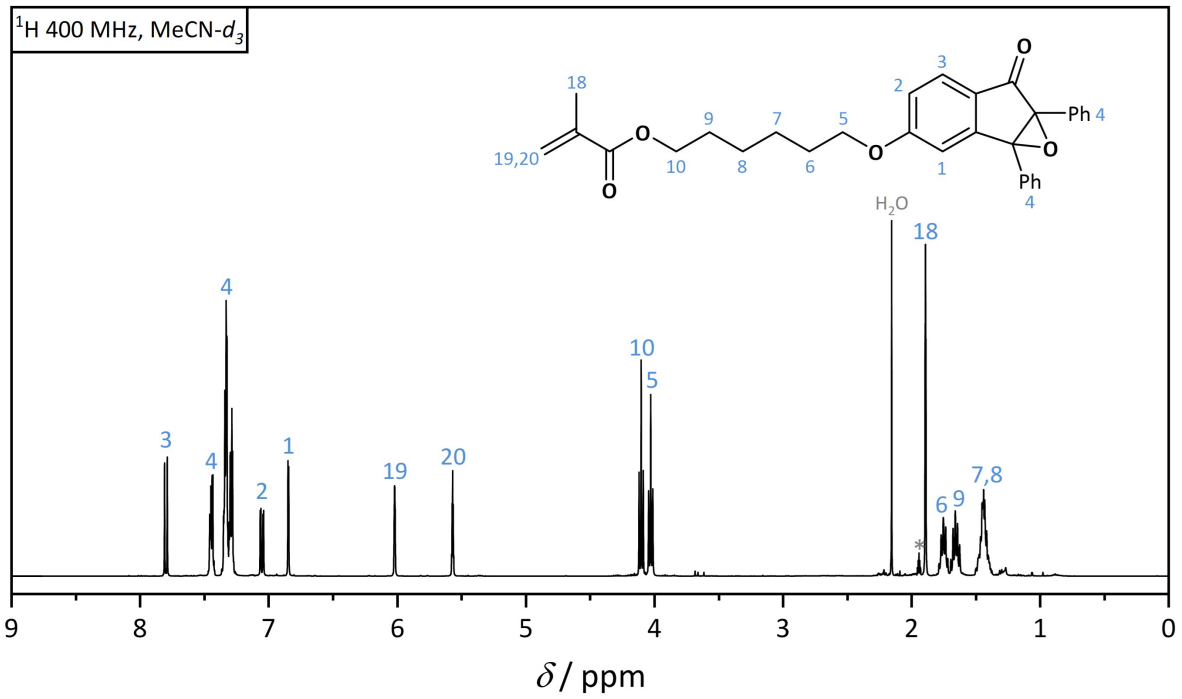

Figure S76. ^{1}H NMR (400 MHz) spectrum of **3** in MeCN-d_3 (*) at ambient temperature.

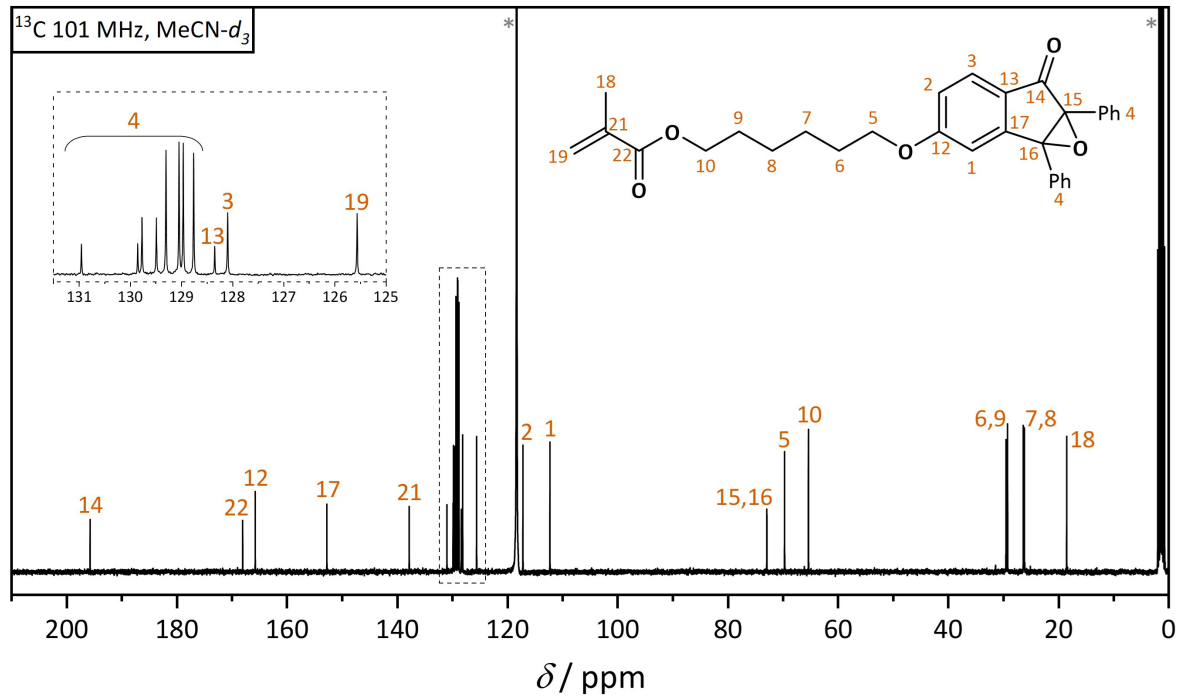

Figure S77. ^{13}C NMR (101 MHz) spectrum of **3** in MeCN-d_3 (*) at ambient temperature.

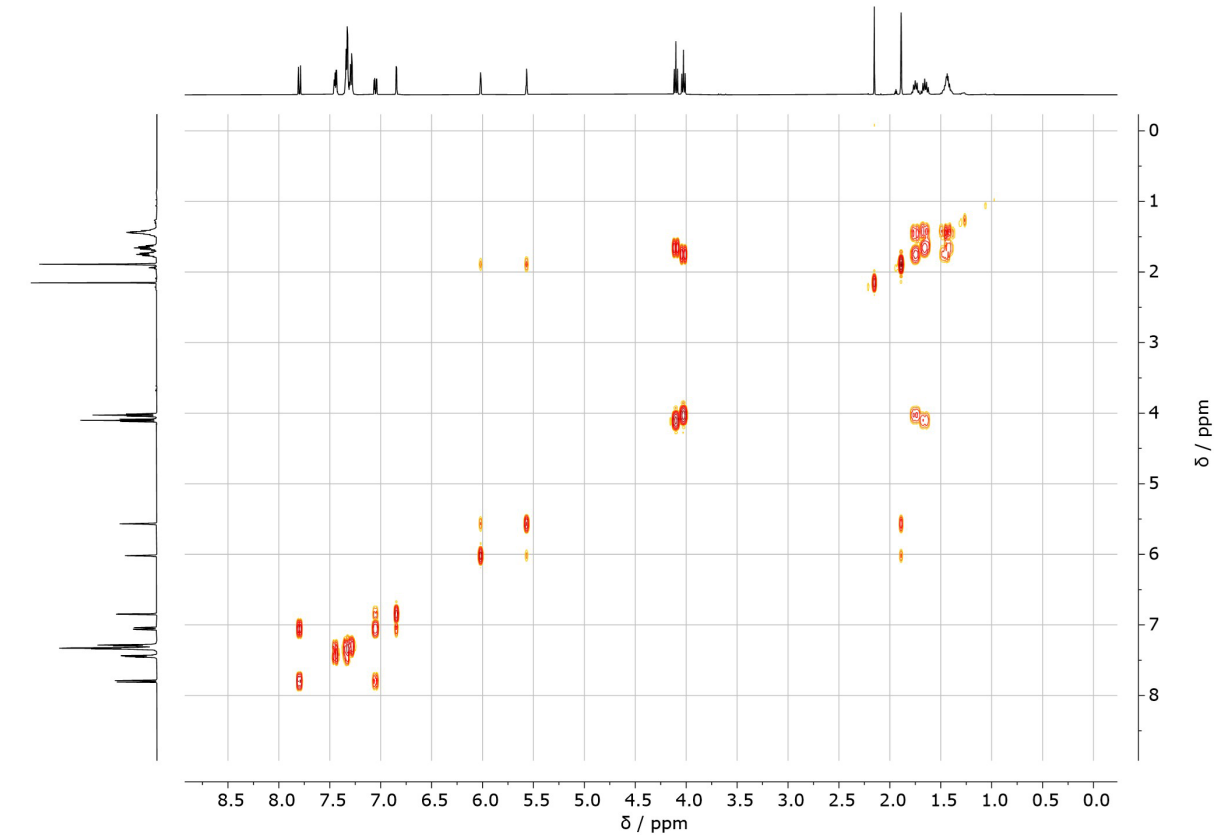

Figure S78. ^{1}H-^{1}H COSY (400 MHz) spectrum of **3** in MeCN-d_3 at ambient temperature.

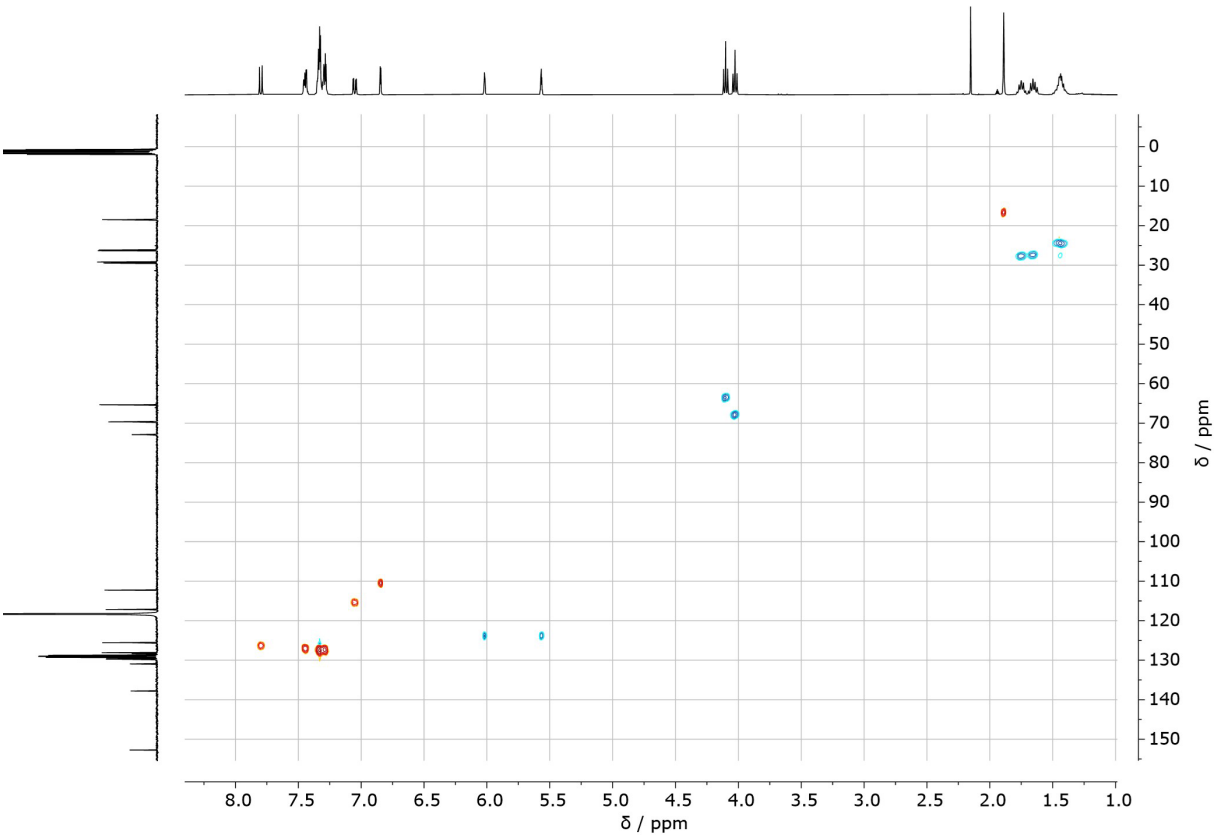

Figure S79. ^{1}H (400 MHz) - ^{13}C (101 MHz) HSQC spectrum of **3** in MeCN-d_3 at ambient temperature.

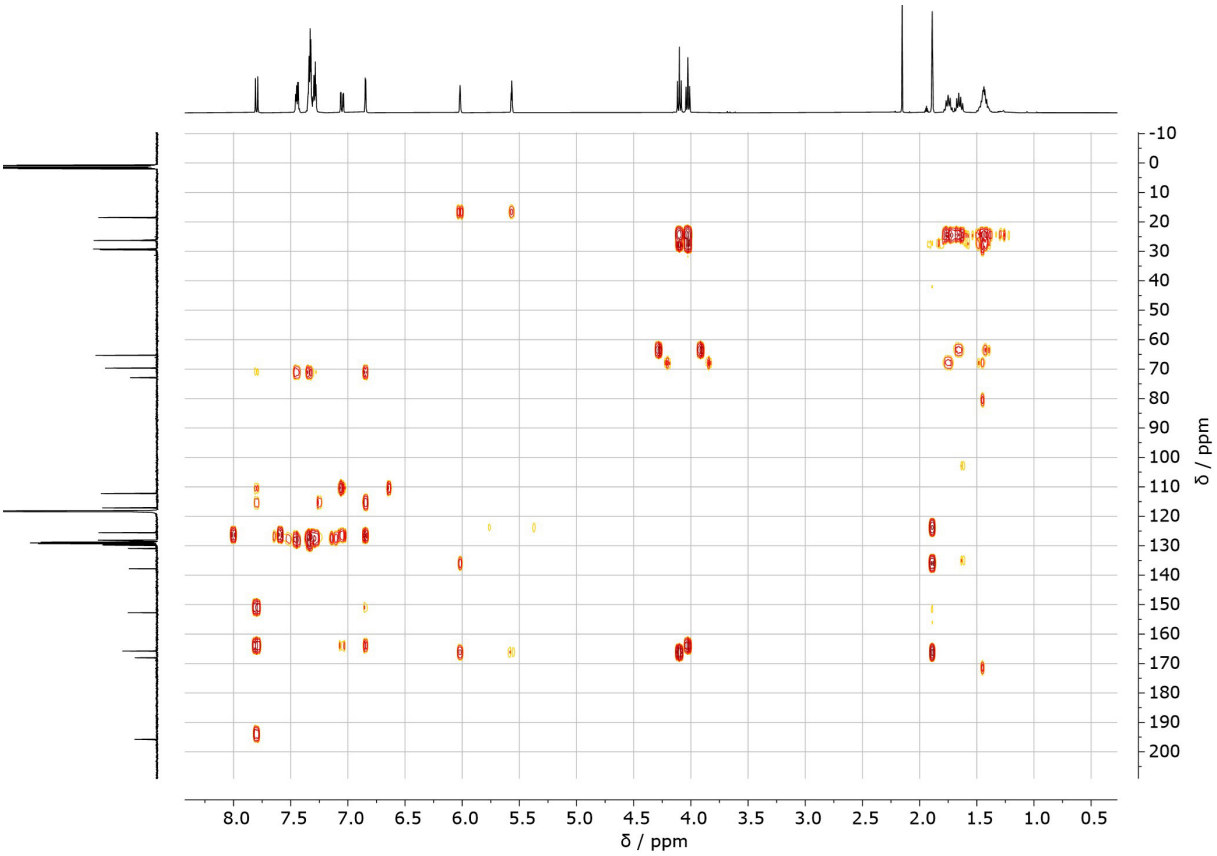

Figure S80. ^{1}H (400 MHz) - ^{13}C (101 MHz) HMBC spectrum of **3** in MeCN-d_3 at ambient temperature.

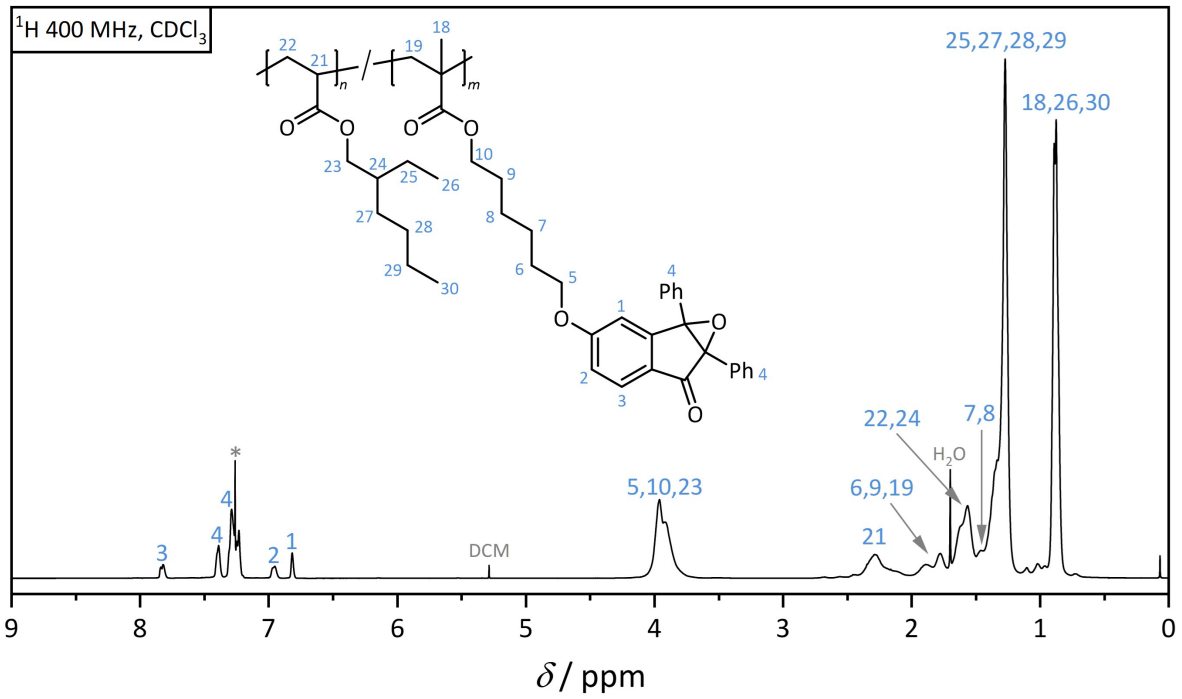

Figure S81. ^{1}H NMR (400 MHz) spectrum of **polyDIO** in $CDCl_3$ (*) at ambient temperature.

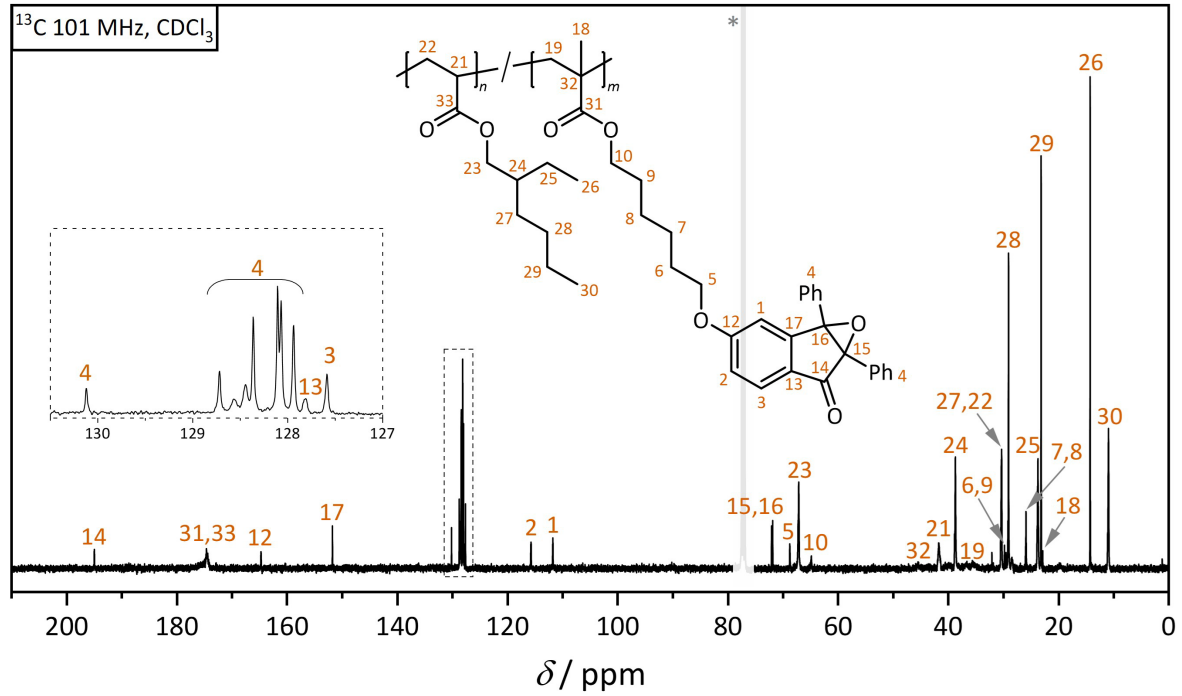

Figure S82. ^{13}C NMR (101 MHz) spectrum of **polyDIO** in $CDCl_3$ (*) at ambient temperature.

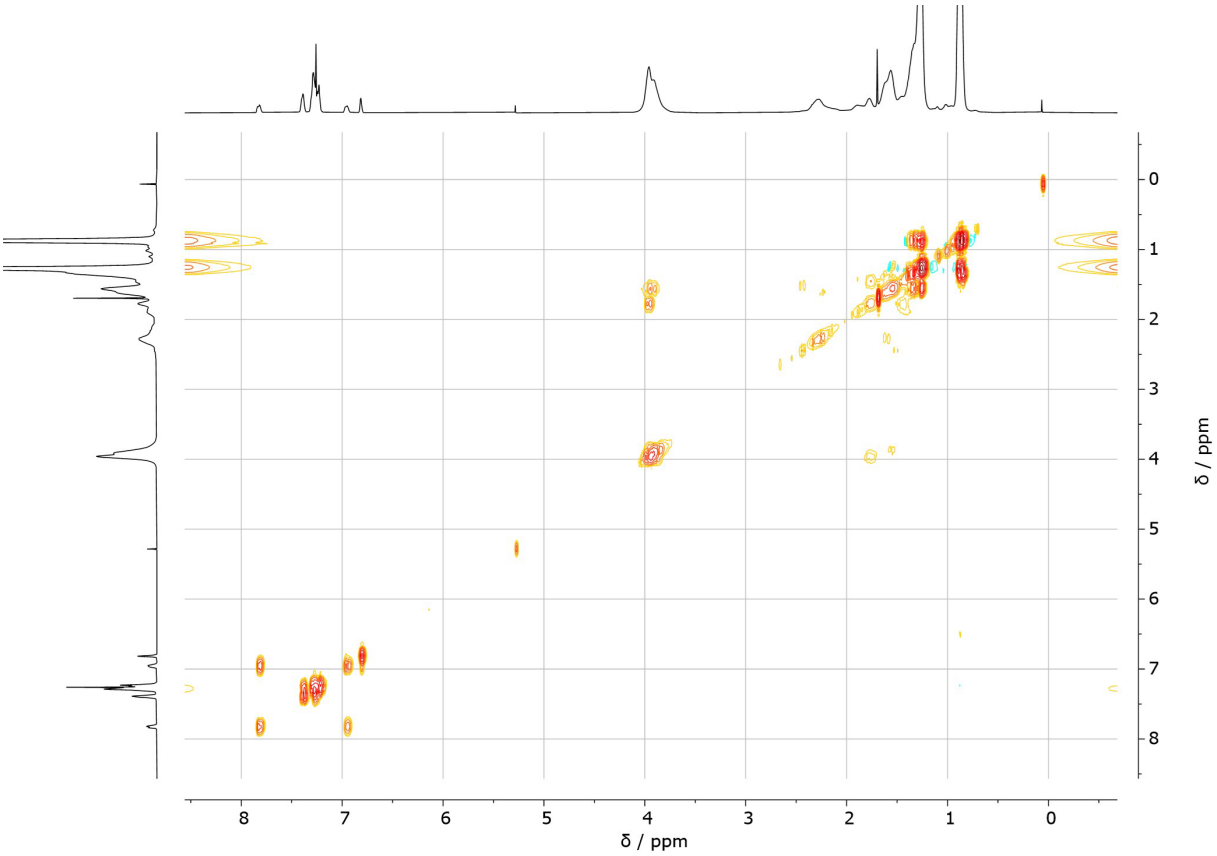

Figure S83. ^{1}H-^{1}H COSY (400 MHz) spectrum of **polyDIO** in $CDCl_3$ at ambient temperature.

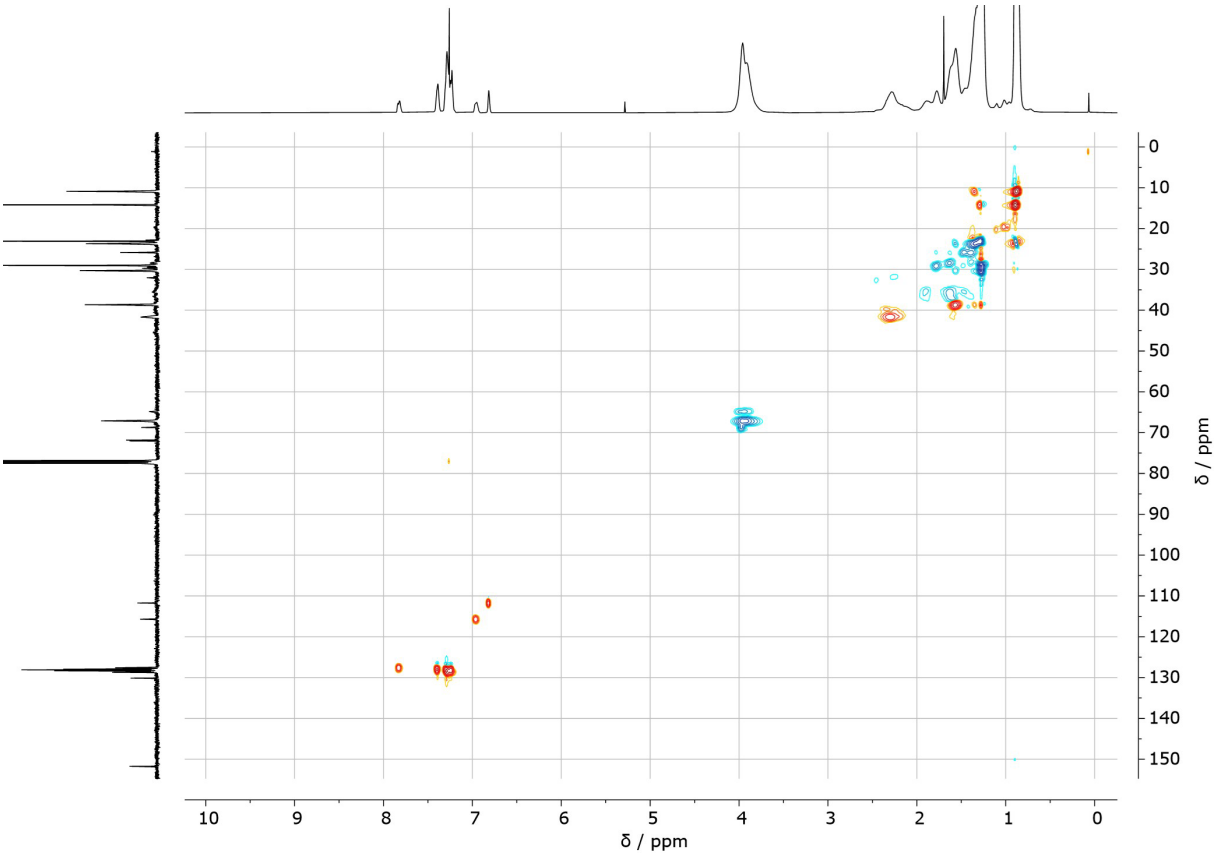

Figure S84. ^{1}H (400 MHz) - ^{13}C (101 MHz) HSQC spectrum of **polyDIO** in $CDCl_3$ at ambient temperature.

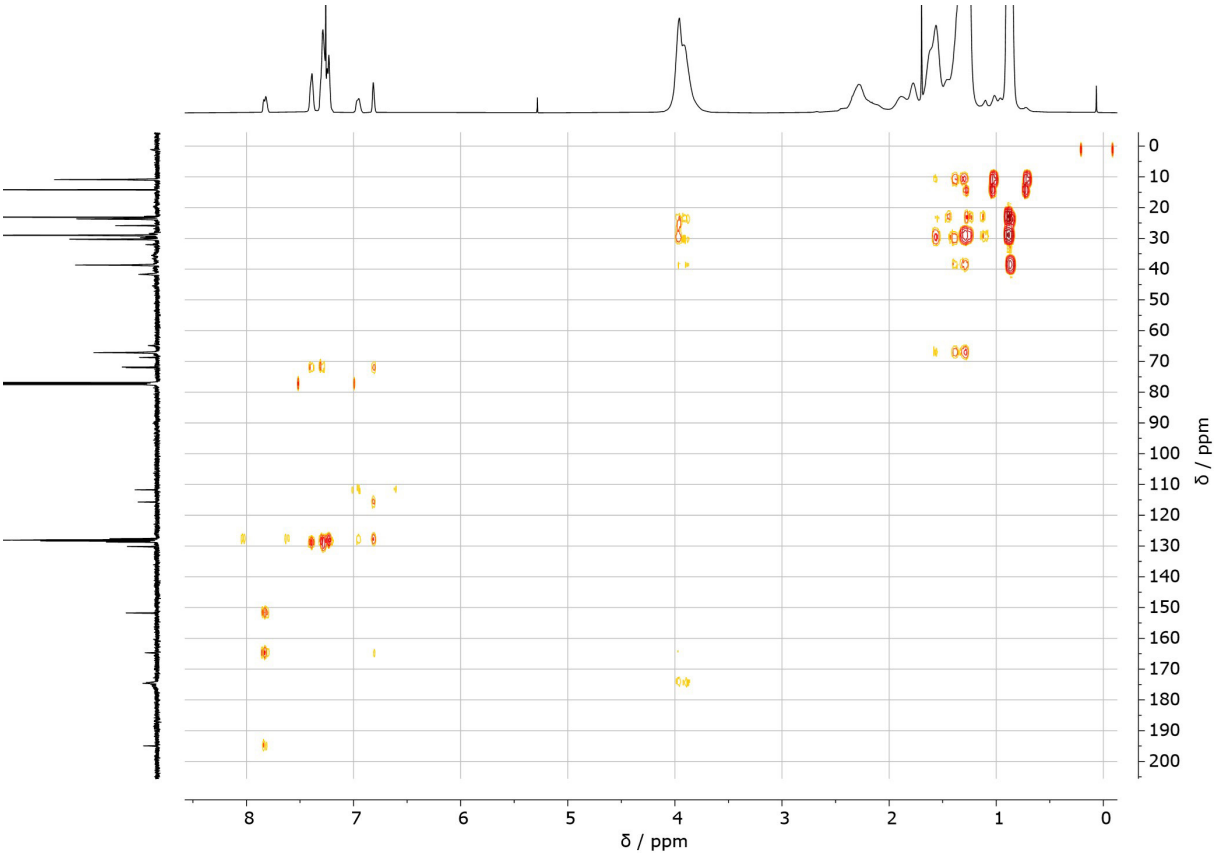

Figure S85. ^{1}H (400 MHz) - ^{13}C (101 MHz) HMBC spectrum of **polyDIO** in $CDCl_3$ at ambient temperature.

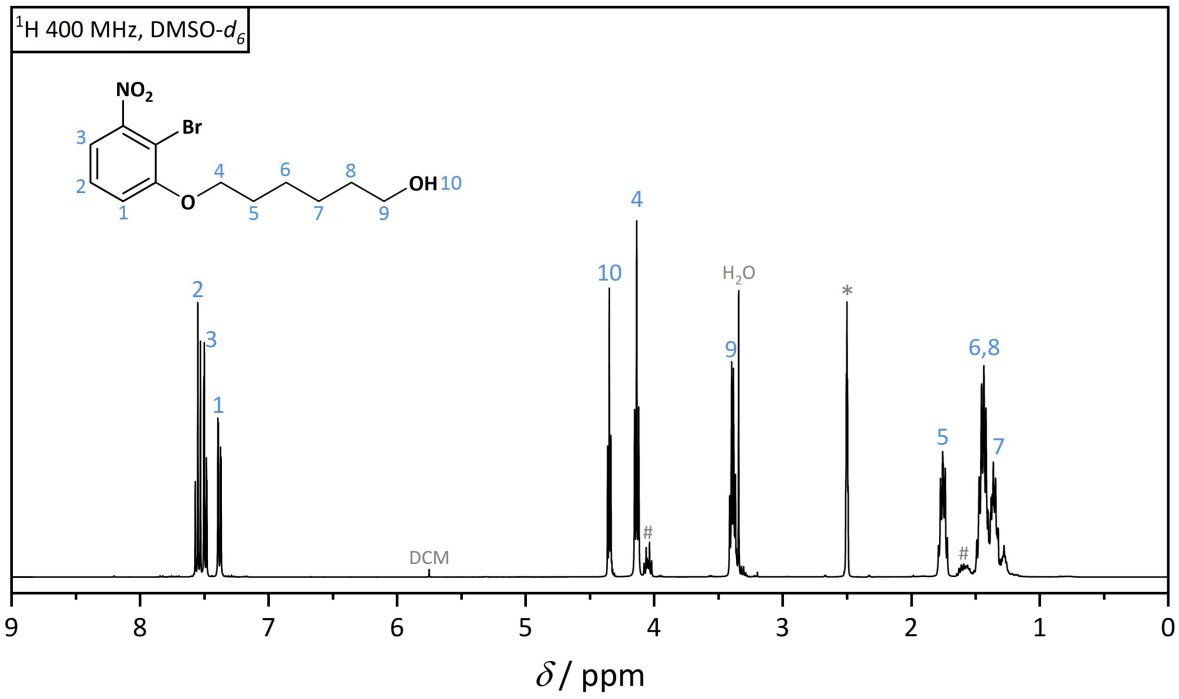

Figure S86. ^{1}H NMR (400 MHz) spectrum of **4** in DMSO-d_6 (*) at ambient temperature.

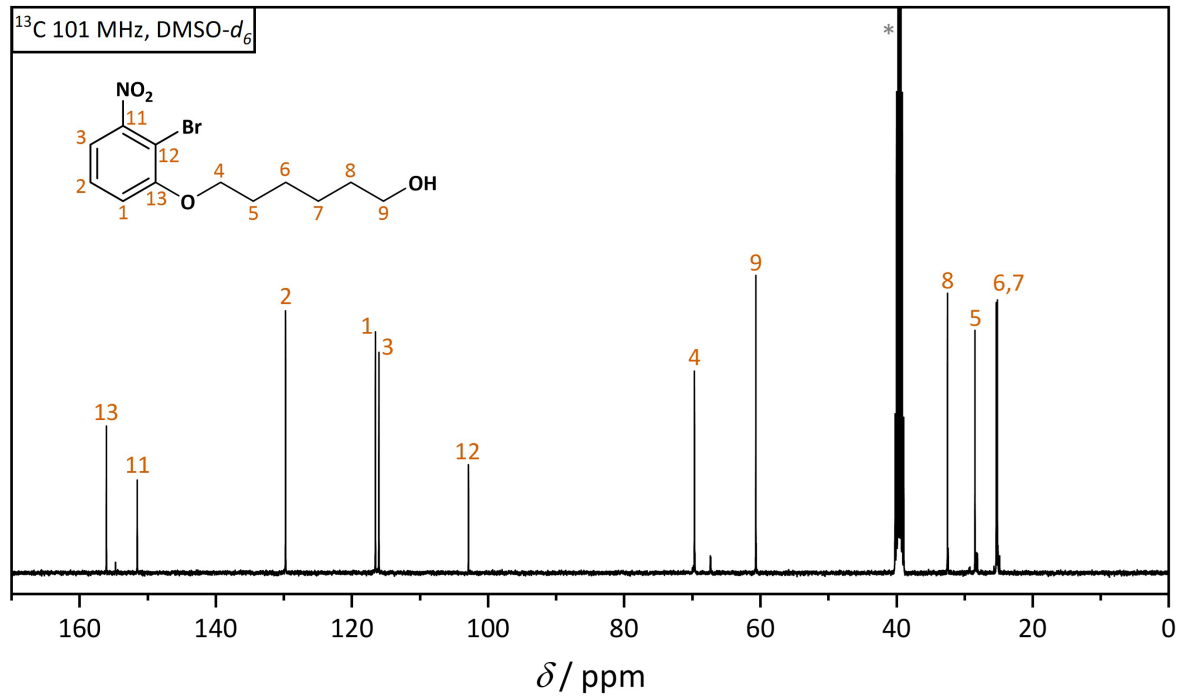

Figure S87. ^{13}C NMR (101 MHz) spectrum of **4** in DMSO-d_6 (*) at ambient temperature.

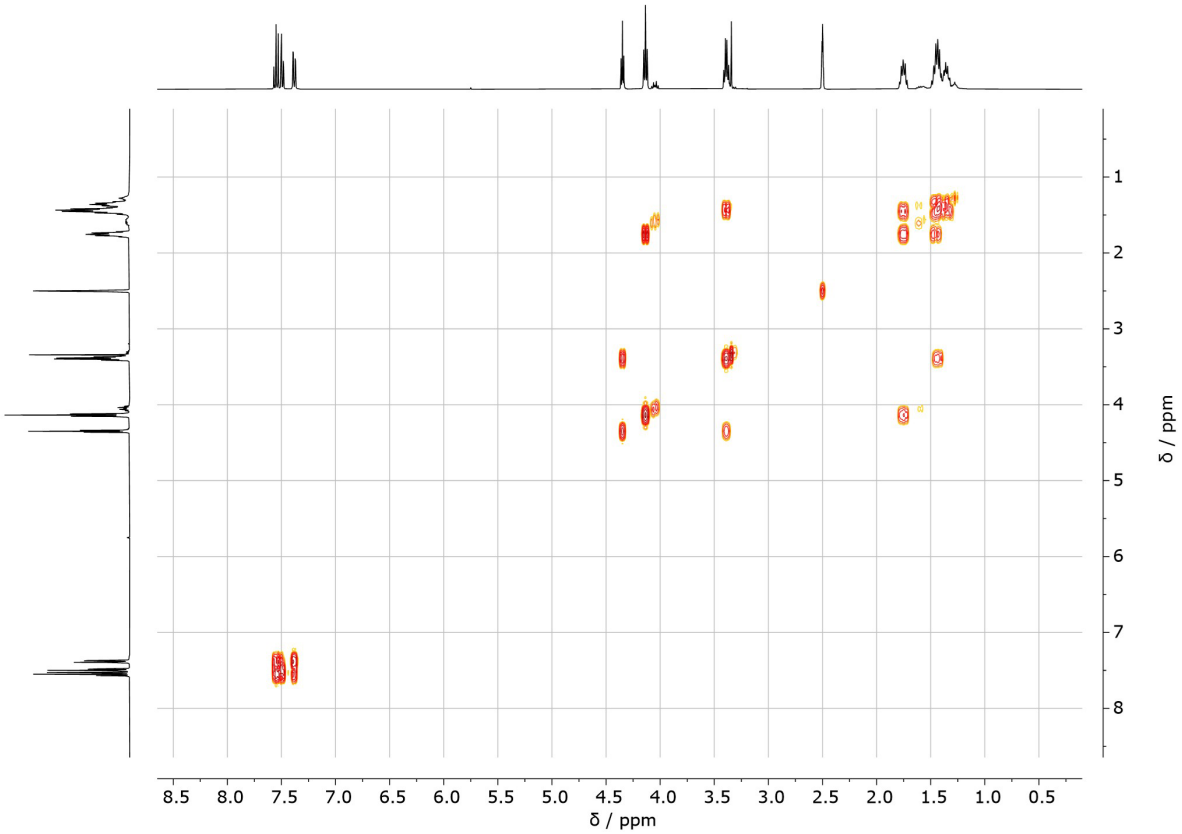

Figure S88. ^{1}H-^{1}H COSY (400 MHz) spectrum of **4** in DMSO-d_6 at ambient temperature.

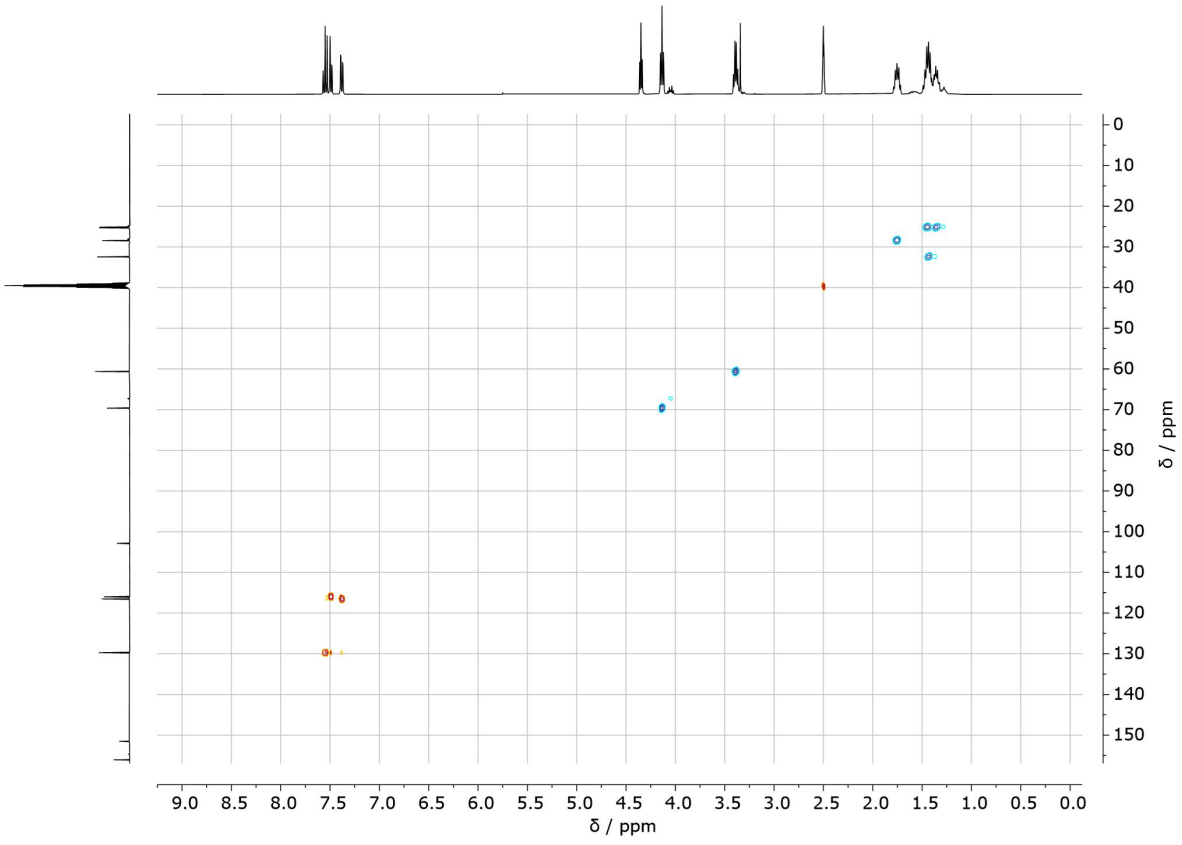

Figure S89. ^{1}H (400 MHz) - ^{13}C (101 MHz) HSQC spectrum of **4** in DMSO-d_6 at ambient temperature.

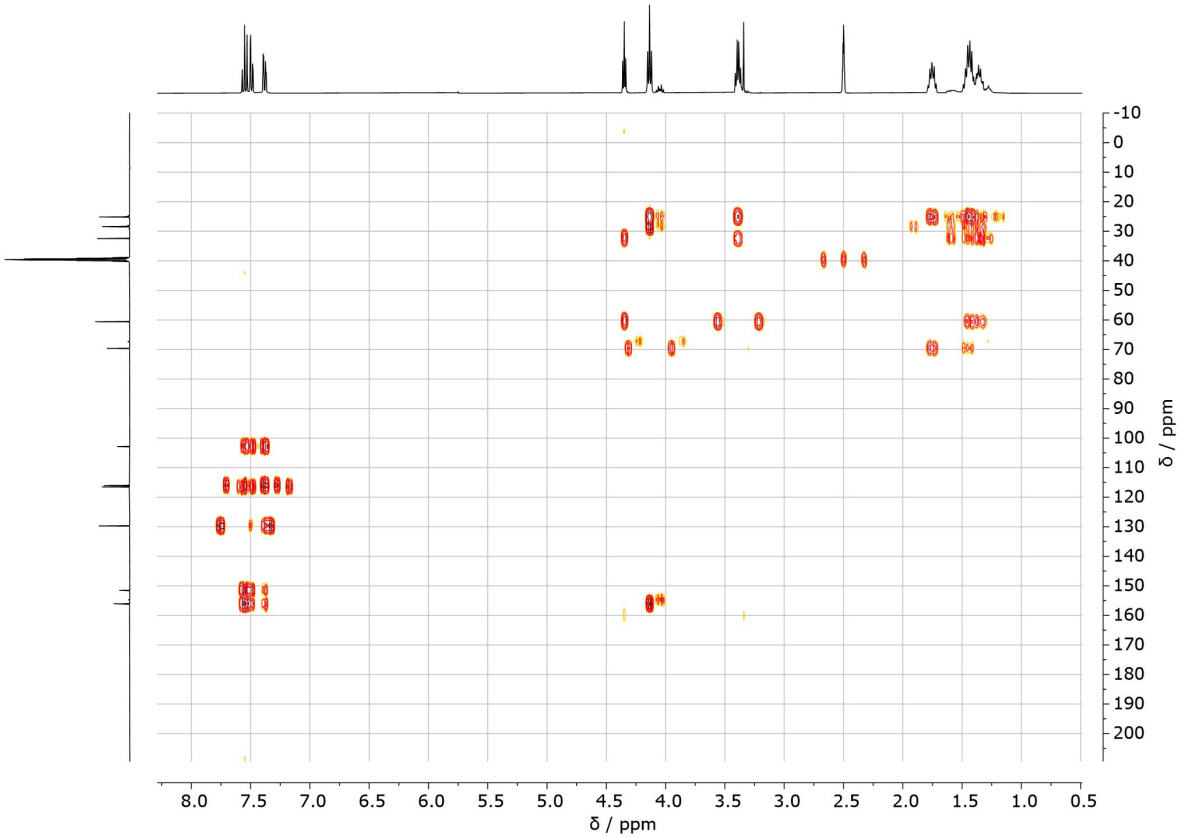

Figure S90. ^{1}H (400 MHz) - ^{13}C (101 MHz) HMBC spectrum of **4** in DMSO-d_6 at ambient temperature.

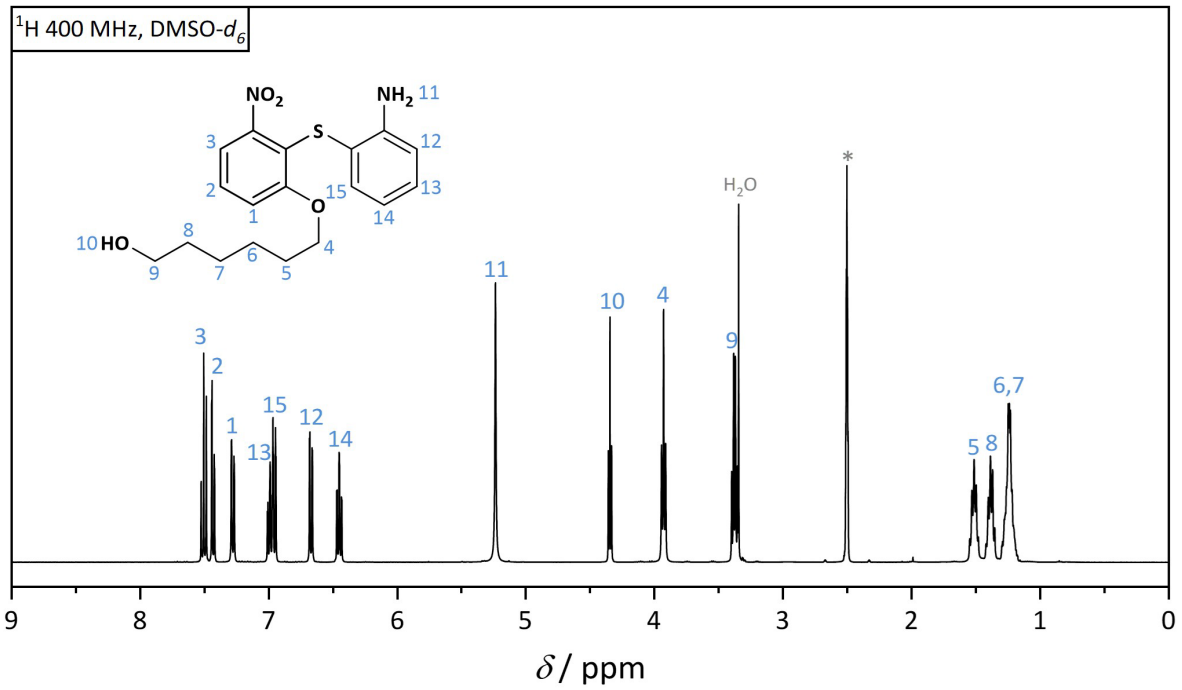

Figure S91. ^{1}H NMR (400 MHz) spectrum of **5** in DMSO-d_6 (*) at ambient temperature.

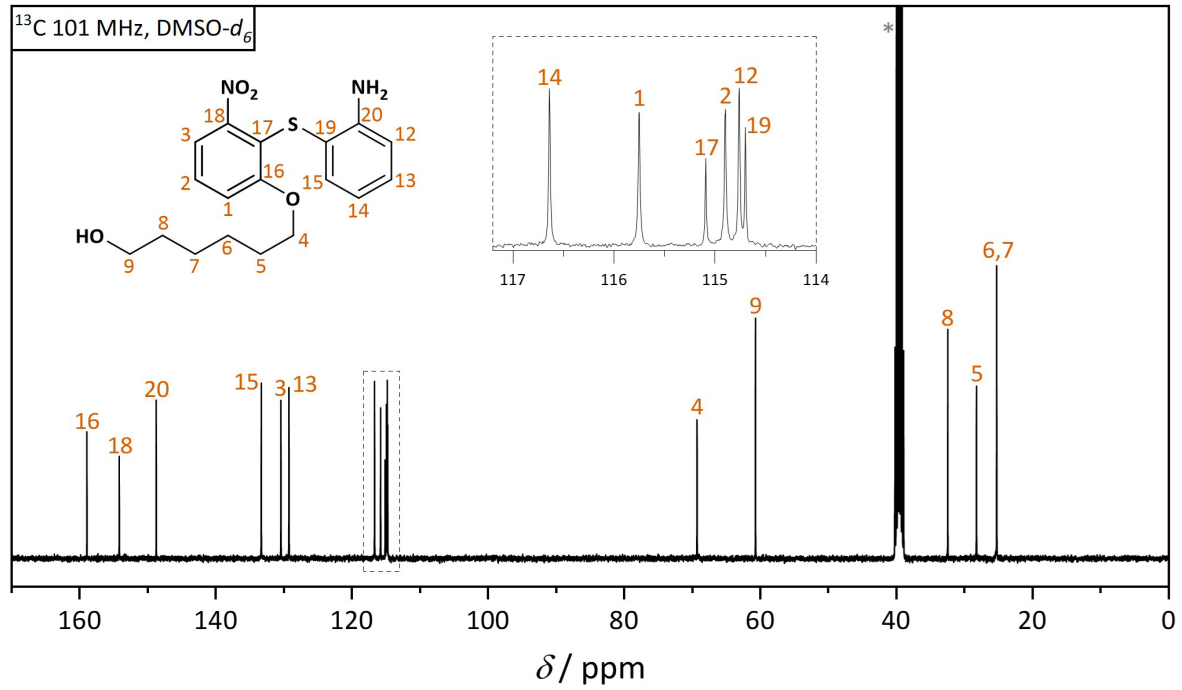

Figure S92. ^{13}C NMR (101 MHz) spectrum of **5** in DMSO-d_6 (*) at ambient temperature.

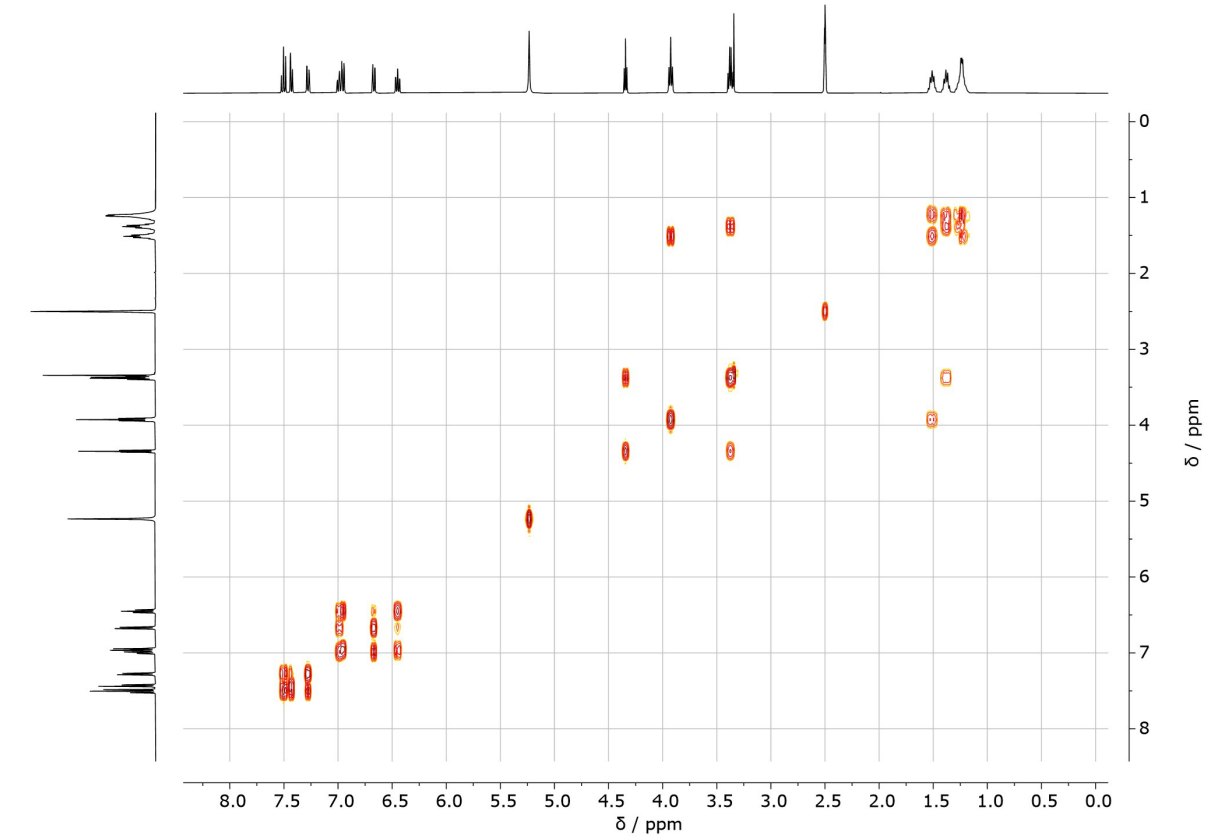

Figure S93. ^{1}H-^{1}H COSY (400 MHz) spectrum of **5** in DMSO-d_6 at ambient temperature.

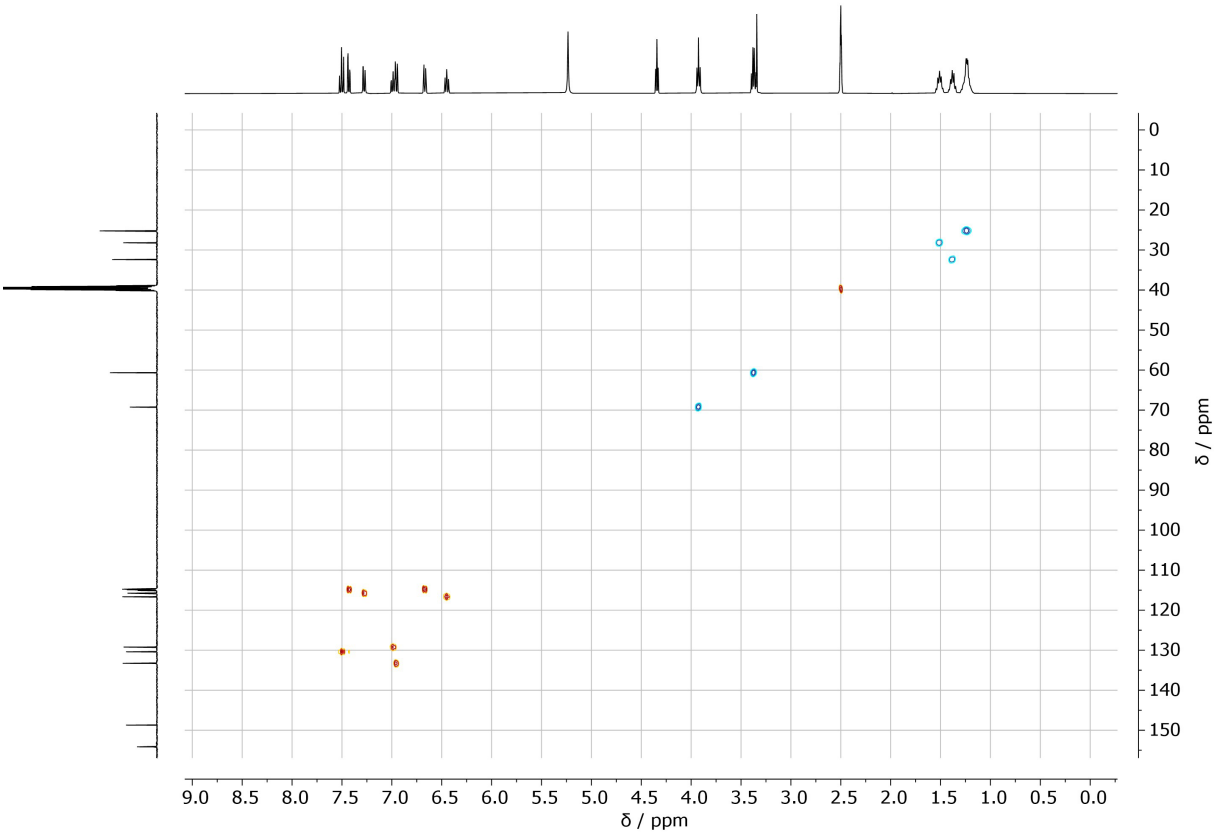

Figure S94. ^{1}H (400 MHz) - ^{13}C (101 MHz) HSQC spectrum of **5** in DMSO-d_6 at ambient temperature.

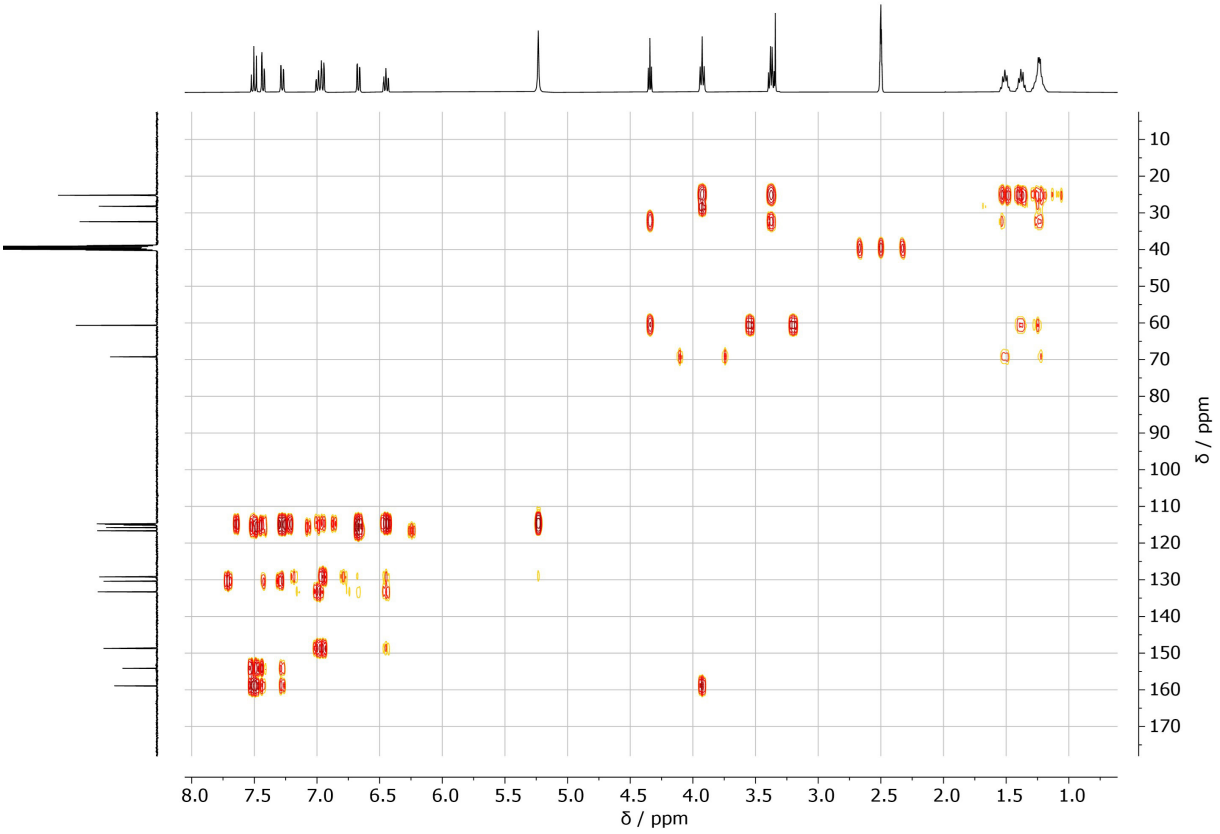

Figure S95. ^{1}H (400 MHz) - ^{13}C (101 MHz) HMBC spectrum of **5** in DMSO-d_6 at ambient temperature.

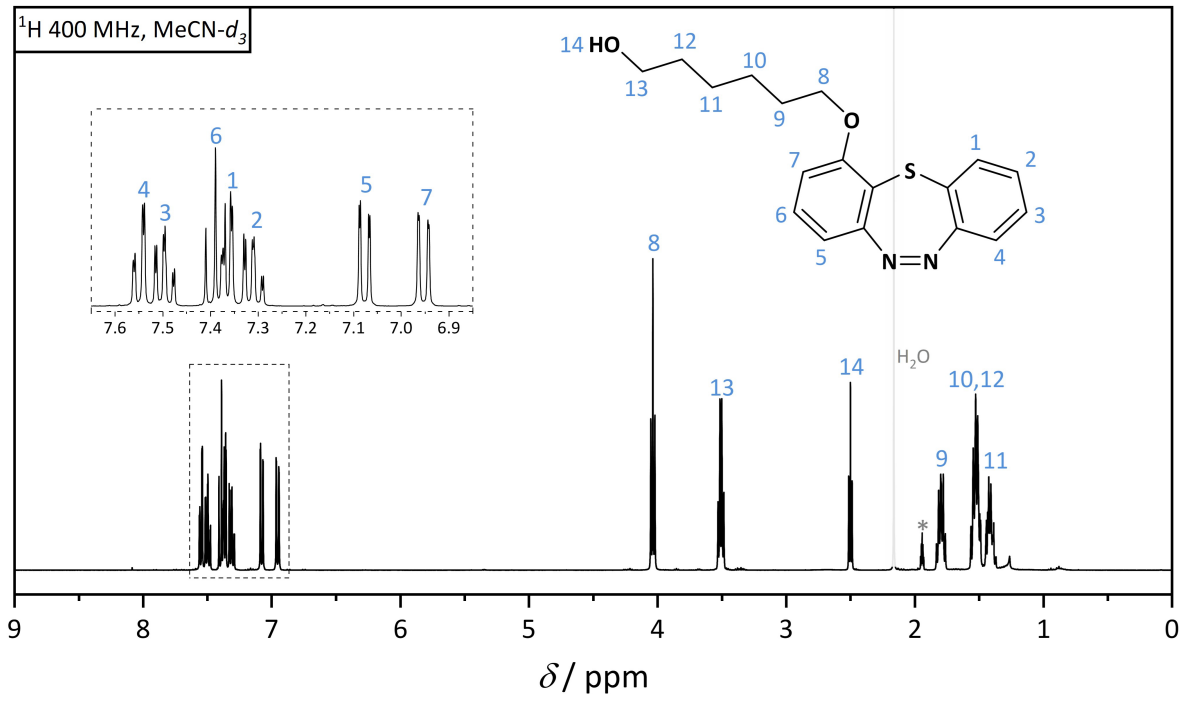

Figure S96. ^{1}H NMR (400 MHz) spectrum of **SA-OH** in MeCN-d_3 (*) at ambient temperature.

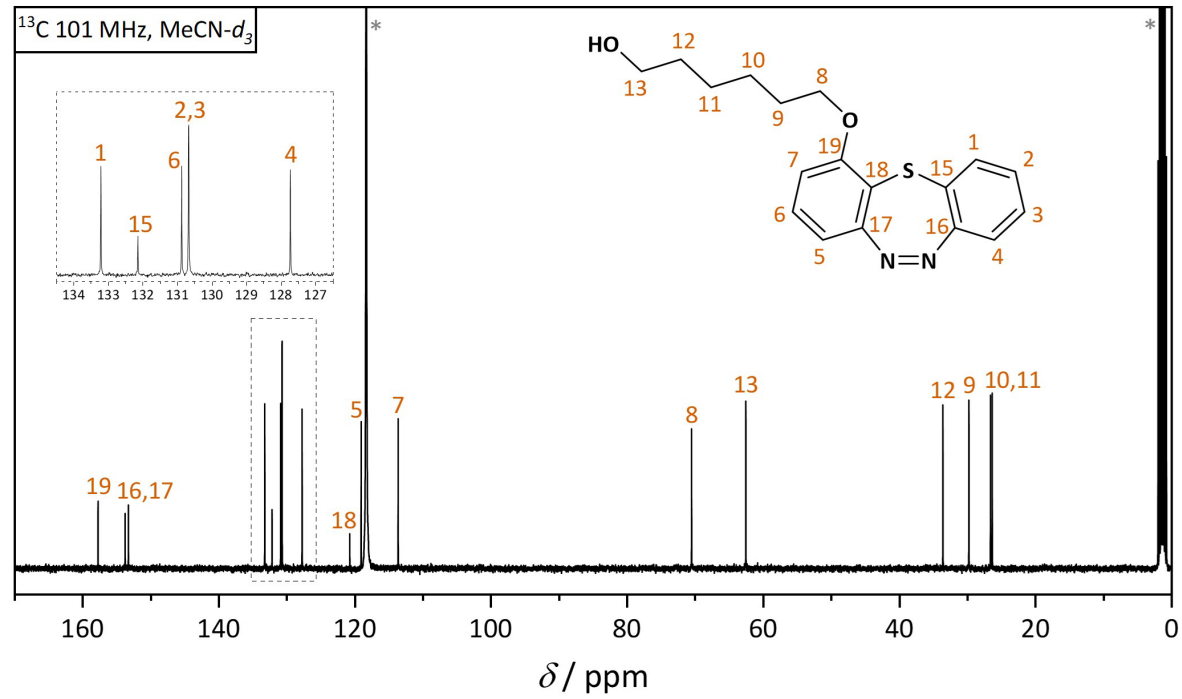

Figure S97. ^{13}C NMR (101 MHz) spectrum of **SA-OH** in MeCN-d_3 (*) at ambient temperature.

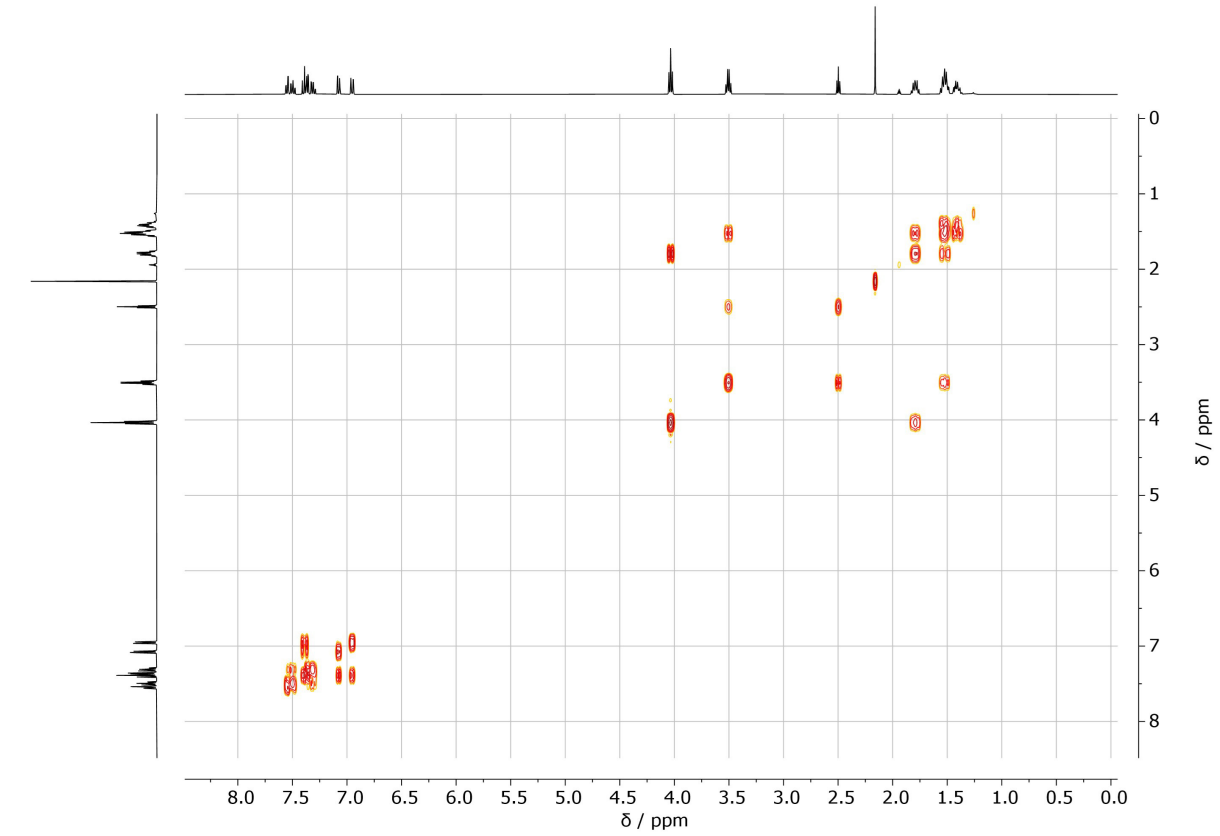

Figure S98. ^{1}H-^{1}H COSY (400 MHz) spectrum of **SA-OH** in MeCN-d_3 at ambient temperature.

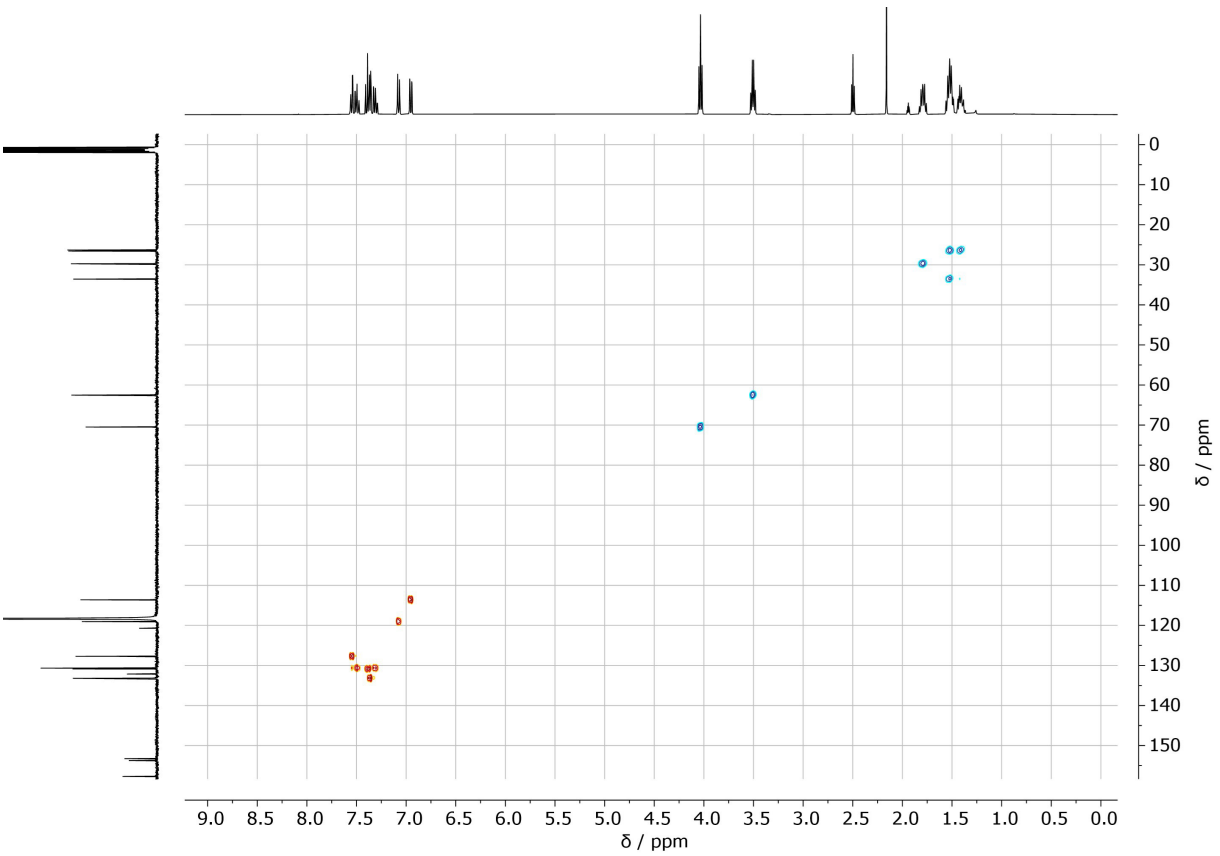

Figure S99. ^{1}H (400 MHz) - ^{13}C (101 MHz) HSQC spectrum of **SA-OH** in MeCN-d_3 at ambient temperature.

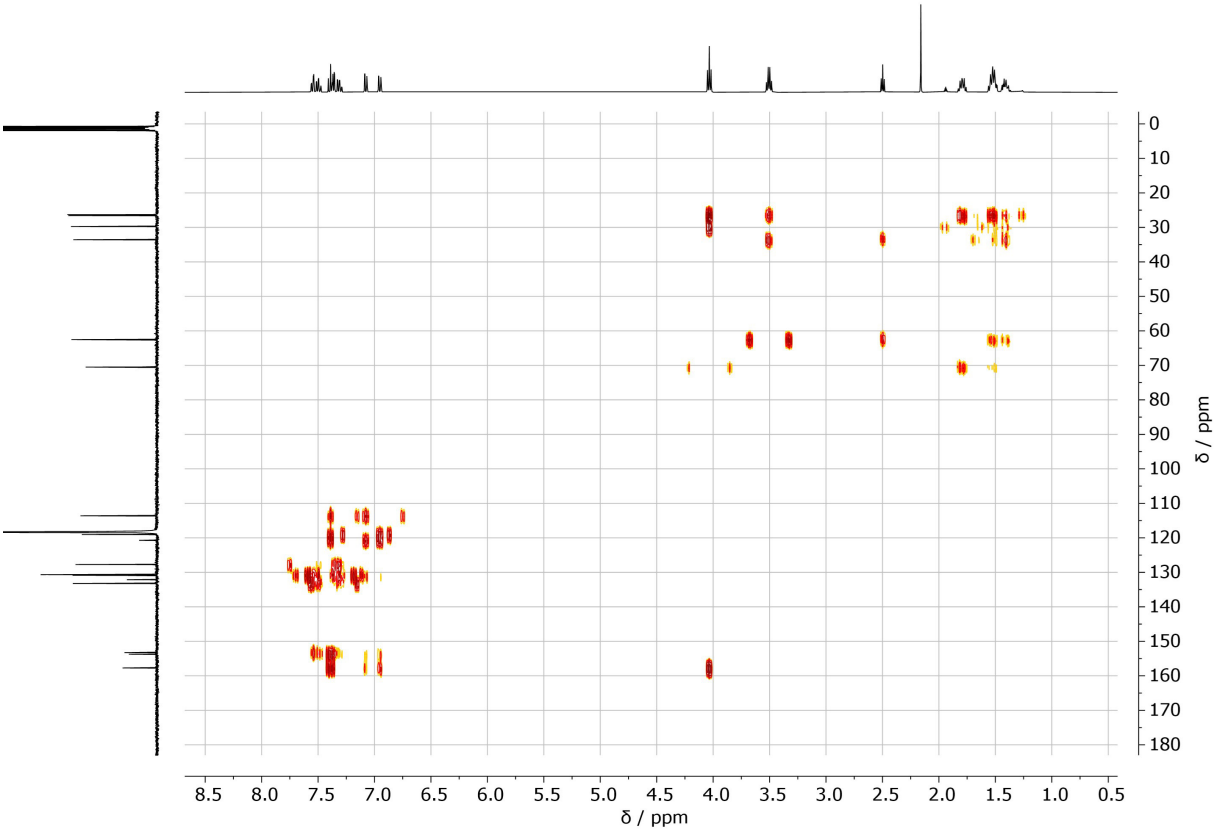

Figure S100. ^{1}H (400 MHz) - ^{13}C (101 MHz) HMBC spectrum of **SA-OH** in MeCN-d_3 at ambient temperature.

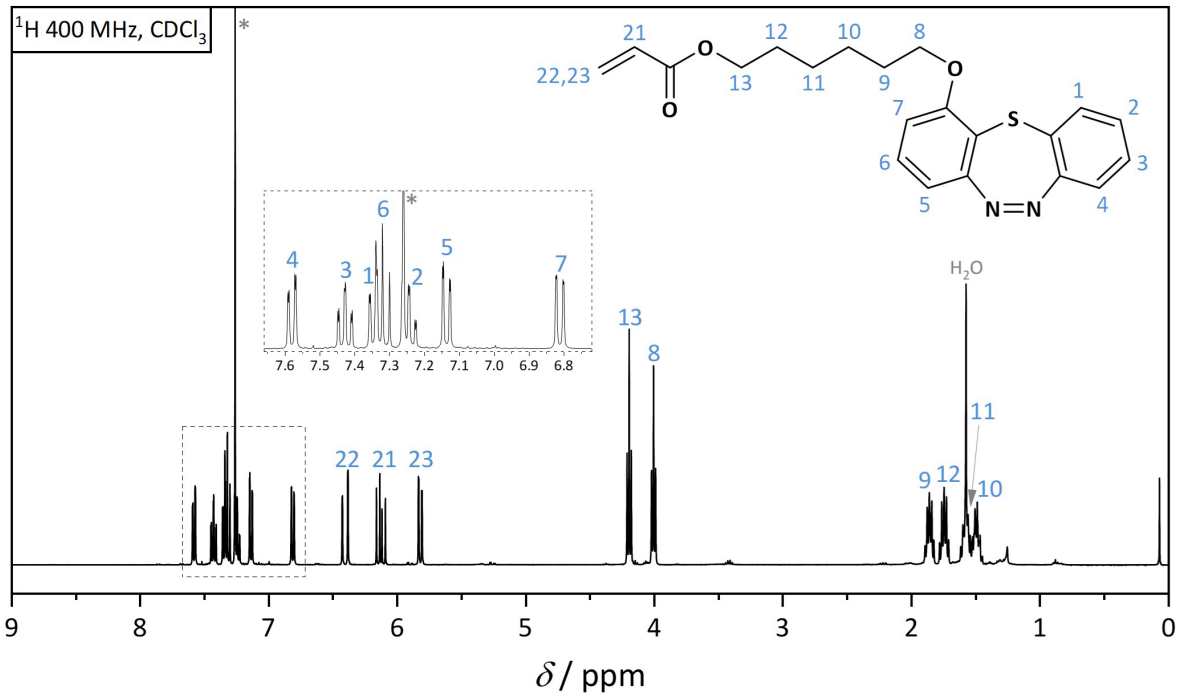

Figure S101. ^{1}H NMR (400 MHz) spectrum of **6** in $CDCl_3$ (*) at ambient temperature.

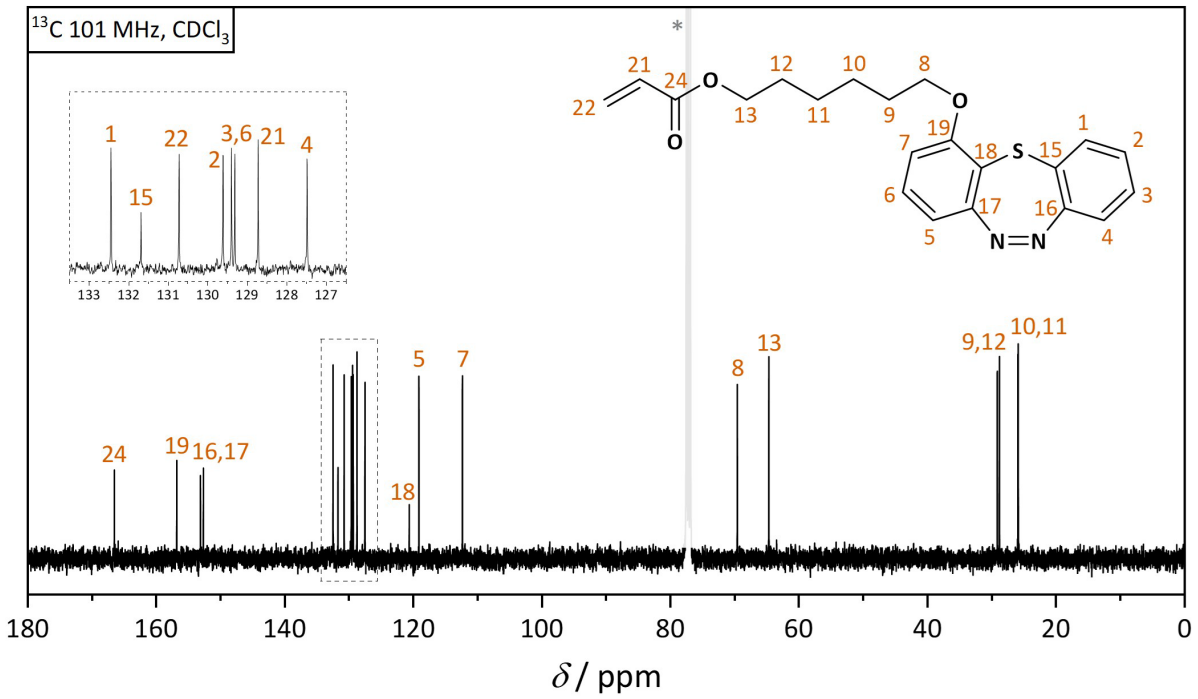

Figure S102. ^{13}C NMR (101 MHz) spectrum of **6** in $CDCl_3$ (*) at ambient temperature.

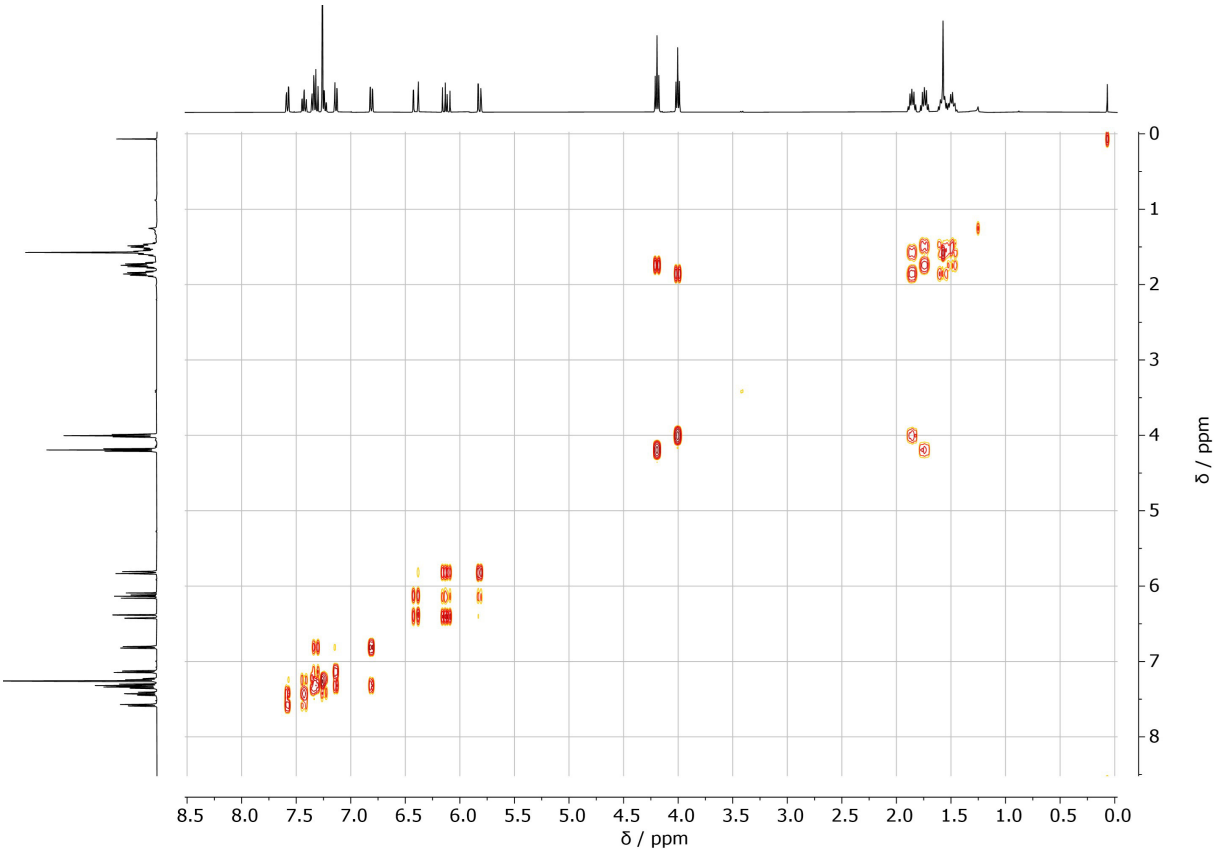

Figure S103. ^{1}H-^{1}H COSY (400 MHz) spectrum of **6** in $CDCl_3$ at ambient temperature.

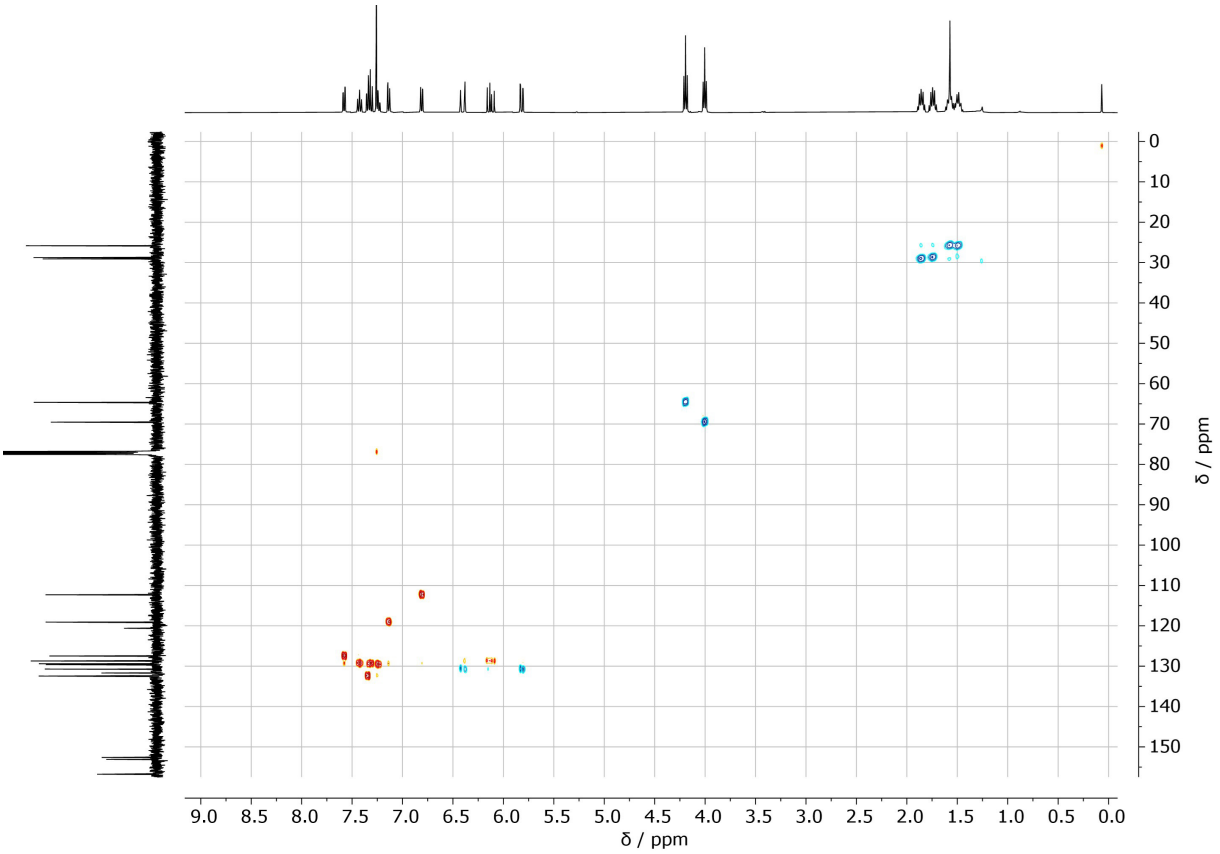

Figure S104. ^{1}H (400 MHz) - ^{13}C (101 MHz) HSQC spectrum of **6** in $CDCl_3$ at ambient temperature.

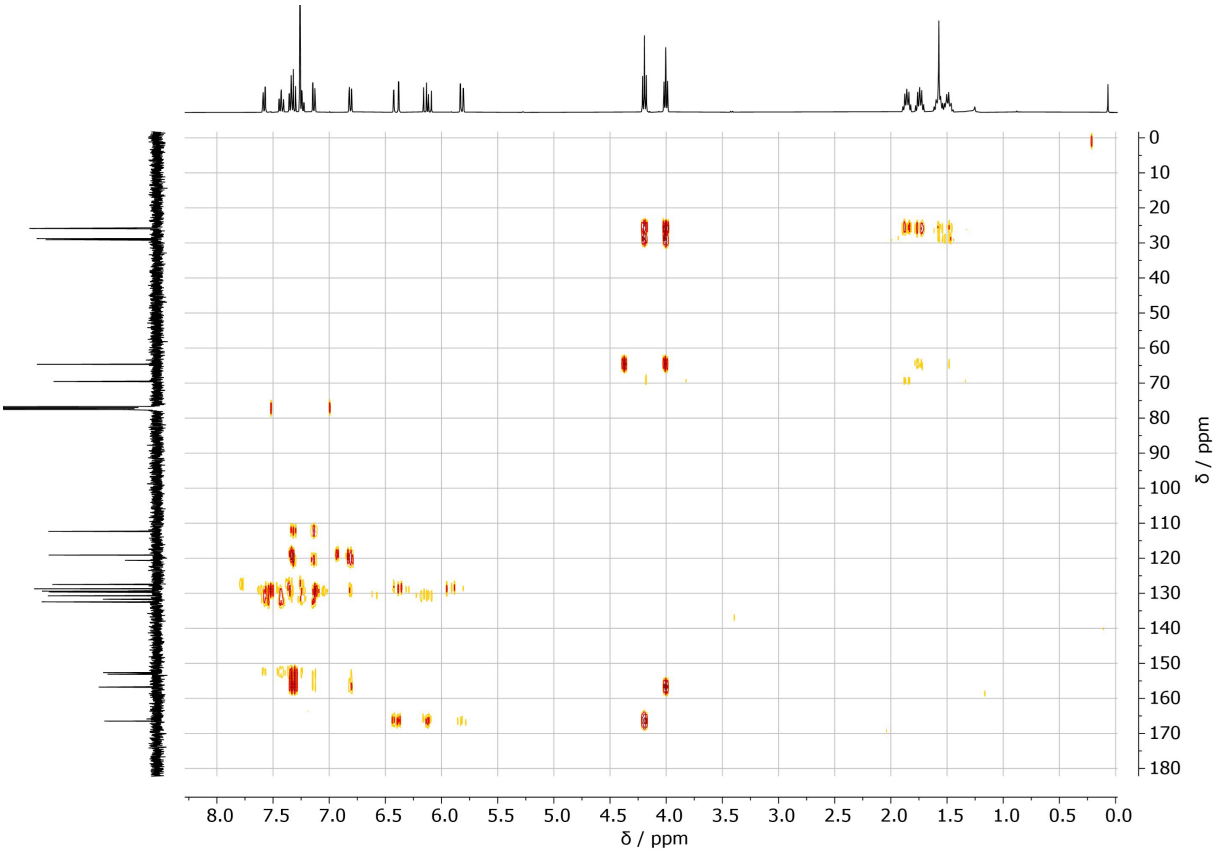

Figure S105. ^{1}H (400 MHz) - ^{13}C (101 MHz) HMBC spectrum of **6** in $CDCl_3$ at ambient temperature.

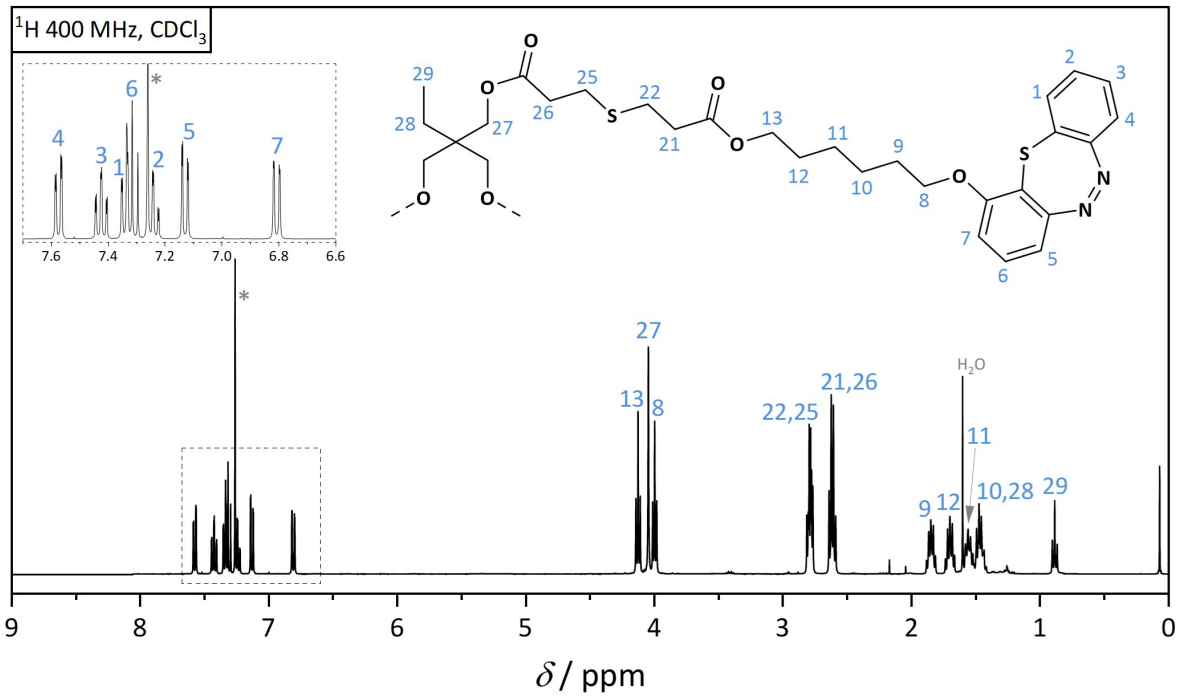

Figure S106. ^{1}H NMR (400 MHz) spectrum of **SA-3arm** in $CDCl_3$ (*) at ambient temperature.

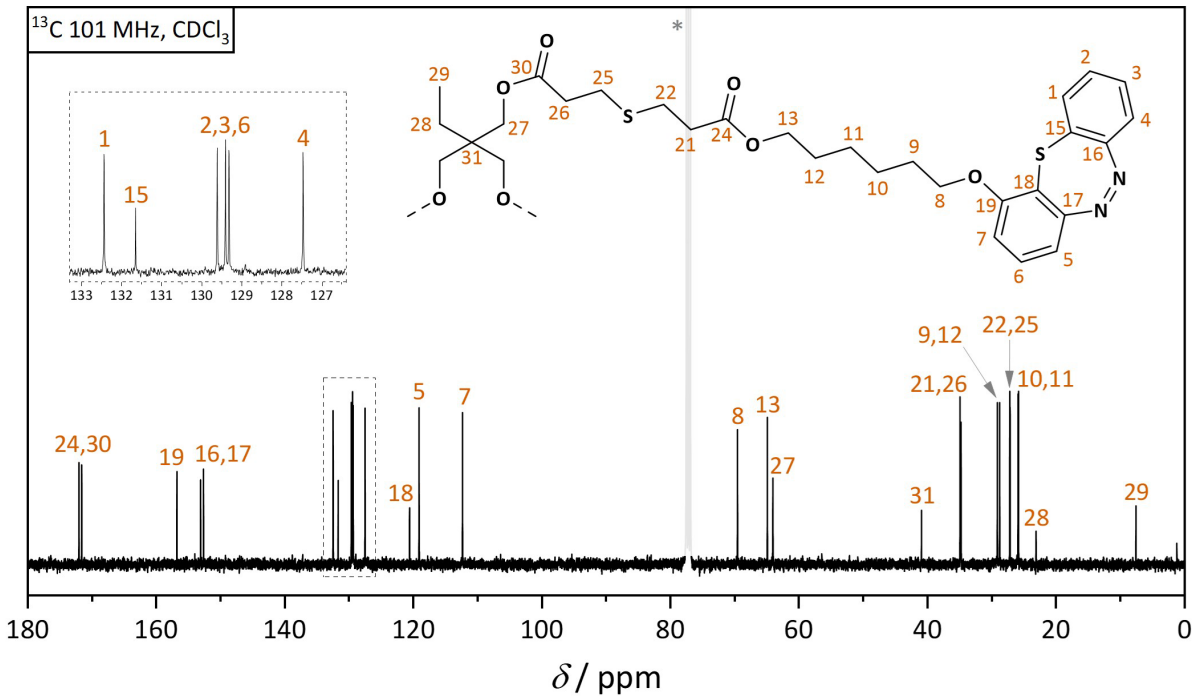

Figure S107. ^{13}C NMR (101 MHz) spectrum of **SA-3arm** in $CDCl_3$ (*) at ambient temperature.

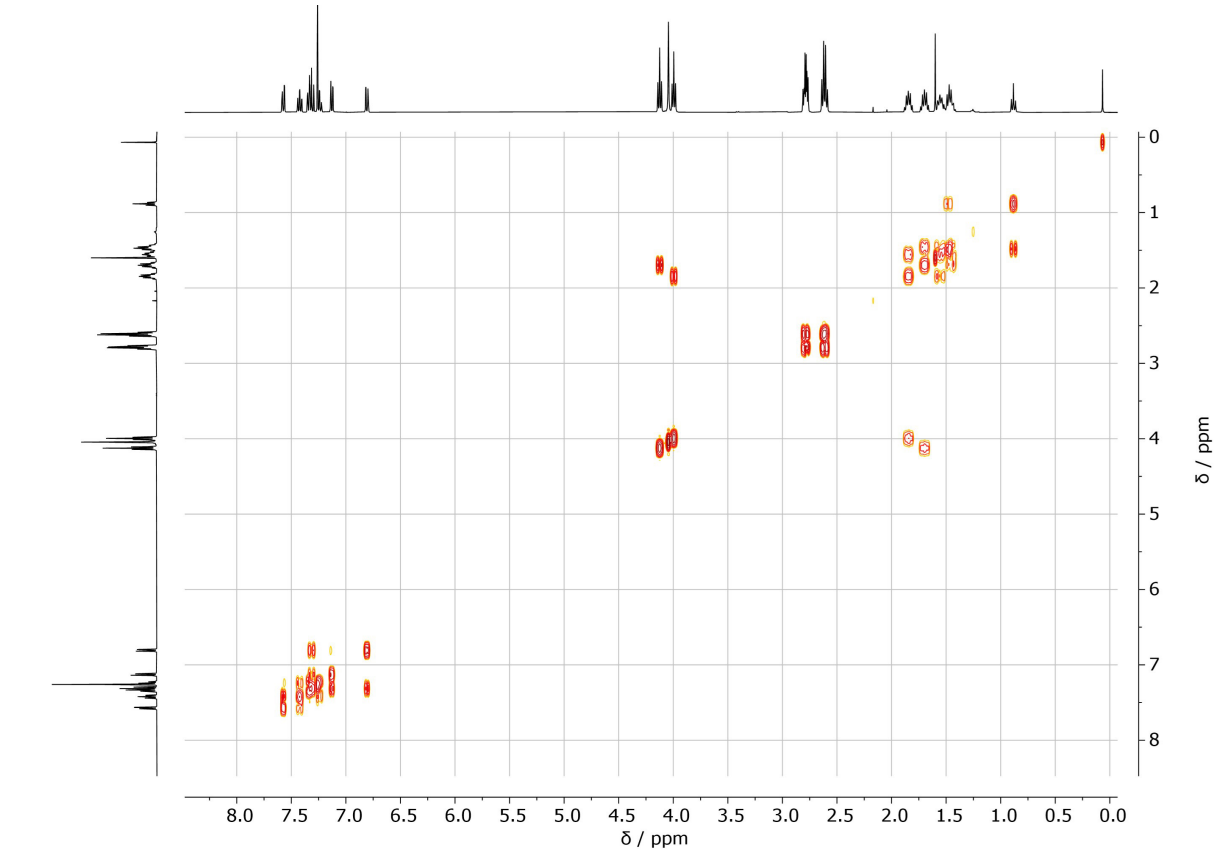

Figure S108. ^{1}H-^{1}H COSY (400 MHz) spectrum of **SA-3arm** in $CDCl_3$ at ambient temperature.

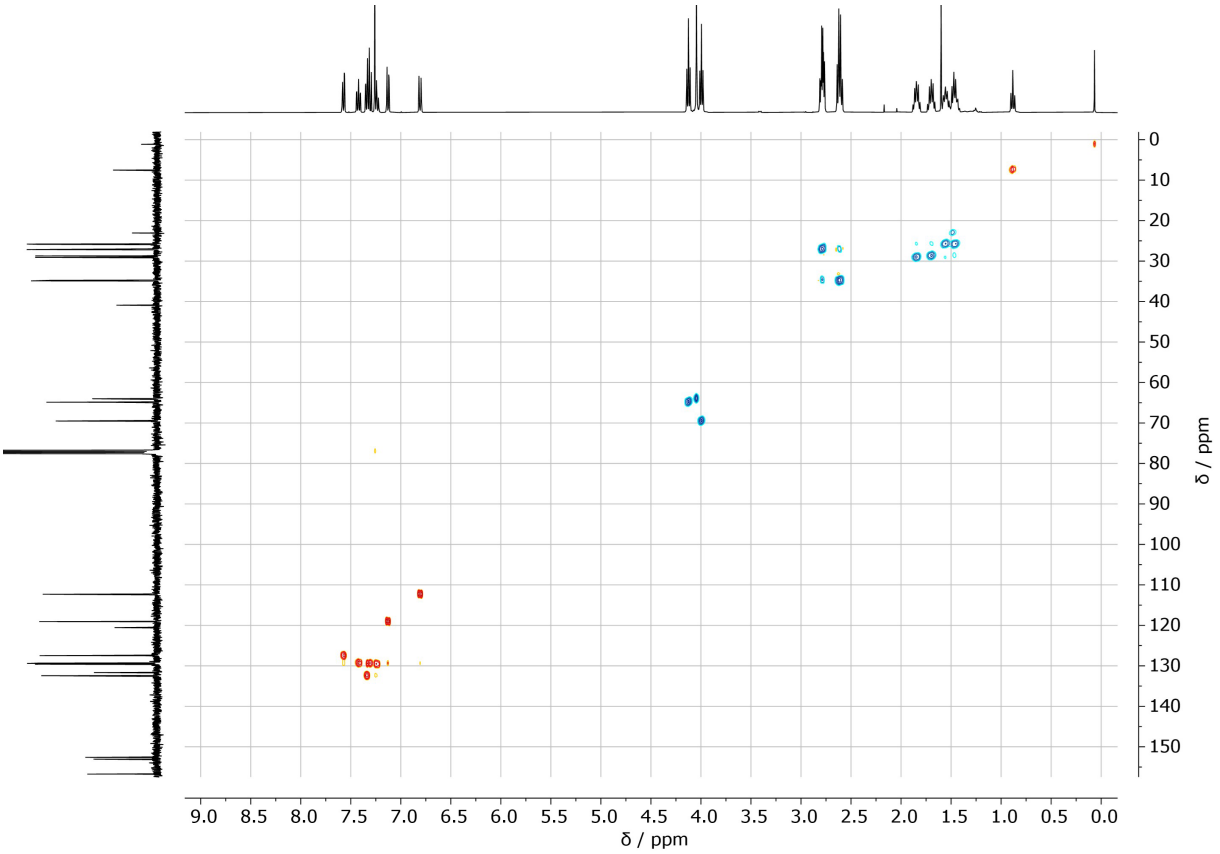

Figure S109. ^{1}H (400 MHz) - ^{13}C (101 MHz) HSQC spectrum of **SA-3arm** in $CDCl_3$ at ambient temperature.

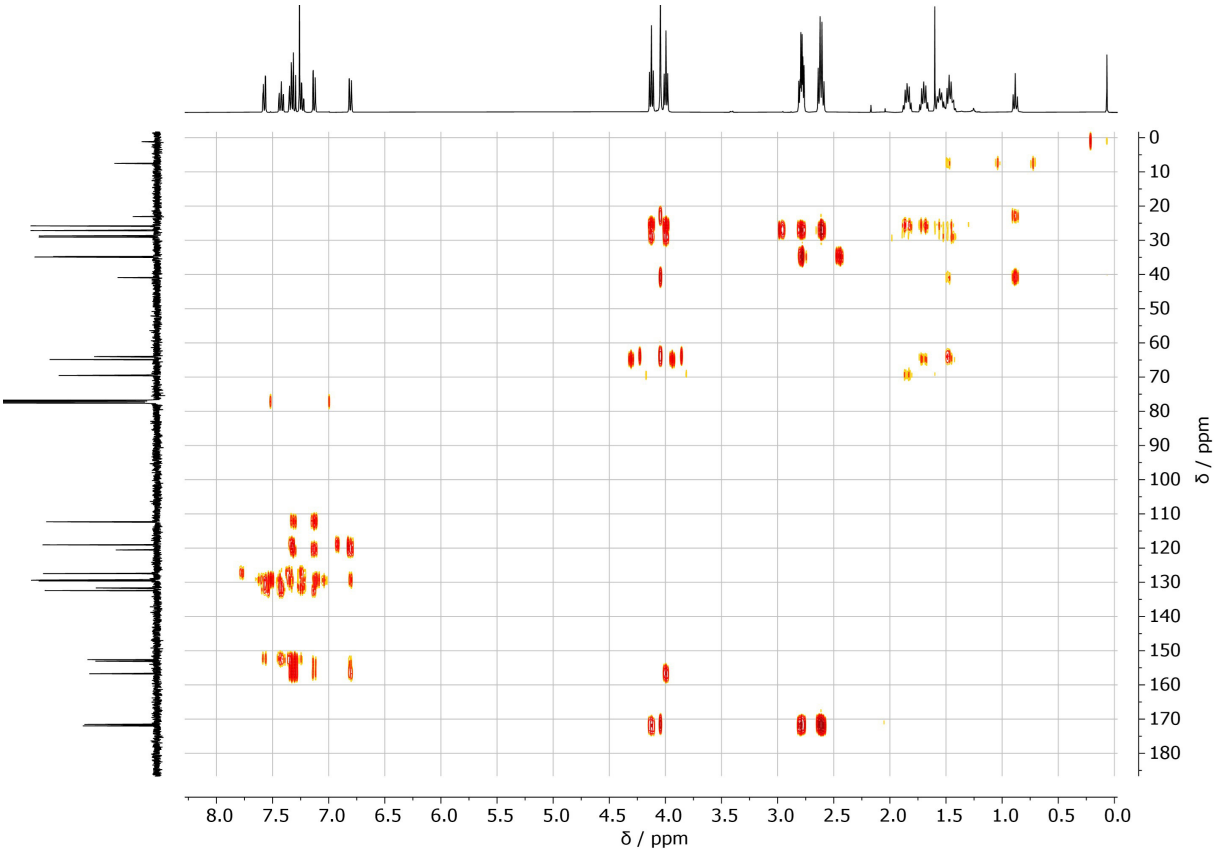

Figure S110. ^{1}H (400 MHz) - ^{13}C (101 MHz) HMBC spectrum of **SA-3arm** in $CDCl_3$ at ambient temperature.

7.8 LC-MS measurements

7.8.1 Small-Molecule Study

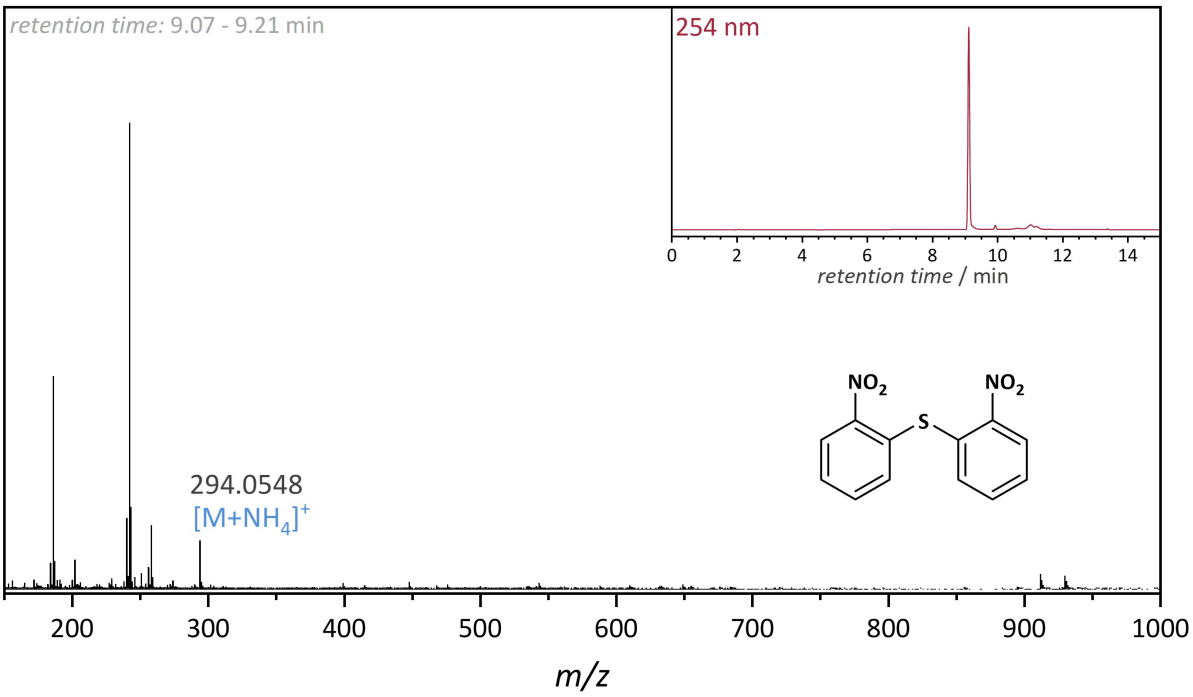

Figure S111. LC-trace (254 nm detector wavelength) and accumulated mass-spectra of **preSA**.

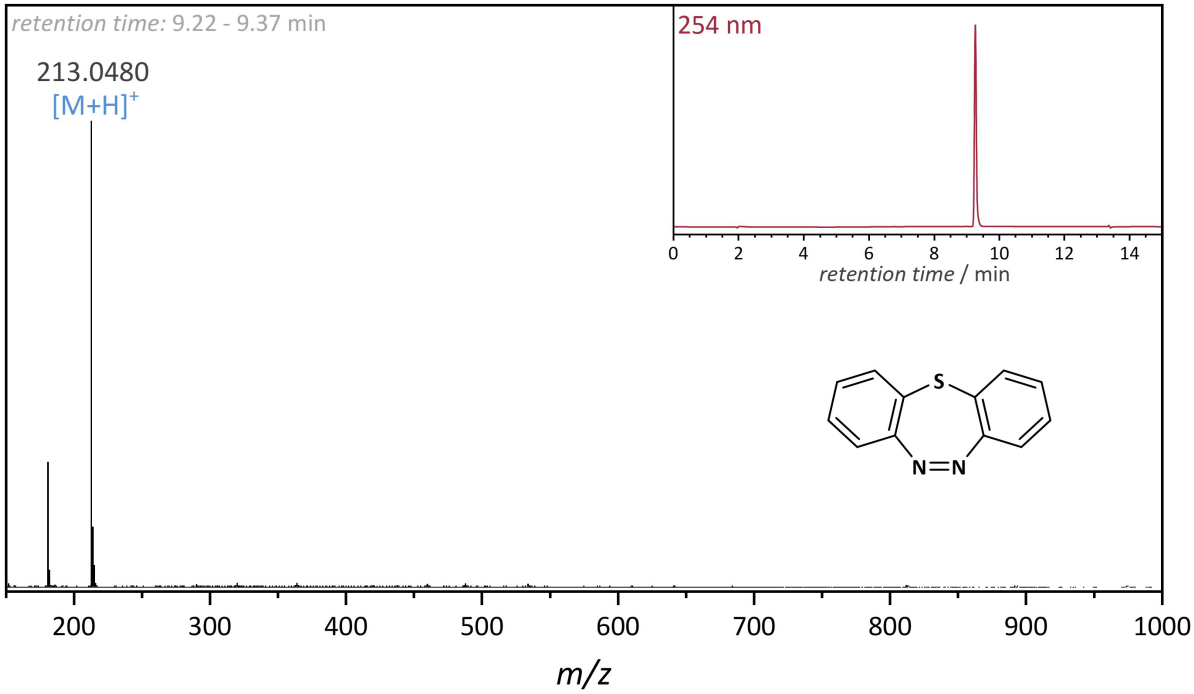

Figure S112. LC-trace (254 nm detector wavelength) and accumulated mass-spectra of **SA**.

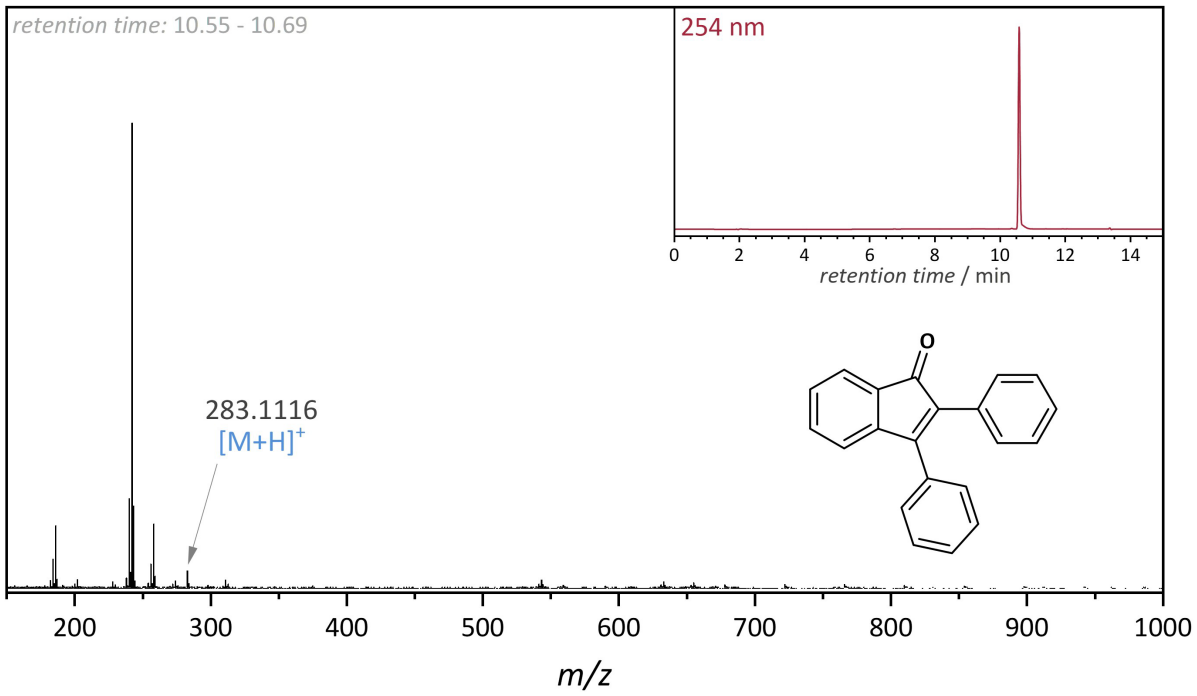

Figure S113. LC-trace (254 nm detector wavelength) and accumulated mass-spectra of **preDIO**.

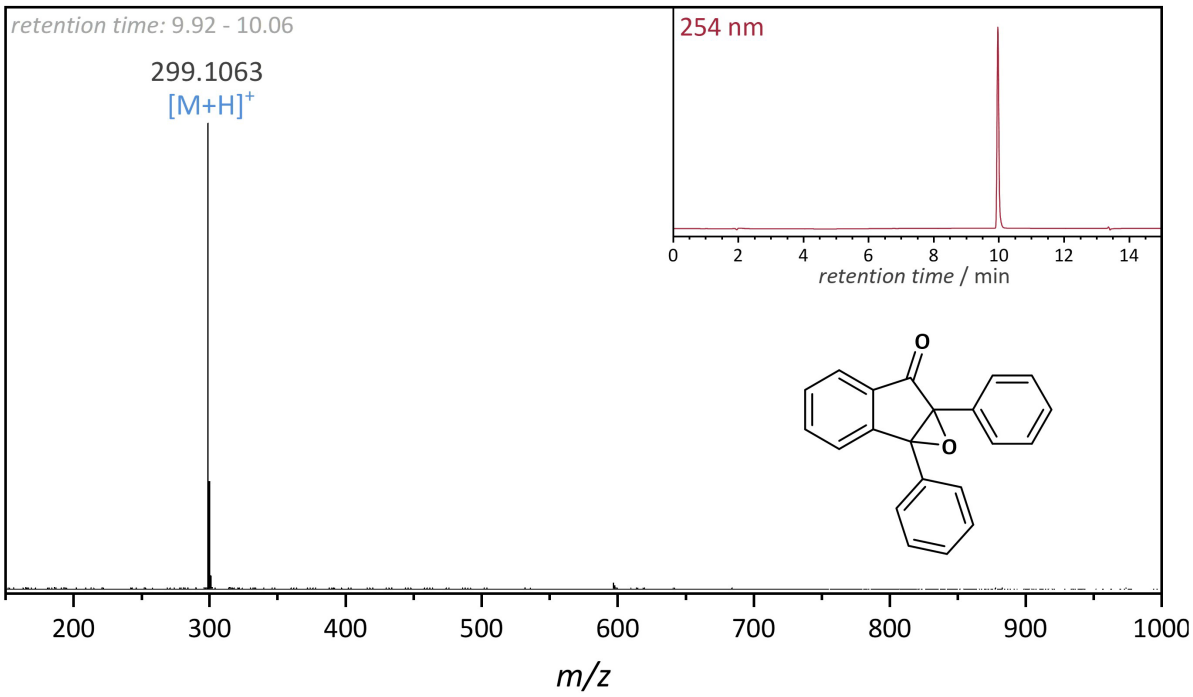

Figure S114. LC-trace (254 nm detector wavelength) and accumulated mass-spectra of **DIO**.

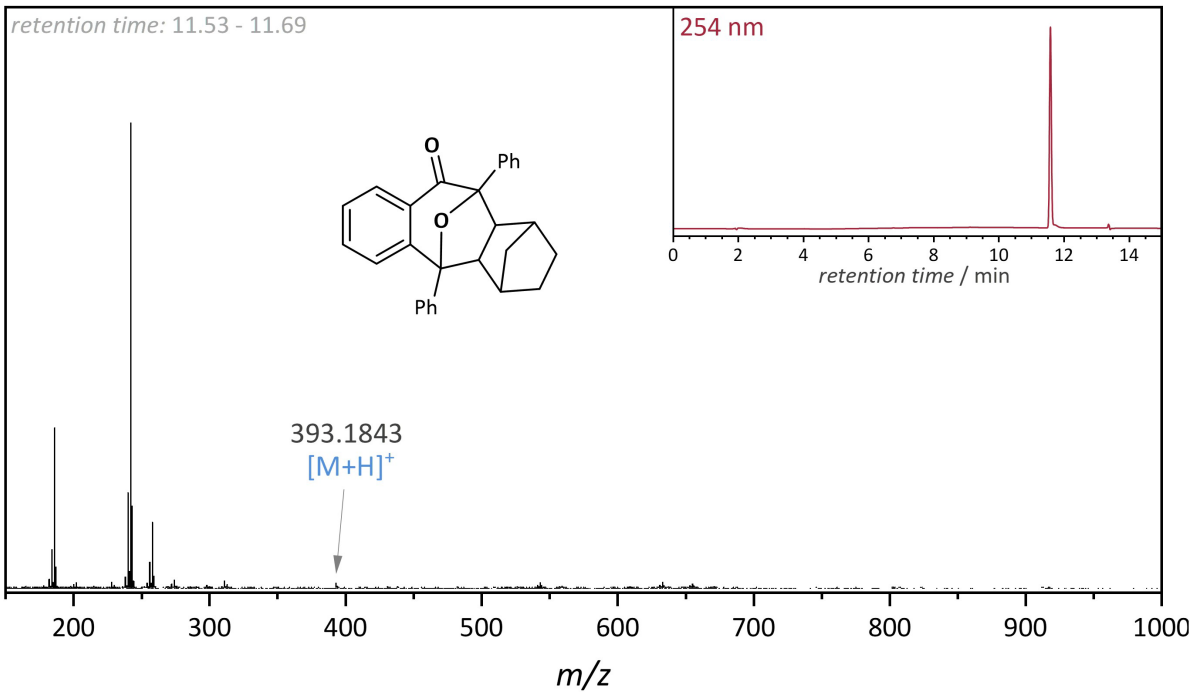

Figure S115. LC-trace (254 nm detector wavelength) and accumulated mass-spectra of **DIOnor**.

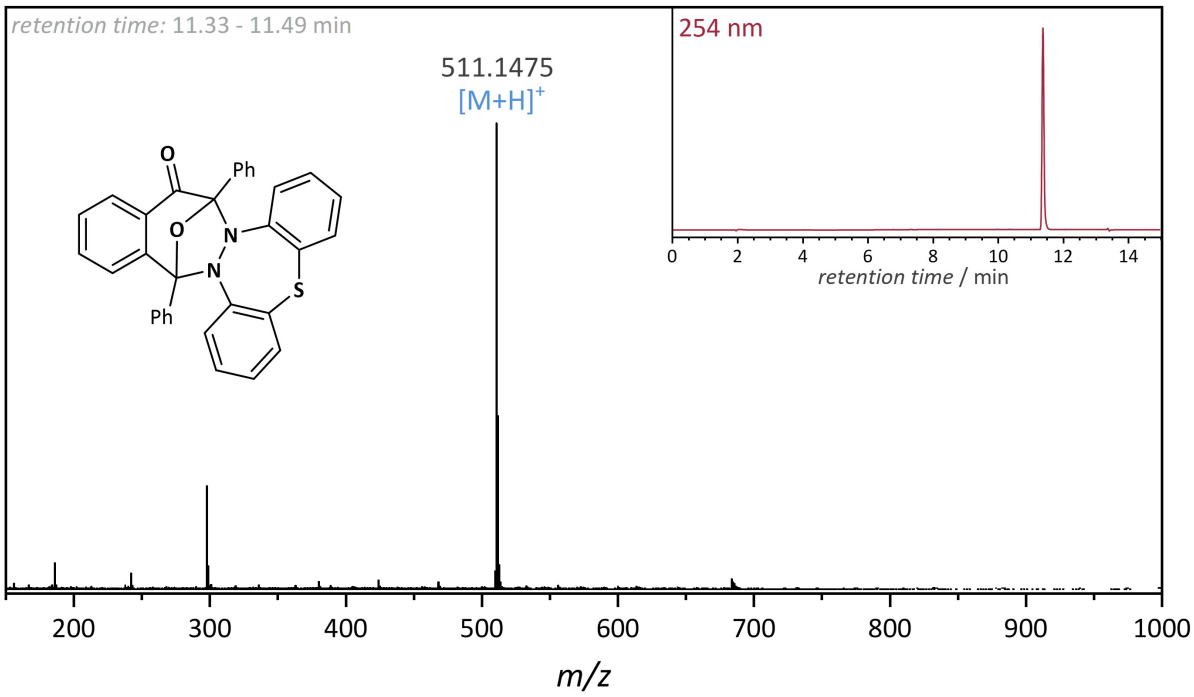

Figure S116. LC-trace (254 nm detector wavelength) and accumulated mass-spectra of **DIOSA**.

7.8.2 Macromolecular study

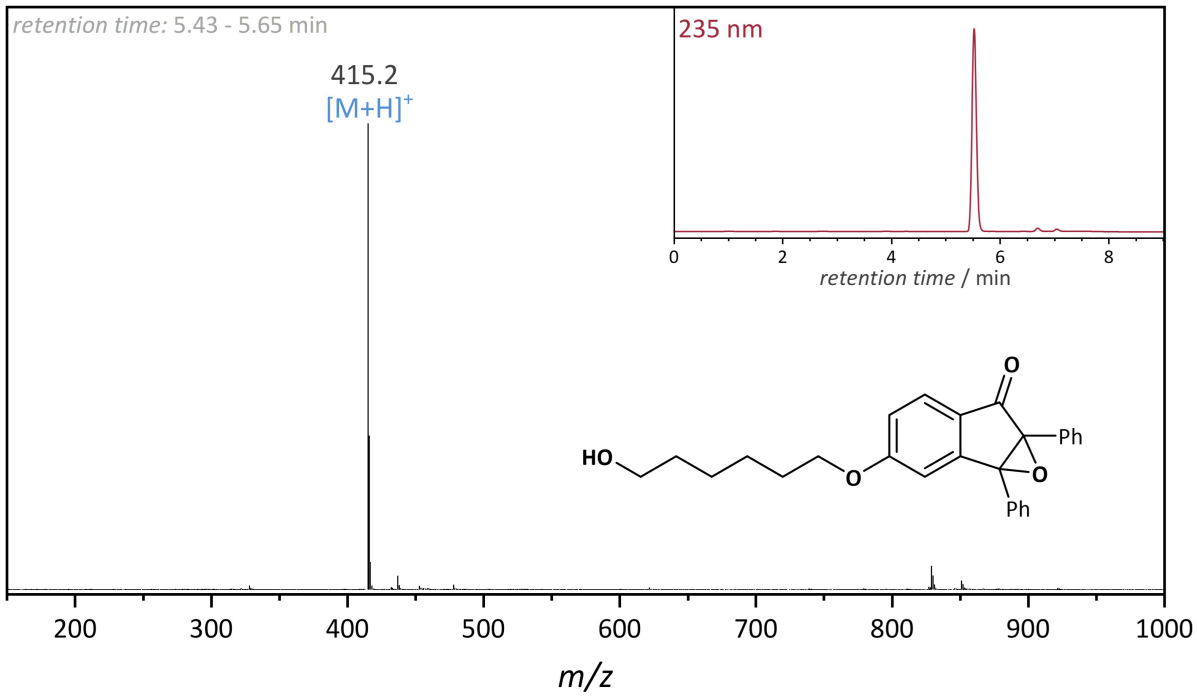

Figure S117. LC-trace (235 nm detector wavelength) and accumulated mass-spectra of **DIO-OH**.

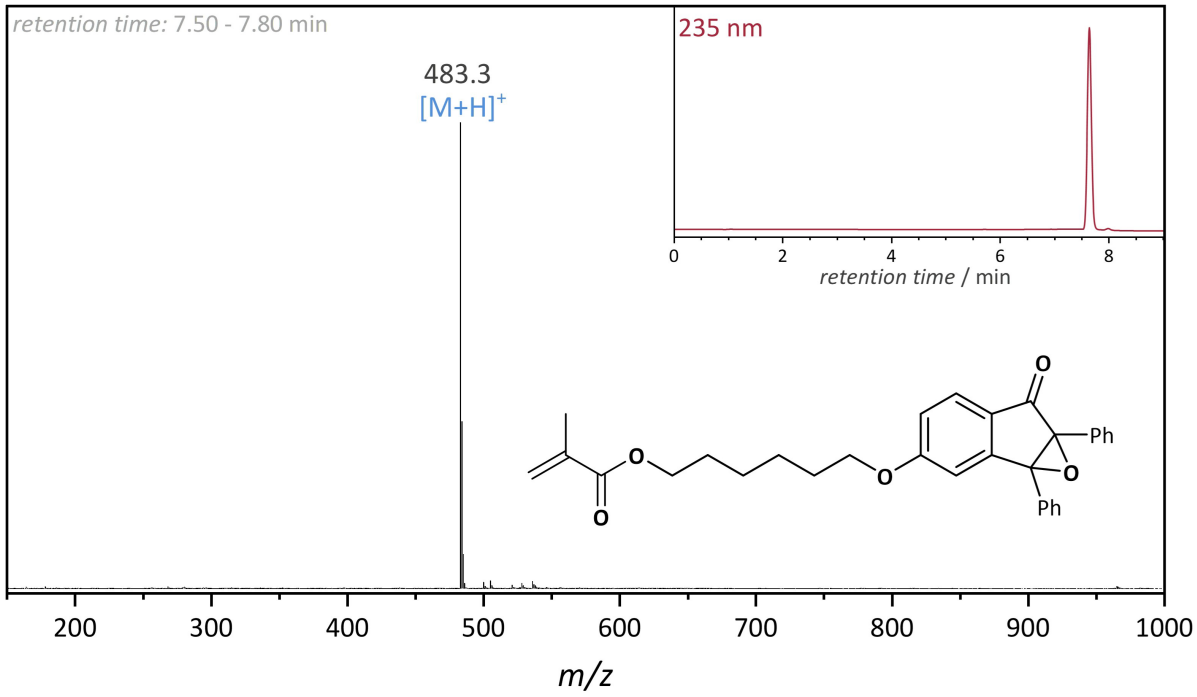

Figure S118. LC-trace (235 nm detector wavelength) and accumulated mass-spectra of **3**.

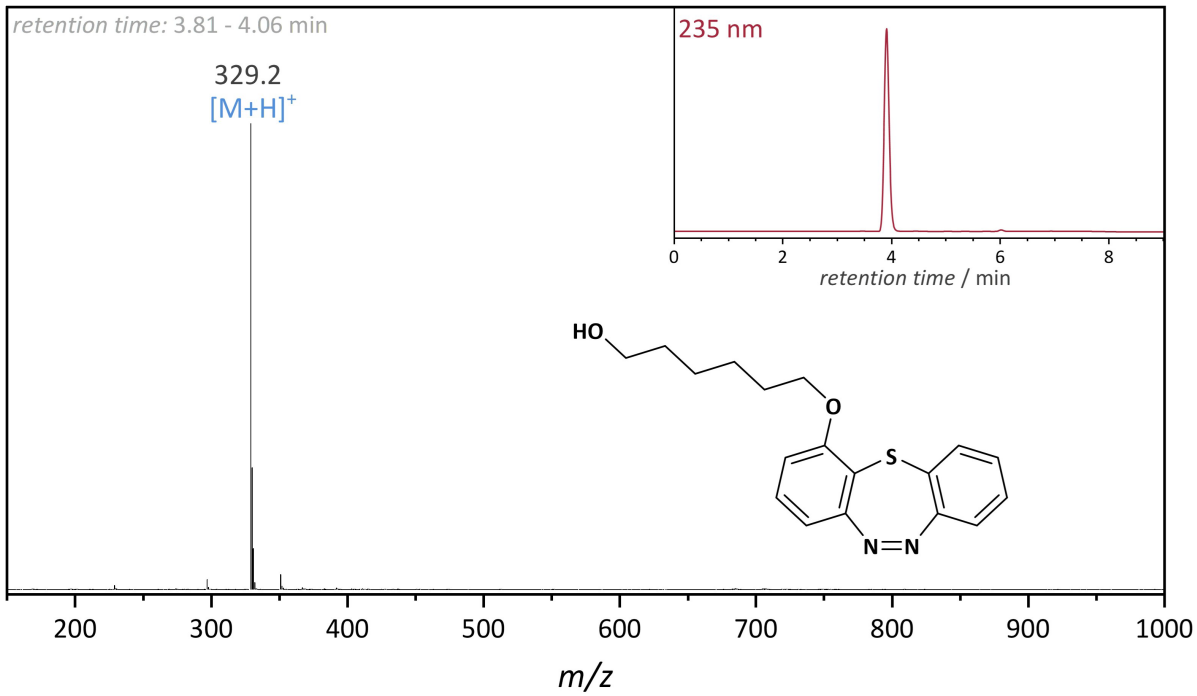

Figure S119. LC-trace (235 nm detector wavelength) and accumulated mass-spectra of **SA-OH**.

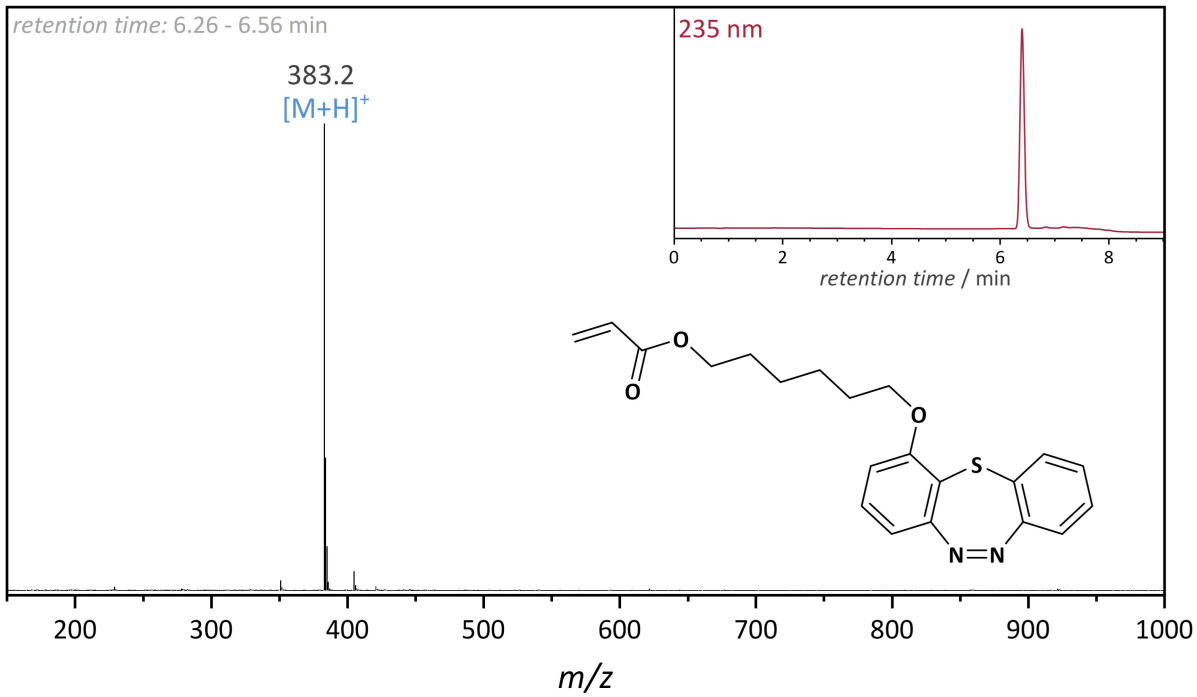

Figure S120. LC-trace (235 nm detector wavelength) and accumulated mass-spectra of **6**.

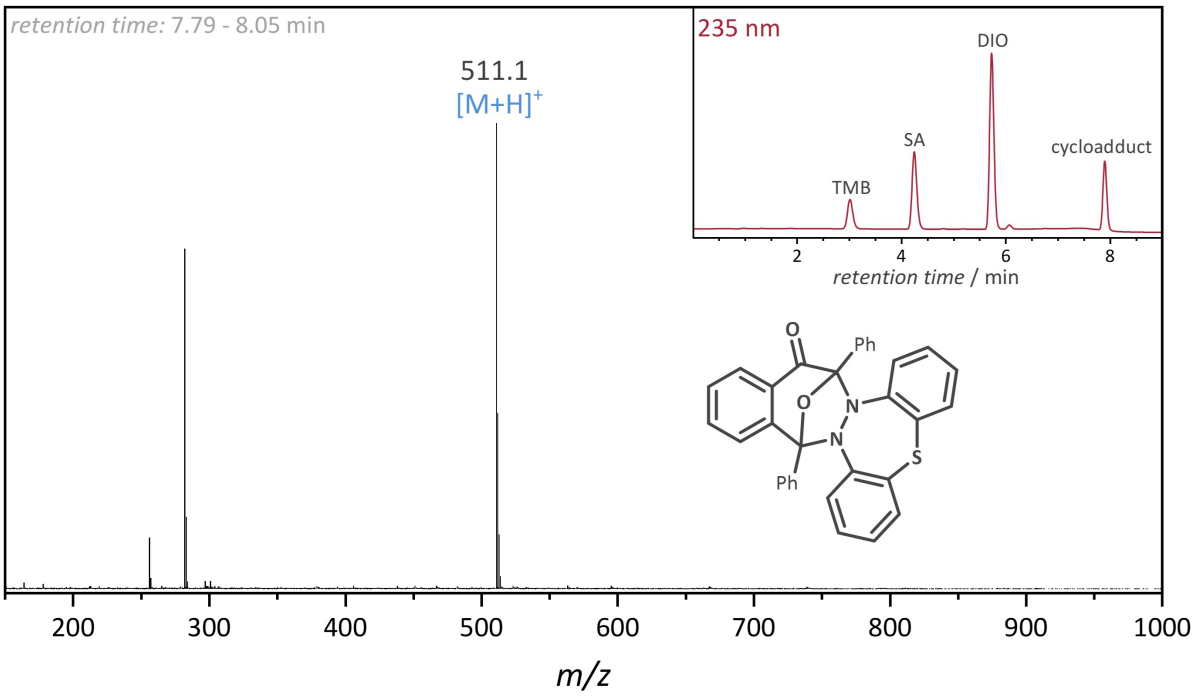

Figure S121. LC-trace (235 nm detector wavelength) of the crude mixture of the two-color photoreaction between **DIO** and **SA** and accumulated mass-spectra of the formed DIOSA derivative (cycloadduct).

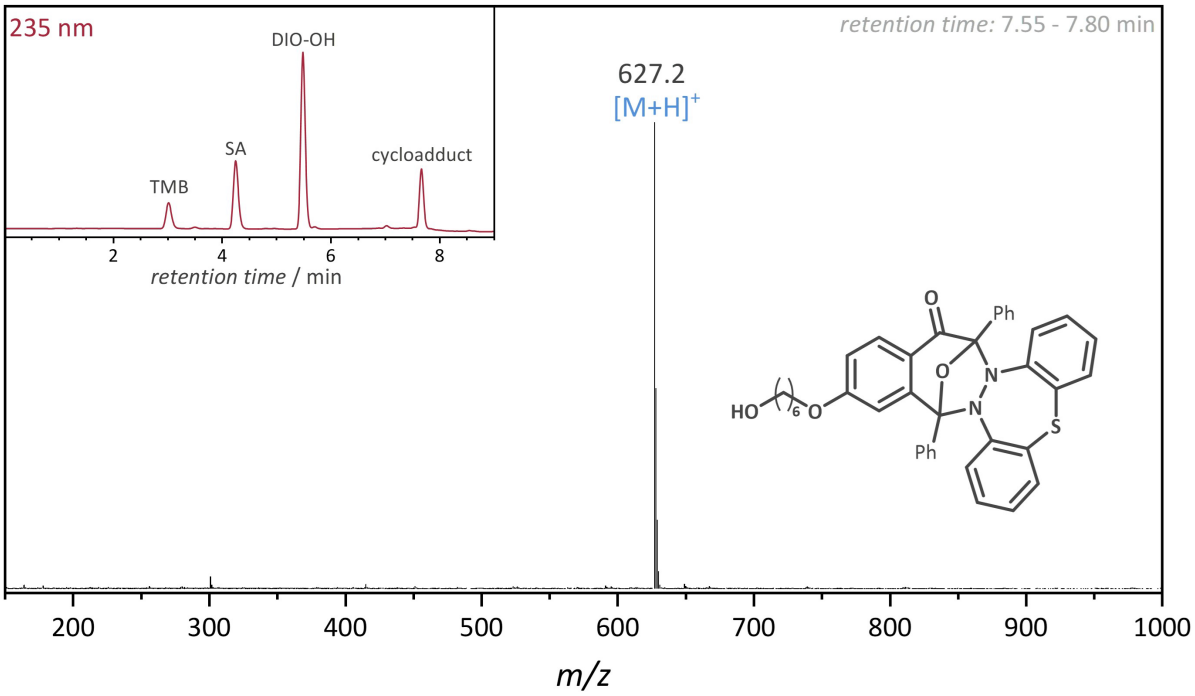

Figure S122. LC-trace (235 nm detector wavelength) of the crude mixture of the two-color photoreaction between **DIO-OH** and SA and accumulated mass-spectra of the formed DIOSA derivative (cycloadduct).

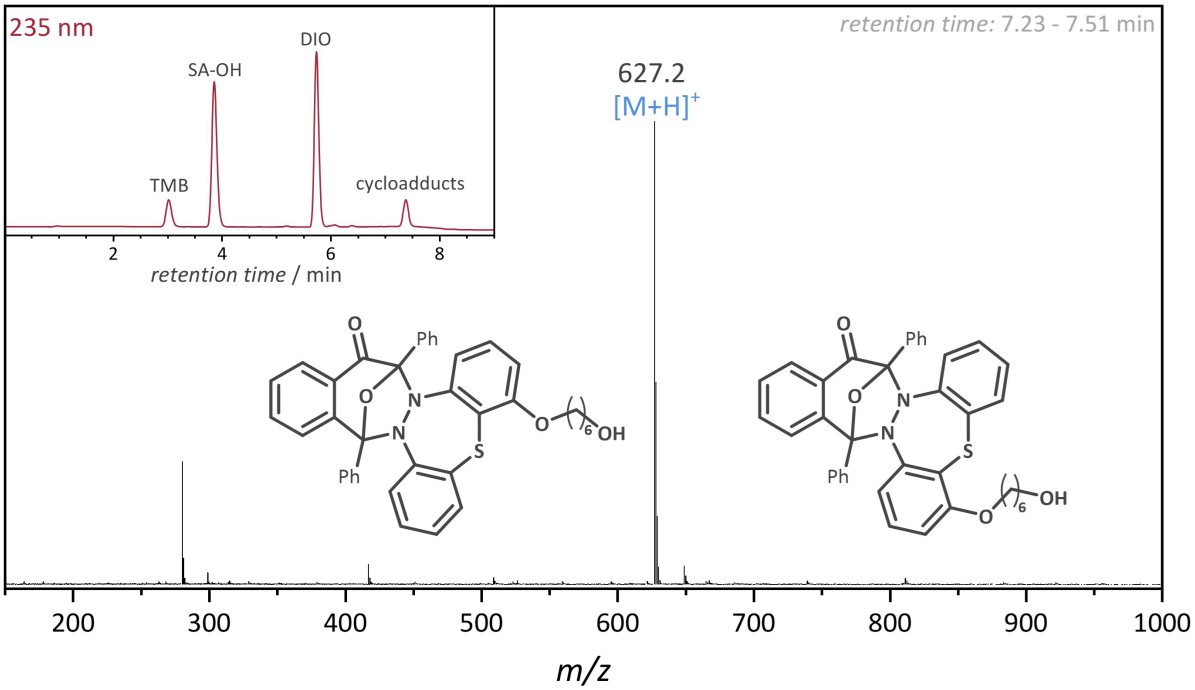

Figure S123. LC-trace (235 nm detector wavelength) of the crude mixture of the two-color photoreaction between DIO and **SA-OH** and accumulated mass-spectra of the formed DIOSA derivatives (cycloadduct).

7.9 UV-Vis spectra

7.9.1 Small-Molecule Study

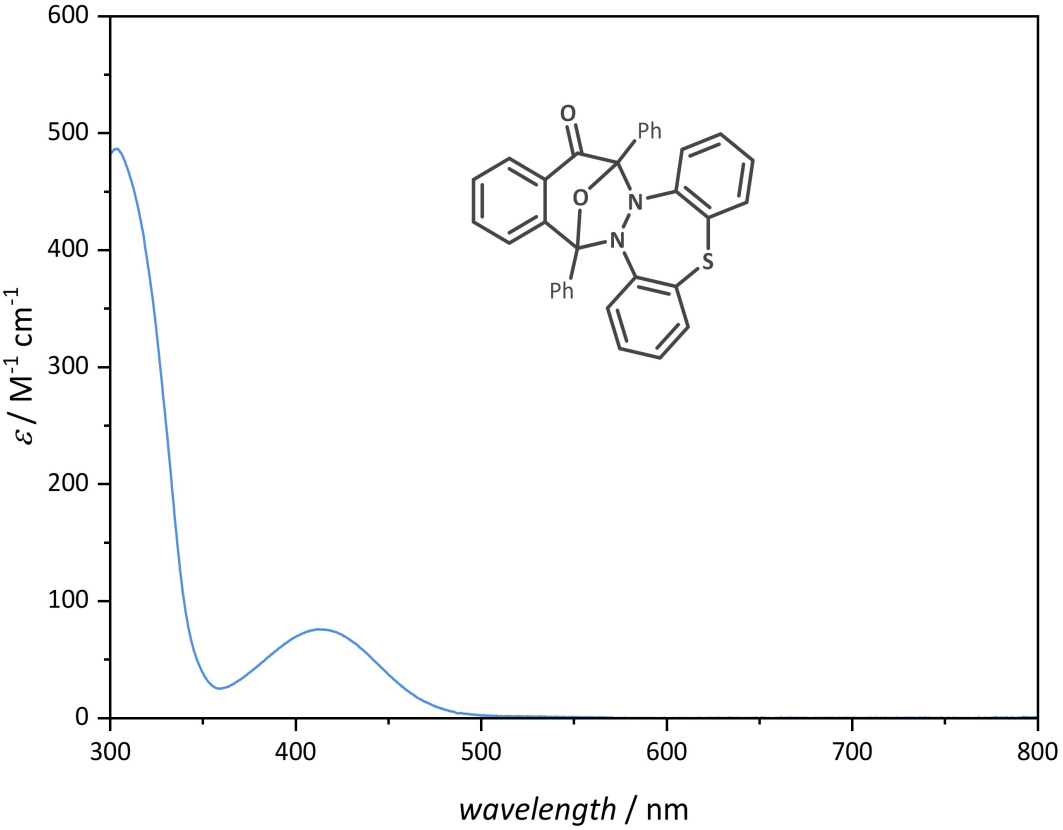

Figure S124. UV-Vis absorbance spectrum of **DIOSA** in acetonitrile.

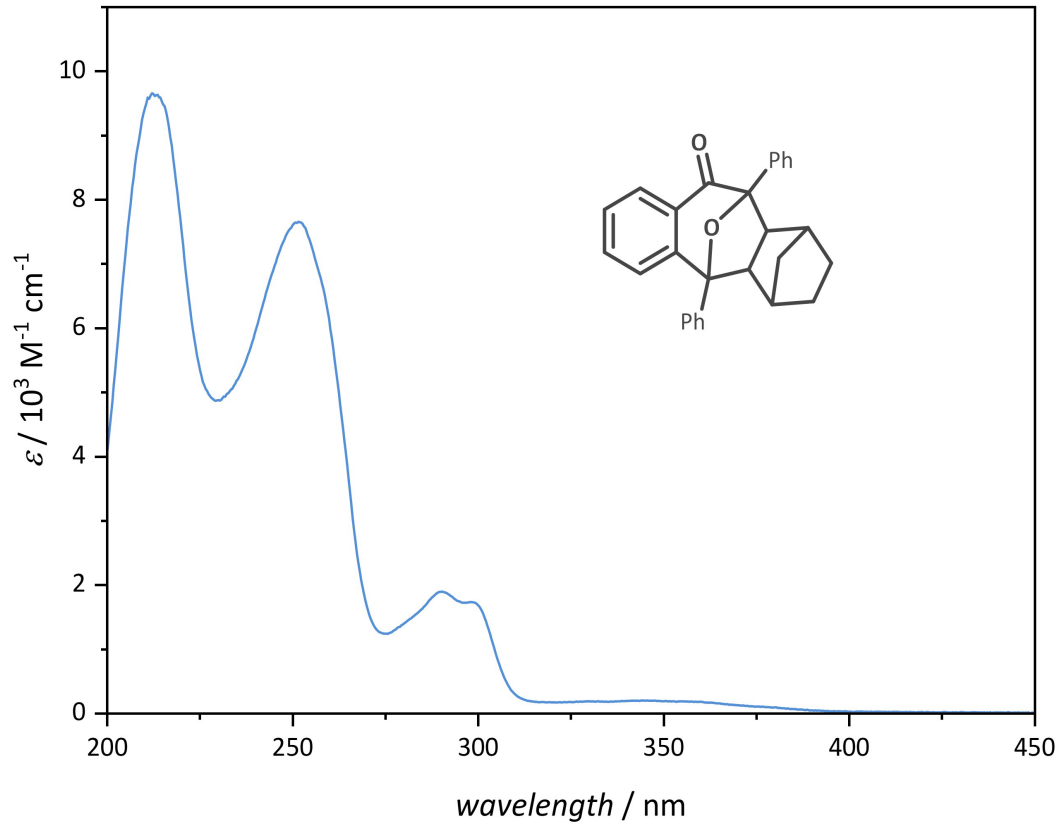

Figure S125. UV-Vis absorbance spectrum of **DIOnor** in acetonitrile.

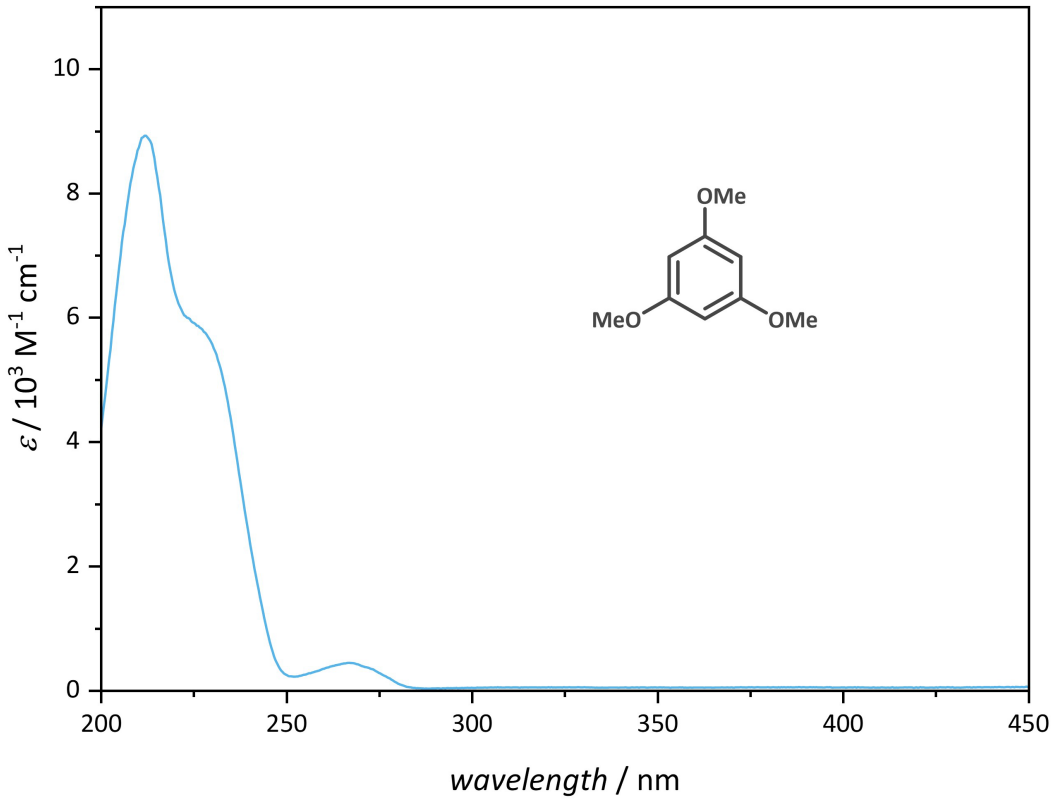

Figure S126. UV-Vis absorbance spectrum of 1,3,5-trimethoxybenzene in acetonitrile.

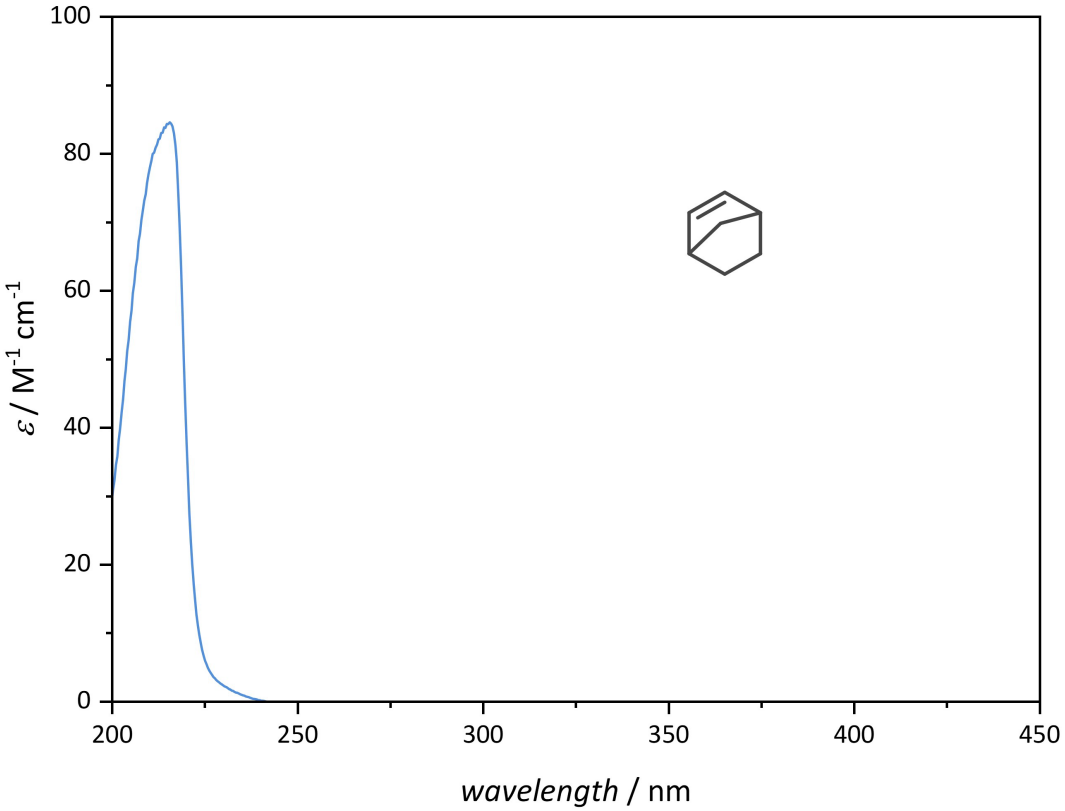

Figure S127. UV-Vis absorbance spectrum of norbornene in acetonitrile.

7.9.2 Macromolecular Study

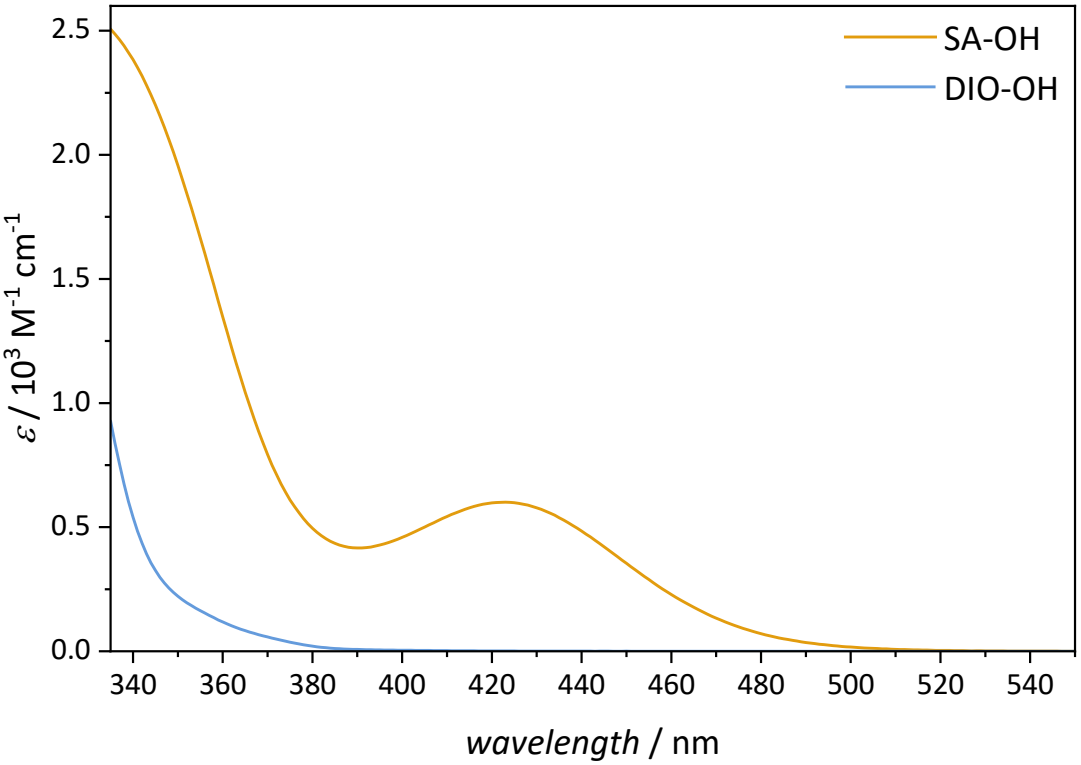

Figure S128. UV-Vis absorption spectra of **DIO-OH** (blue) and **SA-OH** (yellow) in acetonitrile.

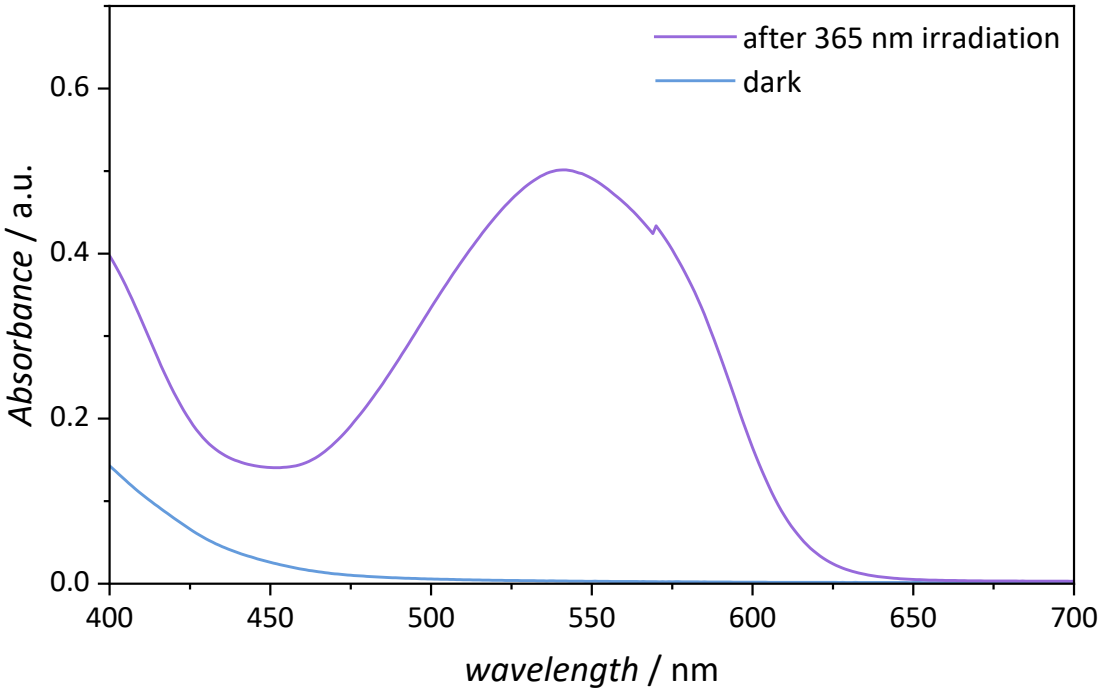

Figure S129. UV-Vis absorption spectra of **polyDIO** (10 mg mL^{-1}) before (blue) and after irradiation with light at 365 nm (pink) in acetophenone, evincing photoswitching.

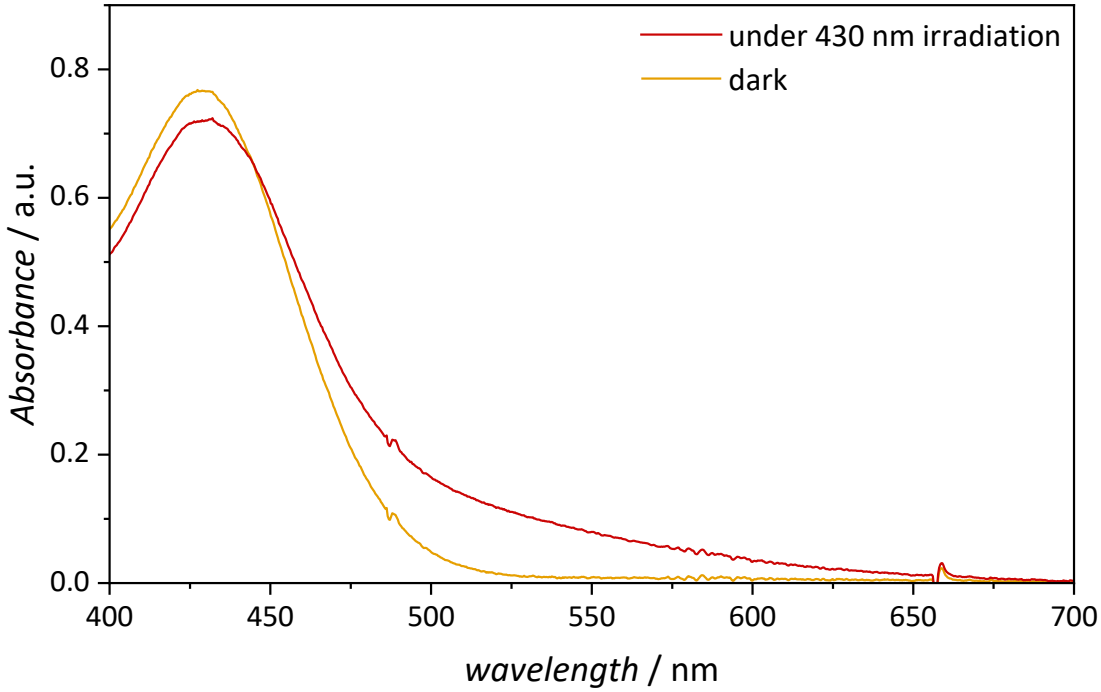

Figure S130. UV-Vis absorption spectra of **SA-3arm** (0.61 mg mL^{-1}) before (yellow) and under irradiation with light at 430 nm (red) in acetophenone, evincing photoswitching.

7.10 ATR-IR spectra

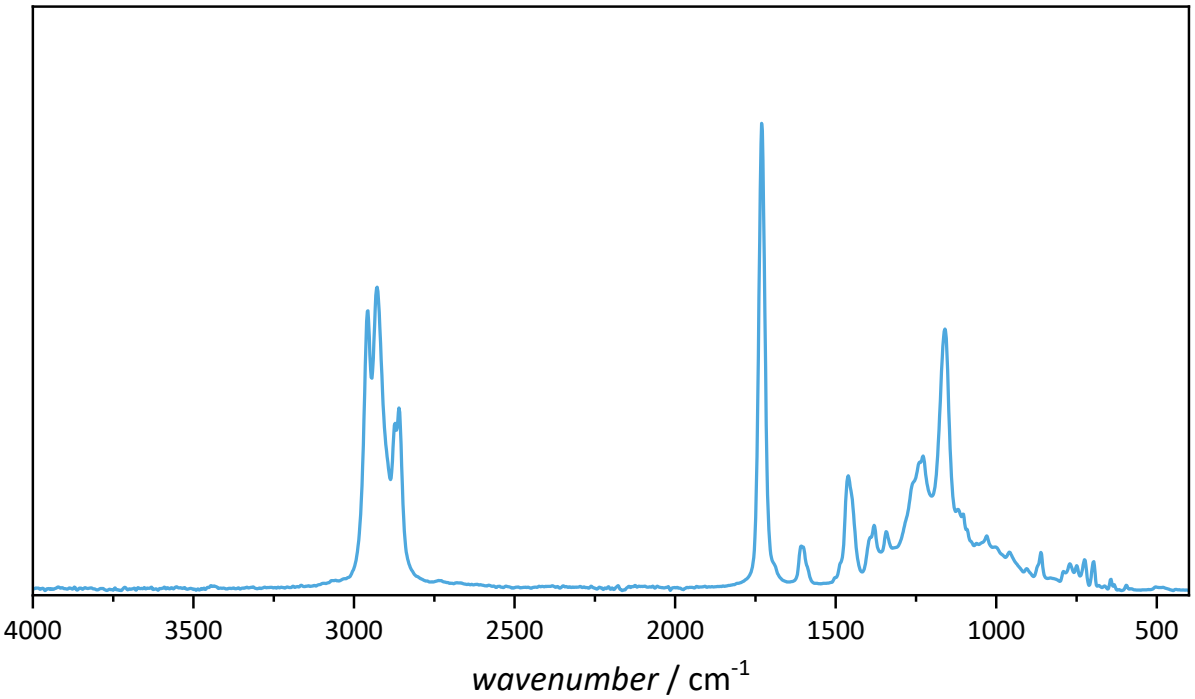

Figure S131. ATR-IR spectrum of **polyDIO** in the range of 400 to 4000 cm^{-1}.

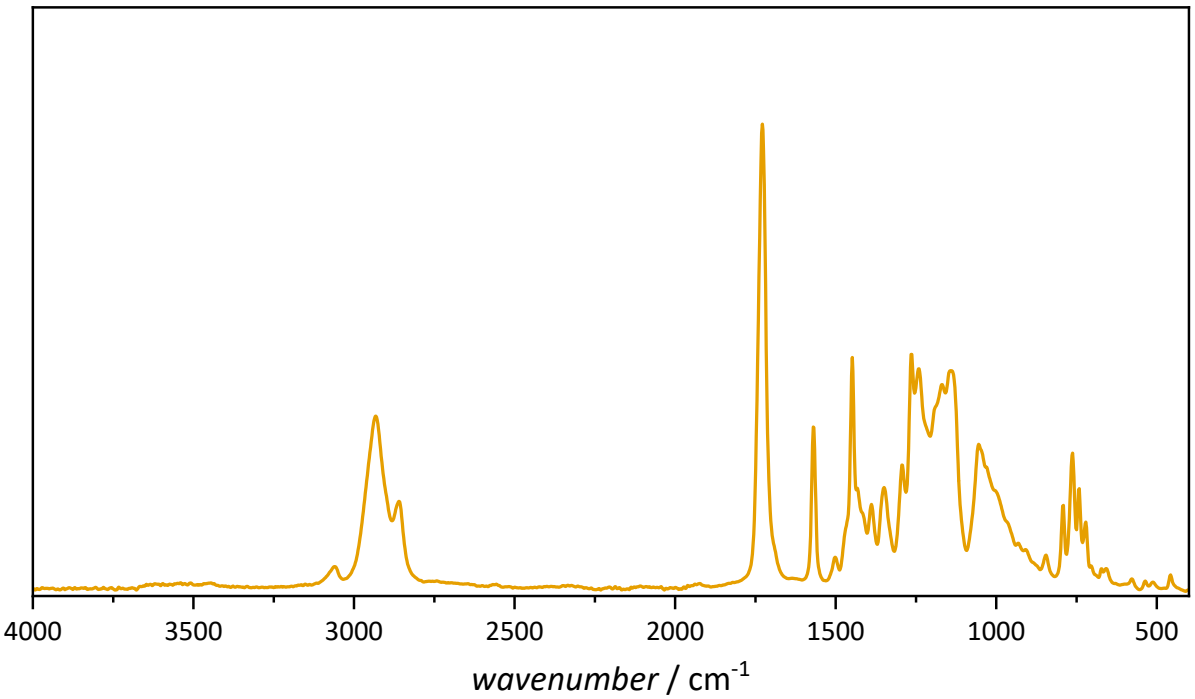

Figure S132. ATR-IR spectrum of **SA-3arm** in the range of 400 to 4000 cm^{-1}.

7.11 Thermal Characterization

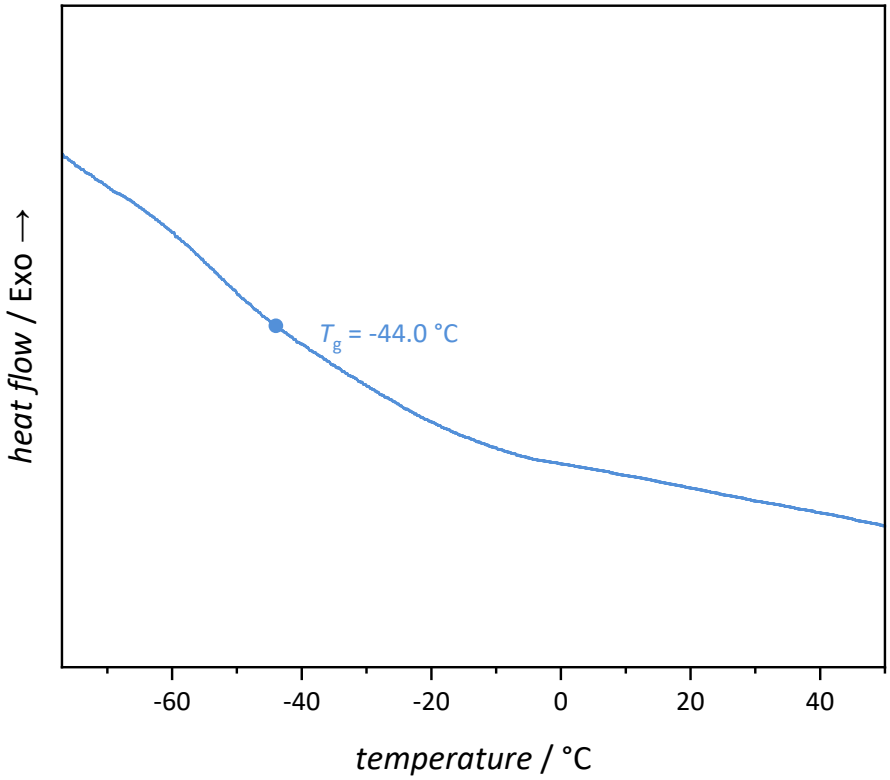

Figure S133. DSC curve of **polyDIO** from -90 to 100 °C (second heating run) with a heating rate of 20 K min^{-1}.

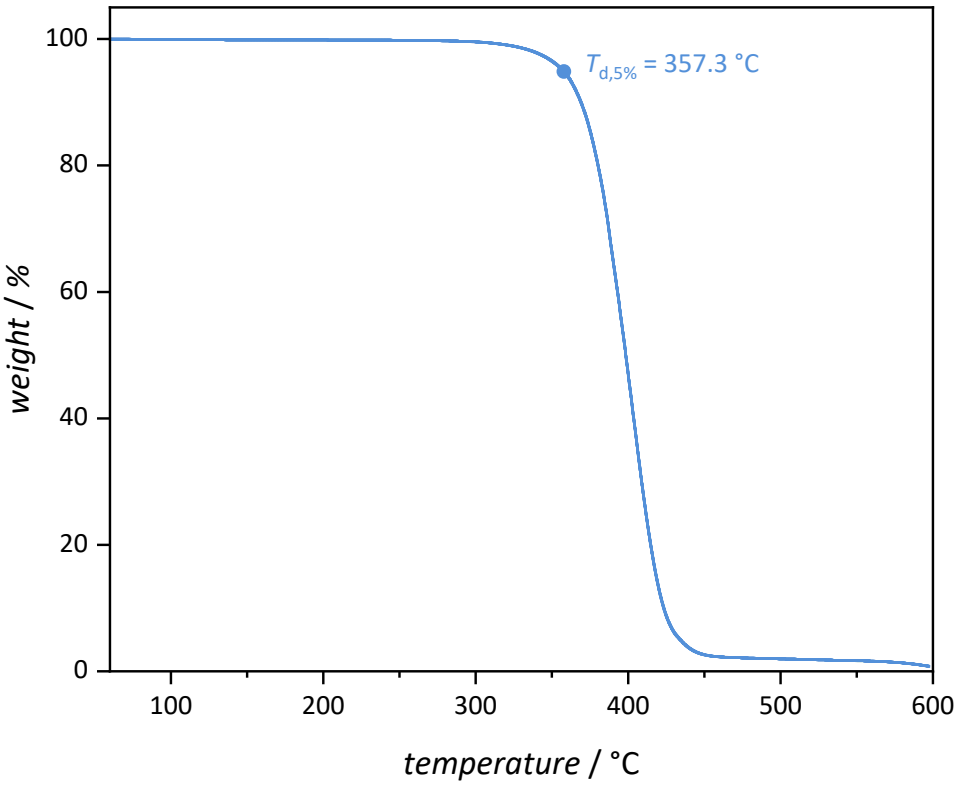

Figure S134. TGA curve of **polyDIO** from 25 to 600 °C with a heating rate of 10 K min^{-1}.

7.12 Crystal Structures

Crystallographic data for compounds DIOnor and DIOSA reported in this paper have been deposited with the Cambridge Crystallographic Data Centre as supplementary information no. CCDC-2355588 and 2355589, respectively. Copies of the data can be obtained free of charge from https://www.ccdc.cam.ac.uk/structures/. Crystallographic data and refinement details are summarized in **Table S7** and **Table S8**.

DIOnor

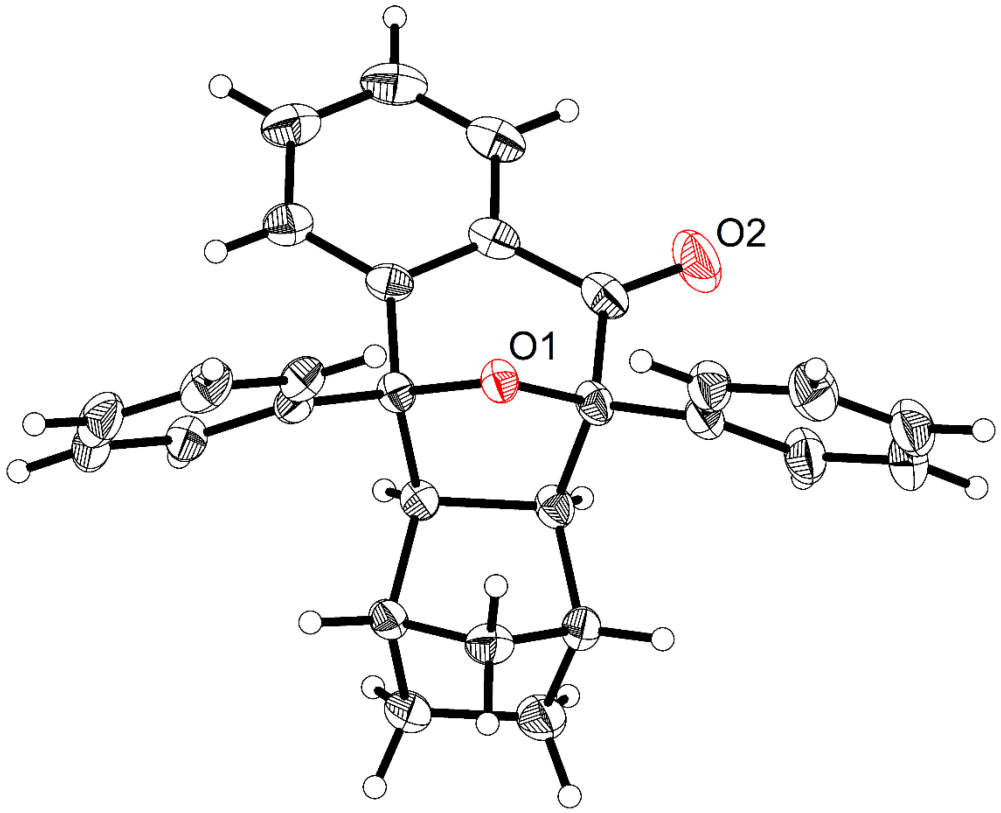

Figure S135. ORTEP plot of **DIOnor** drawn with 50 % probability.

Table S7. Crystallographic data and refinement details of **DIOnor**.

Empirical formula	$C_{28}H_{24}O_2$
Formula weight	392.47
Temperature/K	180
Crystal system	monoclinic
Space group	$P2_1/c$
a/Å	13.3045(3)
b/Å	8.6193(2)
c/Å	18.2074(4)
α/°	90
β/°	108.055(2)
γ/°	90
Volume/Å^3	1985.13(8)
Z	4
ρ_{calc}g/cm^3	1.313
μ/mm^{-1}	0.407
F(000)	832.0
Crystal size/mm^3	0.1 × 0.07 × 0.03
Radiation	Ga Kα (λ = 1.34143)
2Θ range for data collection/°	8.888 to 124.992
Index ranges	-17 ≤ h ≤ 6, -11 ≤ k ≤ 11, -22 ≤ l ≤ 24
Reflections collected	39606
Independent reflections	4755 [R_{int} = 0.0529, R_{sigma} = 0.0369]
Indep. refl. with I≥2σ (I)	3270
Data/restraints/parameters	4755/0/271
Goodness-of-fit on F^2	1.046
Final R indexes [I≥2σ (I)]	R_1 = 0.0407, wR_2 = 0.1046
Final R indexes [all data]	R_1 = 0.0628, wR_2 = 0.1094
Largest diff. peak/hole / e Å^{-3}	0.23/-0.20
CCDC number	2355588

DIOSA

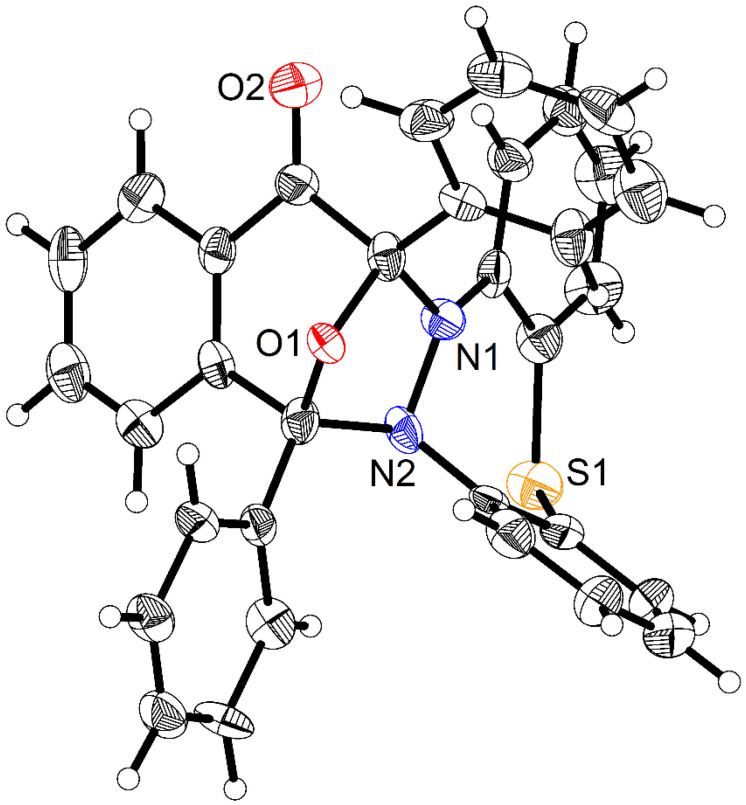

Figure S136. ORTEP plot of **DIOSA** drawn with 50 % probability.

Table S8. Crystallographic data and refinement details of **DIOSA**.

Empirical formula	$C_{33}H_{22}N_2O_2S$
Formula weight	510.58
Temperature/K	180
Crystal system	orthorhombic
Space group	$P2_12_12$
a/Å	34.9121(6)
b/Å	35.2446(8)
c/Å	8.23240(10)
α/°	90
β/°	90
γ/°	90
Volume/Å^3	10129.7(3)
Z	16
ρ_{calc}g/cm^3	1.339
μ/mm^{-1}	0.911
F(000)	4256.0
Crystal size/mm^3	0.18 × 0.04 × 0.03
Radiation	Ga Kα (λ = 1.34143)
2Θ range for data collection/°	6.2 to 99.998
Index ranges	-39 ≤ h ≤ 39, -40 ≤ k ≤ 40, -3 ≤ l ≤ 9
Reflections collected	137281
Independent reflections	15753 [R_{int} = 0.0924, R_{sigma} = 0.0539]
Indep. refl. with I≥2σ (I)	13034
Data/restraints/parameters	15753/0/1370
Goodness-of-fit on F^2	1.049
Final R indexes [I>=2σ (I)]	R_1 = 0.0960, wR_2 = 0.2425
Final R indexes [all data]	R_1 = 0.1068, wR_2 = 0.2489
Largest diff. peak/hole / e Å^{-3}	1.74/-0.52
Flack parameter	0.16(5)
CCDC number	2355589

7.13 Two-Color Lithography

7.13.1 Setup

All components of the two-color lithography setup are mounted on an optical table. As shown in **Figure 48**, we incorporated a continuous-wave (CW) 375 nm laser into our custom-designed Mono LISA 3D printer for two-color lithography. An *Innolas* SpitLight 600 optical parametric oscillator (OPO) wavelength-tunable laser producing 7 ns, 100 Hz pulses serves as 430 nm light source and TOPTICA IBEAM-SMART-PT 375 nm serves as 375 nm light source. The output beam of the pulsed laser passes through a Dove prism (Pr), subsequently through two cylindrical lenses (L1 and L2, f = 250.0 mm and -100.0 mm, respectively) and an attenuator (A, used to adjust the pulsed laser power). It then passes spherical lenses (L3 and L4, f = 50.0 mm and 150.0 mm respectively) and mirrors (F and M1). The flip mirror (F) is employed to direct the pulsed laser beam in the UV region along its designed pathway. To allow the 430 nm beam to pass, F must be flipped down. The pulsed beam is then combined with the CW 375 nm laser via a beam splitter (B, 50:50). The combined beams further pass two spherical lenses (L3 and L5, f = 50.0 mm and 75.0 mm, respectively), a mirror (M1) and a shutter (S), before being directed to the Galvo mirror (dual-axis, 250 µs step response time). After passing two lenses (L6, f = 150.0 mm), the beams are focused on a z-stage (Thorlabs motorized translation stage with a KSC101 - K-Cube Solenoid Controller) via a 45° mirror (M2) and a focusing lens (L7, f = 75.0 mm). The power meter (P) is positioned between L6 and M2 to measure all powers for printing, ensuring both convenience and safety. The movement of the Galvo mirror (G) and the shutter (S, on-off) is controlled by our customized software, programmed in LabView. Upon importing G-code files containing the coordinates and travel speed, the software processes the files to precisely control both the printing trajectory and speed. The resolution of the laser printer is approximately 20 µm, as determined by the focused beam size.

7.13.2 Sample preparation and Lithography

The ink for 2D printing was prepared by mixing polyDIO (720 mg) with SA-3arm (235 mg) in acetophenone (2.146 mL, 2.210 g). After placing the glass sample holder onto the Z stage, the ink was directly deposited onto glass slide for printing. The G-code files for lines, rings and butterflies were generated with UltiMaker Cura (v. 5.6.0). The beam – by passing through the spherical lens (L7) – was focused onto the surface of the glass substrate. The objects were subsequently printed by controlling the motions of the Galvo mirror (G) with the software.

7.13.3 Line testing

To determine the fabrication windows, lines were printed at fixed laser powers at 375 nm and 430 nm, with varying printing speeds. Fabrication windows at 1, 2.5, 5, and 15 mW (375 nm), with or without additional 430 nm irradiation (10 mW), were evaluated, as shown in **Table S9**.

Table S9. Fabrication windows of lines printed with one- or two-color irradiation. 1C stands for one-color irradiation (375 nm) and 2C stands for two-color irradiation (375 nm + 430 nm, 430 nm at 10 mW). Color code: green - printable; grey - not printable.

	v (mm s^{-1}) / *P* (mW)		0.1	0.13	0.16	0.2	0.23	0.26	0.3	0.33	0.36	0.4	0.45	0.5	0.55	0.6	0.65	0.7	0.75	0.8
1C	15																			
2C	15	10																		
1C	5																			
2C	5	10																		
1C	2.5																			
2C	2.5	10																		
1C	1																			
2C	1	10																		

7.13.4 Intricate Structures

A series of ring patterns were designed with varying segments (100%, 75%, 50%, 25%, and 0%) printed using only 375 nm, while the remaining portions were printed using two-color exposure (375 nm + 430 nm) under identical 375 nm conditions.

Figure S137 illustrates the trajectories and coordinates defined in the G-code for each structure. **Figure S138** shows the two-color lithography pathways by fabricating a shared border between the one-color and two-color regions.

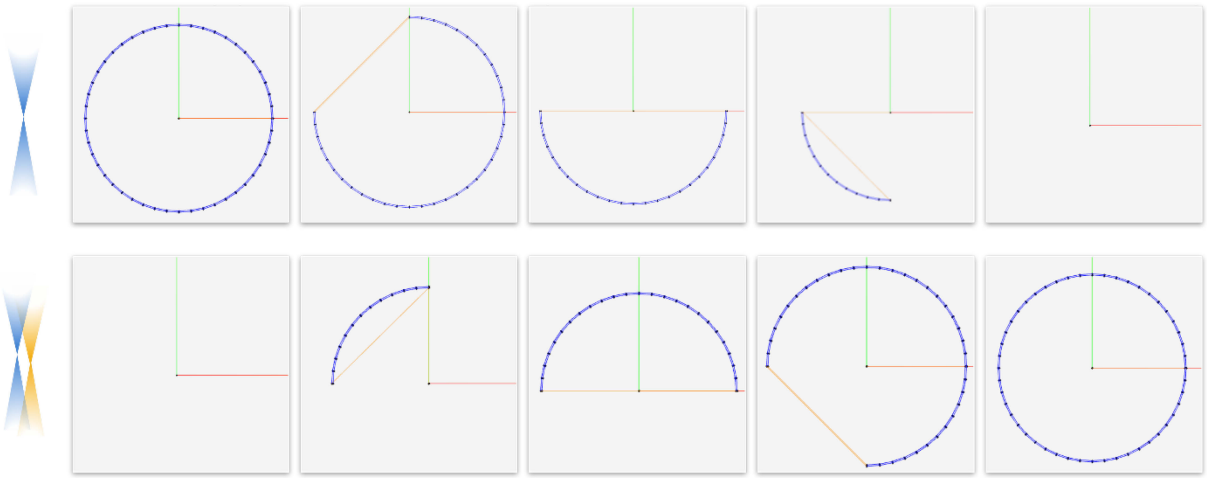

Figure S137. Images illustrating the trajectory of the 2 axes for the series of rings, generated from the G-code files to obtain the corresponding structures. The blue lines represent the trajectory when the shutter is on (i.e., resin exposure to the laser) with blue dots indicating the coordinates. The orange lines show the trajectory when the shutter is off (i.e., resin is not

exposed to the laser). Top: ring segments irradiated with one color (375 nm); bottom: ring segments irradiated with two colors (375 nm + 430 nm).

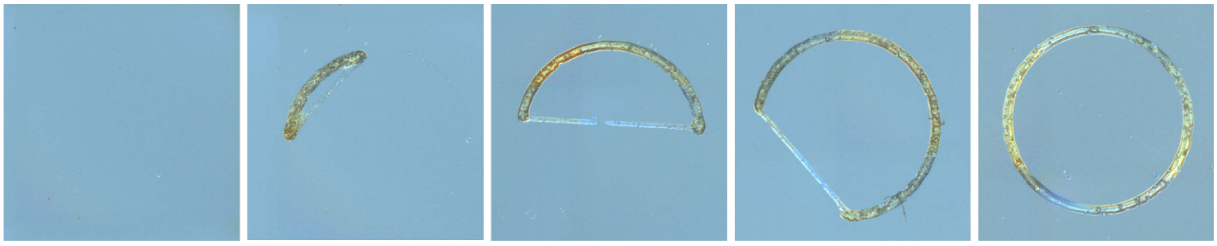

Figure S138. Optical microscopy images of a series of rings with varying fractions (100%, 75%, 50 %, 25 % and 0 %) printed using one-color exposure (375 nm, 5 mW, 0.45 mm s^{-1}), with the remining portions printed using two-color irradiation (375 nm at 5 mW and 430 nm at 10 mW, 0.45 mm s^{-1}). The straight lines were fabricated with two-color irradiation to indicate the two-color pathways.

A butterfly structure was also printed, with the left half fabricated using two colors and the right half using only one color. **Figure S139** illustrates the trajectories and coordinates defined in the G-code for each part of the structure.

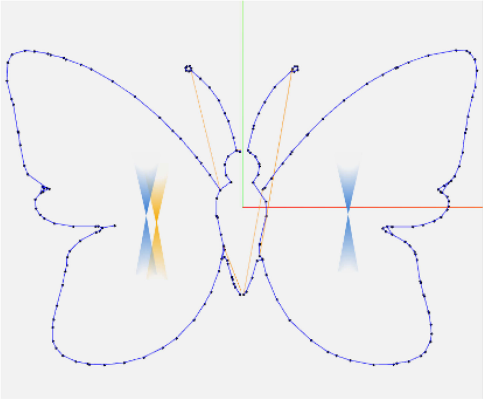

Figure S139. Image illustrates the trajectory of the two axes for the butterfly, generated from the G-code files to obtain the corresponding structures.

8. Bibliography

[1] W. Li, M. Wang, H. Ma, F. A. Chapa-Villarreal, A. O. Lobo, Y. S. Zhang, *iScience* **2023**, *26*, 106039.
[2] J. Huang, Q. Qin, J. Wang, *Processes* **2020**, *8*, 1138.
[3] R. Chaudhary, P. Fabbri, E. Leoni, F. Mazzanti, R. Akbari, C. Antonini, *Prog. Addit. Manuf.* **2023**, *8*, 331.
[4] I. Bernardeschi, M. Ilyas, L. Beccai, *Adv. Intell. Syst.* **2021**, *3*, 2100051.
[5] J. Fischer, M. Wegener, *Laser Photonics Rev.* **2013**, *7*, 22.
[6] D. Gonzalez-Hernandez, S. Varapnickas, A. Bertoncini, C. Liberale, M. Malinauskas, *Adv. Opt. Mater.* **2023**, *11*, 2201701.
[7] K. Jung, N. Corrigan, M. Ciftci, J. Xu, S. E. Seo, C. J. Hawker, C. Boyer, *Adv. Mater.* **2020**, *32*, 1903850.
[8] J. Hobich, E. Blasco, M. Wegener, H. Mutlu, C. Barner-Kowollik, *Macromol. Chem. Phys.* **2023**, *224*, 2200318.
[9] K. Ehrmann, C. Barner-Kowollik, *J. Am. Chem. Soc.* **2023**, *145*, 24438.
[10] C. G. Bochet, *Isr. J. Chem.* **2021**, *61*, 486.
[11] V. Hahn, P. Rietz, F. Hermann, P. Müller, C. Barner-Kowollik, T. Schlöder, W. Wenzel, E. Blasco, M. Wegener, *Nat. Photonics* **2022**, *16*, 784.
[12] M. Regehly, Y. Garmshausen, M. Reuter, N. F. König, E. Israel, D. P. Kelly, C.-Y. Chou, K. Koch, B. Asfari, S. Hecht, *Nature* **2020**, *588*, 620.
[13] P. Somers, A. Münchinger, S. Maruo, C. Moser, X. Xu, M. Wegener, *Nat. Rev. Phys.* **2024**, *6*, 99.
[14] P. N. Bernal, S. Florczak, S. Inacker, X. Kuang, J. Madrid-Wolff, M. Regehly, S. Hecht, Y. S. Zhang, C. Moser, R. Levato, *Nat. Rev. Mater.* **2025**.
[15] N. Corrigan, X. Li, J. Zhang, C. Boyer, *Adv. Mater. Technol.* **2024**, *9*, 2400162.
[16] M.-M. Russew, S. Hecht, *Adv. Mater.* **2010**, *22*, 3348.
[17] D. Bléger, S. Hecht, *Angew. Chem. Int. Ed.* **2015**, *54*, 11338.
[18] Z. L. Pianowski, *Chem. Eur. J.* **2019**, *25*, 5128.
[19] M. Jeong, J. Park, S. Kwon, *Eur. J. Org. Chem.* **2020**, *2020*, 7254.
[20] D. Han, S. Yang, Q. Zhao, L. Zhang, S. Wan, Y. Deng, W. Li, *ACS Appl. Mater. Interfaces* **2024**, *16*, 10916.
[21] M. M. Lerch, M. J. Hansen, W. A. Velema, W. Szymanski, B. L. Feringa, *Nat. Commun.* **2016**, *7*, 12054.
[22] J. Sheng, J. Perego, S. Bracco, P. Cieciórski, W. Danowski, A. Comotti, B. L. Feringa, *Angew. Chem. Int. Ed.* **2024**, *63*, e202404878.
[23] M. Škugor, J. Valero, K. Murayama, M. Centola, H. Asanuma, M. Famulok, *Angew. Chem. Int. Ed.* **2019**, *58*, 6948.
[24] F. Zhao, L. Grubert, S. Hecht, D. Bléger, *Chem. Commun.* **2017**, *53*, 3323.
[25] J. Andréasson, U. Pischel, S. D. Straight, T. A. Moore, A. L. Moore, D. Gust, *J. Am. Chem. Soc.* **2011**, *133*, 11641.
[26] T. Schmitt, L.-Y. Hsu, N. Oberhof, D. Rana, A. Dreuw, E. Blasco, P. Tegeder, *Adv. Funct. Mater.* **2024**, *34*, 2300863.
[27] Z. Zhang, W. Wang, M. O'Hagan, J. Dai, J. Zhang, H. Tian, *Angew. Chem. Int. Ed.* **2022**, *61*, e202205758.
[28] C. Petermayer, H. Dube, *Acc. Chem. Res.* **2018**, *51*, 1153.
[29] M. Dong, A. Babalhavaeji, S. Samanta, A. A. Beharry, G. A. Woolley, *Acc. Chem. Res.* **2015**, *48*, 2662.
[30] S. L. Walden, L. L. Rodrigues, J. Alves, J. P. Blinco, V. X. Truong, C. Barner-Kowollik, *Nat. Commun.* **2022**, *13*, 2943.
[31] J. Hobich, F. Feist, P. Werner, J. A. Carroll, O. Fuhr, E. Blasco, H. Mutlu, C. Barner-Kowollik, *Angew. Chem. Int. Ed.* **2025**, *64*, e202413530.

[32] R. Siewertsen, H. Neumann, B. Buchheim-Stehn, R. Herges, C. Näther, F. Renth, F. Temps, *J. Am. Chem. Soc.* **2009**, *131*, 15594.
[33] X. Xie, F. Hu, Y. Zhou, Z. Liu, X. Shen, J. Fu, X. Zhao, Z. Yu, *Angew. Chem. Int. Ed.* **2023**, *62*, e202300034.
[34] X. Shen, C. Zhang, F. Lan, Z. Su, Y. Zheng, T. Zheng, Q. Xiong, X. Xie, G. Du, X. Zhao, C. Hu, P. Deng, Z. Yu, *Angew. Chem. Int. Ed.* **2022**, *61*, e202209441.
[35] J. Gao, Q. Xiong, X. Wu, J. Deng, X. Zhang, X. Zhao, P. Deng, Z. Yu, *Commun. Chem.* **2020**, *3*, 29.
[36] Q. Xiong, T. Zheng, X. Shen, B. Li, J. Fu, X. Zhao, C. Wang, Z. Yu, *Chem. Sci.* **2022**, *13*, 3571.
[37] I. M. Irshadeen, S. L. Walden, M. Wegener, V. X. Truong, H. Frisch, J. P. Blinco, C. Barner-Kowollik, *J. Am. Chem. Soc.* **2021**, *143*, 21113.
[38] J. Hobich, X. Wu, F. Feist, W. Scheibel, N. Herdt, P. Somers, E. Blasco, H. Mutlu, C. Barner-Kowollik, *Angew. Chem. Int. Ed.* **2025**, e202518815.
[39] F. Pashley-Johnson, X. Wu, J. A. Carroll, S. L. Walden, H. Frisch, A.-N. Unterreiner, F. E. Du Prez, H.-A. Wagenknecht, J. Read de Alaniz, B. L. Feringa, A. Heckel, C. Barner-Kowollik, *Angew. Chem. Int. Ed.* **2025**, e202502651.
[40] L. O. Björn, *Photobiology: The science of light and life*, 3rd ed., Springer, New York, **2015**.
[41] M. F. Hohmann-Marriott, R. E. Blankenship, *Annu. Rev. Plant Biol.* **2011**, *62*, 515.
[42] T. Bach, *Angew. Chem. Int. Ed.* **2015**, *54*, 11294.
[43] S. Chatani, C. J. Kloxin, C. N. Bowman, *Polym. Chem.* **2014**, *5*, 2187.
[44] N. R. B. Boase, *Macromol. Rapid Commun.* **2020**, *41*, 2000305.
[45] F. A. Leibfarth, K. M. Mattson, B. P. Fors, H. A. Collins, C. J. Hawker, *Angew. Chem. Int. Ed.* **2013**, *52*, 199.
[46] P. Lu, D. Ahn, R. Yunis, L. Delafresnaye, N. Corrigan, C. Boyer, C. Barner-Kowollik, Z. A. Page, *Matter* **2021**, *4*, 2172.
[47] S. Aubert, M. Bezagu, A. C. Spivey, S. Arseniyadis, *Nat. Rev. Chem.* **2019**, *3*, 706.
[48] L. Kowalik, J. K. Chen, *Nat. Chem. Biol.* **2017**, *13*, 587.
[49] A. Albini, *Photochem. Photobiol. Sci.* **2016**, *15*, 319.
[50] J. W. Draper, *Philos. Mag.* **1841**, *19*, 195.
[51] T. G. Mayerhöfer, S. Pahlow, J. Popp, *ChemPhysChem* **2020**, *21*, 2029.
[52] H. G. Pfeiffer, H. A. Liebhafsky, *J. Chem. Educ.* **1951**, *28*, 123.
[53] J. R. Lakowicz, *Principles of fluorescence spectroscopy*, 3rd ed., Springer, Baltimore, **2006**.
[54] A. Jablonski, *Nature* **1933**, *131*, 839.
[55] N. A. F. Al-Rawashdeh, in *Macro To Nano Spectroscopy* (Ed.: J. Uddin), IntechOpen, Rijeka, **2012**, pp. 209-250.
[56] M. Y. Berezin, S. Achilefu, *Chem. Rev.* **2010**, *110*, 2641.
[57] P. W. Kamm, PhD thesis, Queensland University of Technology (Brisbane, Australia), **2022**.
[58] P. Sammes, *Q. Rev. Chem. Soc.* **1970**, *24*, 37.
[59] E. G. Leggesse, W.-R. Tong, S. Nachimuthu, T.-Y. Chen, J.-C. Jiang, *J. Photochem. Photobiol. A: Chem.* **2017**, *347*, 78.
[60] M. Spichty, N. J. Turro, G. Rist, J.-L. Birbaum, K. Dietliker, J.-P. Wolf, G. Gescheidt, *J. Photochem. Photobiol. A: Chem.* **2001**, *142*, 209.
[61] T. Morofuji, S. Nagai, Y. Chitose, M. Abe, N. Kano, *Org. Lett.* **2021**, *23*, 6257.
[62] P. J. Behrendt, H.-C. Kim, N. Hampp, *J. Photochem. Photobiol. A: Chem.* **2013**, *264*, 67.
[63] E. Zwicker, L. Grossweiner, N. Yang, *J. Am. Chem. Soc.* **1963**, *85*, 2671.
[64] P. K. Das, J. C. Scaiano, *J. Photochem.* **1980**, *12*, 85.
[65] A. Goulet-Hanssens, F. Eisenreich, S. Hecht, *Adv. Mater.* **2020**, *32*, 1905966.
[66] N. A. Simeth, S. Crespi, M. Fagnoni, B. König, *J. Am. Chem. Soc.* **2018**, *140*, 2940.
[67] H. Qian, S. Pramanik, I. Aprahamian, *J. Am. Chem. Soc.* **2017**, *139*, 9140.
[68] M. Cacciarini, M. B. Nielsen, in *Molecular Photoswitches* (Ed.: Z. L. Pianowski), Wiley-VCH, Weinheim, **2022**, pp. 379-400.
[69] J. Boelke, S. Hecht, *Adv. Opt. Mater.* **2019**, *7*, 1900404.

[70] I. M. Welleman, M. W. H. Hoorens, B. L. Feringa, H. H. Boersma, W. Szymański, *Chem. Sci.* **2020**, *11*, 11672.
[71] P. Klán, J. Wirz, in *Molecular Photoswitches* (Ed.: Z. L. Pianowski), Wiley-VCH, Weinheim, **2022**, pp. 1-18.
[72] S. Nigel Corns, S. M. Partington, A. D. Towns, *Color. Technol.* **2009**, *125*, 249.
[73] G. Chandra, U. Rani, B. Mahto, G. K. Mahato, in *Dye Chemistry - Exploring Colour From Nature to Lab* (Ed.: B. Kumar), IntechOpen, Rijeka, **2024**.
[74] G. S. Hartley, *Nature* **1937**, *140*, 281.
[75] R. Herges, P. Lentes, in *Molecular Photoswitches* (Ed.: Z. L. Pianowski), Wiley-VCH, Weinheim, **2022**, pp. 65-81.
[76] A. Mukherjee, M. D. Seyfried, B. J. Ravoo, *Angew. Chem. Int. Ed.* **2023**, *62*, e202304437.
[77] V. Koch, S. Bräse, in *Molecular Photoswitches* (Ed.: Z. L. Pianowski), Wiley-VCH, Weinheim, **2022**, pp. 39-64.
[78] J. Sun, F. Wang, H. Zhang, K. Liu, *Adv. NanoBiomed. Res.* **2021**, *1*, 2100020.
[79] C. Fedele, T.-P. Ruoko, K. Kuntze, M. Virkki, A. Priimagi, *Photochem. Photobiol. Sci.* **2022**, *21*, 1719.
[80] L. Dong, Y. Feng, L. Wang, W. Feng, *Chem. Soc. Rev.* **2018**, *47*, 7339.
[81] E. Fischer, Y. Hirshberg, *J. Chem. Soc.* **1952**, 4522.
[82] R. Klajn, *Chem. Soc. Rev.* **2014**, *43*, 148.
[83] A. Fagan, M. Bartkowski, S. Giordani, *Front. Chem.* **2021**, *9*, 720087.
[84] N. Shao, Y. Zhang, S. Cheung, R. Yang, W. Chan, T. Mo, K. Li, F. Liu, *Anal. Chem.* **2005**, *77*, 7294.
[85] P. Müller, R. Müller, L. Hammer, C. Barner-Kowollik, M. Wegener, E. Blasco, *Chem. Mater.* **2019**, *31*, 1966.
[86] L. Kortekaas, W. R. Browne, *Chem. Soc. Rev.* **2019**, *48*, 3406.
[87] E. F. Ullman, W. A. Henderson, *J. Am. Chem. Soc.* **1964**, *86*, 5050.
[88] E. F. Ullman, W. A. Henderson, *J. Am. Chem. Soc.* **1966**, *88*, 4942.
[89] E. Hadjoudis, G. Bersos, *J. Photochem.* **1981**, *15*, 47.
[90] R. Larock, M. Doty, S. Cacchi, *J. Org. Chem.* **1993**, *58*, 4579.
[91] E. F. Ullman, J. E. Milks, *J. Am. Chem. Soc.* **1962**, *84*, 1315.
[92] V. Singh, U. Murali Krishna, Vikrant, G. K. Trivedi, *Tetrahedron* **2008**, *64*, 3405.
[93] L. P. Bejcek, R. P. Murelli, *Tetrahedron* **2018**, *74*, 2501.
[94] K. Gao, Y.-G. Zhang, Z. Wang, H. Ding, *Chem. Commun.* **2019**, *55*, 1859.
[95] F. Hu, C. Zhang, Z. Liu, X. Xie, X. Zhao, Y. Luo, J. Fu, B. Li, C. Hu, Z. Su, Z. Yu, *Chem. Sci.* **2023**, *14*, 13254.
[96] M. Hammerich, C. Schütt, C. Stähler, P. Lentes, F. Röhricht, R. Höppner, R. Herges, *J. Am. Chem. Soc.* **2016**, *138*, 13111.
[97] M. Schehr, C. Lanes, J. Weisner, L. Heintze, M. P. Müller, C. Pichlo, J. Charl, E. Brunstein, J. Ewert, M. Lehr, U. Baumann, D. Rauh, U. Knippschild, C. Peifer, R. Herges, *Photochem. Photobiol. Sci.* **2019**, *18*, 1398.
[98] P. Lentes, E. Stadler, F. Röhricht, A. Brahms, J. Gröbner, F. D. Sönnichsen, G. Gescheidt, R. Herges, *J. Am. Chem. Soc.* **2019**, *141*, 13592.
[99] Y. Feng, K. Zhang, X. Gao, W. Yang, J. Wan, H.-R. Fu, H. Guo, Z. Li, *Responsive Mater.* **2025**, *3*, e20250003.
[100] R. Siewertsen, J. B. Schönborn, B. Hartke, F. Renth, F. Temps, *Phys. Chem. Chem. Phys.* **2010**, *13*, 1054.
[101] S. Samanta, C. Qin, A. J. Lough, G. A. Woolley, *Angew. Chem. Int. Ed.* **2012**, *51*, 6452.
[102] W. Moormann, D. Langbehn, R. Herges, *Synthesis* **2017**, *49*, 3471.
[103] P. Kobauri, F. J. Dekker, W. Szymanski, B. L. Feringa, *Angew. Chem. Int. Ed.* **2023**, *62*, e202300681.
[104] G. Cabré, A. Garrido-Charles, À. González-Lafont, W. Moormann, D. Langbehn, D. Egea, J. M. Lluch, R. Herges, R. Alibés, F. Busqué, P. Gorostiza, J. Hernando, *Org. Lett.* **2019**, *21*, 3780.
[105] E. Benchimol, J. Tessarolo, G. H. Clever, *Nat. Chem.* **2024**, *16*, 13.

[106] T. Ko, M. M. Oliveira, J. M. Alapin, J. Morstein, E. Klann, D. Trauner, *J. Am. Chem. Soc.* **2022**, *144*, 21494.
[107] A. P. Demchenko, V. I. Tomin, P.-T. Chou, *Chem. Rev.* **2017**, *117*, 13353.
[108] D. E. Fast, A. Lauer, J. P. Menzel, A.-M. Kelterer, G. Gescheidt, C. Barner-Kowollik, *Macromolecules* **2017**, *50*, 1815.
[109] K. Kalayci, H. Frisch, V. X. Truong, C. Barner-Kowollik, *Nat. Commun.* **2020**, *11*, 4193.
[110] F. Feist, J. P. Menzel, T. Weil, J. P. Blinco, C. Barner-Kowollik, *J. Am. Chem. Soc.* **2018**, *140*, 11848.
[111] J. Bachmann, C. Petit, L. Michalek, Y. Catel, E. Blasco, J. P. Blinco, A.-N. Unterreiner, C. Barner-Kowollik, *ACS Macro Lett.* **2021**, *10*, 447.
[112] R. T. Michenfelder, F. Pashley-Johnson, V. Guschin, L. Delafresnaye, V. X. Truong, H.-A. Wagenknecht, C. Barner-Kowollik, *Adv. Sci.* **2024**, *11*, 2402011.
[113] S. L. Walden, P. H. D. Nguyen, H.-K. Li, X. Liu, M. T. N. Le, L. Xian Jun, C. Barner-Kowollik, V. X. Truong, *Nat. Commun.* **2023**, *14*, 8298.
[114] M. D. Hall, B. Zhao, E. Liarou, T. Junkers, D. Haddleton, *Chem. Sci.* **2025**, *16*, 17436.
[115] S. F. Kim, H. Schwarz, J. Jurczyk, B. R. Nebgen, H. Hendricks, H. Park, A. Radosevich, M. W. Zuerch, K. Harper, M. C. Lux, C. S. Yeung, R. Sarpong, *J. Am. Chem. Soc.* **2024**, *146*, 5580.
[116] S. L. Walden, J. A. Carroll, A.-N. Unterreiner, C. Barner-Kowollik, *Adv. Sci.* **2024**, *11*, 2306014.
[117] J. A. Carroll, F. Pashley-Johnson, H. Frisch, C. Barner-Kowollik, *Chem. Eur. J.* **2024**, *30*, e202304174.
[118] J. A. Carroll, F. Pashley-Johnson, M. Klein, T. Stephan, A. K. Pandey, M. Walter, A.-N. Unterreiner, C. Barner-Kowollik, *J. Am. Chem. Soc.* **2025**, *147*, 26643.
[119] A. P. Demchenko, *Luminescence* **2002**, *17*, 19.
[120] A. P. Demchenko, in *Methods in Enzymology, Vol. 450* (Eds.: L. Brand, M. L. Johnson), Academic Press, San Diego, **2008**, pp. 59-78.
[121] N. Corrigan, C. Boyer, *ACS Macro Lett.* **2019**, *8*, 812.
[122] N. Corrigan, M. Ciftci, K. Jung, C. Boyer, *Angew. Chem. Int. Ed.* **2021**, *60*, 1748.
[123] V. Hahn, F. Mayer, M. Thiel, M. Wegener, *OPN* **2019**, *30*, 28.
[124] J. Fischer, G. von Freymann, M. Wegener, *Adv. Mater.* **2010**, *22*, 3578.
[125] T. N. Eren, F. Feist, K. Ehrmann, C. Barner-Kowollik, *Angew. Chem. Int. Ed.* **2023**, *62*, e202307535.
[126] S. Bialas, L. Michalek, D. E. Marschner, T. Krappitz, M. Wegener, J. Blinco, E. Blasco, H. Frisch, C. Barner-Kowollik, *Adv. Mater.* **2019**, *31*, 1807288.
[127] C. Barner-Kowollik, M. Bastmeyer, E. Blasco, G. Delaittre, P. Müller, B. Richter, M. Wegener, *Angew. Chem. Int. Ed.* **2017**, *56*, 15828.
[128] C. W. J. Lim, K. Q. Le, Q. Lu, C. H. Wong, *IEEE Potentials* **2016**, *35*, 18.
[129] C.-Y. Liaw, M. Guvendiren, *Biofabrication* **2017**, *9*, 024102.
[130] J.-Y. Lee, J. An, C. K. Chua, *Appl. Mater. Today* **2017**, *7*, 120.
[131] C. A. Spiegel, M. Hippler, A. Münchinger, M. Bastmeyer, C. Barner-Kowollik, M. Wegener, E. Blasco, *Adv. Funct. Mater.* **2020**, *30*, 1907615.
[132] J. Zhang, P. Xiao, *Polym. Chem.* **2018**, *9*, 1530.
[133] R. Nurmi, *Team Perform. Manag.* **1996**, *2*, 9.
[134] M. Herder, Y. Garmshausen, M.-P. C. Tauber, Y. Arzhangnia, M. Reuter, *Proc. SPIE 13381* (**2025**), 133810C.
[135] N. F. König, M. Reuter, M. Reuß, C. S. F. Kromer, M. Herder, Y. Garmshausen, B. Asfari, E. Israel, L. Vasconcelos Lima, N. Puvati, J. Leonhard, L. Madalo, S. Heuschkel, M. Engelhard, Y. Arzhangnia, D. Radzinski, *Adv. Mater.* **2025**, *37*, 2413391.
[136] P. W. Kamm, L. L. Rodrigues, S. L. Walden, J. P. Blinco, A.-N. Unterreiner, C. Barner-Kowollik, *Chem. Sci.* **2022**, *13*, 531.
[137] G. Barany, R. Merrifield, *J. Am. Chem. Soc.* **1977**, *99*, 7363.
[138] M. Schelhaas, H. Waldmann, *Angew. Chem. Int. Ed.* **1996**, *35*, 2056.

[139] H. Frisch, D. E. Marschner, A. S. Goldmann, C. Barner-Kowollik, *Angew. Chem. Int. Ed.* **2018**, *57*, 2036.
[140] J.-W. Kim, M. J. Allen, E. A. Recker, L. M. Stevens, H. L. Cater, A. Uddin, A. Gao, W. Eckstrom, A. J. Arrowood, G. E. Sanoja, M. A. Cullinan, B. D. Freeman, Z. A. Page, *Nat. Mater.* **2025**, *24*, 1116.
[141] I. Cazin, K. Plevová, W. Alabiso, E. Vidović, S. Schlögl, *Adv. Eng. Mater.* **2024**, *26*, 2301699.
[142] H. Frisch, F. R. Bloesser, C. Barner-Kowollik, *Angew. Chem. Int. Ed.* **2019**, *58*, 3604.
[143] U. Shaukat, A. Thalhamer, E. Rossegger, S. Schlögl, *Addit. Manuf.* **2024**, *79*, 103930.
[144] M. Bergoglio, E. Rossegger, S. Schlögl, T. Griesser, C. Waly, F. Arbeiter, M. Sangermano, *Polymers* **2024**, *16*, 1510.
[145] U. Shaukat, E. Rossegger, S. Schlögl, *Polymers* **2022**, *14*, 2449.
[146] E. A. Recker, X. Chen, J.-W. Kim, Z. A. Page, *ACS Cent. Sci.* **2025**, *11*, 1527.
[147] J. J. Schwartz, A. J. Boydston, *Nat. Commun.* **2019**, *10*, 791.
[148] N. D. Dolinski, Z. A. Page, E. B. Callaway, F. Eisenreich, R. V. Garcia, R. Chavez, D. P. Bothman, S. Hecht, F. W. Zok, C. J. Hawker, *Adv. Mater.* **2018**, *30*, 1800364.
[149] E. Rossegger, J. Strasser, R. Höller, M. Fleisch, M. Berer, S. Schlögl, *Macromol. Rapid Commun.* **2023**, *44*, 2200586.
[150] K. C. H. Chin, G. Ovsepyan, A. J. Boydston, *Nat. Commun.* **2024**, *15*, 3867.
[151] X. Wu, K. Ehrmann, C. T. Gan, B. Leuschel, F. Pashley-Johnson, C. Barner-Kowollik, *Adv. Mater.* **2025**, *37*, 2419639.
[152] T. Hortobágyi, P. DeVita, *Exerc. Sport Sci. Rev.* **2006**, *34*, 29.
[153] P. Müller, M. M. Zieger, B. Richter, A. S. Quick, J. Fischer, J. B. Mueller, L. Zhou, G. U. Nienhaus, M. Bastmeyer, C. Barner-Kowollik, M. Wegener, *ACS Nano* **2017**, *11*, 6396.
[154] M. He, Z. Zhang, C. Cao, G. Zhou, C. Kuang, X. Liu, *Laser Photonics Rev.* **2022**, *16*, 2100229.
[155] C. Ding, X. Liu, Q. Liu, D. Zhu, M. Luo, X. Gao, Z. Yang, Q. Sun, Q. Qian, X. Shen, C. Cao, S. You, L. Xu, M. He, Y. Liu, C. Kuang, X. Liu, *Laser Photonics Rev.* **2024**, *18*, 2300645.
[156] N. Liaros, J. T. Fourkas, *Opt. Mater. Express* **2019**, *9*, 3006.
[157] M. Mao, J. He, X. Li, B. Zhang, Q. Lei, Y. Liu, D. Li, *Micromachines* **2017**, *8*, 113.
[158] H. Vijayamohanan, E. F. Palermo, C. K. Ullal, *Chem. Mater.* **2017**, *29*, 4754.
[159] Y. Chen, *Microelectron. Eng.* **2015**, *135*, 57.
[160] J. Fischer, M. Wegener, *Opt. Mater. Express* **2011**, *1*, 614.
[161] L. Möckl, D. C. Lamb, C. Bräuchle, *Angew. Chem. Int. Ed.* **2014**, *53*, 13972.
[162] B. Harke, W. Dallari, G. Grancini, D. Fazzi, F. Brandi, A. Petrozza, A. Diaspro, *Adv. Mater.* **2013**, *25*, 904.
[163] J. Fischer, J. B. Mueller, A. S. Quick, J. Kaschke, C. Barner-Kowollik, M. Wegener, *Adv. Opt. Mater.* **2015**, *3*, 221.
[164] A. Marco, M. Villabona, T. N. Eren, F. Feist, G. Guirado, R. M. Sebastián, J. Hernando, C. Barner-Kowollik, *Adv. Funct. Mater.* **2025**, *35*, 2415431.
[165] M. Villabona, S. Wiedbrauk, F. Feist, G. Guirado, J. Hernando, C. Barner-Kowollik, *Org. Lett.* **2021**, *23*, 2405.
[166] X. Kuang, D. J. Roach, J. Wu, C. M. Hamel, Z. Ding, T. Wang, M. L. Dunn, H. J. Qi, *Adv. Funct. Mater.* **2019**, *29*, 1805290.
[167] S. Shinde, R. Mane, A. Vardikar, A. Dhumal, A. Rajput, *Eur. Polym. J.* **2023**, *197*, 112356.
[168] J. Chen, C. Virrueta, S. Zhang, C. Mao, J. Wang, *Mater. Today* **2024**, *77*, 66.
[169] A. M. Doerr, J. M. Burroughs, S. R. Gitter, X. Yang, A. J. Boydston, B. K. Long, *ACS Catal.* **2020**, *10*, 14457.
[170] D. Martella, S. Nocentini, D. Nuzhdin, C. Parmeggiani, D. S. Wiersma, *Adv. Mater.* **2017**, *29*, 1704047.
[171] E. Yarali, M. J. Mirzaali, A. Ghalayaniesfahani, A. Accardo, P. J. Diaz-Payno, A. A. Zadpoor, *Adv. Mater.* **2024**, *36*, 2402301.
[172] L.-Y. Hsu, C. A. Spiegel, E. Blasco, in *Smart Materials in Additive Manufacturing* (Eds.: M. Bodaghi, A. Zolfagharian), Elsevier, Amsterdam, **2022**, pp. 231-263.
[173] S. Y. Hann, H. Cui, M. Nowicki, L. G. Zhang, *Addit. Manuf.* **2020**, *36*, 101567.

[174] P. W. Kamm, J. P. Blinco, A.-N. Unterreiner, C. Barner-Kowollik, *Chem. Commun.* **2021**, *57*, 3991.
[175] J. P. Olson, M. R. Banghart, B. L. Sabatini, G. C. R. Ellis-Davies, *J. Am. Chem. Soc.* **2013**, *135*, 15948.
[176] L. M. Stevens, E. A. Recker, K. A. Zhou, V. G. Garcia, K. S. Mason, C. Tagnon, N. Abdelaziz, Z. A. Page, *Adv. Mater. Technol.* **2023**, *8*, 2300052.
[177] S. M. Müller, S. Schlögl, T. Wiesner, M. Haas, T. Griesser, *ChemPhotoChem* **2022**, *6*, e202200091.
[178] L. M. Stevens, N. T. Almada, H. S. Kim, Z. A. Page, *Acc. Chem. Res.* **2025**, *58*, 250.
[179] I. Mohamed Irshadeen, V. X. Truong, H. Frisch, C. Barner-Kowollik, *Chem. Commun.* **2023**, *59*, 11959.
[180] M. Higgins, *UV+EB Technology* **2016**, *2*, 46.
[181] V. Heiskanen, M. R. Hamblin, *Photochem. Photobiol. Sci.* **2018**, *17*, 1003.
[182] K. Ueura, T. Satoh, M. Miura, *J. Org. Chem.* **2007**, *72*, 5362.
[183] A. Bagheri, J. Jin, *ACS Appl. Polym. Mater.* **2019**, *1*, 593.
[184] D. J. Haloi, S. Roy, N. K. Singha, *J. Polym. Sci. Part A: Polym. Chem.* **2009**, *47*, 6526.
[185] J. Hintermeyer, A. Herrmann, R. Kahlau, C. Goiceanu, E. A. Rössler, *Macromolecules* **2008**, *41*, 9335.
[186] L. Cui, Y. Zhao, A. Yavrian, T. Galstian, *Macromolecules* **2003**, *36*, 8246.
[187] S. C. Gauci, A. Vranic, E. Blasco, S. Bräse, M. Wegener, C. Barner-Kowollik, *Adv. Mater.* **2024**, *36*, 2306468.
[188] R. Palucci Rosa, G. Rosace, *Macromol. Mater. Eng.* **2021**, *306*, 2100345.
[189] J. Y. Han, S. Warshawsky, D. L. DeVoe, *Sci. Rep.* **2021**, *11*, 10980.
[190] H. J. Sanders, H. F. Keag, H. S. McCullough, *Ind. Eng. Chem.* **1953**, *45*, 2.
[191] F. Pashley-Johnson, R. Munaweera, S. I. Hossain, S. C. Gauci, L. Delafresnaye, H. Frisch, M. L. O'Mara, F. E. Du Prez, C. Barner-Kowollik, *Nat. Commun.* **2024**, *15*, 6033.
[192] A. S. Quick, H. Rothfuss, A. Welle, B. Richter, J. Fischer, M. Wegener, C. Barner-Kowollik, *Adv. Funct. Mater.* **2014**, *24*, 3571.
[193] M. M. Zieger, P. Müller, E. Blasco, C. Petit, V. Hahn, L. Michalek, H. Mutlu, M. Wegener, C. Barner-Kowollik, *Adv. Funct. Mater.* **2018**, *28*, 1801405.
[194] T. N. Eren, J. Liang, J. L. G. Schneider, M. Wegener, J. Bauer, K. Ehrmann, F. Feist, C. Barner-Kowollik, *Adv. Funct. Mater.* **2025**, e02876.
[195] J. P. Menzel, B. B. Noble, A. Lauer, M. L. Coote, J. P. Blinco, C. Barner-Kowollik, *J. Am. Chem. Soc.* **2017**, *139*, 15812.
[196] Y. Fu, N. A. Simeth, R. Toyoda, R. Brilmayer, W. Szymanski, B. L. Feringa, *Angew. Chem. Int. Ed.* **2023**, *62*, e202218203.
[197] Y. Fu, G. Alachouzos, N. A. Simeth, M. Di Donato, M. F. Hilbers, W. J. Buma, W. Szymanski, B. L. Feringa, *Chem. Sci.* **2023**, *14*, 7465.
[198] F. Xu, L. Pfeifer, S. Crespi, F. K.-C. Leung, M. C. A. Stuart, S. J. Wezenberg, B. L. Feringa, *J. Am. Chem. Soc.* **2021**, *143*, 5990.
[199] T. Halbritter, C. Kaiser, J. Wachtveitl, A. Heckel, *J. Org. Chem.* **2017**, *82*, 8040.
[200] R. T. Michenfelder, L. Delafresnaye, V. X. Truong, C. Barner-Kowollik, H.-A. Wagenknecht, *Chem. Commun.* **2023**, *59*, 4012.
[201] H. E. Gottlieb, V. Kotlyar, A. Nudelman, *J. Org. Chem.* **1997**, *62*, 7512.
[202] O. V. Dolomanov, L. J. Bourhis, R. J. Gildea, J. A. K. Howard, H. Puschmann, *J. Appl. Cryst.* **2009**, *42*, 339.
[203] G. Sheldrick, *Acta Cryst. A* **2015**, *71*, 3.
[204] G. Sheldrick, *Acta Cryst. C* **2015**, *71*, 3.
[205] S. Roy, P. Phukan, *Tetrahedron Lett.* **2015**, *56*, 2426.